Doctoral thesis

Multiscale coupling of X-ray physics and engineering mechanics, for supporting Computed Tomography-based orthopedics and bone remodeling

submitted in satisfaction of the requirements for the degree of Doctor of Science in Civil Engineering of the Vienna University of Technology, Faculty of Civil Engineering

---

Dissertation

Mehrskalige Kopplung von Strahlenphysik und Ingenieurmechanik, als Unterstützung für Computertomographie-basierte Orthopädie und Knochenbiologie

ausgeführt zum Zwecke der Erlangung des akademischen Grades eines Doktors der technischen Wissenschaft eingereicht an der Technischen Universität Wien Fakultät für Bauingenieurwesen

von
Romane Blanchard
Matrikelnummer: 0929438
Tivoligasse 21/5, 1120 Wien

Prüfer und Betreuer: Univ.-Prof. Dipl.Ing. Dr. techn. Christian Hellmich
Institut für Mechanik der Werkstoffe und Strukturen,
Technische Universität Wien

Prüferin: Prof. Marie-Christine Ho Ba Tho
UMR 7338 : BioMécanique et BioIngénierie (BMBI)
Université de Technologie de Compiègne - France

Wien, September 2014

ABSTRACT

While Computer Tomography has become a standard tool in clinical biomechanics and biomaterials studies, much of the physical and chemical information contained in such scans remain unused. Instead, the grey values of the Computed Tomographs are, as a rule, directly related, by some empirical functions, to mass density or to mechanical properties of interest. However, a suitable combination of X-ray physics fundamentals, multiscale continuum micromechanics, and Finite Element analyses, as reviewed shortly in **Chapter 1**, indeed bears the potential for transforming the aforementioned, somehow hidden information, into tissue composition and microstructure, its heterogeneous distribution across investigated organs or implants, and the corresponding mechanical properties resulting from microscopic interaction of material constituents across several length scales. Chapters 2 to 5 contain corresponding examples for increasingly mature CT-to-mechanics conversion schemes, dealing with bone biomaterials and bony organs at different scales. Chapter 6 provides an outlook for extending such studies even to evolving biological systems, by combining trabecular bone micromechanics with advanced bone remodeling algorithms.

In **Chapter 2**, the voxel-specific volume fractions of mineral, collagen, and water are derived from the measured X-ray attenuation information quantified in terms of grey values , by accounting for tissue-independent bilinear relations between mineral and collagen content in extracellular bone tissue (J. Theor. Biol. 287: 115, 2011). The aforementioned volume fractions enter a micromechanics representation of bone tissue, so as to deliver elastic properties in terms of voxel-specific stiffness tensors. The insertion of these properties into a FE simulation reveals that the choice of appropriate material properties influences the strain energy density in the extracellular matrix (governing the stiffness of the organ), and also affects the discretization level needed for obtaining converged numerical results.

In **Chapter 3**, driving the field of Computed Tomography towards more quantitative, rather than qualitative, approaches, a new evaluation method is presented, which uses the unique linear relationship between grey values and X-ray attenuation coefficients, together with the energy-dependence of the latter, in order to identify the average X-ray energy employed in the scanner, and the nanoporosity of a tricalcium phosphate scaffold.

This approach is extended in **Chapter 4** by re-constructing the linear relation between the clinically accessible grey values making up a Computed Tomograph and the X-ray attenuation coefficients quantifying the intensity losses from which the image is actually reconstructed. Therefore, X-ray attenuation averaging at

different length scales and over different tissues is combined with recently identified "universal" composition characteristics of the latter. This gives access not only to the normally non-disclosed X-ray energy employed in the CT-device, but particularly to *in vivo*, patient- and location-specific bone composition variables, such as voxel-specific mass density, as well as mineral and collagen contents. This is shown by example of a third lumbar vertebra. The corresponding vascular porosity values enter a continuum micromechanics model for bone (Ultrasonics 54:1251, 2014), which thereupon delivers voxel-specific elastic properties. The latter are mapped onto a 3D Finite Element mesh developed from the same patient data. The stress states resulting from corresponding Finite Element analyses are inputs for a six-scale strength upscaling model for bone, so as to compute element-specific proportionality factors to material yield or material failure. The implementation of patient-specific material properties highlights that simulations with averaged properties underestimate the fracture risk in bone, while the new approach reliably considers the effect of the material heterogeneities arising from bone remodeling triggered by everyday spinal loading; and is also relevant for even more heterogeneous, pathological cases.

The last work, presented in **Chapter 5**, is using a multiscale analytical approach, which combines bone structural information at multiple scales to the remodeling cellular activities, and more precisely the mechanical stimulus sense by the osteocytes, in order to form an efficient, accurate, and beneficial framework for the prognosis of changes in bone properties due to aging or pathologies.

This latter approach, once combined with the CT-based technique covered in Chapters 2 to 4, holds the promise to establish new forms of simulation-supported therapeutic activities in orthopaedy.

KURZFASSUNG

Obwohl die Computertomographie die Medizin, und dort insbesondere die biomechanische und werkstoffbezogene Forschung, durchdrungen hat, bleibt ein Grossteil der in CT-Bildern enthaltenen physikalischen und chemischen Informationen ungenutzt. Stattdessen werden Grauwerte von CT-Aufnahmen normalerweise direkt, mittels empirischer Methoden, mit Massendichten oder mechanischen Größen in Verbindung gebracht. Allerdings hat eine geeignete Kombination von strahlenphysikalischen und kontinuumsmikromechanischen Gesetzen in Verbindung mit der Finite Elemente Methode (**Kapitel 1** liefert einen Überblick ber entsprechende Grundlagen) durchaus das Potential, die zuvor genannten, gleichsam versteckten physikalischen und chemischen Informationen zu verwenden, um Aufschlüsse über Gewebszusammensetzung und -mikrostruktur, deren heterogene Verteilung über das untersuchte Organ oder Implantat, und daraus folgende mechanische Eigenschaften zu erhalten. Die Kapitel 2 bis 5 beschreiben zunehmend ausgereifte Schemata zur Übersetzung von CT-Daten in mechanische Kenngrößen, welche auf verschiedenen Längenskalen auf verschiedene Biomaterialien und Organe angewendet werden.

Kapitel 2 beschreibt die Bestimmung der Voxel-spezifischen Mineral-, Kollagen- und Wassergehalte aus CT-Daten, auf Basis einer gewebsunabhängigen Regel für die Zusammensetzung extrazellulären Materials (J. Theor .Biol. 287, 115, 2011). Entsprechende Volumsanteile dienen als Input für eine mikromechanische Repräsentierung von Knochengewebe, zwecks Lieferung von Voxel-spezifischen Steifigkeitstensoren. Verwendung dieser Tensorfelder in einer FE Simulation macht deutlich, dass die Wahl adäquater Materialeigenschaften sowohl die Verzerrungsenergie in der extrazellulären Matrix massgeblich beeinflusst (und damit die vorhergesagte Stetigkeit des Organs), als auch den Diskretisierungsaufwand für konvergente Lösungen festlegt.

Kapitel 3 ist ein Beitrag in Richtung quantitativerer Auswertungsmethoden für CT-Daten: Ein neuer Ansatz erlaubt die Rckbestimmung der für eine CT-Aufnahme verwendeten massgeblichen Photonenenergie, aus der Existenz eines eindeutigen Zusammenhanges zwischen Grauwerten und Röntgen- Abschwächungskoeffizienten, und der Energieabhängigkeit letzterer. Dies wird zur Bestimmung der Nanoporositätsverteilungen von resorbierbaren Tri-Kalzium-Phosphat-Keramiken für den Knochenersatz verwendet.

Dieser Ansatz wird in **Kapitel 4** modifiziert und weiterentwickelt, zwecks Studiums von klinischen CT-Daten eines Lendenwirbels. Dies liefert Voxel-spezifische Massendichten, sowie Mineral- und Kollagengehalte, und dann mittels eines kon-

tinuumsmikromechanischen Modells (Ultrasonics 54: 1251, 2014), Voxel-spezifische Elastizitätstensorkomponenten als Input für ein FE Modell. Letzteres erlaubt die Bestimmung von typischen Spannungszuständen unter normaler physiologischer Belastung, welche dann zur Sicherheitsanalyse des Organs herangezogen werden. Dazu werden sie proportional gesteigert und ihre Auswirkungen auf die Knochen-mikrostruktur mittels eines Mehrskalen-Elastoplastizitätsmodells untersucht: Bei Reißen der Kollagenfasern ist die Knochenmaterialfestigkeit erreicht. Zugehörige Simulationen mit räumlich gemittelten Materialeigenschaften unterschätzen das Bruchrisiko beachtlich, während die Berücksichtigung heterogener Materialeigen-schaftsverteilungen realistische Sicherheitswerte liefert.

Kapitel 5 behandelt einen analytischen Mehrskalenansatz, welcher mittels Mikro-mechanik die Stimulation von Knochenzellen quantifiziert, sowie die daraus er-wachsenden Umbauten des Gewebes.

Kombination dieses Verfahren mit den in Kapiteln 2 bis 4 beschriebenen En-twicklungen lässt neue Formen simulationsunterstützter Therapiemethoden in der Orthopädie erhoffen.

Il suivait son idée.
C'était une idée fixe,
et il était surpris de ne pas avancer.
Jacques Prévert

ACKNOWLEDGEMENTS

CONTENTS

Contents

Contents

LIST OF FIGURES

List of Figures

LIST OF TABLES

INTRODUCTORY REMARKS

1.1 COMPUTED TOMOGRAPHY

The development of Computed Tomography has been encouraged as a non-destructive method to study the composition and the microstructure of materials and living organisms. The two techniques giving the images used further in this the-
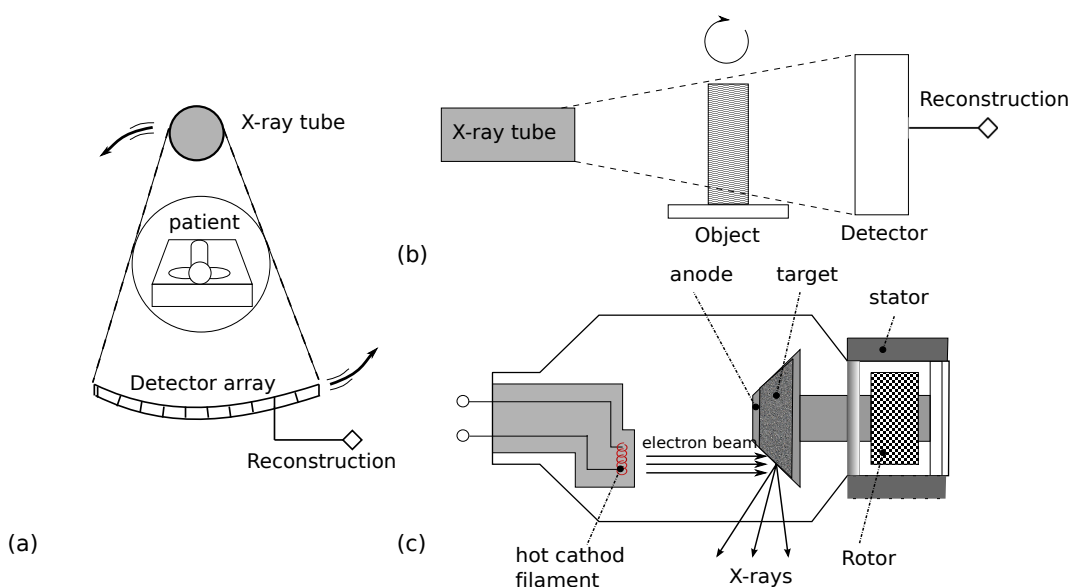
Figure 1.1.: Illustration of: (a) a clinical CT installation, (b) a microCT installation, and (c) an X-ray tube

sis are the clinical CT, with a pixel resolution of a mm, and micro-CT with pixel resolution 1-10 μm, they are illustrated Fig.1.1. More techniques are available for research (for instance using synchrotron radiation) or clinical purposes (dual CT, spiral CT, etc.), however, they are out of the scope of this work and will not be further described. In the following, the theoretical background of Computed Tomography in order to shed light on the physical principles underlying the mechanical and compositional studies published and collected in this thesis. As demonstrated in the next section, the theory of CT induces the need of scanning the object at dif-

ferent angles, spanning an entire demi-circle of 180 degrees around the scanned object. In the microCT system, this can be achieved by rotating the small objects within a fixed X-ray emitting and sensing device, while in a clinical setting, the patient has to be motionless - hence, X-ray source and detector need to rotate in such a system.

1.1.1 *Generation of X-ray beam*

X-rays are electromagnetic radiations, such as visible light, infrared, ultraviolet, etc., situated at the end of the electromagnetic spectrum.
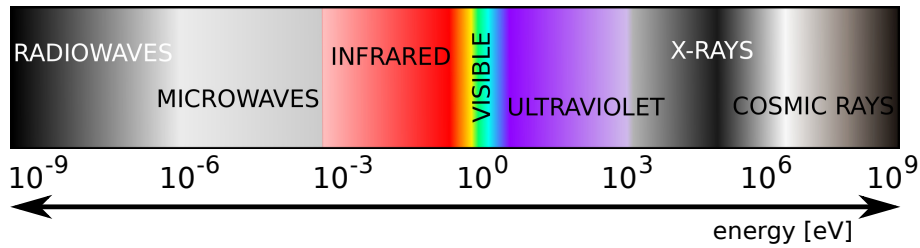
Figure 1.2.: Electromagnetic spectrum

The energy E of each X-ray photon is proportional to its frequency ν [229] and reads as:

$$E = h\nu = \frac{hc}{\lambda} \tag{1.1}$$

with h the Planck's constant amounting to $6.63 \cdot 10^{-34}$ J.s, c the speed of light, and λ the wavelength of the X-ray beam. The wavelength of diagnostic X-rays usually lies between 0.1 and 0.01 nm, also expressed in eV: between 12.4 and 124 keV.

Practically, the X-ray beam is generated in a so-called X-ray tube, see Fig.1.1(c) a vacuum tube that uses high voltage to accelerate the electrons released by a hot cathode, or negative electrode, to a high voltage. The energy of the freed electron is usually expressed in electron-volt unit (eV), which represents the amount of kinetic energy reached by an accelerated electron across an electrical potential. The resulting value of the unit amounts to: 1 eV=$1.602 \cdot 10^{-19}$ J. The energy attained by the electrons produced by the cathode $\mathcal{E}_{cathode}$ and accelerated across a potential difference $V_{cathode}$ is related to the voltage of the tube by:

$$\mathcal{E}_{cathode} = V_{tube} \times N_{\mathcal{E}} \tag{1.2}$$

After leaving the cathode, the accelerated electrons are projected onto the anode, a target material, where different types of collisions take place. The largest number of these collisions are leading to an ionization of the target atoms and do not produce X-ray radiations but secondary electrons, knocked out of the target
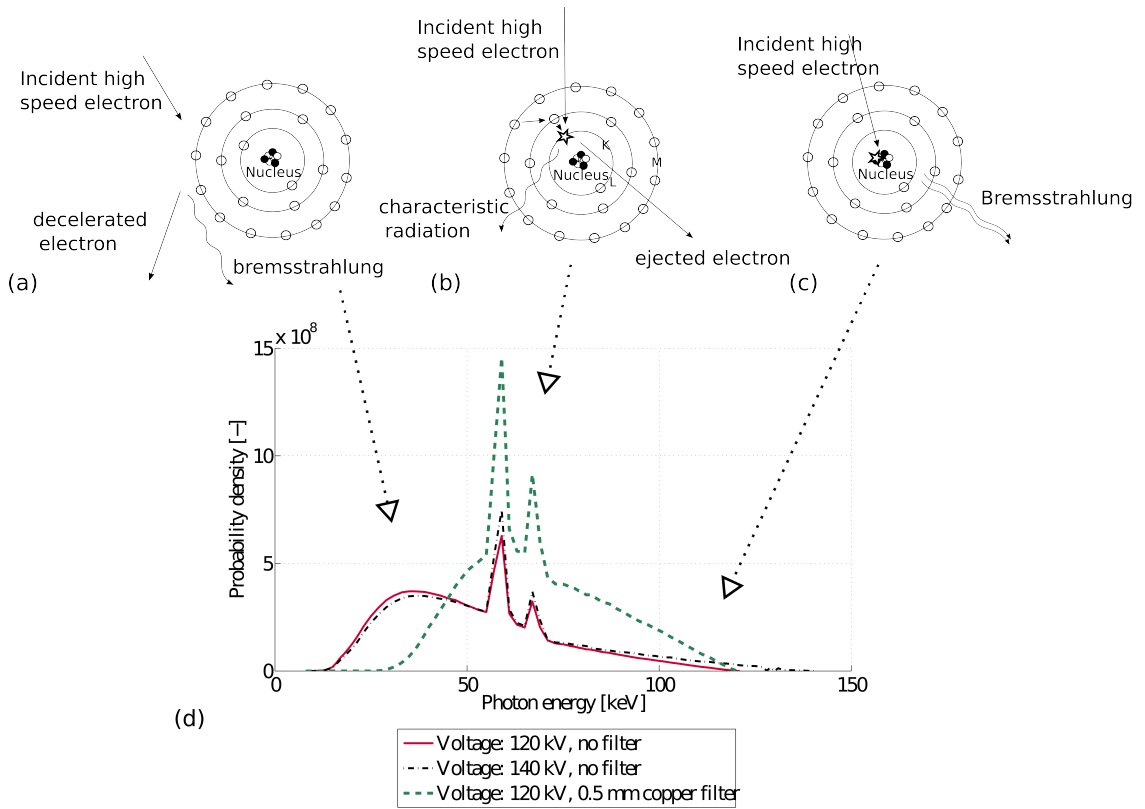
Figure 1.3.: Collisions on the target and delivered X-ray spectrum: a) Three mechanisms of collision and creation of X-ray photons; b) X-ray spectrum delivered by a clinical X-ray [140] with a tungstene anode for different voltages cathode voltage and with or without filter. Illustration inspired from [127]

atoms after collisions, and heat [127]. 99% of the input energy is converted to heat. Moreover, the last 1% of input energy is dissipated in three more types of interactions, which are generating X-rays:

- The first type of interaction can be described as the following: An electron approaches the nucleus of an atom due to the attraction between the positive nucleus and the negative electron, and suffers of radiation loss, also called *Bremsstrahlung* radiation [116], see Figure 1.3a). The total intensity of the *Bremsstrahlung* radiation I, resulting from a charged particle of mass m and charge $z \cdot e$ on the target nuclei with charge $Z \cdot e$ reads as [25, 127]

$$I \propto \frac{Z^2 z^4 e^6}{m^2} \tag{1.3}$$

19

The intensity of the radiation produced by this type of collision can be increased by reducing the mass of the incident particle and increasing the atomic number Z of the target material. Therefore are high-speed electrons used as incident particles and Tungsten, Tungsten/Rhenium alloy, Molybdenum, or Rhodium, having respectively Z=74,75,42, and 45 are chosen as target materials. This collisions are responsible for the low-energy photons of Fig. 1.3(d).

• The second interaction with the target consists in the collision of an high-speed electron with an electron of the inner shell of the target atom liberates the latter electron [127]. The hole produced by the collision is filled by an electron of the outer shell. This mechanism generates a characteristic radiation. The energy of the emitted X-ray photon depends on the shell where the collision takes place and its binding energy, well defined in the Bohr model of the atom [22]. Hence, this energy is the difference between the energies of two shells. The characteristic X-ray energy is therefore unique for the chosen target material. For instance, the peaks illustrated Fig 1.3(d) are the characteristic energy needed for an electron to go from the M and L shells to the most inner shell of a tungsten atom, building up the target material in this example.

• In the last interaction, an electron collides directly with the nucleus of the target atom, the entire energy is dissipated as *bremsstrahlung* and appears at the end of the X-ray spectrum. The probability of such collision is very low and such high energy photons are very rare [127]. This high energy photons are visible at the end of the curve Fig. 1.3(d) and are highly dependent on the voltage of the X-ray tube. Therefore, the indication of the electrical potential in kV, often the only available indication about the energy inside the CT, gives only information about the maximum energy which is emitted from the target and hits the scanned object, but does not indicate the most frequent energy created by the tube. The variation of the photon energy spectrum caused by the modification of the cathode's voltage is illustrated Fig.1.3(d).

1.1.2 *Attenuation of the X-ray beam*

The X-ray beam generated by the collision with the anode conveys to the objects and its photons are either being absorbed by the atoms of the material when meeting the scanned object, or scattered away from their original direction of travel. Two main mechanisms are responsible for this phenomenon of attenuation [127, 144]
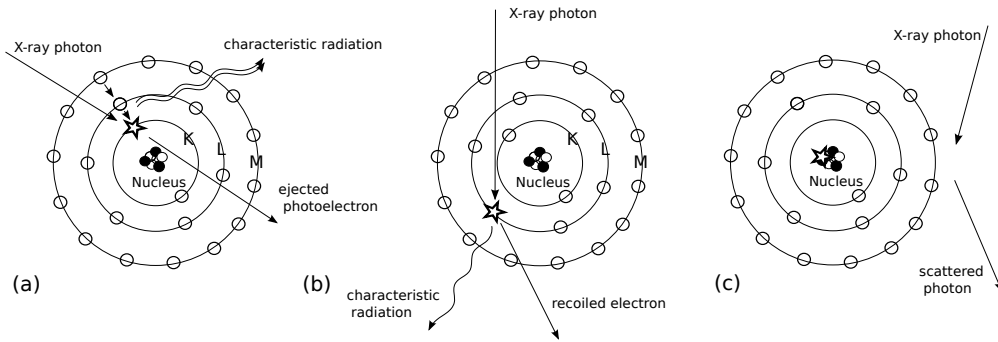
Figure 1.4.: Collision between the X-ray photons and the studied object: (a) with photoelectric effect, (b) with Compton effect, and (c) with scattering effect

- The photoelectric effect: The X-ray photon collides a tightly bound inner electron in an atom. The latter electron uses this energy to free itself from its shell and is ejected of the atom with the energy left as kinetic energy, see Fig.1.4. An electron of the outer shell fills the resulting hole [81]. From this interaction results a positive ion, a photoelectron, and a photon of characterisitic radiation. In biological tissues, the bounding energies are very low and the X-rays produced by the collisions are reabsorbed very fast by the surrounding elements. The probability of the photoelectric interaction can be written as [127, 205]:

$$P_{PE} \propto \frac{Z^3}{E^3} \tag{1.4}$$

Consequently, a small difference in atomic number produce a great difference in P_{PE} and leads to a better contrast between different tissues. This interaction is therefore driving the low-contrast differentiation of tissues.

- The Compton effect: the energy of the incident X-ray photon is much higher than the binding energy of the electron. The Compton interaction produces a positive ion, a "recoiled" electron, and a scattered photon [55]. The deflected photon may undergo additional collisions. The probability of a Compton interaction depends on the electron density of the material, not the atomic number Z. This property explains the consequently little contrast information given by this type of interaction. Therefore, most of the new medical devices minimize the impact of the Compton effect by collimation before detection, or by algorithmic correction.

An additional type of interaction, which does not consist in a collision but of the scattering of the incident X-ray photon when approaching the atom, is called coherent scattering. Although this mechanism of photon emission is also studied

for clinical applications [131], it is yet the least interesting interaction with the matter.

As the mechanisms responsible for attenuation have been previously defined, the total attenuation of the beam can logically be introduced as the photon loss rates due respectively to the photoelectric effect τ, the Compton effect σ, and the scattering effect σ_r [144]:

$$\mu = \tau + \sigma + \sigma_r \tag{1.5}$$

Consequently, the attenuation coefficients depends mainly on the ability of the atom to loose electrons on their outer and inner shells. This is not only a question of density or chemical composition but of how much energy is necessary to free one electron of the shells.

1.1.3 *Detection of the attenuated photon energy*

The detector has the task to transform the incident radiations into an amplified electrical signal, and to convert it from analog to digital form. There are two conversion principles mainly used for CT detectors: the ionization chambers, generally filled with Xenon gas under high pressure, and the scintillation detectors in the form of crystals or ceramics materials. The first technology is using the ionization of the xenon atoms under the effect of the detected X-rays in order to create an electrical potential between two electrodes placed in the chamber. In the second technology, luminescent materials are used to absorb the energy and produce light. This scintillation is measured by photo diodes which transforms the radiation in an electrical potential [127, 144, 145]. Although the choice of a detector influences the presence of artifacts, the image contrast, and the effective energy of the scanner, this topic will not be further developed in this work as we are employing standard machines for production of the CT images.

1.1.4 *Image reconstruction*

The image reconstruction consists in the association of the aforementioned attenuation information with the localization of the measurement within the object. Although it has been demonstrated that an entire spectrum of photon energies are going through the object, the beam is considered monochromatic in the following section.

The intensity of the monochromatic ray across an homogeneous object of thickness x in a certain time interval is denoted I. The intensity $I - \Delta I$ is detected, either through photons unaffected by the absorption or scattered, but traveling in

their original direction of travel. With the hypothesis that all photons possess the same energy, then the following relationship is respected [144]:

$$\frac{\Delta I}{I} \cdot \frac{1}{\Delta x} = -\mu \tag{1.6}$$

Taking the limit of Eq. (1.6) to zero, the following differential equation is obtained:

$$\frac{1}{I}dI = -\mu dx \tag{1.7}$$

which can be solved by integrating across the thickness of the object:

$$\int_{I_0}^{I} \frac{dI}{I} = -\mu \int_0^x dx \tag{1.8}$$

with I_0 the intensity of the beam before entering the object.

$$\ln I - \ln I_0 = -\mu x \tag{1.9}$$

and thus the intensity as function of the thickness of the object reads as

$$I(x) = I_0 \cdot e^{-\mu x} \tag{1.10}$$

In the more general case, where the studied object is heterogeneous, the linear attenuation μ is not constant over the interval of integration $[0 \; x]$. Considering a cross-section of the object, the attenuation can be considered as a function of the two space coordinates and therefore can be written $\mu(x, y)$. Equation (1.10) can be reestablished such as:

$$I(x) = I_0 \cdot e^{-\int_0^d \mu(x,y)dS} \tag{1.11}$$

and consequently, the projection p is defined as:

$$p = \int_0^d \mu(x, y)dS = \ln \frac{I_0}{I} \tag{1.12}$$

Considering that the X-ray beam follows a line that can be mathematically described by the equation $x \cos\theta + y \sin\theta = t$, the projection along this line reads as:

$$P_\theta(t) = \int_{-\infty}^{\infty} f(x, y)\delta(x \cos\theta + y \sin\theta - t)dxdy \tag{1.13}$$

This equation is known as the Radon's transform of the function $f(x, y)$ [232]. The step called "image reconstruction" consists in the inversion of this equation to

solve the unknown object function $f(x, y)$. Applying the Fourier's transform to this equation, the object attenuation along the line reads as [127]

$$f(x, y) = \int_0^\pi d\theta \int_{-\infty}^\infty P(\omega, \theta)|\omega| e^{j2\pi\omega(x\cos\theta + y\sin\theta)} d\omega \tag{1.14}$$

The projection is filtered by a function whose frequency domain response is $|\omega|$. By modifying the projection band width, the frequency parameters of these filters, the quality of the reconstruction can be improved and/or adapted to the study cases. To reconstruct $N \times N$ image matrix, containing N^2 unknown values of attenuation, N_x independent equations have to be resolved, corresponding to the measured projections.

1.1.5 *Extension to a polychromatic beam*

In the reality, the photon beam is not monochromatic but consists in a broad range of energies. Equation (1.10) can be then rewritten such as [27, 127, 145]:

$$I_E = I_{0,E} e^{-\int \mu_{E,s} dS} \tag{1.15}$$

with the intensity depending on the energy and the attenuation coefficient also. The photons with low energy are preferentially absorbed, and particularly by soft tissues and water. The beam becomes harder along its path through the project, therefore this effect is called beam hardening.

The energy frequency distribution $\Omega(E)$ of the beam, with the sum under the curve equal to 1, can be included in the previous equation.

$$I = I_0 \int \Omega(E) e^{-\int \mu_{E,s} dS} dE \tag{1.16}$$

The projection reads then as:

$$p = -\log(\frac{I}{I_0}) = -\log \int \Omega(E) e^{-\int \mu_{E,s} dS} dE \tag{1.17}$$

This equation demonstrates the non-linear variation of the projection along the path length of the beam. The main effect resulting from this effect is to induce a decrease of the intensity in the middle of the object [27]. This is of very high importance for quantitative computed tomography. Therefore, most of the present CT systems incorporate beam hardening corrections in order to recreate the linear relationship of the projection data through the object. The first correction is the presence of a filter, usually a thin metal sheet made of aluminum or copper, and placed between the target and the scanned object. The material filters the low energy photons which are preferentially absorbed and reduces the beam width. The

last curve of Fig.1.3(d) illustrates the photon energy spectrum change after application of a copper filter between the X-ray tube and the scanned object. However, for clinical applications, the body being mostly made of water and soft tissues [2], this solution is not sufficient. A second and usually complementary algorithmic correction has been therefore developed and consist in iterative reconstruction steps in order to obtain a linear projection [27,212,301]. These corrections are very efficient and the effect of beam hardening can be usually neglected for the quantitative computations.

1.2 MULTISCALE REPRESENTATION OF BIOMATERIALS FOR ELASTICITY AND STRENGTH

The study of mechanical properties of complex materials such as biological materials requires the development of theoretical tools in order to predict mechanical behavior through microscopic and macroscopic scales. The identification of the different scales is determined by the type and size of the heterogeneities whithin the material. The characteristic size of these heterogeneities is denoted d. A Representative Volume Element (RVE), or a piece of the material at a certain scale, is seen as homogeneous at the upper scale and considered heterogeneous at the microscale, and can be described as an assembly of phases. The smallest level is chosen considering two rules [308]:

- the purpose of the model must be considered (elasticity, plasticity,...): The question of which phases are contributing to the mechanical properties of the macroscopic materials need to be answered;

- the characterization tools for materials available at very low scales

Furthermore, the size of the microscopic scale is denoted by L, and the size of the Representative Volume Element is designated by l. The so called "separation of scale" principle can be then described by:

- $d \gg l$ such as the RVE can be represented by an homogeneous law.

- $L \gg l$ in order to be able to consider the structure as a continuum, i.e to apply differential calculus throughout the investigated domain.

Respecting the separation of scale allows us to study what happens at the microscopic level such as phase transformations, interaction between inclusions, chemical reactions, etc. When the different scales have been identified, follows the description of the material at the different scales considered (shape of inclusions, distribution in space, ...), and of the mechanical properties of constituents (Young's modulus, Poisson's ratio, ...).

This methodology can be employed for all kind of materials and will be used in this work for a two-scale ceramic scaffold and a multiscale model of bone.

1.2.1 *Tissue engineering scaffold*

Pursuing the dream to regenerate bone using the natural process of bone remodeling, the last decades have seen a very intense development in the field of regenerative medicine [10]. This triggered the development of new materials, biocompatible and having an added value for bone regeneration *in vivo*. Ideally, stem cells from the patient are inserted into a scaffold *in vitro* and implanted at the place of the damaged bone. The scaffold would eventually bring mechanical support to the skeletton and create a favorable medium, bringing chemical compounds helping osteogenesis. In the example studied in Chapter 3, namely a ceramic scaffold made of β-TCP. The macroporosity allows for the circulation of blood vessels and nutriments into its pores and the microstructure of the aforementioned material dissolves, providing minerals, i.e. calcium and phosphorus to catalyze the bone creation process and degrades along the time, letting the space to the newly formed bone. The tricalcium phosphate scaffold is produced from TCP powder, itself produced by several methods, such as solid-state reaction or aqueous precipitation. A sintering process makes the scaffold with a precised macroporosity and geometry. The tricalcium phosphate material has three allotropic forms, α, α', and β, obtained for different sintering temperature ranges. The β phase is stable below 1180°C, α phase lies between 1180 and 1400°C, and finally the α' phase above 1470°C. The β phase is frequently used for biomedical applications such as othopaedics, dental and plastic surgeries because of its good mechanical properties, its excellent biocompatibility, and its high biodegradability [250].

To represent the scaffold microstructure in the frame of multiscale modeling, the latter is modeled as an representative volume element filled with a two-phases polycrystal constituted of discs made of β-TCP, and spherical inclusions of water.

1.2.2 *Bone*

Following this methodology, a multiscale model for bone has been developed over the past decade [90, 92, 118, 209], and is constituted of five levels of hierarchical organization:

- The macrostructure at an observation scale of several mm to cm, where cortical and trabecular bone can be distinguished

- The microstructure (or extravascular bone matrix) at an observation scale of several mm, where cylindrical units called osteons build up cortical bone

- The ultrastructure (or extracellular bone matrix) at an observation scale of several μm, comprising the material building up both trabecular struts and osteons

- Within the ultrastructure, collagen-rich domains can be distinguished at an observation scale of several hundreds nanometers.

- At an observation scale of several ten nanometers, the so-called elementary components of mineralized tissues can be distinguished:

  - plate-shaped mineral crystals consisting of impure hydroxyapatite (HA; $Ca_{10}[PO_4]_6[OH]_2$) with typical 1–5 nm thickness, and 25–50 nm length,

  - long cylindrically shaped collagen molecules with a diameter of about 1.2 nm and a length of about 300 nm which are self assembled in fibrils with characteristic diameters of 50–500 nm; several covently bonded fibrils are sometimes referred to as fibers,

  - different non-collagenous organic molecules, predominantly lipids and proteins,

  - water.

The deep insight into bibliography of the last century also demonstrated very interesting "universal" rules for bone composition. Although each individual is specific, the composition of bone at the level of the ultrasctucture lies on bilinear relationships as illustrated Fig 1.5.
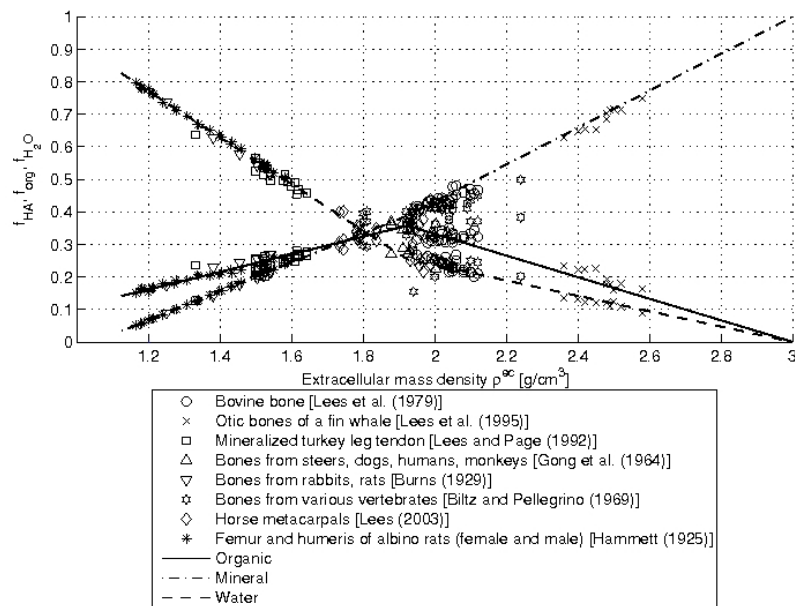
Figure 1.5.: Universal bilinear relationships from [285]

The relationships are of extreme interest for the studies proposed in the next chapters: the knowledge of the volume fraction of one of the principal components,

namely HA, collagen, and water, or of the extracellular bone matrix mass density allows to compute the other missing variables.

1.2.3 *Multiscale continuum micromechanics for elasticity and strength*

From the morphological and compositional considerations developed in subsections 2.1 and 2.2, the identification of Representative Volume Elements is the basis of application of the Eshelby matrix-inclusion problem [83, 165] to estimate for the homogenized stiffness of the upscaled material [308].

$$
\mathbb{C}^{hom} = \sum_r f_r \mathbb{c}_r : [\mathbb{I} + \mathbb{P}_r^0 : (\mathbb{c}_r - \mathbb{C}^0)]^{-1}
$$
$$
: \left\{ \sum_s f_s : [\mathbb{I} + \mathbb{P}_s^0 : (\mathbb{c}_s - \mathbb{C}^0)]^{-1} \right\}^{-1}
$$

(1.18)

where $\mathbb{c}_r$ and f_r the elastic stiffness and volume fraction of phase r, respectively, and $\mathbb{I}$ the fourth-order unity tensor. The fourth-order Hill tensor $\mathbb{P}_r^0$ accounts for the characteristic shape of the inclusions in a matrix of stiffness $\mathbb{C}^0$

The stiffness $\mathbb{C}^0$ can be the stiffness $\mathbb{C}^{hom}$ in the case of the material can be represented as a polycrystal and the self consistent scheme is chosen to represent the best the matrix-inclusions interactions [122, 123], or the stiffness of the matrix material in case of a composite material and the Mori-Tanaka scheme represents the RVE the best [207, 288].

In the case of the β-TCP scaffold of Section 2.1, the self-consistent scheme is chosen with a RVE made of disc of mineral. In order to model the bone, a 6-step homogenization model has been developped and is illustrated Fig. 1.6.

This model has been extensively validated by sets of experiments including de-organification, demineralization, dehydration and ultrasonic measurements [173, 285].

In the works described in this thesis, the higher scales are mainly considered, from extracellular bone matrix to macroscopic bone material. Although the entire model is used in order to retrieve the homogenized properties, no research has been performed below the ultrastructural level. The first three papers will deal with elasticity and the last work will present the application of a novel strength model to a patient-specific application.

1.3 BONE MODELING AND REMODELING

Since the first observations of the necessary bone adaptation o the best mechanical resistance for the lowest organ weight [84, 298] it has been hypothesized that it exists a mechanism for the bone to feel mechanical stimulation and adapt bone
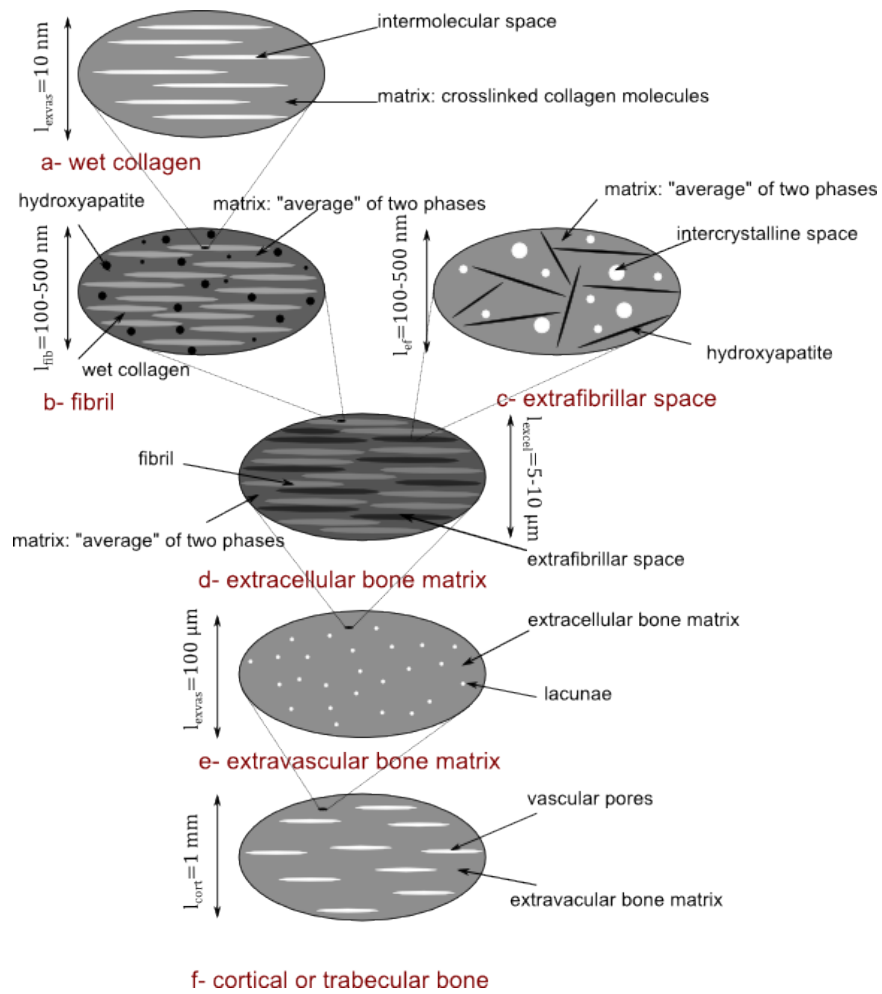
Figure 1.6.: Multiscale model of bone

structure in accordance to the best response to loading. Based on the mechanostat proposed by [97], models aiming to represent the coupling between bone resorption and bone formation [180, 227] have been developed. This coupling is found in the role of the osteocytes, bone cells lying in the ultrastructure and conforming to the shape of the lacunae. Their processes are lying in the caniculi.

On one hand, the osteoclasts are responsible for bone resorption. They create a depression on cancellous bone or periosteal surfaces or a cutting cone through cortical bone. They solubilize the bone mineral using the acidification of the medium [28]. The osteoclasts are resorbing poor quality bone and mechanically inefficient material. On the other hand, the bone formation is performed by the osteoblasts, found in the advancing surface of developing or growing bone. They form a layer of cells on the site of active deposition. Many osteoblasts surround
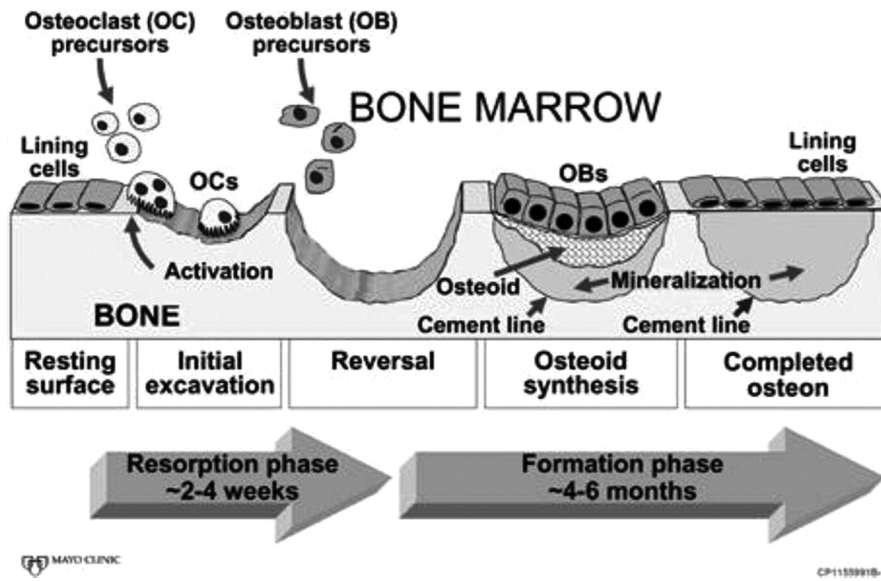
Figure 1.7.: Illustration of the bone remodeling process, reproduced from [243]

themselves with matrix and consequently become osteocytes. The main role of these cells is to produce and secrete the organic matrix, but they may also influence the mineralization of bone matrix [28].

The work in Chapter 5 will approach the simulation of bone remodeling without going into details of the phenomenon responsible for the activation of the osteocytes. A relation between the intensity of the mechanical stimulus and the activity of the osteocytes is hypothesised and allows to reconstruct the trabecular morphology after bone remodeling.

1.4 FINITE ELEMENT METHODS

The Finite Element (FE) method idealized a complex continuous system as an assembly of elements, changing the continuous system into a discrete system, solvable by algebraic equations. The use of Finite Element Modeling is motivated by the complicated systems that are biological structures, because of their heterogeneity in terms of material properties and geometry. The methods employed in this work are restricted to linear analyses, i.e. infinitesimal displacements and linear elastic laws.

In order to set up a Finite element analysis, a four-step methodology can be followed: the creation of the object geometry, the assignment of material properties, and finally the application of loads and boundary conditions onto the model. Concerning the first aspect, the geometry of the studied object, two different approachs have been employed in the following chapters:

- For the first example, each voxel becomes an element of the discretized organ. This method has the advantage to have a direct connection with the CT images. It is then possible to have elements of the size of the voxels measured by CT. The disadvantage is that many singularities are appearing because of the complex geometry. Also, application of boundary conditions are more complex because there is no continuous geometry to gather as element sets. This type of mesh is also acting dramatically on the convergence of the analysis: The structural heterogeneity induced by the hexaedric elements increases the importance of having a sufficient number of elements in the model.

- The second type of mesh, adapted from the organ geometry through 3D design softwares, is more stable and offers a bigger flexibility in terms of load application surfaces. Nevertheless, more steps are necessary in order to interpolate the data from the CT images to the Finite Element mesh.

The novelty in the approach, following the work began in [74, 118, 257] is the application of material properties directly derived from the X-ray physics measurements taken from the Computer Tomographs.

Then, the choice of the loading conditions comes into play. In the following examples, the load cases were always kept as simple as possible but also mechanically relevant for the studied structure. Therefore, only the load induced by standing has been considered.

<div style="text-align: right;">2</div>

INTRAVOXEL BONE MICROMECHANICS FOR MICRO-CT-BASED FINITE ELEMENT SIMULATIONS (BLANCHARD ET AL., 2013)

TYPE OF COLLABORATION

This paper results from a collaboration between the Institute for Mechanics of Materials and Structures of TU Wien and the company Skyscan (now Bruker-microCT), represented by Evi Bongaers. She provided the investigated images, as well as fundamental information on microCT-scanning and its realization within the devices developed and sold by Skyscan (Bruker-microCT). Alexander Dejaco provided support in computer science questions and programming, in particular as regards the realization of boundary conditions on voxel-based meshes. Christian Hellmich directed the overall research strategy, and the writing of the paper. Method development, data processing, code implementation and testing, as well as documentation rested primarily on the thesis author, which qualified her as first author.

2.1 INTRODUCTION

Ever since the pioneering work of Rietbergen et al. [242], so-called micro Finite Element models of bone, stemming from conversion of computer tomographic (CT) voxels into micron-sized finite elements, have become an integral part of bone biomechanics. MicroFE studies have elucidated important load-carrying features of trabecular systems (including bending as probable dominant deformation mode [242], or their weak scattering characteristics when subjected to ultrasound [220]), and they have also revealed characteristics of whole bone structures, where e.g. strain magnitudes in osteoporotic bone appear much higher and less uniform than in healthy bone [278]. In addition, such analyses have also entered the biomaterials field, driving forward the understanding of processes in regenera-

tive medicine [74,162,254,257]. Traditionally, such approaches are based on one set of tissue properties (such as Young's modulus and Poisson's ratio), which are assigned to all finite elements making up the investigated structure [278]. However, it is known that at the ten-to-hundred micrometers scale, tissue densities, X-ray attenuation characteristics, and therefore mechanical properties, are all inhomogeneously distributed throughout bony organs [23,143,157,215,217,267,283,306], and we observe growing scientific interest in understanding potential effects of this inhomogeneity on the overall load carrying behavior of the investigated organ [235,236,281]. The aforementioned studies were all based on empirical relations between CT data and elastic properties, gained from radiographic and mechanical tests on tissues similar to those making up the structure modelled by finite elements [66,211]. However, there is a discussion on such empirical relationships differing from each other [56,297], and on corresponding uncertainties which may compromise the overall reliability of respective simulation results. As a remedy, we here develop a novel strategy for converting X-ray attenuation information into voxel-specific elastic properties. This strategy does not involve regression or back-analysis of tissue parameters, but instead, is directly based on the fundamentals of X-ray physics and micromechanics. Extending a similar methodology developed for bone biomaterials [74,257], we start with a micro computer tomographic image of a mammalian bone (here a mouse femur), and first translate, based on the average rule for X-ray attenuation coefficients [63,120], and on a universal composition law for extracellular bone matrix [285], the voxel-specific X-ray attenuation coefficients into voxel-specific volume fractions of hydroxyapatite, collagen, and water (with non-collageneous organics). These composition data then enter a multiscale micromechanics representation of bone tissue [95,96], which has undergone extensive experimental validation [285]. This leads us to voxel-specific elastic properties, which we map on regular Finite Element meshes, based on which we aim to provide a reliable answer to the following research question: (i) how large are the effects of tissue inhomogeneity when estimating stresses and strain energy densities throughout an entire mammalian bone?

2.2 MATERIALS AND METHOD

2.2.1 *Source - Micro Computer Tomograph of Mouse Femur*

The investigated mouse femur was microCT scanned in an Skyscan 1172 microCT desktop machine with the following parameters: source voltage: 49 kV, source current: 200 microampere, exposure time: 1200 ms, source filter: aluminium 0.5 mm, rotation step: 0.3°, frame averaging number: 5, image pixel size: 6.775 micrometer. Through the Radon Transformation as inbuilt into Skyscan's image evaluation software CTan [268], the scanned projection images were transformed into a stack

of 576 planar images, of size 720×720 pixels. Hence, the reconstructed spatial domain consists of $720 \times 720 \times 576 \approx 3 \times 10^9$ voxels with an edge length of 6.775 microns. In this domain, we need to distinguish the solid structure from the space surrounding it, as well as from the pore spaces inside the whole bone. Therefore, a statistical analysis of the voxel-specific attenuation information in terms of grey values is carried out, leading to the histogram depicted in Figure 2.1. We identify the minimum value between the air peak at zero grey value, and the peak at GV=148, relating to the most frequently occurring solid voxel, as the threshold value GV_{thr} between the solid and the non-solid voxels, $GV_{thr} = 75$. All voxels with $GV < GV_{thr}$ will be regarded as zero-stiffness "air voxels", their grey values being labeled as GV^{air}, while the remaining "solid voxels", with $GV > GV_{thr}$, are considered to be filled with extracellular bone matrix, their grey values being labelled as GV^{ec}. Their attenuation, composition, and elastic properties will be of particular interest in the following. Therefore, as a first step, the grey values need to be related to the actual physical quantity measuring X-ray attenuation coefficients μ with dimension one over length; and the corresponding relation is a linear one [268],

$$\mu = a \times GV + b \tag{2.1}$$

with so far unknown proportionality coefficients a and b. These coefficients are intrinsic to the specific micro-CT scan used in the present investigation, and for their determination, we employ the average rule for X-ray attenuation coefficients, and universal bone composition rules, as described next.

2.2.2 *Average rule for X-ray attenuation coefficients*

The X-ray attenuation coefficient of a composite material located inside one voxel is identical to the spatial average of the X-ray attenuation coefficients of the material's single constituents [63, 120],

$$\mu = \sum_{i}^{N_c} \mu_i \times f_i \tag{2.2}$$

with μ_i, $i = 1, ..., N_C$, as the X-ray attenuation coefficient of constituent i, N_C as the total number of constituents, and with f_i as the volume fraction of constituent i. When applied to bone tissue (extracellular bone matrix - *ec*), consisting of hydroxyapatite (HA), organics (org) and water with non-collageneous proteins (H_2O), Eq.(2.2) can be specialized to

$$
\begin{aligned}
\mu^{ec} &= \mu_{HA} \times f_{HA} + \mu_{org} \times f_{org} + \mu_{H_2O} \times f_{H_2O} \\
\text{with} \quad & f_{HA} + f_{org} + f_{H_2O} = 1
\end{aligned}
\tag{2.3}
$$
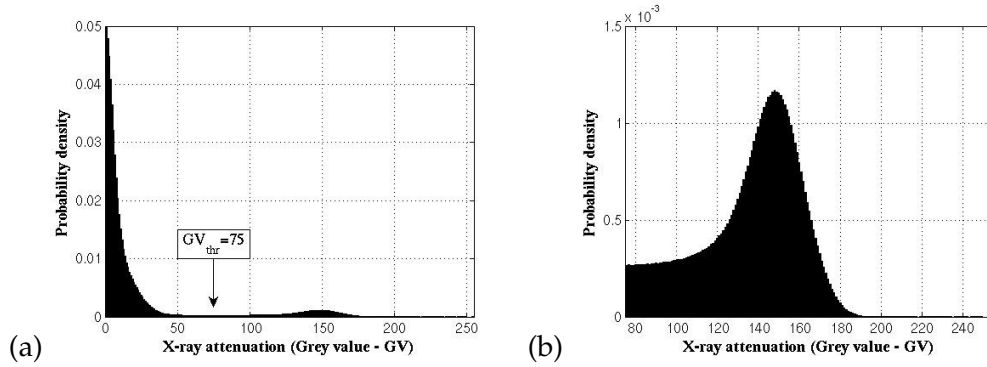
Figure 2.1.: (a) Histogram of attenuation-related grey values GV throughout entire scanned domain, (b) zoom into grey values related to solid voxels with $GV > GV_{thr}$.

The X-ray attenuation coefficients of collagen, hydroxyapatite, and water can be gained from the public data base of the National Institute of Standards and Technology (NIST) [1]: more specifically, this data base provides the mass attenuation coefficients $(\mu/\rho)_i$, $i = HA$, org, H_2O, as functions of the photon energy of the used X-ray [see Figure 2.2(a)]. Combining these functions with the real mass densities of hydroxyapatite, collagen, and water (with non-collagenous organic matter), $\rho_{HA} = 3$ g/cm³ [170], $\rho_{org} = 1.41$ g/cm³ [170], $\rho_{H_2O} = 1$ g/cm³, one arrives at the X-ray attenuation coefficients shown in Figure 2.2(b). In particular for the peak of photon energy, amounting to 10 keV, the X-ray attenuation coefficients read as $\mu_{HA} = 141.6$ cm⁻¹, $\mu_{org} = 5.71$ cm⁻¹, $\mu_{H_2O} = 5.33$ cm⁻¹.
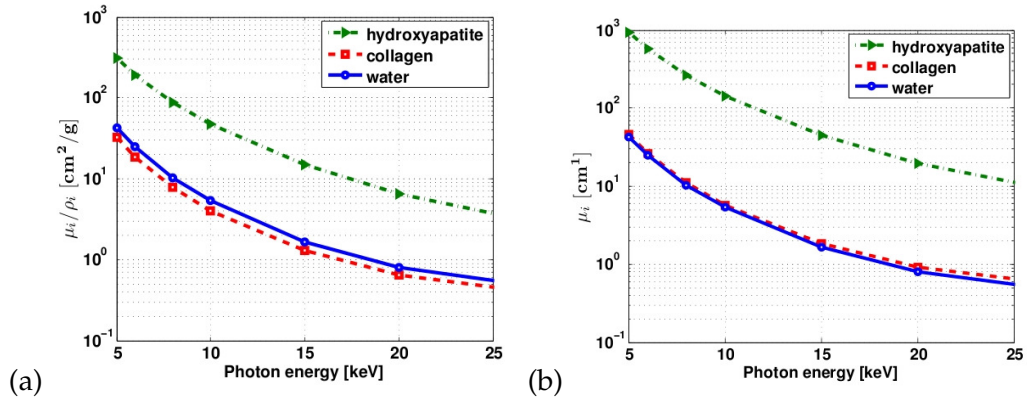
Figure 2.2.: (a) Mass attenuation coefficients, (b) X-ray attenuation coefficients of the elementary constituents of bone tissue, as functions of the photon energy

2.2.3 *"Universal" composition laws for bone tissues*

Careful evaluation of a data base spanning eigthy years of experimental research on dehydratation, deorganification, demineralization, and ashing of bone tissue [18, 32, 105, 112, 171, 173, 176, 178] revealed an astonishing bilinear relationship between mineral and collagen concentrations in bone tissues across different organs, ages, and species [285], see Figure 2.3(a),

$$\rho^*_{org} = A \times \rho^*_{HA} + B \qquad \text{for } 0 < \rho^*_{HA} < \rho^{*,crit}_{HA} \tag{2.4}$$

$$\rho^*_{org} = [A \times \rho^{*,crit}_{HA} + B] \times \left[1 - \frac{\rho^*_{HA} - \rho^{*,crit}_{HA}}{\rho_{HA} - \rho^{*,crit}_{HA}}\right] \qquad \text{for } \rho^{*,crit}_{HA} < \rho^*_{HA} < \rho_{HA} \tag{2.5}$$

with ρ^*_{org} and ρ^*_{HA} as the apparent mass densities ("concentrations") of organic matter and hydroxyapatite per volume of bone tissue, with proportionality constants $A = 0.29$ and $B = 0.17$ g/cm³, and with the critical apparent mass density of mineral, $\rho^{*,crit}_{HA} = 1.18$ g/cm³. Combination of the bilinear relationship Eq.(2.4) and (2.5) with the relations between apparent mass densities and volume fractions,

$$f_i = \rho^*_i/\rho_i \,, \quad i = org, HA, H_2O \tag{2.6}$$

and with the averaging rule for mass densities,

$$\rho^{ec} = f_{H_2O} \times \rho_{H_2O} + f_{org} \times \rho_{org} + f_{HA} \times \rho_{HA} \tag{2.7}$$

yields the consituent volume fractions as functions of the extracellular mass density, see also Figure 2.3(b),

$$
\begin{aligned}
f_{org} &= (\rho^{ec} - \rho_{HA}) \times \rho_{HA} \times (B + A\rho^{*,crit}_{HA}) \Big/ \tag{2.8}\\
&\quad \left[\rho_{H_2O} \times \rho_{HA} \times (B + A\rho^{*,crit}_{HA}) - ((B + \rho_{H_2O} - \rho_{HA}) \times \rho_{HA} + \right.\\
&\quad \left. +(-\rho_{H_2O} + \rho_{HA} + A \times \rho_{HA}) \times \rho^{*,crit}_{HA}) \times \rho_{org}\right]\\
f_{H_2O} &= ((\rho^{ec} - \rho_{HA}) \times (B \times \rho_{HA} + A \times \rho_{HA} \times \rho^{*,crit}_{HA} + \tag{2.9}\\
&\quad +(-\rho_{HA} + \rho^{*,crit}_{HA}) \times \rho_{org}))\\
&\quad \Big/ \left[(\rho_{H_2O} \times \rho_{HA} \times (B + A \times \rho^{*,crit}_{HA}) - ((B + \rho_{H_2O} - \rho_{HA}) \times \rho_{HA} \right.\\
&\quad \left. +(-\rho_{H_2O} + \rho_{HA} + A \times \rho_{HA}) \times \rho^{*,crit}_{HA}) \times \rho_{org})\right]\\
f_{HA} &= 1 - f_{H2O} - f_{org} \tag{2.10}
\end{aligned}
$$

Figure 2.3.: Universal composition laws in bone tissue: (a) bilinear relation between apparent mass density of mineral and collagen; and (b) resulting bilinear relations between constituent volume fractions and tissue mass density.

2.2.4 *Determination of grey value proportionality values from average tissue mass density*

Attenuation averaging rule (2.3), mass density averaging rule (2.7), and volume fraction – mass density relations (2.8) to (2.10) can be used for determination of proportionality values a and b in Eq.(2.1), once an additional physical property is known, namely the tissue mass density averaged over all solid voxels, $\overline{\rho^{ec}}$. As a rule, such average values are organ- and species- specific, but in adult tissue, they

do not vary in time and space, see [120,190] for detailed discussions on that aspect. We here adopt a value of $\overline{\rho^{ec}} = 2\,\text{kg}/\text{dm}^3$, which is typical for mammalian femoral bone [285]. By means of averaging the volume fraction – density relations (8)-(10), the aforementioned mean tissue mass density value can be related to mean mineral, organic, and water volume fractions, amounting to $\overline{f_{HA}} = 0.43$, $\overline{f_{org}} = 0.34$, $\overline{f_{H_2O}} = 0.23$. Use of these values in the attenuation average rule (2.3) yields the mean X-ray attenuation coefficient of extracellular femoral bone tissue as $\overline{\mu^{ec}} = 64.06\,\text{cm}^{-1}$. This value, and the comparatively negligible attenuation coefficient of air, $\overline{\mu^{air}} \approx 0$, will be used for determination of the proportionality constants a and b, by solving two equations stemming from averaging (2.1) over the solid as well as over the non-solid compartments of the scanned object,

$$\begin{cases} \overline{\mu^{ec}} = \overline{GV^{ec}} \times a + b \\ \overline{\mu^{air}} = \overline{GV^{air}} \times a + b \end{cases} \tag{2.11}$$

where $\overline{GV^{air}} = 0$ and $\overline{GV^{ec}} = 136$ follow from averaging over the histogram of Figure 2.1. Then, Eq.(2.11) allows for determination of the proportionality constants a and b: $a = 0.471$ and $b = 0$. Based on these values, Eq.(2.1) translates any grey value GV found in the scan of Figure 1, into an attenuation coefficient μ, in particular, for $GV > GV_{thr}$, GV^{ec} values are converted into μ^{ec} values. Use of the latter values in Eq.(2.3), in combination with Eq.(2.4)-(2.6) allows for expression of the volume fractions f_{H_2O}, f_{org}, f_{HA} as functions of the grey values GV^{ec}, $GV^{ec} > GV_{thr} = 75$,

$$\begin{aligned} f_{HA} &= \Big[\rho_{HA} \times (\mu_{org} - \mu_{H_2O}) \times (B + A \times \rho_{HA}^{*,crit}) + \mu_{H_2O} \times \rho_{org} \times & (2.12) \\ &\quad (\rho_{HA} - \rho_{HA}^{*,crit}) - a \times GV^{ec} \times (\rho_{HA} - \rho_{HA}^{*,crit}) \times \rho_{org}\Big] & (2.13) \\ &\quad \Big/ \Big[(\mu_{org} - \mu_{H_2O}) \times \rho_{HA} \times (B + A \times \rho_{HA}^{*,crit}) + \\ &\quad (-\mu_{HA} + \mu_{H_2O}) \times (\rho_{HA} - \rho_{HA}^{*,crit}) \times \rho_{org}\Big] \\ f_{org} &= \Big[\mu_{HA} \times \rho_{HA} \times (B + A \times \rho_{HA}^{*,crit}) - a \times GV^{ec} \times \rho_{HA} \times & (2.14) \\ &\quad \times (B + A \times \rho_{HA}^{*,crit})\Big] \Big/ \Big[-(\mu_{org} - \mu_{H_2O}) \times \rho_{HA} \times \\ &\quad \times (B + A \times \rho_{HA}^{*,crit}) + (\mu_{HA} - \mu_{H_2O}) \times (\rho_{HA} - \rho_{HA}^{*,crit}) \times \rho_{org}\Big] \\ f_{H_2O} &= 1 - f_{HA} - f_{org} & (2.15) \end{aligned}$$

2.2.5 *Translation of voxel-specific bone tissue composition into components of elasticity tensor*

Each seven micron-sized voxel hosts extracellular bone material, the elastic behavior of which can be predicted from the dosages of mineral (quantified through volume fraction f_{HA}), collagen (with volume fraction $f_{col} = 0.9 \times f_{org}$ [170, 276, 294]), and water with non-collageneous organic matter (with volume fraction $f_{wnc} = 1 - f_{HA} - f_{org}$), based on universal mechanical interaction patterns of these consituents throughout the hierarchical organization of bone tissue. The latter have been quantified in a multiscale homogenization scheme [95, 96, 285] which relates the stiffness of material phases (i.e. quasi-homogeneous subdomains) within a representative volume element (RVE) [e.g. molecular collagen within RVE of wet collagen in Figure 2.4, or mineralized collagen fibril within RVE of extracellular bone matrix in Figure 2.4], to the stiffness of the RVE itself, as a function of the phase stiffnesses and of the phase volume fractions in all RVEs. The volume fractions needed as input for the homogenizaton scheme (Figure 2.4) are derived from the volume fractions of the constituents of the extracellular bone matrix (water, collagen and hydroxyapatite). The volume fractions of the different RVE in Figure 2.4 are taken from [95, 96, 285], to which we refer for mathematical details and extensive experimental validation across species, organs, and ages. On a mathematical level, this is achieved by setting the phase strain equal to those in ellipsoidal inclusions embedded into infinitely extending matrices of stiffness $\mathbb{C}^0$ subjected to remote strains, and by combining respective semi-analytical relationships [83, 165] with stress and strain average rules [115, 308].

For all four RVEs depicted Figure 2.4, the phase elasticities are related to the overall RVE-specific and homogenized elasticity through the standard expression of matrix-inclusion-problem-based continuum micromechanics [14, 308],

$$\mathbb{C}^{hom} = \sum_r f_r \mathbb{c}_r [\mathbb{I} + \mathbb{P}_r^0 : (\mathbb{c}_r - \mathbb{C}^0)]^{-1} : \left\{ \sum_s f_s [\mathbb{I} + \mathbb{P}_s^0 : (\mathbb{c}_s - \mathbb{C}^0)]^{-1} \right\}^{-1} \quad (2.16)$$

where f_r and $\mathbb{c}_r$ are the volume fraction and the elastic stiffness of phase r, $\mathbb{I}$ is the fourth-order identity tensor, $\mathbb{P}_r$ is the fourth order Hill tensor accounting for the characteristic shape of phase r, and $\mathbb{C}^0$ is an auxiliary matrix stiffness, which is either that of one of the phases (hydroxyapatite foam in RVE of extracellular matrix, molecular collagen in RVE of wet collagen) or equals to the stiffness of the overall RVE (as is the case for the RVEs of hydroxyapatite foam or of mineralized fibril).

If one wishes to do without the tensorial operations of (2.16), use can be made of their (very precise) approximations in terms of mass density-stiffness relations documented in [285] and given in Appendix A. In detail, the voxel-specific grey values are first converted to volume fractions according to (2.12)-(2.14), then the
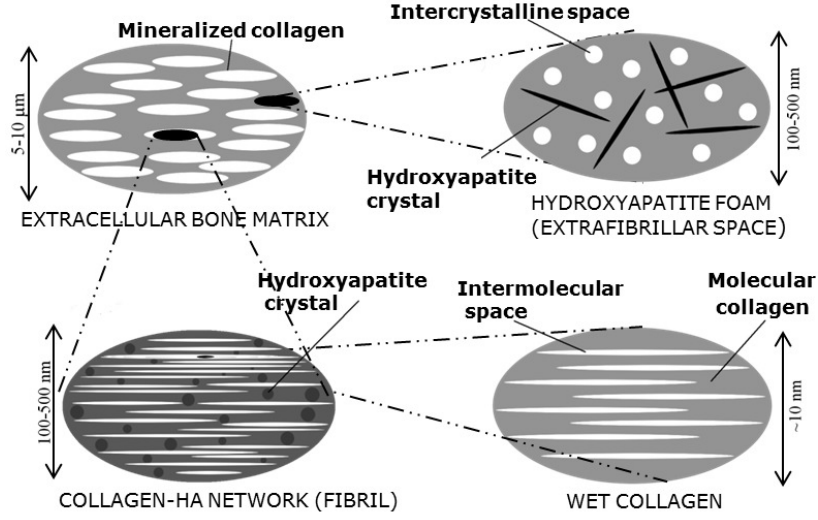
Figure 2.4.: Four-step homogenization scheme after Vuong and Hellmich (2011), Fritsch and Hellmich(2009a)

latter are converted into mass densities according to (2.7), and these numbers enter voxel-specifically equations relating the tissue mass densities to the five independent stiffnesses components of a transversely isotropic material, namely the extracellular bone tissue. Frequently, it is common to define a transversely isotropic stiffness tensor through five engineering constants related to the components of the compliance tensor $\mathbb{D}^{ec}$, which is the inverse of the stiffness tensor $\mathbb{C}^{ec}$,

$$\mathbb{D}^{ec} = \mathbb{C}^{ec,-1} \tag{2.17}$$

These engineering constants are the axial and transverse Young's moduli,

$$E_1^{ec} = \frac{1}{D_{1111}^{ec}}, \qquad E_3^{ec} = \frac{1}{D_{3333}^{ec}} \tag{2.18}$$

the Poisson's ratios

$$\nu_{12} = -D_{1122}^{ec} \times E_1^{ec} \qquad \text{and} \qquad \nu_{31} = -D_{1133}^{ec} \times E_3^{ec} \tag{2.19}$$

and the transverse shear modulus

$$G_{12} = \frac{E_1^{ec}}{2(1 + \nu_{12}^{ec})} \tag{2.20}$$

2.2.6 *Voxel-to-finite element conversion*

The most obvious use of voxel-specific elasticity properties as determined in Section 2.5 is in the context of Finite Element (FE) simulations of the scanned object. Therefore, similar to the procedure outlined in Dejaco et al. [74], different amounts of neighboring voxels (namely, 2×2×2=8 voxels, 3×3×3=27 voxels, 4×4×4=64 voxels, 5×5×5=125 voxels, 6×6×6=216 voxels, and 7×7×7=343) were merged into cubic finite elements (namely 1750508, 513012, 214138, 108718, 62410, and 39004 cubic finite elements), which were assigned the mean grey-scaled attenuation value averaged over all the merged voxels. If this mean attenuation value was below GV_{thr}, it was skipped, otherwise it was assigned volume fractions according to (12)-(14) and elastic properties according to (15). The different merging options, related to in the following through merging factors (MF), MF=2^3, 3^3, 4^3, 5^3, 6^3, 7^3, are central for assessing the precision of FE simulations, in the form of a convergence study, showing strain energy density as function of element size, as described in Section 3.

2.2.7 *Dominant elastic properties in beam-like structures*

Since the structural features of femurs, as well as their most encountered loading scenarios, are rather beam-like, the material stiffness in beam direction is expected to play a much larger role than the stiffnesses measured in directions orthogonal to the beam axis. This dominant stiffness is the one encountered in the direction of the individual trabeculae of spongy bone, as discussed in details by Cowin in 1997 [58]; and more generally, the dominant stiffness is the stiffness related to the collagen orientation direction, both in trabecular and in cortical bone. Accordingly, one may assign formally isotropic material properties to microstructural models of femurs, with Young's modulus and Poisson's ratio being those related to the collagen direction. (It is important to note that this is fundamentally different from orientation-averaging of anisotropic material properties, as to arrive at "equivalent" isotropic material properties). Interestingly, the relevance of the generalization of Cowin's vision of trabecular mechanics, to femurs in general, was convincingly evidenced by two more recent papers, authored by Baca et al. [12] and Peng et al. [224]. For a variety of load cases, the anisotropy-induced differences in maximum von Mises stresses, as compared to the formally isotropic material property assignment, turn out to be less than 1% [224]. Therefore, we here concentrate on the distributions of axial Young's modulus E_3^{ec} [see Eq.(2.18)] and axial Poisson's ratio ν_{31}^{ec} [see Eq.(2.19)] throughout the mouse femur.

2.2.8 *Force estimation*

The focus of our study is not so much the realistic force modeling under different dynamical loading scenarios, but the investigation of how micromechanics-derived inhomogeneous material properties affect the prediction of stress distribution throughout bony organs. Therefore, we restrict our chosen boundary conditions to one very simple load case, namely that of gravitation forces acting on a standing mouse: as underlying structural mechanics system, we consider the spine modeled as an arch subjected to the body weight (BW), see Figure 2.5(a). From a typical body weight of 40 g [260] we substract 15% as the weight of the legs [150], which results in BW=34 g. This body weight, acting in the y-direction of the coordinate system of Figure 2.5, is uniformly partitioned upon the four legs, so that $\frac{1}{4}BW$ is resting on each foot (see Figure 2.5), $F_{BW,y} = 0.083$ N. As the spinal arch does not carry remarkable bending moments at its supports, these foot forces give direct access to the normal forces acting at the spinal ends,

$$\mathbf{F}_{BW} = \begin{pmatrix} F_{BW,x} \\ F_{BW,y} \\ F_{BW,z} \end{pmatrix}_{\mathbf{e}_x,\mathbf{e}_y,\mathbf{e}_z} = \begin{pmatrix} -\frac{BW}{4 \times \cos \alpha_{spine}} \\ -\frac{BW}{4} \\ 0 \end{pmatrix}_{\mathbf{e}_x,\mathbf{e}_y,\mathbf{e}_z} = \begin{pmatrix} -0.144\text{N} \\ -0.083\text{N} \\ 0 \end{pmatrix}_{\mathbf{e}_x,\mathbf{e}_y,\mathbf{e}_z} \tag{2.21}$$

where α_{spine} is the angle between the horizontally oriented femur and the spine [293], see Figure 2.5(b), and where the $\mathbf{e}_x, \mathbf{e}_y, \mathbf{e}_z$ frame follows the anatomical directions, as to keep vector component determination straightforward. The anterior part of the femur is fixed, as to mimick the firmly standing knee, see position B of Figure 2.5. At equilibrium, also the sum of all moments acting with respect to point B of the system vanishes, which gives:

$$\mathbf{M}_B + \mathbf{r} \times \mathbf{F} = 0 \qquad \text{with} \qquad \mathbf{r} = \begin{pmatrix} L_x \\ 0 \\ L_z \end{pmatrix}_{\mathbf{e}_x,\mathbf{e}_y,\mathbf{e}_z} \tag{2.22}$$

with $L_x = 3.35$ mm and $L_z = 1.61$ mm. Hence, it follows

$$\mathbf{M}_B = -\mathbf{r} \times \mathbf{F} = \begin{pmatrix} M_{B,x} \\ M_{B,y} \\ M_{B,z} \end{pmatrix}_{\mathbf{e}_x,\mathbf{e}_y,\mathbf{e}_z} = \begin{pmatrix} 0.134 \text{ N.mm} \\ -0.232 \text{ N.mm} \\ -0.278 \text{ N.mm} \end{pmatrix}_{\mathbf{e}_x,\mathbf{e}_y,\mathbf{e}_z} \tag{2.23}$$

The reaction forces (2.21) and moments (2.23) can be easily checked for physiological relevance [293], for more details, see Appendix B.
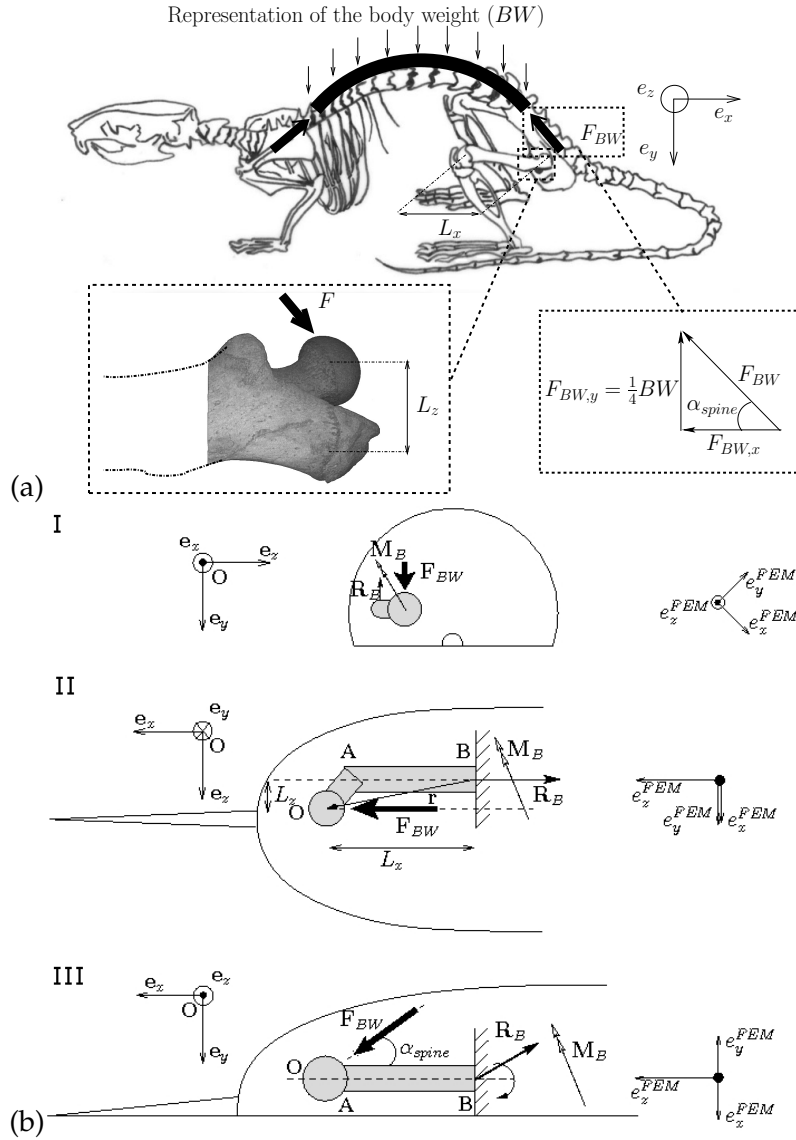
Figure 2.5.: Force estimation in standing mouse: (a) arch-type representation of spine and resulting force acting on femoral head; (b) beam representation of femur: I, back view; II, top view; III, side view; coordinate system $\mathbf{e}_x$, $\mathbf{e}_y$, $\mathbf{e}_z$ refers to equilibrium considerations of forces acting on the structural system; coordinate system $\mathbf{e}_x^{FEM}$, $\mathbf{e}_y^{FEM}$, $\mathbf{e}_z^{FEM}$ is used for Finite Element simulations.

2.2.9 *Boundary conditions applied to the Finite Element model*

Next, we apply the forces and displacement conditions developed for the structural mouse model in the last subsection, as boundary conditions to the 3D FE

models of the mouse femur introduced Figure 9. Since our regular FE meshes are generated from the voxels of the microCT scans, a FEM-related reference frame ($\mathbf{e}_x^{FEM}$, $\mathbf{e}_y^{FEM}$, and $\mathbf{e}_z^{FEM}$) oriented along the voxel edges appears as the most natural choice. In these models, the cross section directed towards the knee is pinned, i.e. the displacements in directions $\mathbf{e}_x^{FEM}$, $\mathbf{e}_y^{FEM}$, and $\mathbf{e}_z^{FEM}$ are fixed there. The load $\mathbf{F}$ is applied onto the femur head, in terms of surface tractions applied to a surface area which remains constant for all different discretizations shown in Figure 2.9. This surface comprises all femur head-related finite element faces with normals $\mathbf{n}$ facing towards the force $\mathbf{F}$, i.e. $\mathbf{F} \cdot \mathbf{n} > 0$; the aforementioned surface is identified by a fast software algorithm written in GNU C [151], reading in the FE model directly from ABAQUS [3]. Then, for each of the directions $\mathbf{e}_x^{FEM}$, $\mathbf{e}_y^{FEM}$, and $\mathbf{e}_z^{FEM}$, the program iterates through all cross-sections of the FE model, and catches all faces with $\mathbf{F} \cdot \mathbf{n} > 0$, adding them to the overall surface set, unless there exists a previously selected surface element which covers the currently checked element face. This way, the resulting surface-set contains exactly the complete set of sought outward-facing surface elements. In the finest discretization of Figure 2.9, the identified surface area consists of 456 finite element faces. As relates to the magnitude and the 3D vector representation of the load $\mathbf{F}$, we refer to Appendix C.

2.2.10 *Evaluation of FE results*

The results of the FE simulations performed through ABAQUS version 6.10 are reported in terms of element-specific maximum principal stresses throughout the organ. In addition, we report the element-specific strain energy density derived from the transversely isotropic elastic properties of Figure 2.6,

$$\Psi^{ec} = \frac{1}{2} \begin{pmatrix} \varepsilon_I \\ \varepsilon_{II} \\ \varepsilon_{III} \end{pmatrix} \begin{pmatrix} C_{1111} & C_{1122} & C_{1133} \\ C_{1122} & C_{1111} & C_{1133} \\ C_{1133} & C_{1133} & C_{3333} \end{pmatrix} \begin{pmatrix} \varepsilon_I \\ \varepsilon_{II} \\ \varepsilon_{III} \end{pmatrix} \tag{2.24}$$

with the principal strains ε_I, ε_{II}, and ε_{III}.

As to answer the question on the mechanical effects of inhomogeneity as stated in the Introduction, the following comparison is made: The results of the aforementioned Finite Element models with element-specific elastic properties according to Sections 2.3.5 and 2.3.6 (called "heterogeneous models") are compared to results from corresponding Finite Element models where all solid elements exhibit the mean grey value $\overline{GV^{ec}}$ averaged over all solid voxels (with $GV > GV_{thr}$), amounting to $\overline{GV^{ec}}$ =136 (called "homogeneous models"). The corresponding Young's modulus and Poisson's ratio amount to $E^{ec}(\overline{GV^{ec}})$=23.44 GPa and $\nu^{ec}(\overline{GV^{ec}})$=0.346. Since it is common practice in biomedical modeling to use a Poisson's ratio of

ν^{ec}=0.3 [279], we also perform simulations based on that "average" value for the Poisson's ratio of the extracellular tissue.

2.3 RESULTS

2.3.1 *Composition and stiffness maps*
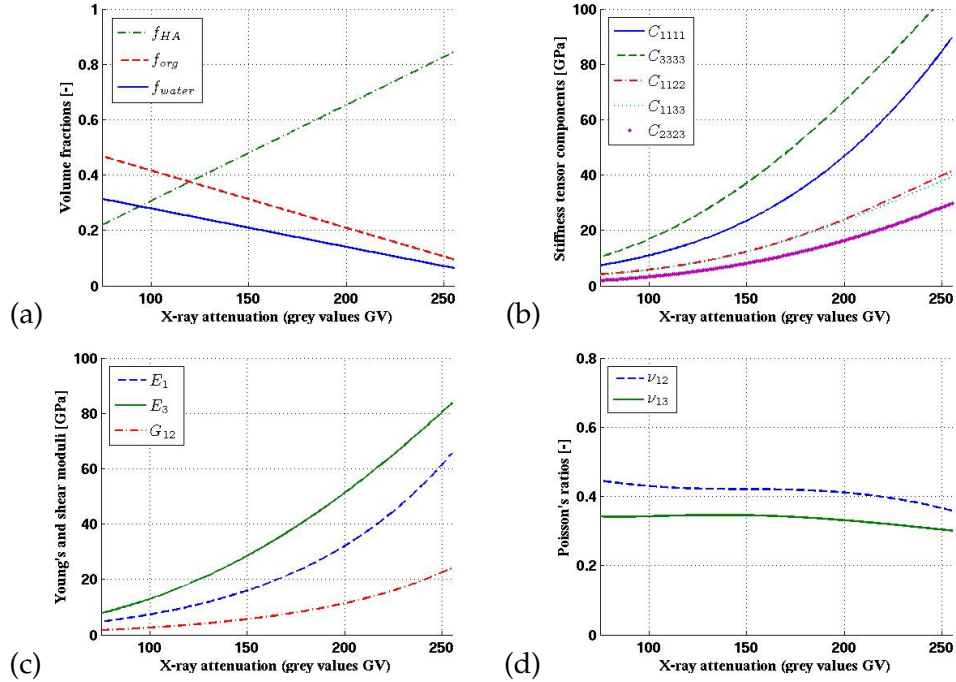
Figure 2.6.: Translation of X-ray attenuation information into tissue composition and elasticity, yielding functions with attenuation-related grey values as arguments: (a) constituent volume fractions, (b) stiffness tensor components, (c) Young's and shear moduli, and (d) Poisson's ratios

An illustration of the attenuation-to-composition relations (2.12)-(2.14) is given in Figure 2.6(a). Evaluation of their relations for the grey value of each and every voxel of the scanned object yields composition maps throughout the mouse femur, see Figure 4.9(a,b); and additional consideration of Eq.(2.7) provides access to mass density maps, see Figure 4.9(c). Subsequent use of (2.12)-(2.14) in (2.16) specified for the four RVEs of Figure 2.4, leads to attenuation-stiffness relations as depicted in Figure 2.6(b-d), and to the stiffness maps of Figure 4.9(d,e). The different voxel-to-element merging options have a discernible influence on the stiffness distributions across the different discretizations of the scanned object, see Figures 2.8. As a rule, merging of ever more voxels (i.e. element enlarge-

45

ment) reduces the probability density of very dense (stiff) elements, and (almost always) increases the probability density of very loose (soft) elements [see Figure 2.8(a)]. Upon close inspection, these differences can be also seen in stiffness maps plotted for different voxel-to-element merging factors [see Figure 2.8(b)], while the attenuation-to-stiffness relations of Figure 2.6 do *not* depend on the merging process.

2.3.2 *Convergence study and effect of inhomogeneity*

The strain energy density values according to [96] are averaged over all (solid) finite elements of each and every simulation, and these average strain energy densities show that convergence is obtained faster in the simulations based on homogeneous material properties (when compared to simulations based on inhomogeneous properties), see Figure 2.9(b).

The convergence behavior can be further characterized by means of a double-logarithmic plot showing the relative discretization error as function of the element size, see Figure 2.9(c), where the simulation with merging factor MF=2 was considered as good approximation of the "true" solution. Remarkably, a slope of two is reached for an element size referring to a merging factor of MF=3. Such a slope indicates, according to [309], so-called robust element behavior. This means that the element behavior is "not sensitive to physical parameters of the differential equation", see page 313 of [309]. Attaining numerical robustness in the aforementioned sense is the motivation to present some characteristic results stemming from the FE simulations with 513012 finite elements: Thereby, we start with a plausibility check: the sum of all reaction forces at the node of the fixed, knee-oriented cross section amounts to:

$$\mathbf{R}_B^{res} = \left\{ \begin{array}{c} R_{B,x}^{res} \\ R_{B,y}^{res} \\ R_{B,z}^{res} \end{array} \right\} = \left\{ \begin{array}{c} 0.0589 \text{ N} \\ 0.0589 \text{ N} \\ 0.1438 \text{ N} \end{array} \right\}_{\mathbf{e}_x^{FEM}, \mathbf{e}_y^{FEM}, \mathbf{e}_z^{FEM}} \tag{2.25}$$

They are in agreement with the reaction force $\mathbf{R}_B$ from the beam model, which underlines the correct application of the force $\mathbf{F}$ onto the FE model of the mouse femur.

The maximum principle stresses evidence, both in the FE models with homogeneous and inhomogeneous properties, large normal tensile loading throughout the femur neck, and no remarkable stress gradient across the neck cross sections (see Figure 2.10). The actual heterogeneous elasticity throughout the solid portion of the mouse femur leads to an average strain energy density which is 1.2 times larger as the one obtained from the homogeneous elasticity distribution (see Table 2.1). The same holds for the maximum strain energy density, while the large

46
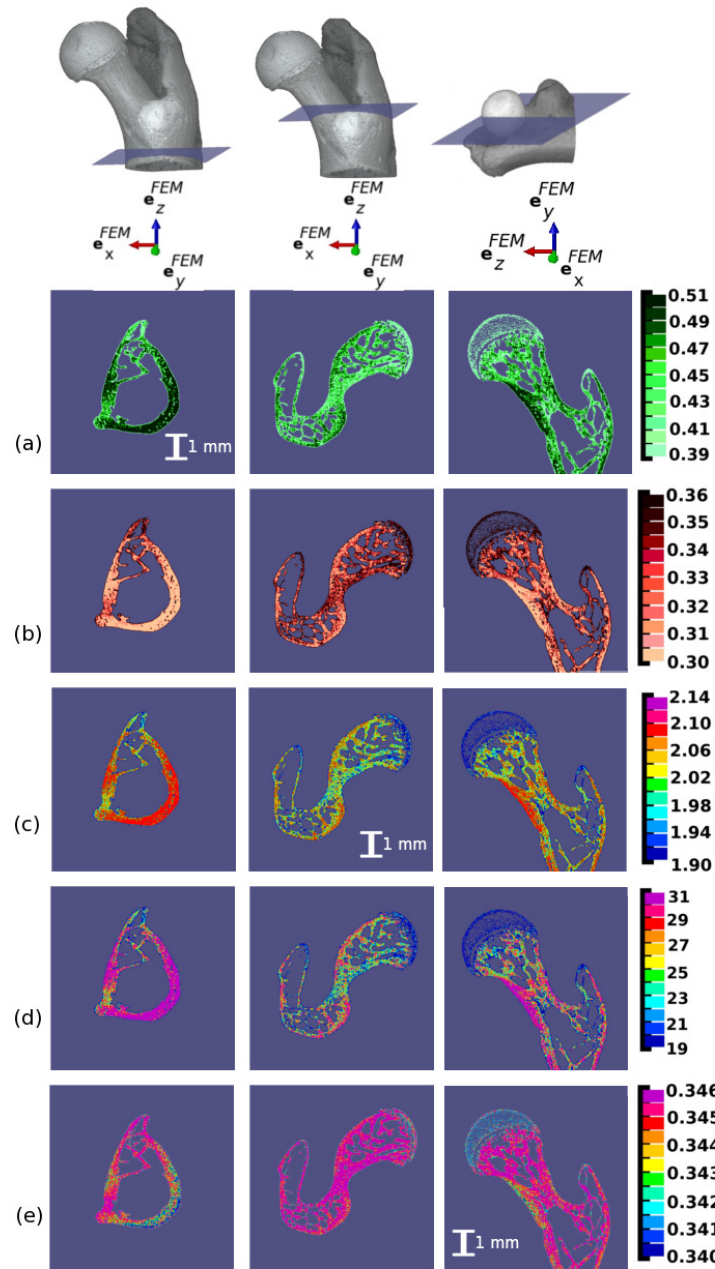
Figure 2.7.: Composition and stiffness maps in cross sections through mouse femur, at the resolution of single voxels: (a) mineral volume fraction, (b) organic volume fraction, (c) mass density [g/cm^3], (d) axial Young's modulus [GPa], (e) axial Poisson's ratio

fluctuation of strain energy density throughout the organ is reflected by minimum strain energy density values of zero. Since the same force **F** leads to a higher strain

47
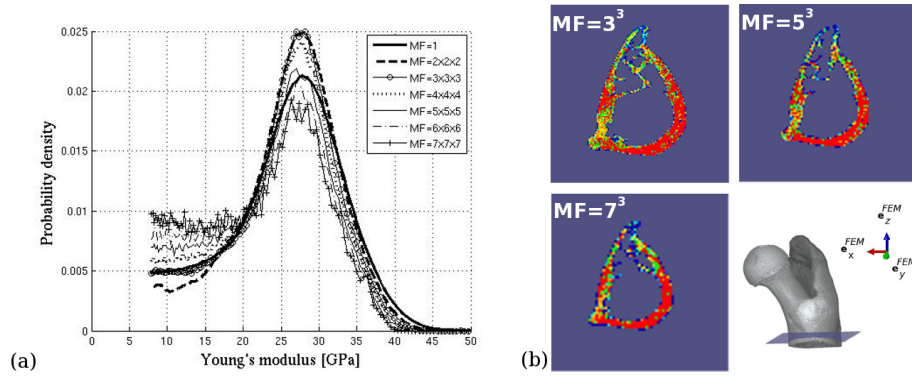
Figure 2.8.: Influence of voxel-to-element merging factor (MF) on stiffness distribution: (a) frequency plots of axial Young's modulus; (b) and exemplary stiffness maps through femur shaft
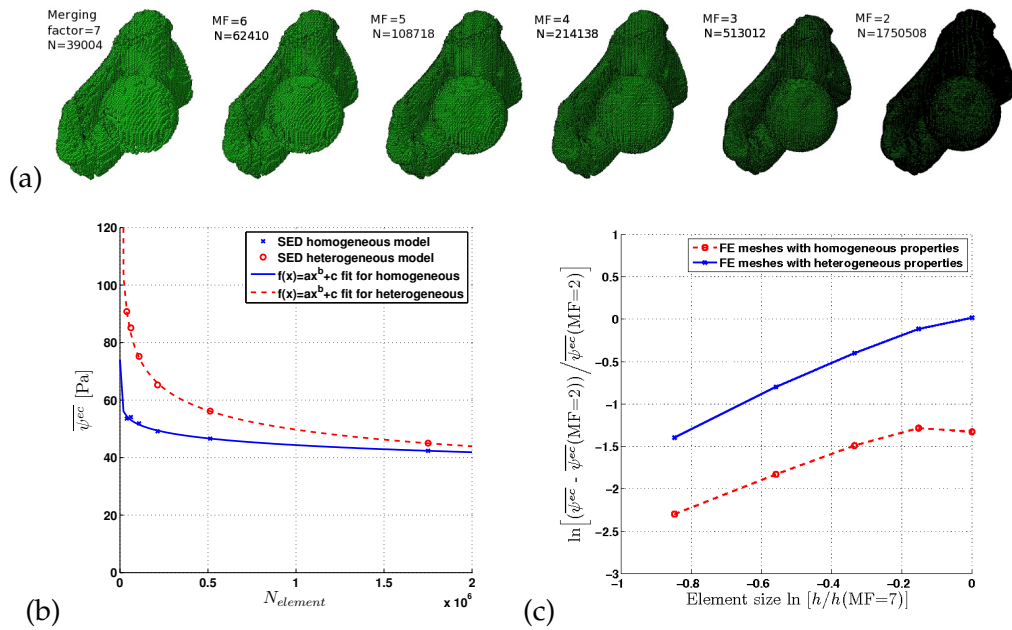
Figure 2.9.: Convergence study: (a) Illustration of the meshes related to merging factors MF=2×2×2 to MF=7×7×7; (b) the strain energy density averaged over all finite elements of the investigated FE mesh, and (c) double logarithmic plot of the energy error versus the element size (N...number of element, h...element size in μm)

energy density, it follows that the force-induced displacements are larger for the simulation with heterogeneous elastic properties, i.e. the heterogeneous structure is softer than the homogeneous one. Replacement of ν^{ec}=0.346 by the frequently
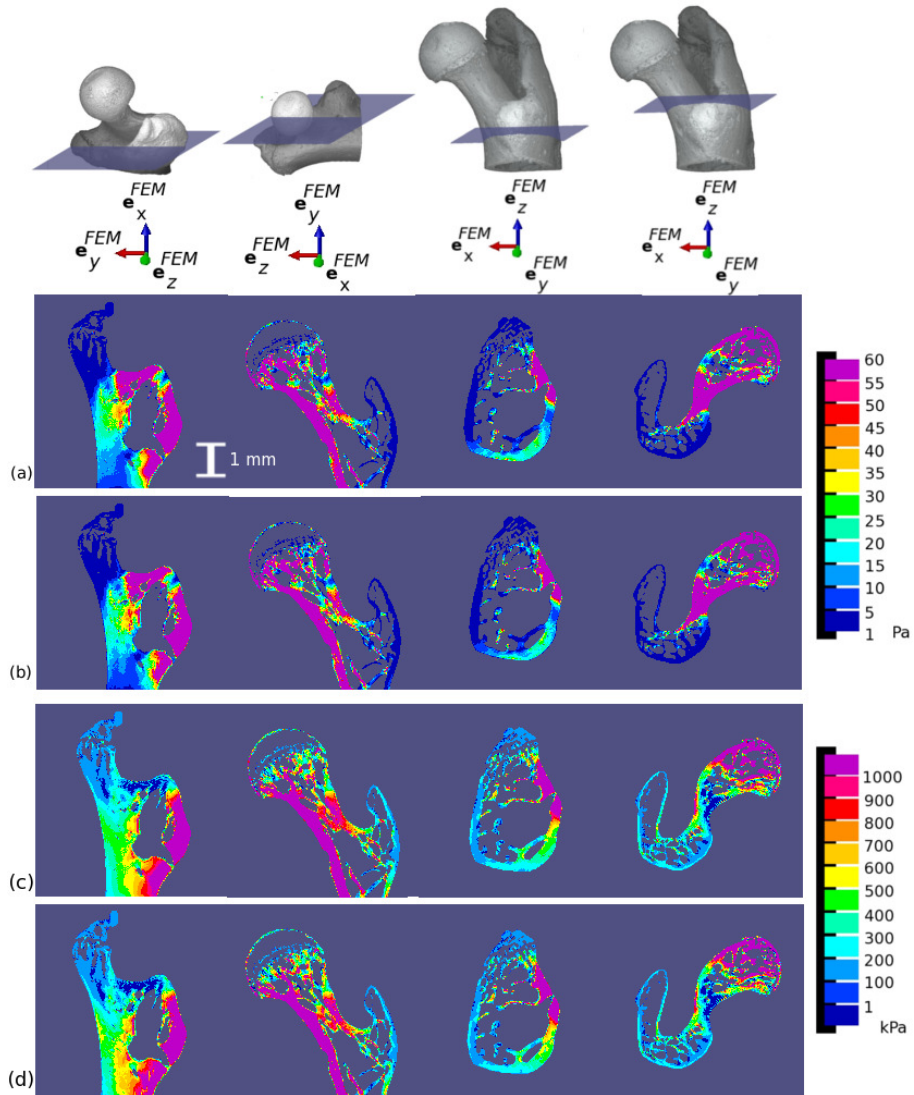
Figure 2.10.: Spatial distributions of strain energy density (a,b) and of maximum principal stress (c,d) throughout characteristic cross sections through the mouse femur, cut orthogonal to direction $\mathbf{e}_x^{FEM}$, $\mathbf{e}_y^{FEM}$, and $\mathbf{e}_z^{FEM}$. The maps are based on the FE simulations with 513012 elements, with homogeneous (a,c) and heterogeneous (b,d) material properties.

used value of ν^{ec}=0.3 in the homogeneous simulations leads to a decrease of the mean strain energy density by 2%.

SED	Homogeneous [Pa]	Heterogeneous [Pa]
Min	0	0
Max	3.05×10^4	7.01×10^4
Mean	46.6	56.2

Table 2.1.: Strain energy density

2.4 DISCUSSION

Combining the "universal" tissue composition rules evidenced in [285] with tissue micromechanics [90, 92], with the average rule for X-ray attenuation coefficients, and with an average tissue density value [74], we here arrive at experimentally and theoretically well founded relations between attenuation-related grey values throughout a micro-computer tomograph of a mouse femur, and corresponding transversely isotropic tissue stiffness components, shown in Figure 6. Traditionally, such relationships are introduced on a purely empirical basis; and only recently, alternative approaches based on tissue composition have been proposed, relating tissue mass densities to elastic properties [285, 287]. While reference [285] rests on experimental data from different laboratories using different chemical analyses methods over a time span of more than 80 years, leading in an astonishing fashion to one *"universal"* tissue composition rule, reference [287], while acknowledging the superiority of composition-based versus purely empirical approaches, rests on the *ad-hoc* assumption of a constant organic volume fraction in tissues of different mass density. However, experimental studies [171] indicate that it is the weight fraction rather than the volume fraction of the organic material in bone tissues, which shows some constancy. Our observation that homogeneous femur models are stiffer than inhomogeneous models is fully consistent with results of Baca et al. [12], which reported a stiffness overestimation of around two when using homogeneous instead of heterogeneous elastic properties. However, they took the homogeneous values directly from the literature [275], rather than deriving them by means of spatial averaging as conducted herein. Similarly, Schneider et al. [259] reported a stiffness overestimation by a factor of 1.6 due to use of homogeneous instead of heterogeneous elastic properties. Since both Baca et al. [12] and Schneider et al. [259] introduce bone material properties at the macroscopic rather than at the micron-level extracellular observation scale, we may conclude that the stiffening effect due to neglection of heterogeneous elasticity distribution is independent of the level of microstructure resolution in the Finite Element analyses. Also, this observation is not restricted to femurs: investigating a full head model of a primate, Wroe et al. [300] reported even 7.2 times higher average strain energy density in heterogeneous than in homogeneous FE models. Thus, stiffness overestimation due to homogeneity assumptions is a well-documented feature observed

in many, very different application cases. The question remains why the aforementioned overestimations vary between 5% and 780%. Are they application-specific, or is there a "deeper" reason for it? Surprisingly, there appears an application-independent feature of all the aforementioned simulations, including our own ones reported in Section 2.3: It relates to the *spatial discretization*, as illustrated in Figure 2.11 where we plot a double logarithmic diagram showing the difference between strain energies encountered in homogeneous and heterogeneous simulations, as function of element-over-structural length, whereby we choose $\mathcal{L}$=2 mm as characteristic structural length. Discretization appears as a major determinant of the homogeneous-to-heterogeneous difference starting from 41% mean strain energy underestimation at $h/\mathcal{L} \approx$0.025, and decreasing to 6% mean strain energy underestimation at $h/\mathcal{L} \approx$0.007. Although this effect has never been explicitly stated in the open literature, it can actually be retrieved by re-evaluation of already published results [12, 259, 300]: see Appendix D for a more detailed discussion. As regards influences beyond discretization, the difference in the behavior of heterogeneous as compared to homogeneous models becomes smaller once the investigated structure is more "material-like", i.e. built up by more or less periodic arrangements of heterogeneities, and subjected to more homogeneously distributed loads or displacements at its boundaries: thereby, homogeneous models still deliver stiffer results, be it 21% stiffness increase in condylar trabecular bone [235], at $h/\mathcal{L} \approx$0.03, and 5% in porous hydroxyapatite granules for bone regeneration [74], also at $h/\mathcal{L} \approx$0.03.

From a more clinical perspective, we regard the proposed CT-to-elasticity conversion as an interesting tool for increasing the reliability of "Virtual physiological human" simulations [88]. While the micromechanics-supported derivation of heterogeneous models from clinical CT has been described in earlier contributions [120, 304], the technique described herein may find direct clinical application in the study of biopsies [139]; and it holds the promise for wide clinical application once clinical micro-CT scanners may be available [290]. More generally, our method is believed to also help in further evaluation of the broad preclinical and fundamental medicine-related mechanical activities in the field, including e.g. microgravity studies [271]. In this context, extensions of the present approach towards elastoplasticity [96, 213] and towards coupled systems biology-micromechanics formulations [29, 256] seem most promising. The former would open the door to rational mechanics-based fracture-risk assessment tools, while the latter may open the door to deciphering the biomechanical and biophysical events triggering mechanics-induced reaction of biological cells. For example, our approach gives direct access to deformation states at bone tissue surfaces, which, when transferred to the biological cells affected to these surfaces, affects their proliferation characteristics, as shown experimentally, e.g. by [142, 147].
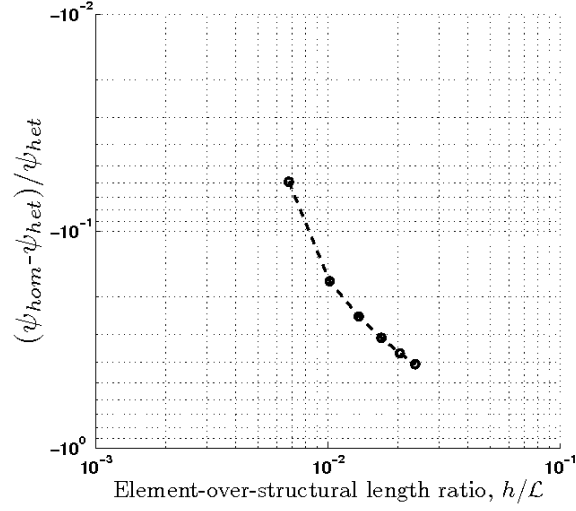
Figure 2.11.: Discretization-dependent influence of heterogeneous versus homogeneous models, on predicted strain energy density

In this context, it is interesting to already note the mechanobiological effect of the uniform tensile stresses across the femoral neck, namely a preservation of bone tissue in the neck seen in Figure 2.10. The situation is fundamentally different in a human femur, where bending moment acts in the femoral neck, which leads to strong resorption of trabeculae in the central portions of the cross sections through the femoral neck [12].

2.5 APPENDIX

2.5.1 *Appendix A. Stiffness tensor components*

The micromechanics-derived stiffness tensor components of extracellular bone tissue can be approximated through polynomials with the tissue mass density ρ^{ec} as argument [285];

$$C_{1111}^{ec} = (4.6826x^3 - 6.0171x^2 + 2.8081x - 0.447)C_{1111}^{HA} \qquad (2.26)$$

$$C_{3333}^{ec} = (-6.8447x^4 + 17.63x^3 - 13.5048x^2 + 4.2118x - 0.4573)C_{1111}^{HA} \quad (2.27)$$

$$C_{1122}^{ec} = (-11.0152x^5 + 29.7474x^4 - 28.7144x^3 + 12.587x^2 - \qquad (2.28)$$
$$-2.3375x + 0.1188)C_{1111}^{HA}$$

$$C_{1133}^{ec} = (-5.0088x^4 + 13.7237x^3 - 12.4876x^2 + 4.8307x - 0.6745)C_{1111}^{HA}(2.29)$$

$$C_{2323}^{ec} = (4.1245x^5 - 14.9352x^4 + 21.9578x^3 - 15.1486x^2 + 4.9459x - \qquad (2.30)$$
$$-0.6169)C_{1111}^{HA}$$

whereby we use the abbreviation

$$x = \rho^{ec}/\rho_{HA} \qquad \text{and} \qquad C_{1111}^{HA} = 137 \, \text{GPa} \qquad (2.31)$$

2.6 APPENDIX B: PHYSIOLOGICAL RELEVANCE OF INVESTIGATED LOAD CASE

In a coordinate system similar to that shown in Figure 2.5, the ratio of the maximum reaction force component over the maximum moment component amounts to 0.144 N/0.278 N.mm $\approx$ 1/2 mm^{-1}; and this is very close to the corresponding ratio throughout a whole gait cycle [293]: 5 BW/10 (BW.mm)=1/2 mm^{-1}. During the gait cycle the axial (tensile) forces in the femur range between 0 and 6 body weights, while our analysis refers to the order of 1 BW or less: hence, our simulations are expected to produce stress distributions similar to those occurring under physiological conditions, at magnitudes which are also relevant for the beginning of the stance phase (as well as for the standing mouse).

2.6.1 *Appendix C. Representation of load in FEM-specific bone frame*

The magnitude of the load **F** amounts to:

$$|\mathbf{F}^{FEM}| = \sqrt{(F_x^{FEM,2} + F_y^{FEM,2} + F_z^{FEM,2}} = 0.166 \, \text{N} \qquad (2.32)$$

The magnitude of the surface traction is the value of the force divided by the sum of the element surface areas onto which it acts. This gives the numerical value of 0.88 MPa for the uniformly distributed surface traction on an area amounting to 0.188 mm². For the FEM analysis, a base frame different from those in Section 2.7 is used, see Figure 2.5; corresponding transformation of the components of load **F** is performed by means of the standard transformation matrix **Q**, reading as

$$\mathbf{Q} = \begin{pmatrix} \cos\alpha_{11} & \cos\alpha_{12} & \cos\alpha_{13} \\ \cos\alpha_{21} & \cos\alpha_{22} & \cos\alpha_{23} \\ \cos\alpha_{31} & \cos\alpha_{32} & \cos\alpha_{33} \end{pmatrix} = \begin{pmatrix} 0 & \cos 45 & \cos 45 \\ 0 & -\cos 45 & \cos 45 \\ 1 & 0 & 0 \end{pmatrix} \qquad (2.33)$$

with α_{ij} being the angle between base vector $\mathbf{e}_i^{FEM}$ of the FEM-related system, and the base vector $\mathbf{e}_j$ of the beam theory-related base frame, i.e $\alpha_{ij} = (\angle\mathbf{e}_i^{FEM}, \mathbf{e}_j)$. Then, based on the transformation rule,

$$\mathbf{F}^{FEM} = \mathbf{Q} \cdot \mathbf{F} \qquad (2.34)$$

the components of the vector $\mathbf{F}$ in the base frame used for the FE model are computed:

$$\mathbf{F}^{FEM} = \begin{pmatrix} 0.059 \text{ N} \\ -0.059 \text{ N} \\ 0.144 \text{ N} \end{pmatrix} \tag{2.35}$$

2.6.2 *Appendix D. Discretization-dependent homogeneous and heterogeneous material properties – re-evaluation of results in the open literature*

For the "small" cortical tissue specimens" of Baca et al. [12], with $h/\mathcal{L} \approx 0.5$, i.e. much larger than our value in Figure 2.11, the relative error in a chosen displacement goes up to around 44 % (see Table 2.2 of [12]). For the "global proximal femur model" of Baca et al. [12], with $h/\mathcal{L} \approx 0.025$, i.e. close to our largest values given in Figure 2.11, the relative error of 30% is almost identical to our value in Figure 2.11. For yet another global proximal femur model, the one of Schneider et al. [259], the element-over-structural length ratio amounts to $h/\mathcal{L} \approx 0.05$, i.e. the element-over-structural length ratio chosen there is larger than all the values investigated in our study; and consistently, the difference between simulation results from homogeneous and heterogeneous meshes is higher than in our investigated cases; it is quantified in terms of 80% reaction force overestimation in homogeneous computations under displacement control. Our general reasoning also holds for organs other than femurs: From Figure 1 of Wroe et al. [300], who describe a hominid skull model, the element-over-structural length can be roughly estimated as $h/\mathcal{L} \approx 0.2$, i.e. significantly larger than in all our simulations; and the corresponding strain energy underestimation due to homogeneous property assumption is significantly larger as well, namely more than 700%.

NOMENCLATURE

BW body weight

$\mathbb{c}_{ec}$ stiffness tensor of extracellular bone matrix

C_{ijkl} stiffness tensor component

$\mathbb{C}^{hom}$ stiffness tensor of the homogenized RVE

$\mathbb{C}^0$ stiffness tensor of the matrix phase

$\mathbb{D}^{ec}$ compliance tensor of the extracellular bone matrix

D_{ijkl}^{ec} component of the compliance tensor

E_1 Young's modulus in radial direction

E_3 Young's modulus in axial direction

f_i volume fraction of material constituent i

$\overline{f_i}$ mean volume fraction of material constituent i

$\mathbf{F}$ Force applied on the femur head

$F_{i,e}^X$ force in Newton applied by i in direction e in referential X

G_{12} shear modulus in radial-circumferential direction

$\hat{G}^{ec}$ isotropic elastic shear modulus

GV^i value of the peak of the constituent i on the grey scale [0 255]

GV_{thr} value of the threshold

$\mathbb{I}$ fourth-order identity tensor

I_1^Σ first invariant of the element-specific strain tensor

I_2^Σ second invariant of the element-specific strain tensor

L_x length in direction x

L_y length in direction y

M_I moment at point I

$\mathbb{P}_r^0$ Hill's tensor of the phase r

$\mathbf{Q}$ transformation matrix

$R_{I,e}$ reaction forces in point I and direction e

$\mathbf{r}$ lever arm

tr trace operator

α_{spine} angle between the femur and the spine

$\boldsymbol{\varepsilon}$ strain tensor

$\hat{\lambda}^{ec}$ isotropic elastic constants Lamé coefficient

μ^{ec} X-ray attenuation coefficient of the extracellular bone matrix

μ_i X-ray intensity attenuation coefficient of constituent i

ν_{12} Poisson's ratio in radial-circumferential plane

ν_{31} Poisson's ratio in radial-axial plane

ρ^{ec} mass density of the extracellular bone matrix

$\overline{\rho^{ec}}$ mean mass density of the extracellular bone matrix in mice

ρ_i "real" mass density of material constituent i

ρ_i^* "apparent" mass density of the constituent i

Ψ^{ec} strain energy density of bone tissue

3

QUANTITATIVE INTRAVOXEL ANALYSIS OF MICRO-CT-SCANNED RESORBING CERAMIC BIOMATERIALS (CZENEK ET AL., 2014)

PUBLICATION AUTHORED BY A. CZENEK, R. BLANCHARD, A. DEJACO, Ó. E. SIGURJÓNSSON, G.ÖRLYGSSON , P. GARGIULO, AND C. HELLMICH CONDITIONALLY ACCEPTED BY *JOURNAL OF MATERIALS RESEARCH*

TYPE OF COLLABORATION

This paper results from a collaboration between the Institute for Mechanics of Materials and Structures of TU Wien, the Reykjavik University and the University Hospital, as well as the Innovation Center Iceland. It was nurtured through a research stay of Agnes Czenek at TU Wien, in course of her Master's thesis supervised by Paolo Gargiulo, who set up the medical research question, together with his clinical partner Gissur Örlygsson and and his materials science collaborator Ólafur Sigurjónsson. Christian Hellmich set up the strategy to adapt the method described in Chapter 1 for ceramic biomaterial scanning, supported by Alexander Dejaco, who played a particular essential role as concerns image analyses and processing. Agnes Czenek was deeply involved in all research steps, from sample preparation, over imaging technique application, to computational analysis and post-processing. The thesis author played the essential role in realization and documentation of the newly developed computational method, and also her supervising work needs to be mentioned explicitly. This clearly qualified her as the second author of the paper.

3.1 INTRODUCTION

Micro-Computed Tomography (microCT) has become a standard tool in biomaterial characterization. It allows for assessment of pore morphology [124, 237] for quantifying the newly formed bone tissue in tissue engineering scaffolds [38, 101, 141] and the identified topology has been used to feed various types of numerical analyses, being related to elastic properties [136, 257], to permeability or to

mechanobiology [252, 253]. All these approaches are based on some kind of statistical evaluation of the grey values standardly defining the three-dimensional CT "images", while the deeper physical meaning of these grey values remains somewhat unconsidered. Actually, these voxel-specific grey values, being defined on 8-bit or 16-bit scales, are proportional to the X-ray attenuation coefficient of the material found within the respective voxel. The X-ray attenuation coefficient, in turn, measures the relative decrease of X-ray beam intensity per length of pervaded matter, and it is a function of the chemical composition of that matter - the latter being of obvious interest for the materials scientist, biomedical engineer, or clinician; and it is the key issue to be tackled in the present paper. However, the proportionality constants defining the aforementioned relation between grey values and attenuation coefficients are standardly neither documented nor disclosed with the available commercial equipment, and in addition, the X-ray attenuation coefficients are no material properties in a strict sense, but depend on the used X-ray energy. In the sequel, we will present a novel method for retrieving both the proportionality constants and the used X-ray energy, from statistical analyses performed on the grey values imaging ceramic biomaterials, in combination with fundamental X-ray physics, comprising chemistry- attenuation relations published by NIST [129, 130, 261] on the one hand, and the volume average rule for X-ray attenuation coefficients [63, 120] on the other hand. Thereby, the key ingredient of the analysis will be the unique existence of one X-ray energy (or of the peak of one X-ray energy spectrum) used for the 3D CT image under consideration. From an applied perspective, the method will provide an answer to the following question: Does cell culturing of ceramic biomaterials in physiological fluid not only affect the several-hundred-microns-to-a-few-millimeters-sized pores provided for tissue ingrowth, but also alter the nanostructure of the solid phase of the ceramic scaffold, i.e. does culturing also increase the nanoporosity found in each and every solid scaffold voxel? Finally, the paper will be concluded by a broader perspective concerning future application of the presented method, together with an overview on how it relates to former "landmark" contributions in the field all paving the way to a more mature, computer-aided biomedicine in general, and biomaterial design in particular.

3.2 MATERIALS AND METHOD

3.2.1 *Test protocol*

As typical ceramic biomaterials for bone tissue engineering, we consider six 3D beta-tri-calcium phosphate (β-TCP) scaffolds (Becton, Dickinson and Company, La Jolla, CA, USA), with an average pore size of 200-400 microns. The samples, installed in plastic flacon tubes together with a phantom of aluminum, were scanned

by means of a Phoenix Nanotom S (General Electric Measurement and Control, X-ray microCT system) at Innovation Center Iceland, Reykjavik, Iceland, at a source current of 160 μA, a source voltage of 90 kV, and a sampling distance of 7.33 microns. The β-TCP scaffolds underwent the following protocol:

First, they were scanned as produced, i.e. with empty pores. Then, they were seeded with the pre-osteoblastic cell line MC3T3-E1 (clone 4; ATCC, Wesel, Germany) and cultured in an alpha-minimum medium (α-MEM) containing 10 % fetal bovine serum (FBS; Lifetechnologies, Boston, MA, USA) mixed with Ascorbic Acid and β-Glycerophosphate (Glucerol 2-phospate disodium salt hydrate; Sigma-Aldrich Chemie GmbH, Taufkirchen, Germany) at 37C, 5% CO2 and 95% relative humidity (RH), for 3, 6, and 8 weeks, respectively. The cell-containing scaffolds were then washed in phosphate buffered saline (PBS), fixed with paraformaldehyde (4% v/v), subjected to a dehydration gradient with an increasing concentration of ethanol, and finally kept in 96% ethanol until further use. The latter consisted of re-installing them into plastic flacons, this time filled with ethanol as well, in order to scan the scaffolds once again. Eventually, they were dried in a CO_2 Critical Point Dryer (Bio-Rad Polaron Division, Watford, England) before being coated by a conductive layer of sputtered gold for further investigation by means of scanning electron microscopy (SEM; LEO Supra 25, Zeiss, Oberkochen, Germany). Respective micrographs were taken at an accelerating voltage of 10 kV, at different magnifications. Anticipating, for the sake of more clearly developing the remaining methods sections, two such micrographs in Figure 3.1, we observe that the investigated scaffolds exhibit a double porous nature: "large", several-hundreds-micrometers-to-a-few-milimeter-sized "macropores" can be clearly distinguished from sub-micrometer-sized "nanopores". Micro Computed Tomography will allow for detailed resolution of the "macropores", while the nanopores will govern the "density" of the individual microCT voxels.

3.2.2 *MicroCT evaluation procedure I: conversion of CT grey values to energy-dependent attenuation coefficients, based on air and aluminum characteristics*

Radon transform-based reconstruction of X-ray projection images recorded by the microCT scanner delivers a 3D image consisting of cubes called voxels, which are characterized by 8-bit grey values being related to the X-ray attenuation coefficients. The latter relation is a linear one, with coefficients a and b depending on the photon energy $\mathcal{E}$ used in the scanner,

$$\mu(\mathcal{E}) = a(\mathcal{E})GV + b(\mathcal{E}) \tag{3.1}$$

Coefficients a and b are standardly not disclosed by a conventional CT equipment, and we will retrieve them from a statistical image analysis in combination
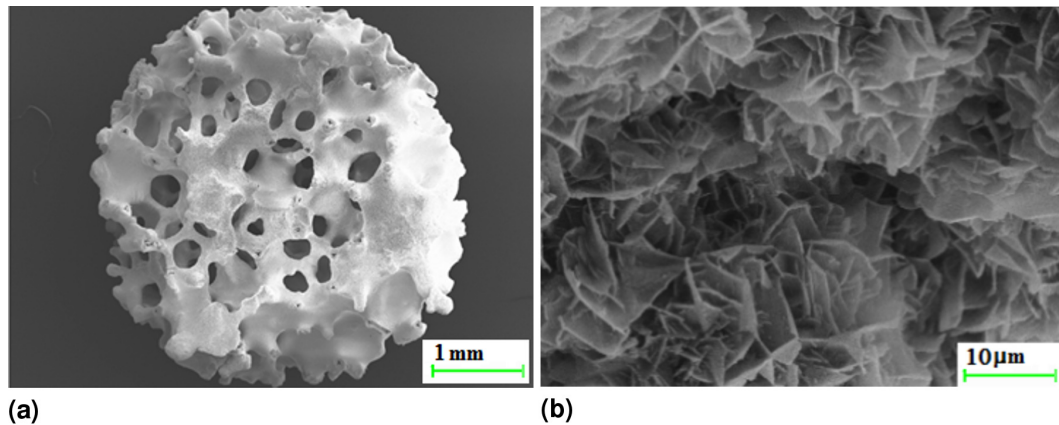
Figure 3.1.: Double porous structure of investigated ceramic biomaterial, as revealed by means of Scanning Electron Microscopy: (a) "macropores" of several hundreds of micrometers size, and (b) "nanopores" at the sub-micrometer scale

with knowledge on the chemical nature of the scanned materials. Therefore, probability density plots of all the grey values found in each of the investigated 3D images are used, in order to identify several landmark values in each of these histograms:

- The leftmost peak of each histogram indicates the most frequent grey value in the image domain illustrating the air which surrounds the depicted scaffold; this grey value is denoted as GV_{air};

- The peak on the right side of each histogram indicates the most frequent grey value of all the voxels containing solid scaffold material, this grey value is denoted as GV_{scaff}^{peak}.

- As a third landmark, the grey value of the aluminum phantom scanned simultaneously with the ceramic scaffold is identified. Since it cannot be determined as a peak on any of the histograms concerning the overall images, the image domains illustrating the phantom material were cropped, and the most frequent grey values occurring in each of these subdomains, denoted as GV_{Al}, was identified.

The X-ray attenuation coefficients of the materials related to the landmark points can be retrieved from the NIST-database of mass attenuation coefficients μ/ρ, based on the mass densities of air, ρ_{air} = 0.0012 g/cm^3, of pure β-TCP, $\rho_{\beta-TCP}$ = 3.07 g/cm^3, of ethanol, $\rho_{C_2H_6O}$ = 0.789 g/cm^3, and of aluminum, ρ_{Al} = 2.699 g/cm^3, see Figure 3.2 for their dependence on the X-ray energy $\mathcal{E}$.
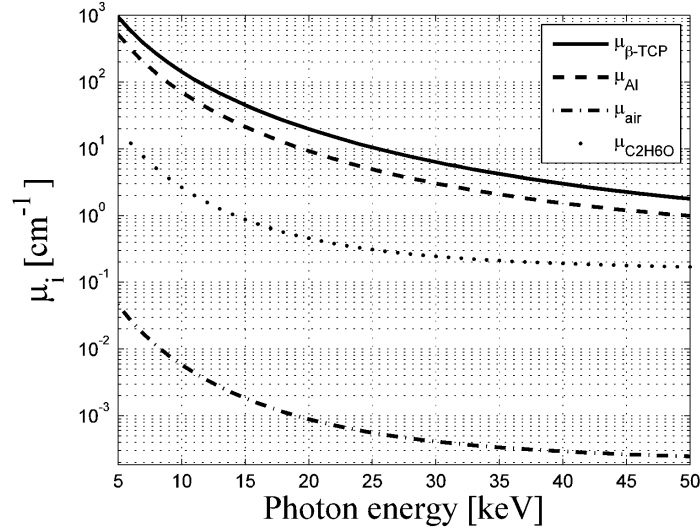
Figure 3.2.: X-ray attenuation coefficients of pure β-TCP, of aluminum, of ethanol, and of air, as functions of the photon energy $\mathcal{E}$ Specification of Eq.(3.1) for the attenuation coefficients and the grey values of air and of aluminum, μ_{air} and μ_{Al}, as well as GV_{air} and GV_{Al}, respectively, yields a linear system of equations for the energy-dependent coefficients a and b

$$\begin{cases} \mu_{air}^{NIST}(\mathcal{E}) = a(\mathcal{E}) \times GV_{air} + b(\mathcal{E}) \\ \mu_{Al}^{NIST}(\mathcal{E}) = a(\mathcal{E}) \times GV_{Al} + b(\mathcal{E}) \end{cases} \tag{3.2}$$

with the solution,

$$\begin{cases} a(\mathcal{E}) = \frac{\mu_{air}^{NIST}(\mathcal{E}) - \mu_{Al}^{NIST}(\mathcal{E})}{GV_{air} - GV_{Al}} \\ b(\mathcal{E}) = \frac{(\mu_{air}^{NIST}(\mathcal{E}) \times GV_{Al} - \mu_{Al}^{NIST}(\mathcal{E}) \times GV_{air}}{GV_{Al} - GV_{air}} \end{cases} \tag{3.3}$$

Coefficients $a(\mathcal{E})$ and $b(\mathcal{E})$ allow for energy-dependent conversion of grey values to X-ray attenuation coefficients according to Eq.(3.1).

3.2.3 *MicroCT evaluation procedure II: identification of used photon energy and of intravoxel nanoporosity, based on attenuation average rule applied to nanoporous ceramic*

In order to identify the actual values for the coefficients a and b, we explicitly consider that relation (3.1) needs to be unique, i.e. per used photon energy $\mathcal{E}$ only one pair of coefficients a and b exists. Accordingly, value-specific, rather than

function-specific, identification of *a* and *b* is based on deriving and then setting equal, of two independent expressions for the photon energy-dependent X-ray attenuation coefficient of the most frequently occurring grey value in the scaffold domain. The first expression relates to the average rule for X-ray attenuation coefficients [63, 120], which when applied to the matter found within a scaffold voxel, reads as

$$\mu_{scaff}^{up} = \mu_{\beta-TCP}(1-\phi) + \mu_{air}\phi \tag{3.4}$$

in the case of untreated (empty) scaffolds, and

$$\mu_{scaff}^{up} = \mu_{\beta-TCP}(1-\phi) + \mu_{C_2H_6O}\phi \tag{3.5}$$

in the case of cultured scaffolds, with ϕ as the voxel-specific nanoporosity found within one voxel, and $\mu_{C_2H_6O}$ as the attenuation coefficient of ethanol. Superscript "up" indicates that Eqs.(3.4) and (3.5) allow for up-scaling of physical quantities (here attenuation coefficients) from the sub- or intra-voxel level, up to the level of the entire voxel. The second expression for the most frequently encountered attenuation value found in the scaffold image domain results from respective specification of Eq.(3.1),

$$\mu_{scaff}^{up} = a(\mathcal{E}) \times GV_{scaff}^{peak} + b(\mathcal{E}) \tag{3.6}$$

Setting Eq.(3.6) equal to specifications of (3.4) and (3.5) for the most frequently encountered nanoporosity value, denoted as ϕ^{peak}, yields an equation in the format,

$$a(\mathcal{E}) \times GV_{scaff}^{peak} + b(\mathcal{E}) = \mu_{\beta-TCP} \times (1-\phi^{peak}) + \mu_i \times \phi^{peak} \tag{3.7}$$

with i = air for the untreated (empty) scaffolds, and i = C_2H_6O otherwise. Eq. (3.7) establishes a non-bijective function between ϕ^{peak} and $\mathcal{E}$: it assigns none, or one, or two values of $\mathcal{E}$ to a specifically chosen value for ϕ^{peak}.

However, only one photon energy was used in any of the considered images, so that only the one unique solution which is related to only one value for the photon energy, remains physically admissible. This gives access to both the photon energy $\mathcal{E}$ used for the considered image, and to the most frequently encountered nanoporosity value, ϕ^{peak}. Once knowing the unique value for the photon energy $\mathcal{E}$, all grey values encountered in the images can be converted into attenuation coefficients μ, by means of Eq.(3.1) with now known functions $a(\mathcal{E})$ and $b(\mathcal{E})$. Use of these attenuation coefficients in average rules (3.4) and (3.5) finally yields voxel-specific nanoporosities according to

$$\phi = \frac{\mu - \mu_{\beta-TCP}}{\mu_i - \mu_{\beta-TCP}} \tag{3.8}$$

	$\overline{\mathcal{A}_v}$	$\overline{\mathcal{B}_v}$	$\overline{\mathcal{C}_v}$	$\overline{\mathcal{D}_v}$	$\overline{\mathcal{E}_v}$
a^*	-1.0521	2.2684	-0.8121	0.3602	0.2394
b^*	0.2197	-0.4645	0.1662	-0.0718	0.1496

Table 3.1.: Proportionality constants a^* and b^* defining, according Eq.(3.11), the polynomial coefficients $\overline{\mathcal{A}_v}$, $\overline{\mathcal{B}_v}$, $\overline{\mathcal{C}_v}$, $\overline{\mathcal{D}_v}$, and $\overline{\mathcal{E}_v}$ for approximation, according to Eq.(3.10), of Poisson's ratio of single crystal v_s

with i = air for the untreated (empty) scaffolds, and i = C_2H_6O otherwise.

3.2.4 *MicroCT evaluation III: micromechanics-base nanoporosity-to-elastic conversion*

Porosity is well-known to strongly govern the mechanical properties of a material [48]. Our present focus is on the nanoporous β-TCP polycrystal found in each and every voxel of the 3D micro Computer Tomographs of the investigated bioceramic scaffolds. As identified in Figure 3.1(b) the β-TCP crystals are of disc-type shape. A recent micromechanics study [94], based on self-consistent estimates for infinitely many, spatially oriented crystal phases [89, 92, 93, 251] and validated on a variety of ceramic material systems [7, 51, 61, 75, 161, 201, 218, 219, 238, 272] has revealed the Young's modulus E of such disc-composed porous polycrystals to closely follow a power law relation with the (nano)porosity as argument,

$$\frac{E}{E_s} = B_E(1 - \phi)^{C_E} \tag{3.9}$$

with *Es* as the Young's modulus of a pure β-TCP crystal (which was quantified through molecular dynamics analysis as E_s=110 GPa [184]), and the power function constants B_E and C_E amounting to 0.9867 and 2.053, respectively [94]. Full elastic characterization of the isotropic polycrystal found in each and every voxel also requires knowledge of Poisson's ratio v, which can again be predicted from the aforementioned self-consistent micromechanics approaches (realized with empty pores), and closely approximated by a fourth-order polynomial,

$$v(v_s) \simeq \overline{\mathcal{A}_v} \times (1 - \phi)^4 + \overline{\mathcal{B}_v} \times (1 - \phi)^3 + \overline{\mathcal{C}_v} \times (1 - \phi)^2 + \overline{\mathcal{D}_v} \times (1 - \phi) + \overline{\mathcal{E}_v} \tag{3.10}$$

Coefficients $\overline{\mathcal{A}_v}$, $\overline{\mathcal{B}_v}$, $\overline{\mathcal{C}_v}$, $\overline{\mathcal{D}_v}$, and $\overline{\mathcal{E}_v}$ of fourth-order polynomial approximation of v depend linearly on v_s,

$$q = a^* \times v_s + b^* \tag{3.11}$$

see Table 3.1 for corresponding numbers, and the pure crystals Poisson's ratio, v_s = 0.276, is again known from molecular dynamics [184]. Equations (3.9), (3.10),

and (3.11) allow for conversion of the voxel-specific nanoporosities as derived from Eq. (3.8) into voxel-specific elastic properties.

3.2.5 *MicroCT evaluation IV: macroporosity quantification*

The voxels characterized by 8-bit grey scale are imported into the medical imaging segmentation software MIMICS (Materialise, Leuven, Belgium) for analysis of the macroporosity quantification, or more precisely, of the change of the volume of the (nanoporous) scaffold material due to treatment. Therefore, for each micro Computed Tomograph, a segmentation process based on the respective grey value histogram is peak performed: The minimum probability value left of the scaffold peak value GV_{scaff} is identified as threshold value GV_{thr}, and all voxels with grey values larger than this threshold are considered as "scaffold material voxels". Then, a 3D model is created of the segmented area, for each scaffold, both before and after cultivation. Finally, the volumes of all the 3D models were computed, and values referring to time points before and after cultivation were compared.

3.3 RESULTS

Low magnification scanning electron micrographs (see Figure 3.3 clearly show covering of the scaffolds' surfaces with pre-osteoblastic cells, once the latter were seeded on the former. During ongoing cultivation, the cellular cover tends to grow denser, as is seen in the higher magnification SEMs of Figure 3.4 initially loose fibrous networks of cell processes [as seen after 3 weeks of cultivation, see Figure 3.4(a,b)], finally turn into more compact extracellular matrix after 8 weeks [as seen in Figure 3.4(c,d)], which finally even tends to cover the originally protruding cell nodules [see Figure 3.4(e,f)]. Further insight into the effects of the cultivation process results from studying the micro Computed Tomographs: Histograms of all CT images of the six investigated scaffolds, in untreated and cultured conditions, respectively, show a large number of grey values referring to low-density voxels (typically with $GV < 100$), and a smaller number of denser voxels referring to the ceramic scaffold material, see Figures 3.5. Before treatment in pseudo-physiological conditions, the low density voxels show one (or one dominant) peak, which is related to the attenuation of air alone, GV_{air}, while sometimes the plastic flacon-induced attenuation effects are explicitly visible as well, as seen in Figure 3.6(c,d,e). After cultivation and scanning in ethanol, the situation changes insofar, as a large number of ethanol-filled voxels emerge, which always leads to two clearly distinguishable peaks in the low density grey value range of the respective histograms, see Figure 3.5(g-l). Thereby, the left of these peaks refers to air, and the respective right one represents ethanol-filled voxels inside the plastic flacon tube. The most frequent grey values found, respectively, in the image domains show-
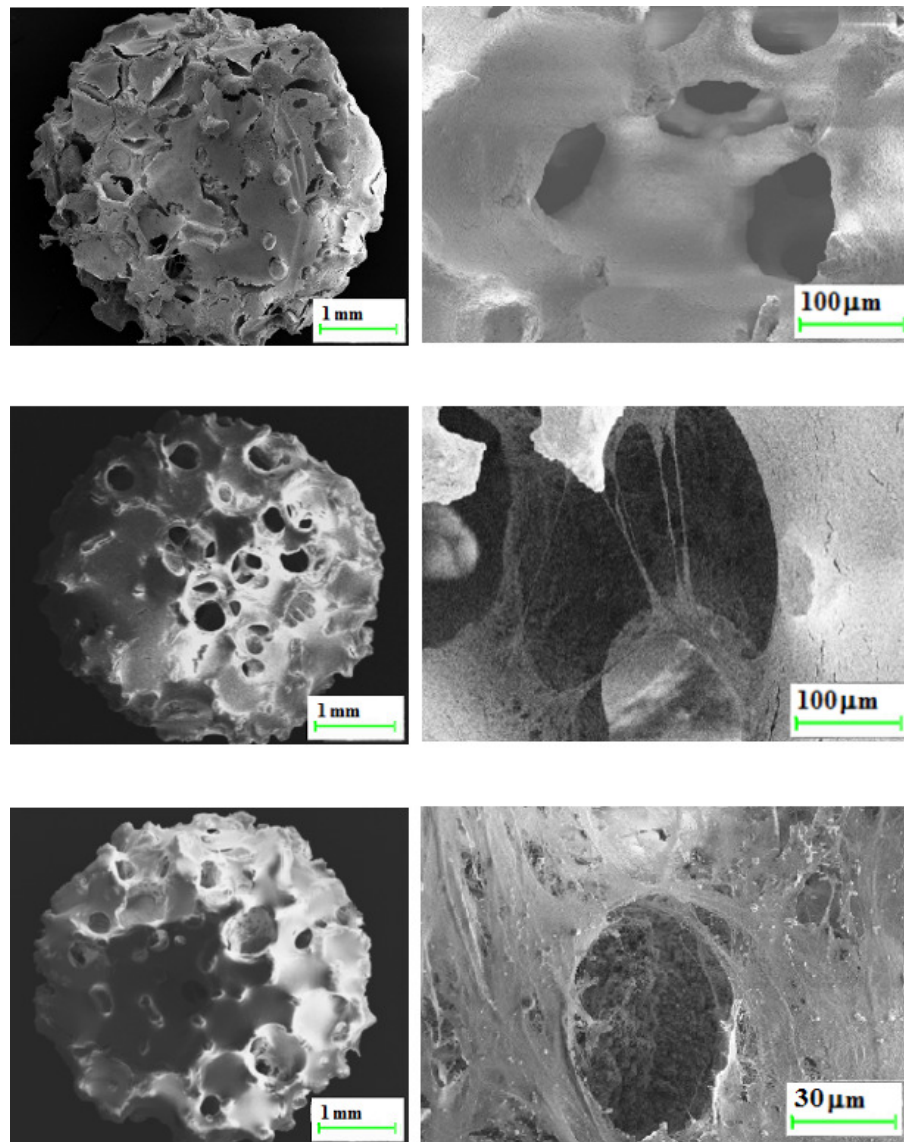
Figure 3.3.: Cell proliferation on ceramic scaffolds as revealed by SEM, at low magnification showing entire scaffolds with approximately 5 mm diameter (a,c,e), and at high magnification zooming into one of the "macropore" cavities (b,d,f): comparison of cell covers after 3 weeks of cultivation (a,b), with the situations after 6 weeks (c,d), and after 8 weeks (e,f)

ing air, GV_{air}, peak scaffold material, GV_{scaff}, and aluminum, GV_{Al}, are varying between all investigated scaffolds, be they treated or untreated, see Table 3.2. Interestingly, there does not emerge any additional peak which would be related to a material with densities somewhere between those of ethanol (or soft tissue) and
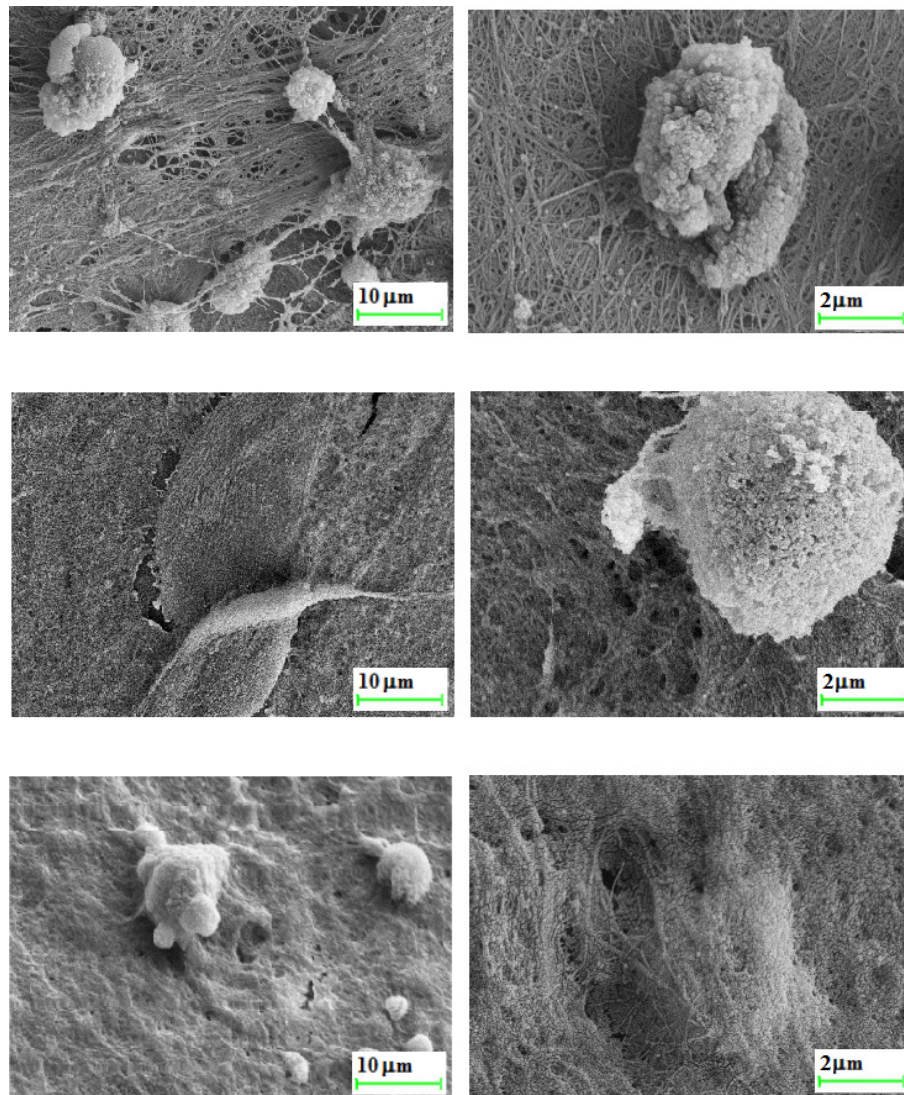
Figure 3.4.: SEM-based close up of immediate vicinity of a cell nodule: after 3 weeks (a,b), after 6 weeks (c,d), and after 8 weeks (e,f)

of ceramic: this clearly shows that the cellular cover on the macropore and the outer surfaces of the scaffolds did not mineralize.

When continuing with the image evaluation steps as described in Section 3.2.2, we find that the proportionality constants a and b relating grey values to attenuation coefficients as given in Eq.(3.1) emerge as decreasing functions of the photon energy, as depicted in Figure 3.6(a,b), plotted based on Eq.(3.3) fed by the data shown in Table 3.2.
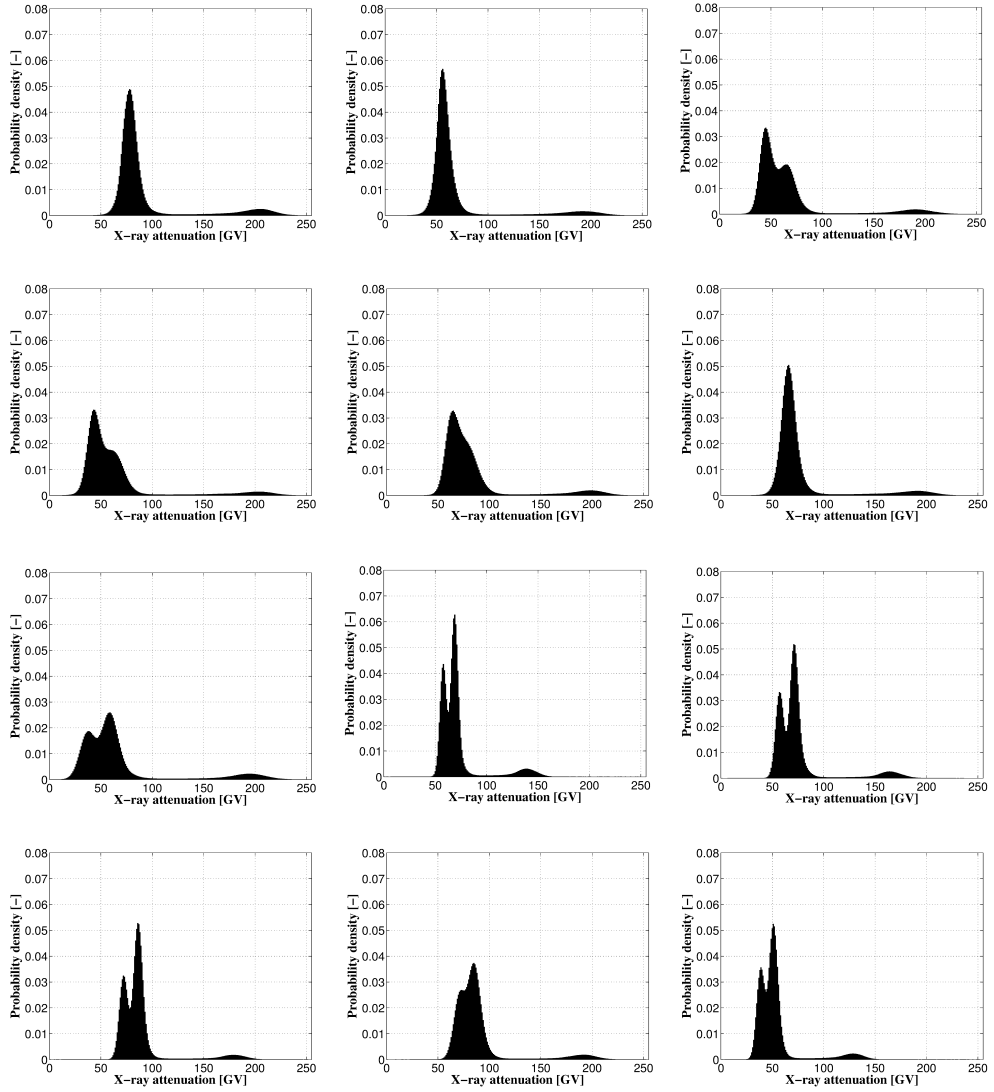
Figure 3.5.: Probability density function of attenuation-related grey values of six CT-imaged β-TCP scaffolds, before cell culturing (a-f): (a) sample I, (b) sample II, (c) sample III, (d) sample IV, (e) sample V, (f) sample VI; and after cell culturing (g-l): (g) sample I after 3 weeks of culturing, (h) sample II after 3 weeks of culturing (i) sample III after 6 weeks of culturing, (j) sample IV after 6 weeks of culturing, (k) sample V after 8 weeks of culturing, (l) sample VI after 8 weeks of culturing

Use of these functions in the identity of upscaled and grey value-determined attenuation coefficients, as given through Eq.(3.7), yields $\mathcal{E}$ - ϕ^{peak} - relations as depicted in Figure 3.6(c). They are used to identify, for each microCT image, the only value of $\mathcal{E}$ which is uniquely related to just one value of ϕ^{peak}: $\mathcal{E}$= 21 keV this

Samples	before cultivation						after cultivation					
	I	II	III	IV	V	VI	I	II	III	IV	V	VI
GV_{air}	77	55	44	42	64	65	37	57	56	71	71	39
GV_{Al}	165	157	168	165	163	144	184	133	155	171	177	122
GV_{scaff}^{peak}	204	193	190	203	196	191	194	138	163	178	191	128
GV_{thr}	127	209	111	113	125	115	115	97	111	122	127	81

Table 3.2.: Landmark grey values of scaffolds before and after cultivation
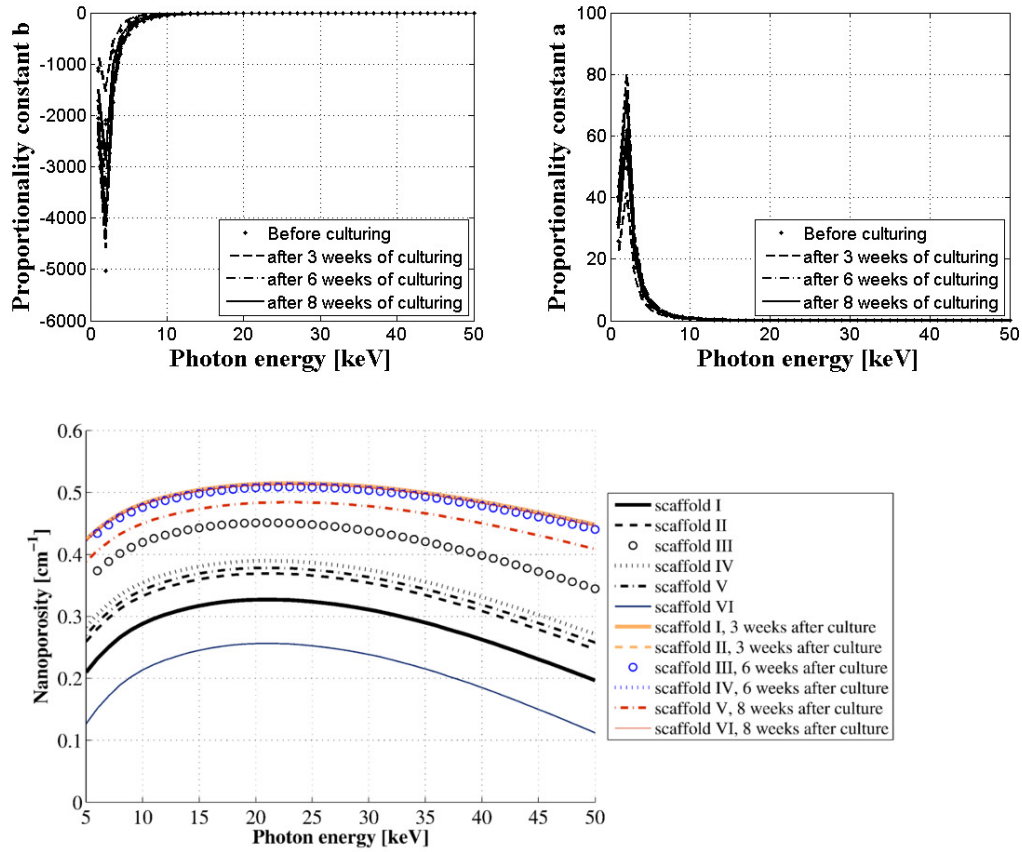
Figure 3.6.: (a,b) Proportionality constants relating grey values to attenuation coefficients, as functions of the photon energy $\mathcal{E}$; (c) scaffold-specific ϕ^{peak} - $\mathcal{E}$ - relations, used for identification of scanner-specific employed photon energy and actual value of most frequently occurring nanoporosity

is the (average) photon energy used for all the images. The corresponding "peak" nanoporosities per investigated scaffold are again scaffold-specific, and increase through treatment, see Table 3.3.

scaffold number	I	II	III	IV	V	VI
before cultivation	0.327	0.369	0.451	0.390	0.379	0.257
after cultivation	0.515	0.516	0.508	0.514	0.484	0.513

Table 3.3.: Most frequently occurring, i.e. "peak", nanoporosities in each scaffold, before and after cultivation

scaffolds' volume (mm^3)	I	II	III	IV	V	VI
before cultivation	0.327	0.369	0.451	0.390	0.379	0.257
after cultivation	0.515	0.516	0.508	0.514	0.484	0.513
change in volume	6%	1%	-4%	-4%	-2%	2%

Table 3.4.: Change in volume (mm^3) of the 3D scaffold's body, due to cultivation

This increase can be studied for all the voxels of all the investigated scaffolds, as depicted in the nanoporosity maps of Figures 3.7 to 3.9

Due to the highly overlinear effect of the nanoporosity on the Young's modulus as quantified through Eq.(3.9), the nanoporostiy increase turns out as quite detrimental for the scaffolds' local stiffnesses (see Figures 3.7 to 3.9), while the voxel-specific Poisson's ratio is also decreasing, i.e. tending towards 0.2 (see Figure 3.7 to 3.9). At the same time, the macroporosities remain fairly constant, as the results of the volume analysis in Table 3.4 show (for corresponding threshold values GV_{thr} used for segmentation, we refer to Table 3.2).

3.4 DISCUSSION

Due to its non-destructive character and its ability to "look deeply" into actually "non-transparent solid microstructures", micro Computed Tomography has become a key tool for the morphological study of biomaterials and tissue engineering scaffolds during the last decade. In the context of calcium phosphate or hydroxyapatite biomaterials, microCT studies allowed for quantification, in time and space, of newly formed bone tissue within *in vivo* implanted ceramic biomaterials [36, 104, 141, 158, 159, 181, 195, 196, 284]. Such analyses are based on segmentation of the grey value-characterized voxels of the micro Computer Tomographs into different subdomains which are defined to lie between certain reasonably chosen threshold values. In the context of bone tissue engineering, the aforementioned subdomains then related to bone tissue, ceramic material, or pore fluid, respectively. In this sense, the voxels within any of these subdomains are not further distinguished, or in other words, the subdomains are considered as "homogeneous". However, quite naturally, there has been the wish to retrieve, from Computed Tomographs, some more detailed, i.e. inhomogeneous, voxel-specific material properties. This aim has been followed perhaps the most pronouncedly,
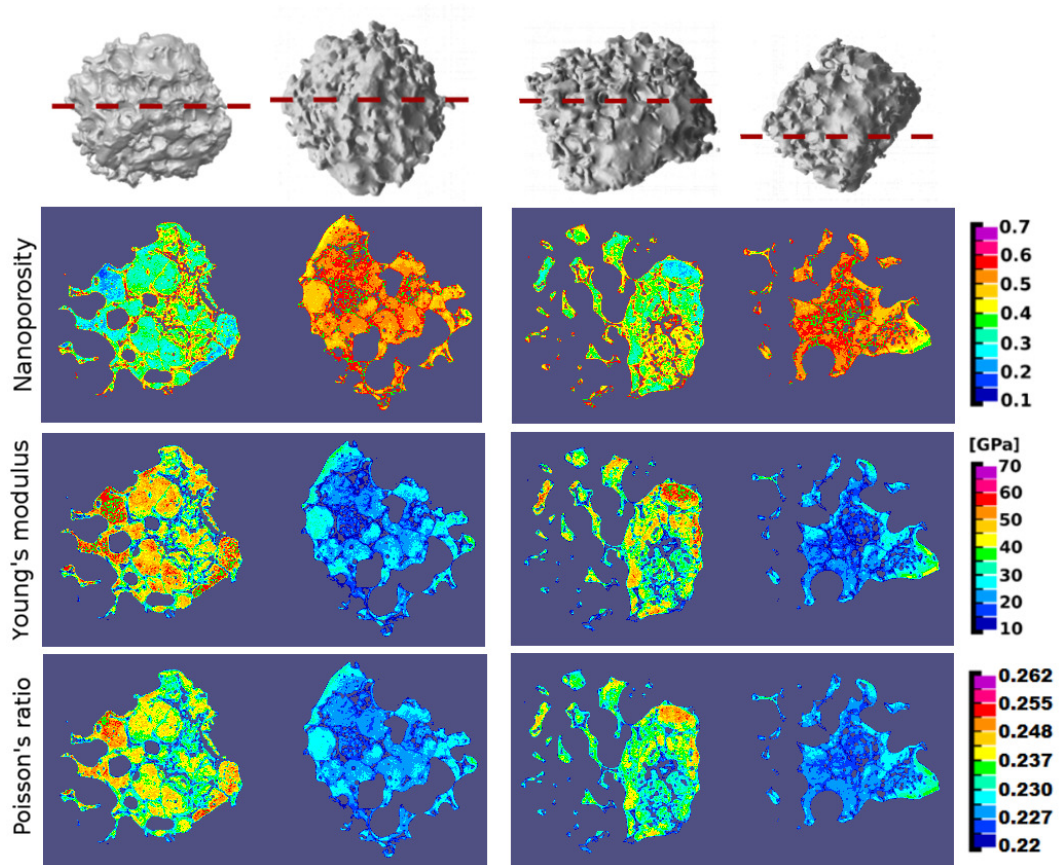
Figure 3.7.: Spatial distributions of voxel-specific nanoporosity and elastic properties, i.e. Young's modulus and Poisson's ratio, over chosen cross sections through: sample I before culturing (a), sample I after 3 weeks of culturing (b), sample II before culturing (c), sample II after 3 weeks of culturing (d)
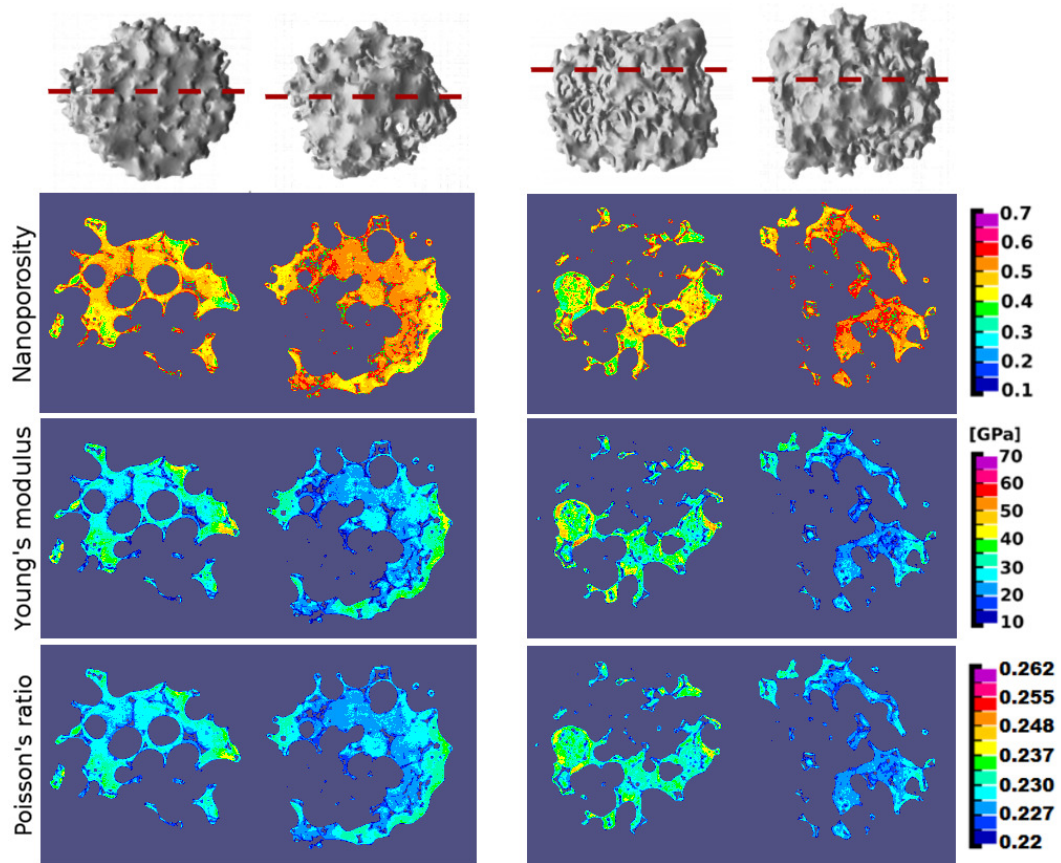
Figure 3.8.: Spatial distributions of voxel-specific nanoporosity and elastic properties, i.e. Young's modulus and Poisson's ratio, over chosen cross sections through: sample III before culturing (a), sample III after 6 weeks of culturing (b), sample VI before culturing (c), sample VI after 6 weeks of culturing (d)
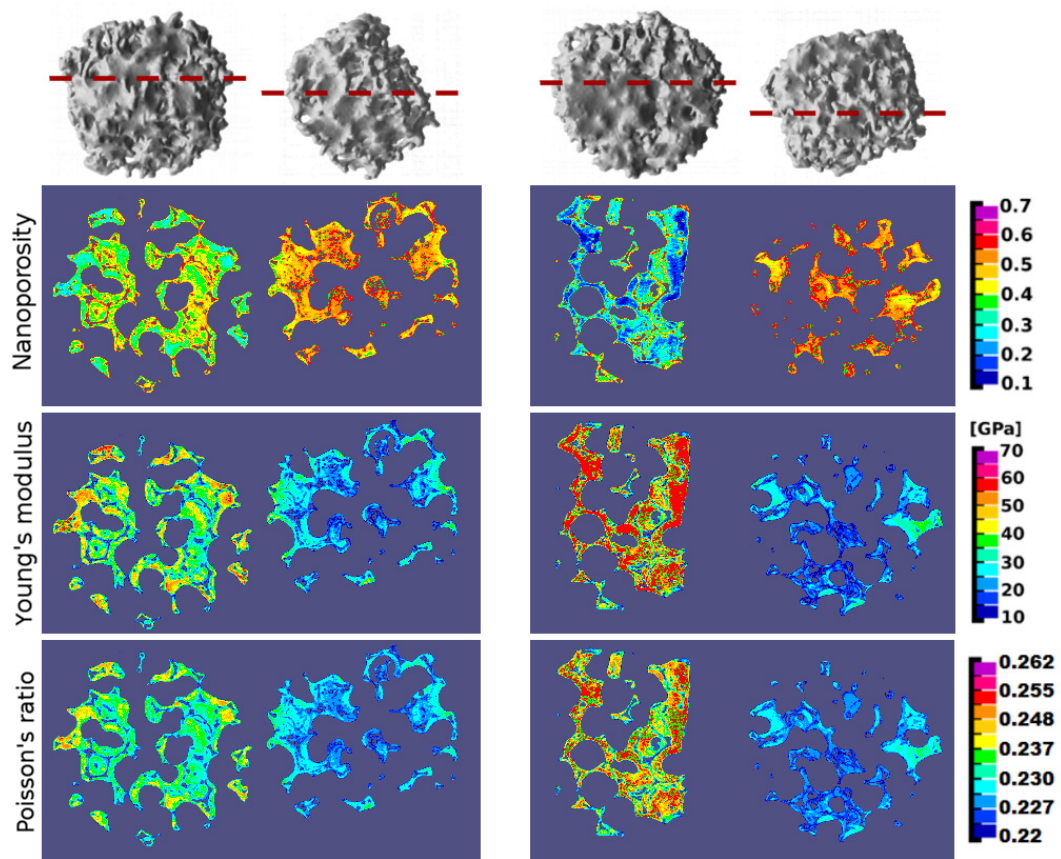
Figure 3.9.: Spatial distributions of voxel-specific nanoporosity and elastic proper-
ties, i.e. Young's modulus and Poisson's ratio, over chosen cross sec-
tions through: sample V before culturing (a), sample V after 8 weeks of
culturing (b), sample VI before culturing (c), sample VI after 8 weeks
of culturing (d)

in the domain of bone imaging: By means of extended regression analyses, relations between X-ray attenuation and mass density of the matter found in respective voxels, on the one hand, and between mass density and Young's modulus, on the other, attenuation-density-elasticity relations have been frequently proposed and reported [56,57,152,239]. However, most of the relationships proposed are not very much in line with each other and the debate on the "proper choice" of regression parameters seems somewhat indeterminable, as a direct consequence of the rather vague physical foundation for the choice of attenuation-density-elasticity relations to be sought for. This situation has provoked the emergence of an alternative view on the issue of proper evaluation of grey values stemming from CT images, with the present contribution marking an important "landmark". In more detail, the steps towards this present landmark have been the following: Instead of directly assuming unique attenuation-to-density relations, the first important step was to remember how, from the basic X-ray physics perspective, attenuation coefficient would be related to mass densities. In fact, it is well known that the attenuation coefficient related to a piece of material is equal to the sum of the material constituents' mass attenuation coefficients times their apparent mass densities (i.e. the constituents' masses over the overall volume of the considered piece of material). This relation could be directly transformed into a volume average rule for attenuation coefficients [120], which opened the way to a physics-based intervoxel analysis: Given a millimeter-sized voxel of a piece of cortical or trabecular bone and provided the attenuation coefficients of bone matrix and of vascular are known, voxel-specific attenuation coefficients can be converted in voxel-specific vascular porosities [120]. In the latter reference, attenuation coefficients were given in terms of Hounsfield numbers (which are attenuation coefficients related to that of water), so that the success of the method depended solely on a reasonably good estimate for the organ-specific, but space- and time-invariant Hounsfield number for the solid bone matrix (in the particulary considered case of a human mandible). Once the spatial porosity distribution throughout the organ was known, it could be further converted, by means of continuum micromechanics models validated for a large number of cortical and trabecular bone samples [117], to voxel-specific transversely isotropic fourth-order stiffness tensors. The situation becomes slightly more tricky if, rather than Hounsfield numbers, only grey values which are linearly proportionally related to the X- ray attenuation coefficients are given (with two *per se* unknown proportionality constants not disclosed by standard microCT equipment). One interesting feature of such attenuation- related grey values is that they still fulfill a volume average rule [257]. In cases where each micro-voxel just comprises a two-phase material, such as a glassy phase and some nanoporosity, the known grey values for voxels filled up by nanopores or by dense glass only, give again access to voxel-specific nanoporosities, which when combined with suitable micromechanics models for porous polycrystals [94], deliver voxel-specific

elastic properties throughout porous bone tissue engineering scaffolds made out of bioglasses [257]. While the identification of the grey value of a pore-filled voxel follows quite unambigously from a histogram made from all voxels found within the considered 3D image, identification of the largest grey value as being actually of dense glass requires that such a completely glass- or ceramic-filled voxel would indeed occur in the investigated construct. In cases where this is not necessarily true the intravoxel analysis method has to be again refined: One way to do that consists of considering additional experiments conducted on the biomaterial scaffold, as it has been the case with hydroxyapatite bioceramics used as maxillofacial restoration tools [74] Again encountering a two-phase "pore-crystal" material in each voxel, mathematical integration of the nanoporous space over the entire scaffold domain gives access to the overall mass density of the scaffold. Alternative, independent retrieval of the latter from direct weighing and volume tests of the scanned granule provides an additional equation for computing the nanoporosity found in the densest voxel. However, in all these contributions, the question remained on whether the proportionality constants between grey values and X-ray attenuation coefficients might be even directly accessible (without the need of additional e.g. mass density experiments), and the corresponding breakthrough was developed in detail in the present contribution: considering both the photon energy dependence of actual X-ray attenuation coefficients as publicly available in the NIST database, and the necessarily unique relation between grey values and X-ray attenuation coefficients, allowed indeed for direct determination of (i) the proportionality constants, (ii) the used photon energy, and (iii) the X-ray attenuation distribution throughout nano- and microporous bioceramic scaffolds. Again, the latter information could be transformed into other, micromorphologically governed physical properties, such as elastic properties. In combination with similar endeavors concerning bone tissue [20], this opens the way to realistic mechanical modeling of bone-tissue composites as encountered in tissue engineering, and when extending the morphology-to-mechanics conversion step towards material strength [92, 96] and viscoelasticity [79], to reliable computer-aided biomaterial design, at a level approaching that of classical civil or mechanical engineering. We regard this as an important complement to various activities in mechanics-based biomaterial research emerging recently on the international engineering science scene [41, 128, 155, 156]. While a more detailed presentation of corresponding mechanics-related results, as currently under intensive investigation, is reserved for future publications, we re-iterate from the results of this paper that also the newly developed intravoxel porosity analysis in itself has revealed remarkable bioresorption and cytocompatibility features, which, to the best knowledge of the authors, have never been described up to the present precision so far: Namely, resorption of β-TCP scaffolds occurs at the sub-micron level much more than at the millimeter level, and pre-osteoblastic cells do proliferate on the scaffolds' internal

and external surfaces, as has been reported in earlier studies [11] however, the life conditions in static cultures do not trigger them as to produce real mineralized bone matrix. Therefore, dynamic conditions such as in a bioreactor [187, 188] may be needed they are at the center of the current and future practical clinical side of the described research endeavors.

3.5 ACKNOWLEDGMENTS

NOMENCLATURE

Variables
a, b coefficients of proportionality
$a*, b*$ proportionality constants
$\overline{\mathcal{A}}, \overline{\mathcal{B}}, \overline{\mathcal{C}}, \overline{\mathcal{D}}, \overline{\mathcal{E}}$ polynomial coefficients
B, C power function constants
$\mathbb{C}$ stiffness matrix
C_{ijkl} stiffness matrix component
E Young's modulus
GV grey value
q
ϵ photon energy
μ attenuation coefficient
ν Poisson's ratio
ϕ nanoporosity
ρ mass density

Subscripts
air ... of air
Al ... of aluminum
C_2H_6O ... of ethanol
E ... for the Young's modulus
s ... of the pure crystals of material
$scaff$ ... of the scaffold
thr ... at threshold
$\beta - TCP$ ... of β tricalcium phosphate

ν ... for the Poisson's ratio

Superscripts
$peak$ ... at peak
$NIST$ ... from the National Institute of Technology database
up ... upscaled

PATIENT-SPECIFIC FRACTURE RISK ASSESSMENT OF VERTEBRAE (BLANCHARD ET AL., 2014)

TWO-PARTS PUBLICATION SUBMITTED TO *JOURNAL OF BIOMECHANICAL ENGINEERING (ASME)*
PART I IS AUTHORED BY R. BLANCHARD, A. MALANDRINO, Z. SANT, AND C. HELLMICH
PART II IS AUTHORED BY R. BLANCHARD, C. MORIN, A. VELLA, Z. SANT, AND C. HELLMICH

TYPE OF COLLABORATION

This paper results from a collaboration between the Institute for Mechanics of Materials and Structures of TU Wien, the University of Malta, and the Catalonian Bioengineering Institute. Andrea Malandrino performed the mass density measurements and evaluated them. Zdenka Sant and Alain Vella provided the used Finite Element models and helped in their adaptation for realization of the new approach described. Claire Morin, formerly at TU Wien and now at Ecole des Mines de Saint Etienne, provided the bone strength upscaling code, supported its adaptation for the present purpose, and Christian Hellmich guided the overall research work, particularly through taking the lead in the documentation. Method development, data processing, code implementation and testing, as well as documentation rested primarily on the thesis author, which qualified her as first author.

4.1 PART I: HIERARCHICAL INTRAVOXEL X-RAY PHYSICS FOR CT GREY VALUE TO BONE COMPOSITION CONVERSION

4.1.1 *Introduction*

Computed Tomography- and Finite Element-based failure risk assessment of bony structures remains one of the central desires in bone biomechanics. This topic has been dealt with extensively, but broad clinical application has not been achieved yet. The reason for this could be that the physical origins of bone strength may

need to be considered more deeply and rigorously than it has been attempted so far. In fact, when screening the comprehensive literature on the topic, it becomes obvious that even the most famous contributions on the topic rely on purely elastic analyses. Typically, linear regression parameters between linear elastic FE analyses and strength tests performed on the same piece of bone are established, which are typically superior to regressions between strength and some direct radiological measures [49, 62, 189]. In other studies, stress states derived from linear Finite Element analyses are averaged over suitably chosen "regions of interest", and corresponding average stress levels are thought to be relevant for fracture risk assessment [154]. Still, one might argue that the choice of such regions of interest may be quite arbitrary, but at the same time very influential on the corresponding simulation results. This would call for a deeper theoretical involvement into the material mechanics of bone, and the obvious next step would be to apply elastoplasticity. In fact, elastoplastic Finite Element simulations on bony organs have already been performed [213], and they have turned out to be useful when it comes to simulate the interaction between an implant and the neighboring bone. Still, this does not render the entire issue of bone strength assessment as being solved: There is a second challenge which needs to be overcome: the determination of relevant mechanical properties (elastic as well as elasto-plastic strength values), from clinically available CT-images. The traditional approach [154] consists of regression analyses between attenuation-related grey values and mechanical properties; however, no consensus exists on unique regression parameters; they most probably depend on various additional variables, such as CT machine settings and X-ray energies used. A more physics-oriented approach would ask for the origin of elasticity and strength of the material found within each voxel to be found in a Computed micrograph – this origin being the material microstructure and the mechanical properties of its elementary components, in the case of bone: hydroxyapatite, collagen, and water with some non-collageneous organics. Thanks to recent discoveries concerning universal patterns in bone tissue composition and microstructure [118, 208, 209, 285], as well as their effects on the tissues' elasticity and strength [90, 92, 210], we are now in the position to rigorously relate tissue mass densities and porosities at different scales of observation, to corresponding elastic and strength values. Still, these mass densities need to be related to the grey values defining a CT-image, in order to obtain the desired (unique and reliable) relation between CT-numbers and mechanical properties; and this task is challenged by the fact that the X-ray attenuation coefficients do not only depend on the material's chemistry (which establishes the link to mass density), but also on the X-ray energy used for the CT image; and as a rule, the latter is not documented in a clinical setting. The present paper describes, by example of a human vertebra, how to overcome this last obstacle, through combining X-ray attenuation averaging at different scales and over different tissues, with "univer-

sal" compositional characteristics of the latter. This opens the way to fully patient- and site-specific mass density and composition maps throughout the investigated organs, as documented and discussed in Sections 4.1.3 and 4.1.4 of the present paper. In the companion paper, Part II, these voxel-specific compositional informations enter multiscale elastoplastic material descriptions for bone tissue, which allow not only for identification of patient-specific elasticity maps, but also for patient-specific fracture risk maps related to a specific mode of loading, in the context of micromechanics-enriched Finite Element analyses. This is regarded as a considerable step towards clinically relevant Finite Element simulations derived from sound quantitative bone biomechanics, biophysics, and biochemistry.

4.1.2 *Methods*

4.1.2.1 *Conversion of CT grey values into energy–dependent attenuation coefficients, based on statistical image evaluation and on soft tissue composition rules*

A CT scan of a motion segment of a 15-years-old male patient, consisting of two lumbar vertebral bodies L3 and L4, was obtained from Mater Dei Hospital, Malta. The HiSpeed Dual medical CT scanner from General Electrics was employed in helical mode, with the following parameters: source voltage: 140 kV, source current: 110 μA, exposure time: 1000 ms, image pixel size: 0.324 mm, and slice spacing: 1.25 mm. In the respective CT images, which capture not only the bone structure of a vertebral body, but also the surrounding soft tissue, the X-ray attenuation information is stored in terms of 8-bit grey values, increasing with intensifying attenuation. In order to separate soft and hard tissues, all the grey values found in the 3D image are evaluated first in terms of a (normalized) histogram, representing a probability density function for the grey value of one voxel which is randomly chosen from the 3D image. More precisely, in such histogram, we identify two peaks related to the most frequently occurring grey values containing (i) adipose tissues (GV_{fat}) and (ii) inner organs (GV_{soft}), with $GV_{fat} < GV_{soft}$. In order to separate bone tissue voxels from their surroundings, we consider the first minimum value of the probability density function, which appears right of GV_{soft}, i.e. for $GV > GV_{soft}$. We denote this minimum value as segmentation threshold GV_{thr}.

In order to back-translate the user-selected grey scale values into the underlying X-ray attenuation values, we consider the linear relation between grey values and X-ray energy-dependent attenuation coefficients, involving three unknowns: two proportionality factors a and b, and the X-ray energy $\mathcal{E}$:

$$\mu(\mathcal{E}) = a(\mathcal{E}) \times GV + b(\mathcal{E}) \tag{4.1}$$
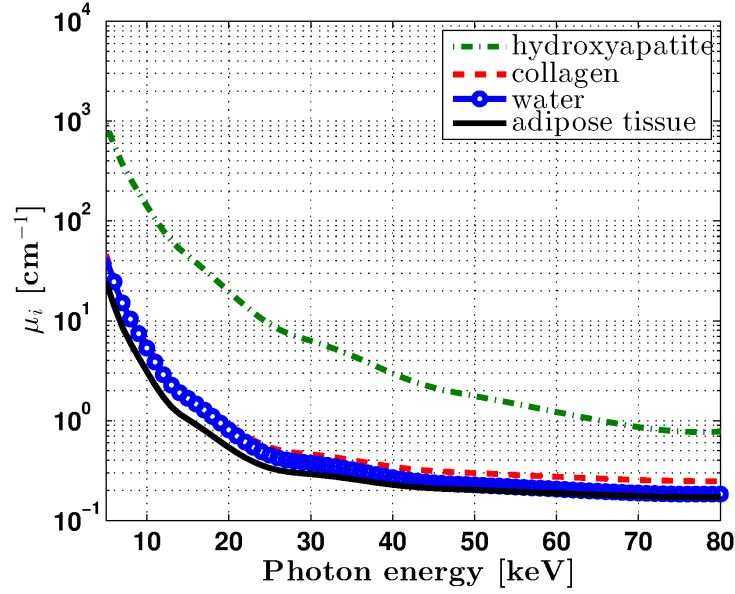
Figure 4.1.: X-ray attenuation coefficients of the elementary constituents of bone tissue, and of adipose tissue, as functions of the photon energy.

Eqn.(4.1) expresses that the X-ray attenuation coefficient is no classical material property. In the sense that it depends not only on the matter contained in a specific voxel, but also on the energy used for X-ray penetration of the investigated object. In order to identify the energy-dependent slope and intercept functions, $a(\mathcal{E})$ and $b(\mathcal{E})$, we specify (4.1) for the aforementioned two landmark values concerning fat and soft tissues:

$$
\begin{cases}
\mu_{fat}(\mathcal{E}) & = a(\mathcal{E}) \times GV_{fat} + b(\mathcal{E}) \quad (4.2a) \\
\mu_{soft}(\mathcal{E}) & = a(\mathcal{E}) \times GV_{soft} + b(\mathcal{E}) \quad (4.2b)
\end{cases}
$$

In order to determine the functions at the left-hand side of Eqn.(4.2a) and (4.2b), we consider two fundamental relations:

- The mass attenuation coefficient of a chemical substance i with mass density ρ_i, $(\mu/\rho)_i$, is a function of its chemical composition, as is openly accessible from the National Institute of Standards and Technology (NIST) [1]; in particular, the mass attenuation coefficient of fat is directly given so that the mass density of fat ρ_{fat}=0.95 g/cm^3 [194] gives access to the attenuation coefficient of fat, as depicted by the black line in Figure 4.1.
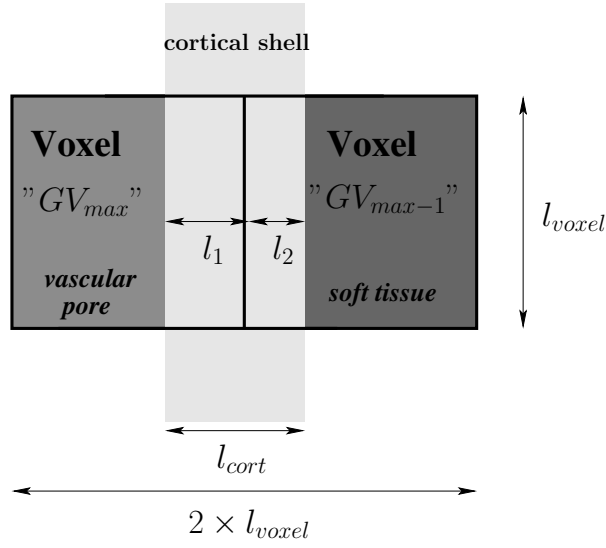
Figure 4.2.: Partition of cortical shell (with thickness l_{cort}) between two neighboring voxels (with edge length l_{voxel})

- The X-ray attenuation coefficient of a composite material located inside one voxel is identical to the volume average of the X-ray attenuation coefficients of the material's single constituents [63, 120, 135]

$$\mu(\mathcal{E}) = \sum_{i}^{N_C} \mu_i(\mathcal{E}) \times f_i \qquad (4.3)$$

with μ_i, $i = 1, ..., N_C$, as the X-ray attenuation coefficient of constituent i, N_C as the total number of constituents, and with f_i as the volume fraction of constituent i within the considered voxel.

Applying Eqn.(4.3) to the soft tissue, i.e. inner organs and muscles localized around the spine, yields the term on the left-hand side of Eqn.(4.2b) also fulfills then Eqn.(4.4).

$$\mu_{soft}(\mathcal{E}) = \mu_{H_2O}(\mathcal{E}) \times f_{H_2O} + \mu_{org}(\mathcal{E}) \times (1 - f_{H_2O}) \qquad (4.4)$$

where the attenuation coefficient of water follows from its chemical formula H_2O, see second-lowest line in Fig.4.1, and that of organic material is approximated by the smallest amino acid, glycine (making up a high percentage of collagen, and being similar in structure to the remaining portion of collagen [102]), with

chemical formula $C_2H_5NO_2$, see dotted line in Fig.4.1. The volume fraction of water, f_{H_2O}, is accessed through the average rule for the soft tissue mass density,

$$\rho_{soft} = f_{H_2O} \times \rho_{H_2O} + (1 - f_{H_2O}) \times \rho_{col} \qquad (4.5)$$

namely through

$$f_{H_2O} = \frac{\rho_{soft} - \rho_{col}}{\rho_{H_2O} - \rho_{col}} \qquad (4.6)$$

with the soft tissue mass density of tissues around the spine being documented as ρ_{soft}= 1.052 g/cm^3 [194] and ρ_{col}=1.042 g/cm^3 [170].

Conclusively, we solve Eqn.(4.2a) and (4.2b), while considering Eqn.(4.3)-(4.6), for $a(\mathcal{E})$ and $b(\mathcal{E})$, yielding the energy-dependent proportionality constants depicted in Fig. 4.6. They allow for (still X-ray energy-dependent) conversion of grey values to the actual physical quantities they represent.

4.1.2.2 *Identification of X-ray photon energy and of extracellular bone tissue mass density, based on general bone tissue composition rules*

As supplementar voxels of interest, we consider the densest voxel in the *corpus vertebrae*, GV_{max}, as well as its densest neighbor, whose grey value is denoted as GV_{max-1}. The latter two voxels contain both extravascular tissue resembling "cortical bone" (as e.g. seen in the microCT image of Figure 4.4), as well as vascular porosity or soft tissue, with GV_{soft}, see Figure 4.2. The grey values related to these two voxels are used for identification of the grey value GV_{ev} being related to a (fictitious) voxel which would be filled by extravascular bone tissue only. Such a voxel does not occur in the investigated CT image since its voxel size amounts to l_{voxel} = 324 μm, while the characteristic size of a cortical shell in vertebrae typically amounts to l_{cort}= 230 μm [245, 263, 295]. This cortical shell thickness either fully lies within one single voxel, or it contributes to the attenuation coefficients of two neighboring voxels. In the latter case, the cortical shell thickness is partitioned between the two neighboring voxels, with voxel-specific parts l_1 and l_2, $l_1 + l_2 = l_{cort}$, see Figure 4.2; and the former case can be seen as a limit of the latter, characterized by $l_2 = 0$ and $l_1 = l_{cort}$. The area of the voxel not covered by the cortical shell is considered as surrounding soft tissue on the outer side, and watery fluid-filled vascular porosity on the inner side. Since both materials exhibit very similar attenuation properties, we consider the same grey value for water and soft tissue. In order to use these partitioning considerations for identification of the *a priori* unknown grey value for the extravascular tissue, GV_{ev}, we use grey

value-to-attenuation relation (4.1) in average rule (4.3), so as to show the existence of an average rule for the grey values as well,

$$GV = \sum_i^{N_C} GV_i \times f_i \tag{4.7}$$

When applying (4.7) to the cortical shell partitioned between two voxels as depicted in Figure 4.2 one arrives at the following system of equations:

$$\begin{cases} \frac{l_1}{l_{voxel}} \times GV_{ev} + (1 - \frac{l_1}{l_{voxel}}) \times GV_{soft} = GV_{max} \\ \frac{l_2}{l_{voxel}} \times GV_{ev} + (1 - \frac{l_2}{l_{voxel}}) \times GV_{soft} = GV_{max-1} \\ l_1 + l_2 = l_{cort} \end{cases} \tag{4.8}$$

Solving these three equations for the unknowns GV_{ev}, l_1, and l_2, yields in particular the sought value for GV_{ev} as function of all the already identified grey values and length dimensions,

$$GV_{ev} = \frac{l_{voxel}}{l_{cort}} \times (GV_{max} + GV_{max-1} - 2GV_{soft}) + GV_{soft} \tag{4.9}$$

In order to identify the X-ray energy $\mathcal{E}$, which then will allow for a unique scaling relation between grey values and attenuation coefficients as given through Eqn.(4.1), we consider two independent ways to access the attenuation coefficient of the extravascular bone material, μ_{ev}. These two ways need to deliver *one single, unique result*:

- The first access to μ_{ev} is provided through

$$\mu_{ev}(\mathcal{E}) = a(\mathcal{E}) \times GV_{ev} + b(\mathcal{E}) \tag{4.10}$$

  fed with the energy-dependent proportionality constants shown in Fig.4.6;

- The second access is provided through repeated use of Eqn.(4.3) for upscaling attenuation coefficients from the level of the elementary constituents of bone tissue, up the level of the extravascular bone material.

As regards the latter item, the NIST-data base allows for retrieval of the attenuation coefficients of the (mechanically relevant) elementary constituents of extracellular bone tissue: hydroxyapatite, organic material, and water. The two latter ones have been already introduced in Section 4.1.2.1, and the chemical formula $Ca_{10}(PO_4)_6(OH)_2$ allows for obtaining the hydroxyapatite-related attenuation

curve, as depicted in Fig.4.1. Use of these functions in Eqn.(4.3), i.e. upscaling from the elementary to the extracellular level, yields

$$
\begin{aligned}
\mu_{ec}^{up}(\mathcal{E}) =& \mu_{HA}(\mathcal{E}) \times f_{HA}^{ec} + \mu_{org}(\mathcal{E}) \times f_{org}^{ec} + + \mu_{H_2O}(\mathcal{E}) \times f_{H_2O}^{ec} \\
& \text{with} \quad f_{H_2O}^{ec} + f_{org}^{ec} + f_{HA}^{ec} = 1
\end{aligned}
\tag{4.11}
$$

The constituent volume fractions f_{HA}^{ec}, f_{org}^{ec}, and $f_{H_2O}^{ec}$ (measured per volume of extracellular (*ec*) material) depend in a unique fashion on the tissue's extracellular mass density ρ_{ec}, see Fig.4.3; as evidenced in [285], from a multitude of weighing tests on dried, demineralized, deorganified, and ashes samples collected over 80 years of research [18, 32, 44, 106, 112, 113, 170–172, 174, 176, 178]. This implies the existence of a function $\mu_{ec}(\mathcal{E}, \rho_{ec})$ which can be upscaled to the extravascular level through

$$
\mu_{ev}^{up}(\mathcal{E}, \rho_{ec}) = \phi_{lac} \times \mu_{H_2O}(\mathcal{E}) + (1 - \phi_{lac}) \times \mu_{ec}(\mathcal{E})
\tag{4.12}
$$

with ϕ_{lac}=0.10 [210, 295]. Expressions (4.10) and (4.12) need to deliver the same result, which we express as a ratio being equal to one,

$$
\mu_{ev}(\mathcal{E}) / \mu_{ev}^{up}(\mathcal{E}, \rho_{ec}) = R(\mathcal{E}, \rho_{ec}) = 1
\tag{4.13}
$$

Equation (4.13) defines a non-bijective function of the mass density as a function of the energy, i.e. more than one energy value, or no energy value, may be related to one and the same mass density value. From this function, the value for the extracellular mass density, which is related to only one, i.e. unique, energy value, will be identified: this provides access to both the X-ray energy used for the image, and to the extracellular mass density of the investigated bone tissue from a human vertebra.

4.1.2.3 *Vertebra tissue mass density from weighting tests*

In order to check the relevance of the value for the tissue mass density retrieved by means of the strategy outlined in Section 4.1.2.2, an independent experimental route towards ρ_{ec} is pursued, through the following protocol: From the mid-height portion of an elderly human vertebral body provided by the Medical University of Vienna, a slice was cut out by means of a band saw under continuous water irrigation (300Cp, Exakt GmbH, Germany). Out of this slice, eight cubes with 5-6 mm edge length were extracted by means of a wheel saw (Isomet, Buehler, USA). All the specimens had a face containing the external vertebral cortex, as can be seen in Fig.4.4. Two exactly parallel opposite surfaces orthogonal to the cortex layer were cut, whereby attention was paid on maintaining the cortex undamaged. Then, the specimens were immersed in an ultrasonic bath with 0.9% saline solution and standard soap, for 3 minutes at 40°C, in order to allow for mixing of the solution with the soap. Afterwards, the specimens were left during 24 hours at
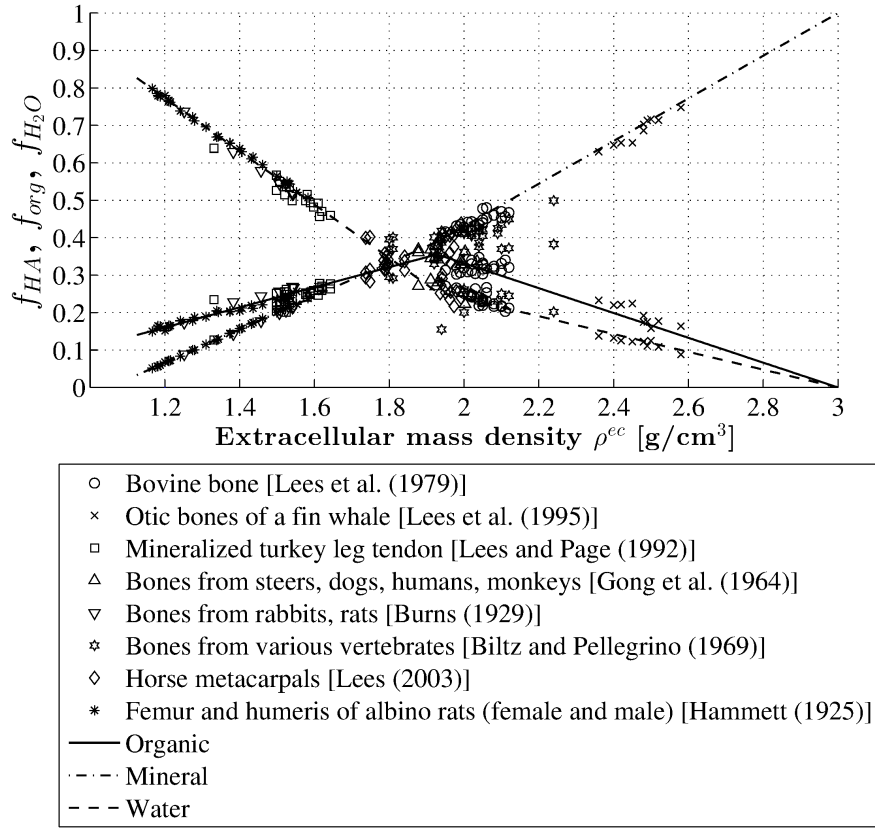
Figure 4.3.: Universal composition rules in bone tissue [285]: bilinear relations between constituent volume fractions and tissue mass density

the same temperature for lipid dissolution. They were then washed with 0.9% saline solution for 10 minutes at 40°C under ultrasonic bath, and finally under flushing water at room temperature, in order to further clean the pores. The extracellular tissue density was measured by means of Archimedes' principle: The weight W_s of each specimen completely submerged in distilled water (air bubbles were removed under vacuum) was recorded by means of an analytical balance (PG403-S, Mettler-Toledo GmbH, Switzerland), as was the weight in air, W_a, the latter being accessible after centrifugation at 400 g for 15 minutes, in order to remove water from the vascular and lacunar pores. The mass density ρ_{ec} of the extracellular bone matrix was then determined according to:

$$\rho^{ec} = \frac{W_a}{W_a - W_s} \tag{4.14}$$
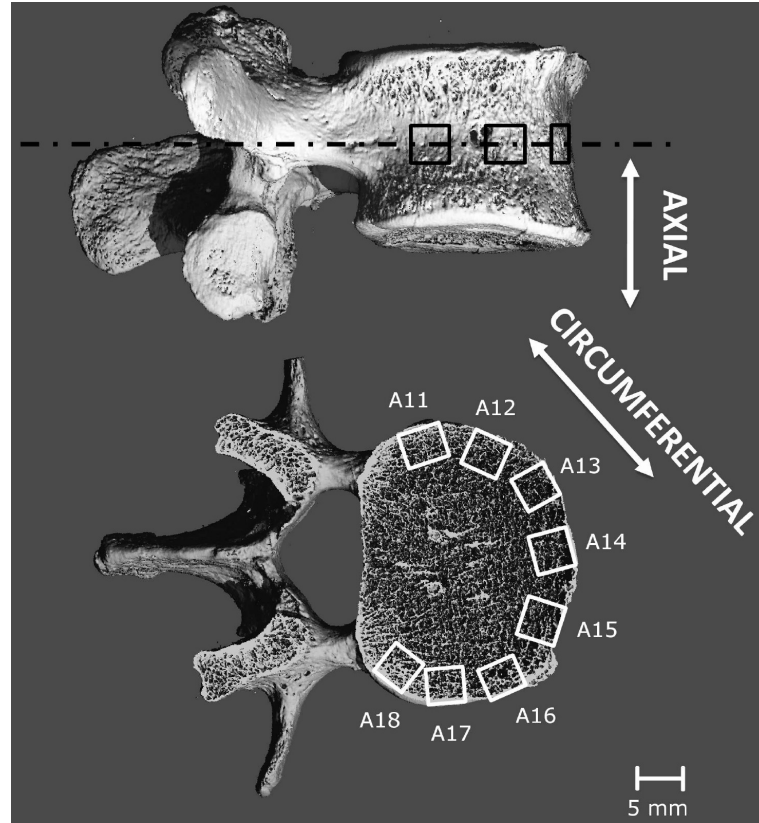
Figure 4.4.: Schematic position and reference orientation chosen for cubic samples cut from one of the mid-height vertebra, shown in a micro-CT image

4.1.2.4 *Voxel-specific tissue composition*

Once the photon energy $\mathcal{E}$ is known, it gives access to the extravascular bone matrix attenuation coefficient via Eqn.(4.12), which can then be upscaled to the macroscopic bone material level: Therefore, we specify the average rule (4.3) for the constituents "extravascular bone matrix" (with volume fraction 1-ϕ_{vas}) and vascular porosity (with volume fraction ϕ_{vas}), yielding

$$\mu_{macro} = \phi_{vas} \times \mu_{H_2O} + (1 - \phi_{vas}) \times \mu_{ev} \tag{4.15}$$

Solving this equation for ϕ_{vas} gives access to voxel-specific values for the vascular porosity,

$$\phi_{vas} = \frac{\mu_{macro} - \mu_{ev}}{\mu_{H_2O} - \mu_{ev}} \tag{4.16}$$

ϕ_{vas} can be also used to provide voxel-specific mass densities at the macroscopic scale

$$\rho_{macro} = \phi_{vas} \times \rho_{H_2O} + (1 - \phi_{vas}) \times \rho_{ev} \tag{4.17}$$

based on mass densities at the extravascular scale

$$\rho_{ev} = \phi_{lac} \times \rho_{H_2O} + (1 - \phi_{lac}) \times \rho_{ec} \tag{4.18}$$

Moreover, we are also interested in the apparent mass densities of mineral and collagen, i.e. the "bone mineral and collagen mass densities", the former one being sometimes referred to as vBMD [214]. Therefore, we convert constituent volume fractions into apparent mass densities of hydroxyapatite, collagen, and water and non collageneous proteins,

$$
\begin{aligned}
\rho_{HA}^{*,ec} &= f_{HA}^{ec} \times \rho_{HA} & (4.19) \\
\rho_{col}^{*,ec} &= 0.9 \times f_{org}^{ec} \times \rho_{col} & (4.20) \\
\rho_{H_2O+ncp}^{*,ec} &= \rho_{ec} - \rho_{HA}^{*,ec} - \rho_{col}^{*,ec} & (4.21)
\end{aligned}
$$

where we consider that 90% of the organic matter in extracellular bone matrix is collagen [276]. The apparent mass densities (19) - (21) are upscaled from the extracellular to the macroscopic level through

$$
\begin{aligned}
\rho_{HA}^{*} &= \rho_{HA}^{ec} \times (1 - \phi_{lac}) \times (1 - \phi_{vas}) \\
\rho_{col}^{*} &= \rho_{col}^{ec} \times (1 - \phi_{lac}) \times (1 - \phi_{vas}) \\
\rho_{H_2O+ncp}^{*} &= \rho_{macro} - \rho_{col}^{*} - \rho_{HA}^{*}
\end{aligned}
\tag{4.22}
$$

4.1.3 *Results*

Evaluation of all grey values found in the investigated clinical CT image in form of the normalized histogram or probability density function depicted in Figure 4.5 allows for identification of the anatomical landmark values related to adipose tissue, as $GV_{fat} = 72$, to soft tissues from inner organs, as $GV_{soft} = 84$, and to bone tissue, as $GV_{bone} = 101$, see Figure 4.5. In addition, the histogram provides the segmentation threshold as $GV_{thr} = 93$. From the landmark grey values for fat and soft tissue, Eq.(4.1) to (4.6) allow for identification of the energy-dependent slope and intercept parameters a and b, see Figure 4.6. As illustrated in Figure 4.7, the maximum grey value occurring in the *corpus vertebrae* amounts to $GV_{max} = 164$, and its densest neighbor exhibits a grey value of $GV_{max-1} = 156$. According to Eqn.(4.8) and (4.9), this allows for identification of the grey value related to extravascular bone as $GV_{ev}=298$. A unique relation between grey values and X-ray attenuation
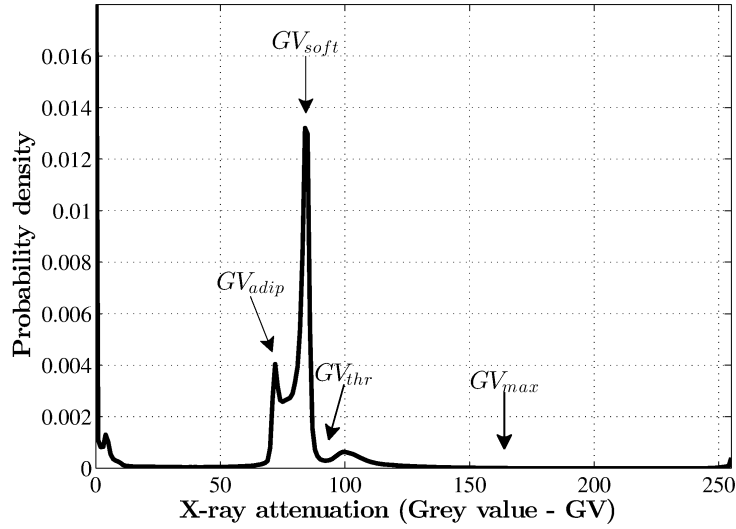
Figure 4.5.: Frequency distribution plot of the attenuation information in terms of grey values of the vertebral body L3
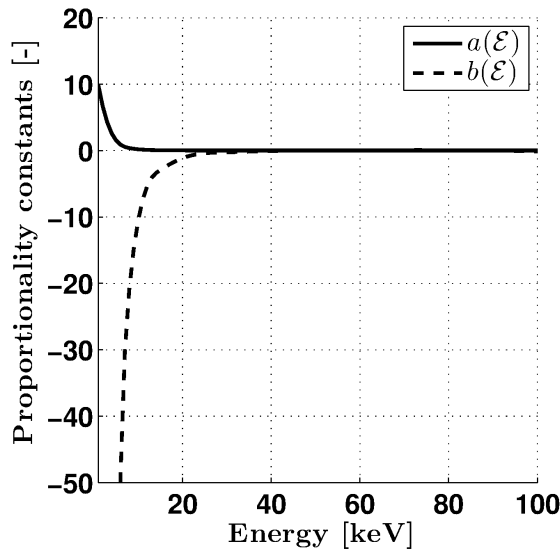
Figure 4.6.: Slope and intercept parameters a and b, as functions of the photon energy $\mathcal{E}$

coefficients can be only obtained for an extracellular mass density of 1.67 g/cm^3, being assigned to an X-ray energy of 24 keV, as is evident from Fig.4.1, drawn on the basis of Eqn.(4.10) to (4.13). This mass density agrees very well with the one measured by Archimedes' principle as determined in Section 4.1.2.3; the latter amounting to 1.71±0.11 g/cm^3 (mean value ± standard deviation). Evaluation of

88
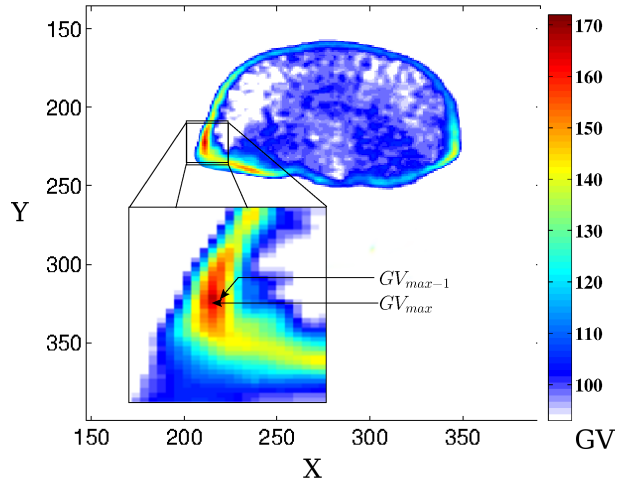
Figure 4.7.: Grey value distribution throughout vertebral cross section where the densest voxel (with GV_{max}) and its neighbor (with GV_{max-1}) occur
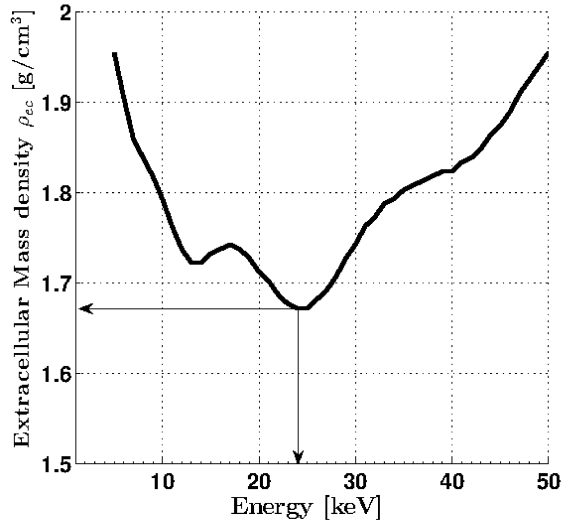
Figure 4.8.: Extracellular mass density as function of photon energy, according to Eqn. (4.1)-(4.17), with $a(\mathcal{E})$ and $b(\mathcal{E})$ as depicted in Figure 4.6

.

the energy-dependent functions of Fig. 4.6 for the photon energy as 24 keV yields the grey value-to-attenuation conversion factors a and b as $a = 0.0107$ cm^{-1} and $b = -0.4154$ cm^{-1}. Evaluation of relations (4.17) and (4.22) for the grey value of each and every voxel of the scanned object yields density and hydroxyapatite/collagen/water content maps throughout the vertebral body, see Figure 4.9 and 4.10,

as well as frequency plots of the aforementioned quantities, see Figure 4.11. The ex-
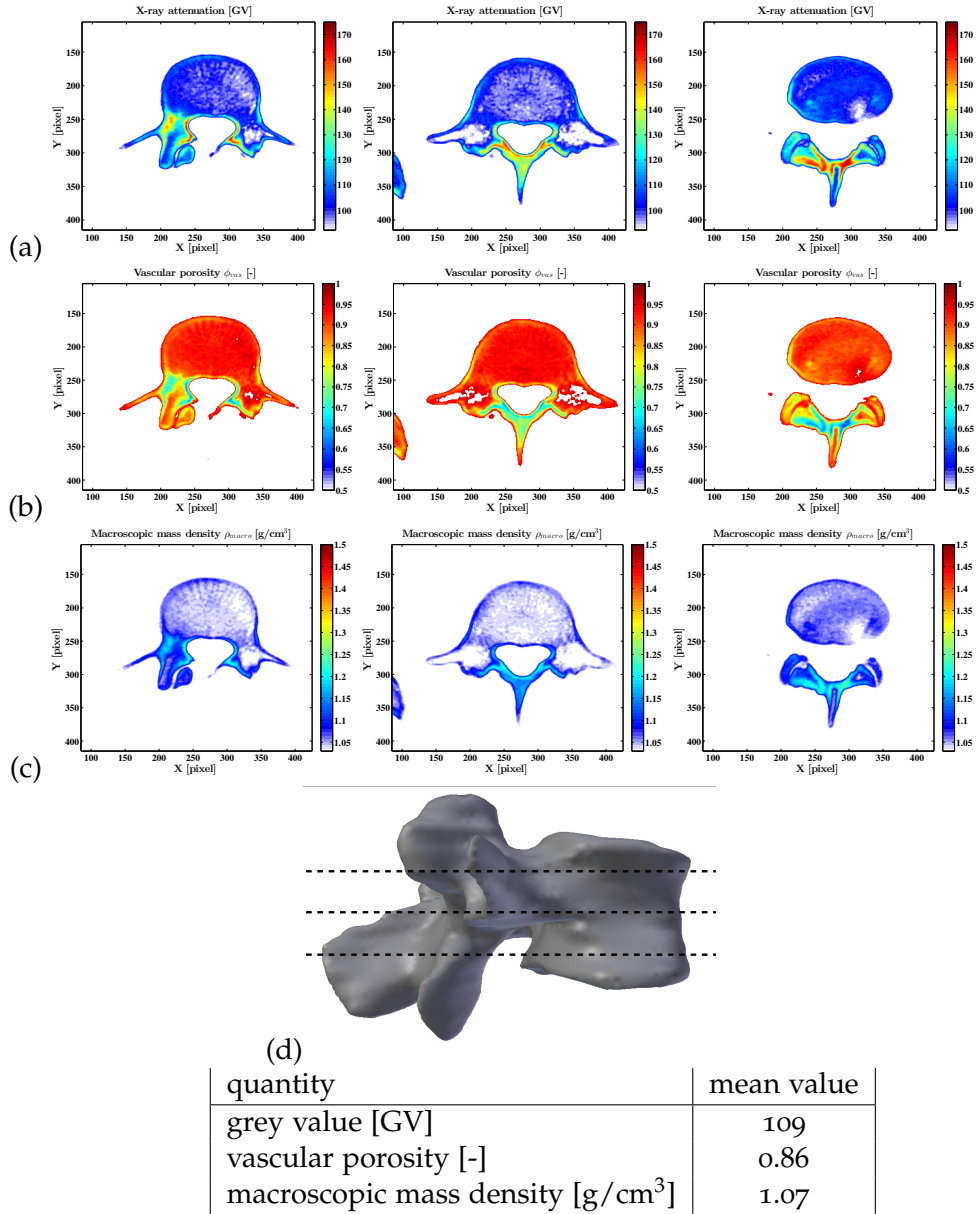
Figure 4.9.: Property maps in CT slices orthogonal to the superior-inferior direction e_z: (a) X-ray attenuation coefficient in terms of grey value, (b) vascular porosity, (c) macroscopic mass density; (d) locations of the mapped cross sections; (e) mean values of the previous quantities

quantity	mean value
grey value [GV]	109
vascular porosity [-]	0.86
macroscopic mass density [g/cm^3]	1.07

pected (i.e. most frequently occurring) values for macroscopic mass density, mineral and collagen content amount to ρ_{macro}^{exp}=1.04 g/cm^3, $\rho_{HA}^{*,exp}$=54.1 mg/cm^3, and $\rho_{col}^{*,exp}$=39.2 mg/cm^3, while their averages over the entire vertebral body amount to $\overline{\rho_{macro}}$=1.07 g/cm^3, $\overline{\rho_{HA}^{*}}$=87.8 mg/cm^3, and $\overline{\rho_{col}^{*}}$=24.2 mg/cm^3.

quantity	mean value [mg/cm^3]
mineral content	87.8
collagen content	39.2
water + ncp content	944
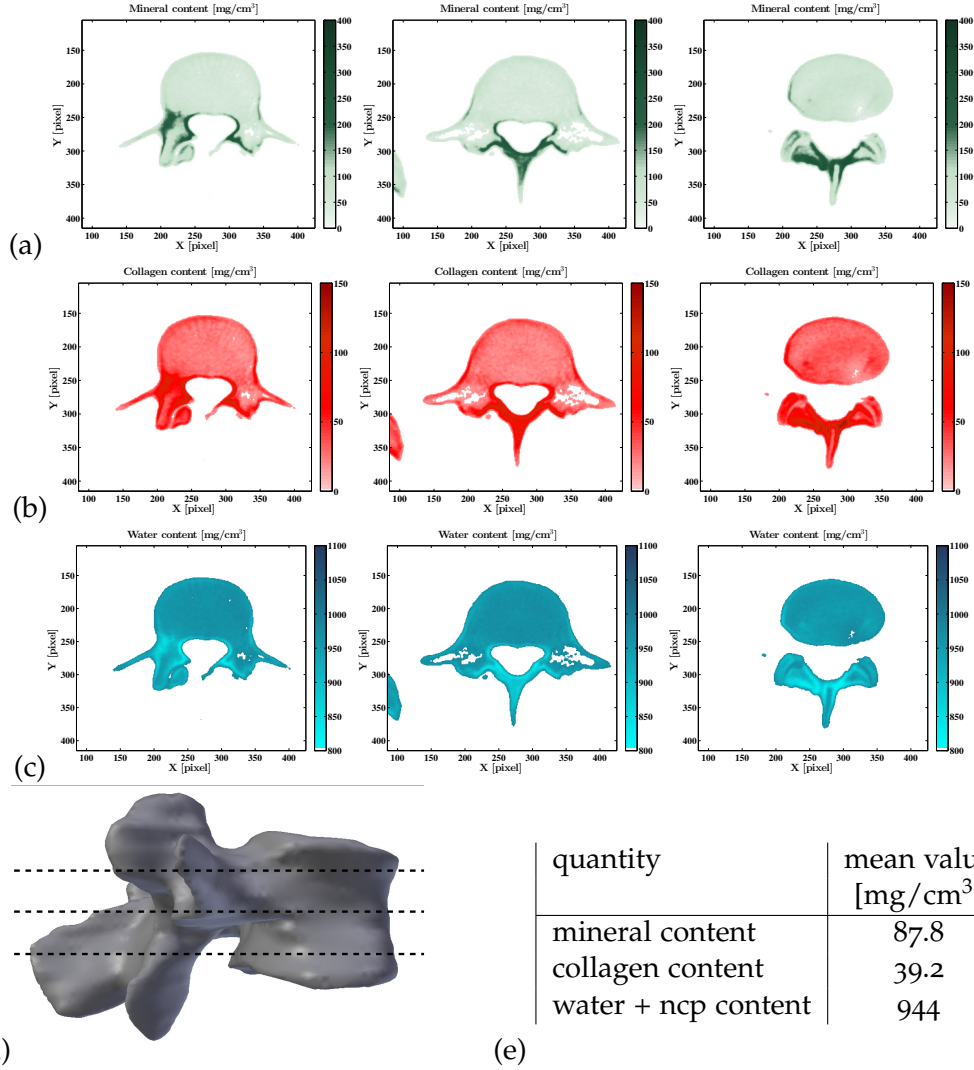
Figure 4.10.: Property maps in CT slice orthogonal to the superior-inferior direction e_z: (a) Mineral content, (b) collagen content, (c) water and non-collageneous proteins content; (d) locations of the mapped cross sections; (e) mean values of the previous quantities
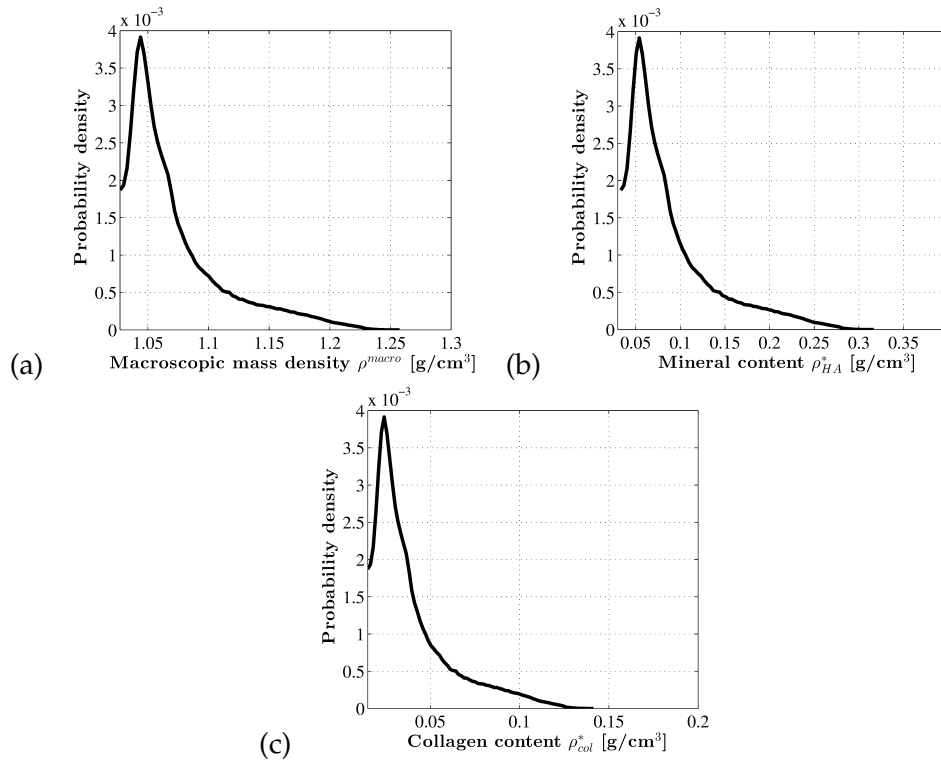
Figure 4.11.: Probability density plots of (a) the macroscopic mass density, (b) the mineral content, and (c) the collagen content.

4.1.4 *Discussion*

Two different techniques, namely Archimedes' principle and evaluation of clinical CT images based on energy-dependent, intravoxel attenuation averaging in conjunction with "universal" compositional rules for soft and hard tissues, delivered the same extracellular bone mass density, when applied to two differently old human vertebrae characterized at different hospitals. This strongly underlines the organ-specificity, but location- and age-independence of extracellular tissue properties (when averaged over one-to-several-millimeter-sized domains). This remarkable extracellular tissue characteristic is also evident from age-independent nanoindentation moduli on human proximal femora [126,241,299], as well as from age- and location-independent mineral contents, as obtained from computerized quantitative contact radiography of whole human iliac bone [23], as observed by means of quantitative backscattered electron imaging of iliac and vertebral trabecular samples [26], as seen under Raman microscopy of femoral cortices [6], or as investigated through a Micro Computer Tomograph of an entire human radius.

Agreement of our tissue mass density result with all these prior investigations nurtures the confidence in our new method, which delivers fully patient- and site-specific data on bone tissue composition, resolved down to the single voxel level. At this stage, it already drives forward the highly desired knowledge on local bone composition characteristics, as it was achieved by HR-pqCT acquisition schemes on radial bones [114, 214, 216], delivering, as a result, bone mineral densities as averages over cortical or trabecular compartments, with values lying well within the ranges illustrated in Figure 4.10. Our method, however, while not being dependent on HR-pqCT (which is only applicable to extremities), but just based on standard clinical CTs, gives not only compartment averages, but bone composition gradients resolved down to a voxel size of $0.324 \times 0.324 \times 1.25$ mm^3. The identifed mass density of 1.67 g/cm^3 underlines that vertebral tissues is remarkably less dense than femoral or tibial tissue, with reported extracellullar mass densities lying between 1.9 and 2.0 g/cm^3 [18, 172, 285]. This is consistent with ultrasonic waves traveling slower through vertebral as compared to femoral tissues [190].

Moreover, our mineral contents derived from *in vivo* CT data without the need of any type of phantom, agree remarkably well with *ex vivo* QCT studies on vertebral autopsies [78]: for an age slightly below 20 years, the latter reference reports bone mineral contents relating to a similarly aged patient between 70 and 200 mg/cm^3, in which interval is lying the mean value in Figure 4.10(e). Hence, we provided a new *in vivo* access to values for the so-called "volumetric Bone Mineral Density - vBMD". The latter are very valuable indicators for clinical decisions, as they have been shown to significantly correlate to the occurrence of bone fracture [163], i.e. they are valuable indicators for bone fracture risk. However, such correlations [204, 286, 305] do not consider the wealth of knowledge on how materials break, as it has been gained in the fields of material physics and mechanics over centuries. How to trigger this knowledge as well, in order to come up with bone fracture risk analysis tools exceeding the reliability and precision of the purely statistical ones by orders of magnitude, is what the companion paper, Part II, is all about.

Lacroix until 2012, and by Jerome Noailly since 2012), at Vienna University of Technology, which was made possible through the bilateral Austro-Spanish scientific exchange grant ES06/2010 AT2009-0029. CT scanning of the aforementioned vertebra was provided by Heinz Redl from the Ludwig Boltzmann Institute for Clinical and Experimental Traumatology, in the framework of the Austrian Cluster for Tissue Regeneration.

NOMENCLATURE

Variables

a slope of linear relation between grey values and X-ray attenuation coefficients

b intercept of linear relation between grey values and X-ray attenuation coefficients

$\mathcal{E}$ photon energy

e_z unit base vector in the vertical direction

f_i^j volume fraction of phase i (if specified, in the RVE j; otherwise, in the macroscopic RVE)

GV X-ray attenuation-related grey value

l characteristic length

μ_i X-ray intensity attenuation coefficient of constituent i

N_C number of constituents in the volume

R Ratio

ρ_i^j "real" mass density of material constituent i, expressed in the phase j

$\bar{\rho}$ average mass density

ϕ_i porosity of constituent i

W weight

Subscripts

a ... dried in air

$bone$ ... of bone

col ... of collagen

$cort$ ... of cortical shell

ec ... of extracellular bone matrix

ev ... at extravascular scale

fat ... of adipose tissues

HA ... of hydroxyapatite

H_2O ... of water

H_2O ... of water and non collageneous proteins

lac ... of lacunae

$macro$ ... of macroscopic bone

max ... maximum value

$max - 1$ ... penultimate maximum value
org ... of organic matter
s ... submerged in water
$soft$ ... of soft tissues
thr ... at threshold value
vas ... of vascular porosity
$voxel$ ... of one voxel of the CT image

Superscripts
ec ... in the extracellular bone RVE
exp ... expected
up ... upscaled
$*$ ... apparent

4.2 PART II: MICRO-ELASTOPLASTICITY FOR COMPOSITION TO SAFETY FACTOR CONVERSION

4.2.1 *Introduction*

The broad scattering of ultimate forces bearable by human vertebrae [42, 62, 198, 225] has motivated the quest for indicators of the actual, i.e. patient-specific, strength exhibited by a particular vertebral body of interest; and the most accepted indicator in this context remains the "bone mineral density - BMD" [19, 203]. However, it is much less clear how and to which extent BMD (alone) would govern bone fracture risk, and there is an ongoing discussion on additional or alternative risk indicators [77, 133, 134, 138, 246, 266], based on quite comprehensive statistical analyses. At the same time, it is clearly felt that an engineering mechanics-based assessment of fracture risk, as it is the basis for structural design in civil and mechanical engineering, should hold the capacity to overcome the shortcomings of the purely statistics-based, population-related approaches referred to above. In a particularly notable engineering mechanics-based approach [85, 258], elastic properties derived from CT- and mass density-based calibration schemes [107, 153, 206], are mapped onto Finite Element meshes, and for a variety of load cases, strains as obtained from an elastic simulation are assessed with respect to a failure criterion based on a constant maximum principal strain. This approach was specifically developed for human femora, where a certain consensus has been gained in the community as regards CT-to-mechanics calibration schemes [273, 274, 303], and the existence of an invariant ultimate principal strain bearable by human femoral bone [64].

Such a consensus (or even enough data for potentially reaching it) is hard to find for other types of bone; and this provides a very pragmatic motivation for the present contribution. Namely, we here aim at opening the way towards a more generally applicable, engineering science-based, patient-specific bone fracture risk analysis tool. This is done (i) by employing fundamental mechanics and physics principles for explicit quantification of the hierarchical microstructure of bone, and its effect on the unique mechanical properties of this biological material - and (ii) by extending a safety assessment philosophy which is used very successfully in everyday steel or concrete engineering, towards the needs of a very intricate life science problem: the breaking of bones.

As regards the use of fundamental principles, X-ray physics-derived (voxel-specific) mineral, collagen, and water contents determined in companion paper Part I [21] for a human vertebra will be fed into a homogenization theory-based multiscale mechanics representation of bone [96, 210], which has been extensively validated experimentally for both elastic and strength properties. This will provide calibration- and phantom-free conversion of CT data into mechanical properties.

As regards the safety assessment concept, voxel-specific elastic properties gained by means of the aforementioned conversion method will enter linear elastic Finite Element simulations, so as to deliver organ-wide stress distributions related to a typical load case. These local, i.e. element-specific, stress states are subsequently increased in a proportional fashion, so as to check which elastoplastic events would develop in the hydrated mineral crystals, before brittle fracture of molecular collagen would mark ultimate material failure. The corresponding proportionality factors quantify the element-specific safety against fracture, which is a lower bound to the overall organ fracture risk.

4.2.2 *Methods*

4.2.2.1 *Intravoxel tissue elasticity*

The ultrastructural mass density and the spatial distribution of vascular porosities determined from a CT scan of a patient by means of a series of X-ray physics considerations, as described in Part I [21] (see in particular Fig. 4.9), are now converted into voxel-specific elastic properties, on the basis of the multiscale homogenization scheme depicted in Figure 4.12. This scheme, described in great detail in [90, 117, 118, 210], quantifies how the elementary mechanical constituents of bone, namely hydroxyapatite, collagen, and water with some non-collageneous organics, as well as their dosages within the extracellular bone matrix, determine the elastic properties of bone at different length scales. It has been extensively validated experimentally, through an ultrasound data base stemming from a wealth of bone sources - equine cortical bone [199], bovine tibia [175], drug-treated rab-
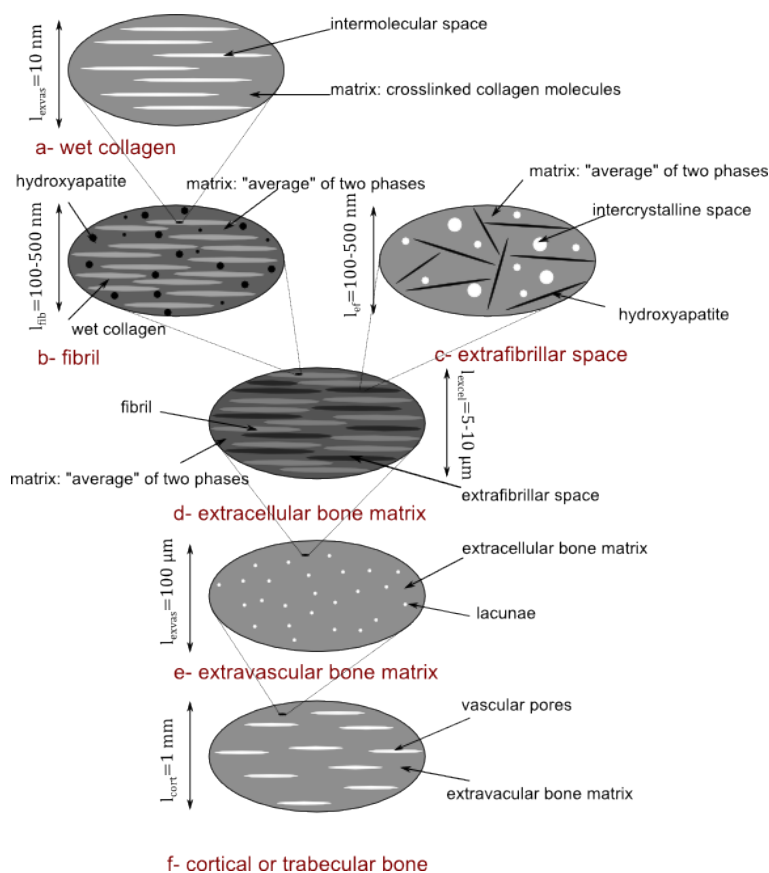
Figure 4.12.: Multiscale micromechanical representation of bone material, according to Morin and Hellmich [210]

bit bone [177], whale malleus, incus, stapes, periotic and t. bulla [176], fin whale t. bulla [168], dugong rib, elephant radius, human femur, deer antler [172] - in combination with "universal" composition and mineralization rules for bone tissues [119, 208, 209, 285]. The latter were derived from a wealth of biophysical, biochemical, and biomechanical experimental sources [15, 18, 24, 32, 106, 112, 125, 148, 167, 169, 171, 174, 179, 200, 231, 248, 310]. In this context, bone is represented by a series of representative volume elements, the size of which is significantly larger than that of the inhomogeneities found within such a volume (see e.g. Figure 4.12(f) with the vascular pores' diameters being scale-separated from the millimeter-size of the cortical or trabecular RVE). Also, representation of the microstructure within the RVE is reduced to the bare minimum needed for elasticity homogenization: the domain within the RVE is subdivided into the minimum number of material phases with distinctively differing physical properties: their volume fractions [such as the vascular porosity in Figure 4.12(f)], their (average) elastic properties [such as those of the vascular pores and of the extravascular

bone matrix in Figure 4.12(f)], the most fundamental shape characteristics (cylinders representing vascular pores in the case of cortical/trabecular bone), and their interaction [pore inclusions embedded into a solid matrix in Figure 4.12(f)]. This representation implies the following Mori-Tanaka-scheme-type expression for the stiffness of cortical/trabecular bone [120],

$$
\begin{aligned}
\mathbb{C}_{macro} = & \left\{ \phi_{vas} \mathbb{C}_{H_2O} [\mathbb{I} + \mathbb{P}_{cyl} : (\mathbb{C}_{H_2O} - \mathbb{C}_{exvas})]^{-1} + (1 - \phi_{vas}) \mathbb{C}_{exvas} \right\} : \\
& : \left\{ \phi_{vas} [\mathbb{I} + \mathbb{P}_{cyl} : (\mathbb{C}_{H_2O} - \mathbb{C}_{exvas})]^{-1} + (1 - \phi_{vas}) \mathbb{I} \right\}^{-1}
\end{aligned}
\tag{4.23}
$$

with ϕ_{vas} the vascular porosity, $\mathbb{C}^{exvas}$ and $\mathbb{C}_{H_2O}$ the elastic stiffness of the extravascular bone matrix and water, $\mathbb{I}$ the fourth-order identity tensor with components $I_{ijkl} = \frac{1}{2}(\delta_{ik}\delta_{jl} + \delta_{il}\delta_{jk})$, with the Kronecker delta δ_{ij} being 1 for $i = j$ and zero otherwise; and $\mathbb{P}_{cyl}$ the fourth-order Hill tensor accounting for the cylindrical shape of the inclusions embedded into a transversely isotropic matrix [118]. Within the investigated vertebral body, the vascular porosity is varying from voxel to voxel, as depicted in Figure 4.9 of the paper Part I [21]; all other quantities in Eqn.(4.23) are constant. Particularly, the extravascular stiffness follows from feeding the homogenization scheme of Figure 4.12 with an ultrastructural mass density identified in companion paper Part I [21], amounting to 1.67 g/cm^3 (and corresponding ultrastructural volume fractions of mineral, collagen, and water as given in Figure 4.9 of paper Part I [21]), and with a lacunar porosity of 10 % [210, 270], yielding

$$
\mathbb{C}_{exvas} = \begin{pmatrix}
C_{1111} & C_{1122} & C_{1133} & 0 & 0 & 0 \\
C_{1122} & C_{2222} & C_{2233} & 0 & 0 & 0 \\
C_{1133} & C_{2233} & C_{3333} & 0 & 0 & 0 \\
0 & 0 & 0 & 2C_{2323} & 0 & 0 \\
0 & 0 & 0 & 0 & 2C_{1313} & 0 \\
0 & 0 & 0 & 0 & 0 & 2C_{1212}
\end{pmatrix} =
$$
$$
= \begin{pmatrix}
10.56 & 4.82 & 5.30 & 0 & 0 & 0 \\
4.82 & 10.56 & 5.30 & 0 & 0 & 0 \\
5.30 & 5.30 & 13.06 & 0 & 0 & 0 \\
0 & 0 & 0 & 5.99 & 0 & 0 \\
0 & 0 & 0 & 0 & 5.99 & 0 \\
0 & 0 & 0 & 0 & 0 & 5.75
\end{pmatrix} \text{ in GPa}
\tag{4.24}
$$

The stiffness tensor of water reads as $\mathbb{C}_{H_2O} = 3\mathbb{I}_{vol}k_{H_2O}$, with the bulk modulus of water amounting to k_{H_2O}=2.3 GPa [109], and with $\mathbb{I}_{vol}$ as the volumetric part of the fourth-order identity tensor, with components $I_{vol,ijkl} = \frac{1}{3}\delta_{ij}\delta_{kl}$.

4.2.2.2 *Linear Finite Element simulations*

The used Finite Element model is based on earlier work published in [255], see Figure 4.13: It consists of 125253 solid elements accounting for the trabecular bone tissue, and 17185 shell elements accounting for the cortical bone tissue. For the present study, we realized a cortical shell thickness of l_{cort}=0.23 mm [245, 263, 295]; while the caudal and cranial (bony) endplates were assigned thicknesses of $l_{end} =$ 1 mm [291, 302]. In order to investigate the effect of heterogeneity at the finite ele-
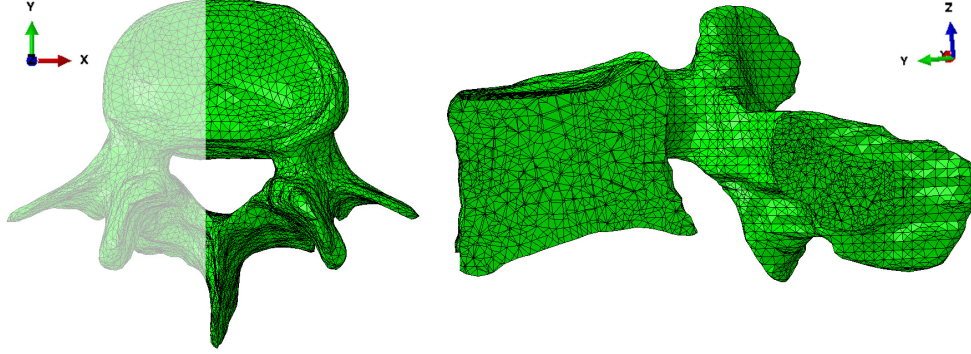
Figure 4.13.: Finite Element mesh of the patient-specific vertebral body

ment level (i.e. with gradients measured along a few millimeters), we considered two ways of assigning material properties to the Finite Element model of Figure 4.13:

- For the so-called "homogeneous model", the entire trabecular bone compartment is assigned the same elastic stiffness tensor, namely that related to the average vascular porosity found in that compartment, ϕ_{vas}^{trab}=0.86. More precisely, given the "short-beam"-type nature of our structure, we assign the longitudinal Young's modulus

$$E_{macro,3} = \frac{1}{C_{macro,3333}^{-1}} = 1322 \text{ MPa} \qquad (4.25)$$

with $C_{macro,3333}^{-1}$ as the component of the compliance tensor $\mathbb{C}_{macro}^{-1}$ and the longitudinal Poisson's ratio

$$\nu_{31} = -C_{macro,1133}^{-1} \times E_{macro,3} = 0.19 \qquad (4.26)$$

as "formally isotropic" material properties to the FE model, as is normally considered as an appropriate approximation in bone organ mechanics [20, 59, 280]. As regards the very thin cortical shell around the organ, whose thickness of 230 microns does not quite allow for accommodation of Haversian

systems (and hence of the vascular porosity), we adopt the "macroscopic" stiffness tensor $\mathbb{C}_{macro}$ related to zero-porosity, i.e. that of the extravascular bone matrix according to Eqn.(4.24). More precisely, as before, we assign as formally isotropic properties, a Young's modulus and a Poisson's ratio of 9406 MPa and of 0.28, respectively, to the shell finite elements.

- For the "heterogeneous model", the cortical shell treatment does not differ, while the element-specific stiffness tensors are computed from the vascular porosity values assigned to the centroids of the finite elements. The interpolation between the CT data and the Finite Elements is made by finding the three CT pixels closest to the finite element centroid, and by assigning the porosity values to the element as if its centroid would be the barycentre of these three points.

Since the focus of the present study is on the effect of material properties rather than on different loading conditions, we consider a very basic load case, related to a "static deadload": 1 MPa pressure applied to the cranial endplate, while pinning the caudal endplate in all space directions. The pressure magnitude is indeed related to "quasi-physiological conditions": the half body weight of a person of 75 kg mass in the gravitational field of the earth would results in a pressure of 0.75 MPa, when evenly distributed across the surface area A_{end}=869 mm^2 of the cranial endplate.

In order to test the robustness of our model, we compare the computation results of four models with increasing element sizes, i.e. decreasing amount of elements, namely 229138, 143159, 105763, and 82848 elements. More precisely, we compute, for all element sizes, the strain energy density in one element n as:

$$\psi_n = \frac{1}{2}\varepsilon_n : \mathbb{C}_{macro,n} : \varepsilon_n \tag{4.27}$$

so that the average strain energy over the entire organ reads as:

$$\overline{\psi}_{organ} = \frac{1}{V_{organ}} \sum_{n=1}^{N} \psi_n \times V_n \tag{4.28}$$

4.2.2.3 *Local safety assessment based on multiscale elastoplasticity*

The results of the linear elastic Finite Element simulations are then used for safety assessment of the investigated structure. More precisely, we check by which proportionality factor the determined element-specific macroscopic stresses needed to be increased, so as to reach ultimate macroscopic bone material failure. This stress increase, however, is subjected to macroscopic bone RVEs in an incremental fashion, allowing for elastoplastic deformation states prior to the ultimate material

failure (which obviously depends on these elastoplastic deformations). In order to quantify them, we extend the hierarchical scheme depicted in Figure 4.12 to the realm of elastoplasticity, extending earlier work published in [96]. There, the liquid crystal-type water interfaces between the mineral crystals and/or crystal clusters in the extrafibrillar space [see Figure 4.12(c)], have been identified as the major nanoscopic origin of bone elastoplasticity, both from the high interaction energies between water and hydroxyapatite as evidenced by several molecular dynamics and nuclear magnetic resonance studies [16, 17, 221, 296, 307], and more importantly, by successfully predicting, based on experimentally obtained upscaling mineral and collagen strengths [37, 46, 103], the macroscopic strengths of different types of bone [33–35, 39, 67–70, 76, 84, 121, 160, 166, 193, 233, 234, 244, 289].

Thereby, the elastoplasticity of the hydrated hydroxyapatite mineral phases, which are oriented uniformly in space directions given through Eulerian angles ϕ and θ related to spherical coordinates, are governed by the following constitutive equations: The needle-shaped mineral phase oriented in space direction (ϕ, θ) follows an elasto-plastic stress-strain relation,

$$\sigma_{HA,\phi\theta} = \mathbb{C}_{HA} : (\varepsilon_{HA,\phi\theta} - \varepsilon^p_{HA,\phi\theta}) \tag{4.29}$$

with $\mathbb{C}_{HA} = 3k_{HA}\mathbb{I}_{vol} + 2\mu_{HA}\mathbb{I}_{dev}$ as the isotropic elasticity of hydroxyapatite, k_{HA}=82.6 GPa and μ_{HA}=44.9 GPa [149], $\mathbb{I}_{dev} = \mathbb{I} - \mathbb{I}_{vol}$, $\varepsilon_{HA,\phi\theta}$ and $\varepsilon^p_{HA,\phi\theta}$ as the (average) total and plastic strains in the $(\phi\theta)$-oriented needle-shaped phase, and $\sigma_{HA,\phi\theta}$ as the corresponding average stress. Plastic events are quantified by means of a Mohr-Coulomb criterion,

$$\mathcal{F}_{HA,\phi\theta} = \mathcal{F}(\sigma_{HA,\phi\theta}) = \beta\sigma^I_{HA,\phi\theta} - \sigma^{III}_{HA,\phi\theta} - \sigma^y_{HA} \leqslant 0 \tag{4.30}$$

with β as the ratio between the compressive and the tensile yield stresses ($\beta = 12$), σ^y_{HA} as the compressive yield stress (σ^y_{HA}=570 MPa), and $\sigma^I_{HA,\phi\theta} \geqslant \sigma^{II}_{HA,\phi\theta} \geqslant \sigma^{III}_{HA,\phi\theta}$ as the (sorted) principal stresses in the $(\phi\theta)$-oriented mineral phase. The strength parameters follow from tests on porous hydroxyapatite polycrystals [5, 9, 40, 73, 92, 186, 191, 223, 262], mimicking those occurring in the extrafibrillar space of Figure 4.12(c). Potential occurence of plastic events follows the Kuhn-Tucker conditions [264] (actually proposed already in 1938 by Melan [202])

$$\dot{\lambda}_{HA,\phi\theta} \geqslant 0, \quad \mathcal{F}_{HA,\phi\theta} \leqslant 0 \quad \text{and} \quad \dot{\lambda}_{HA,\phi\theta} \times \mathcal{F}_{HA,\phi\theta} = 0 \tag{4.31}$$

in conjunction with the following, non-associative, isochoric flow rule:

$$\dot{\varepsilon}^p_{HA,\phi\theta} = \dot{\lambda}_{HA}\frac{\partial \mathcal{G}}{\partial \sigma_{HA,\phi\theta}} \quad \text{with} \quad \mathcal{G}(\sigma_{HA,\phi\theta}) = \sigma^I_{HA,\phi\theta} - \sigma^{III}_{HA,\phi\theta} \tag{4.32}$$

whereby the dot denotes the time derivative, $\mathcal{G}$ denotes the flow potential, the derivative of which accounts for the plastic flow direction, and $\dot{\lambda}_{HA,\phi\theta}$ denotes the plastic multiplier quantifying the amount of plastic strain.

Such plastic events imply more and more micro-stresses to be transferred to the molecular collagen of Figure 4.12(a), which finally fails in a brittle manner, according to a Rankine-type criterion,

$$\mathcal{F}_{col} = \max_{i \in \{I,II,III\}} |\sigma_{col}^i| - \sigma_{col}^{ult} \leqslant 0 \qquad (4.33)$$

with σ_{col}^i, $i = I...III$, as the eigenstresses in the molecular collagen assembly at the wet collagen (microfibrillar) scale, and σ_{col}^{ult} as the strength of molecular collagen. The latter quantity is derived from experiments on rat tail tendon, which, under wet conditions, exhibits a strength of 106.1 MPa [103]. We consider the close packing of collagen, so as to get access to properties of molecular collagen. It is known from neutron diffraction studies [170, 179] that diffractional spacing (a measure for the lateral distance of collagen molecules) reduces from 1.52 nm (for wet collagen) to 1.09 nm (for maximally packed (dry) collagen). Accordingly, the cross sectional area of a tensile specimen would reduce by the ratio $(1.52/1.09)^2$, so that the strength of molecular collagen follows to be $(1.52/1.09)^2$ times higher than that of wet collagen, i.e. 206 MPa.

These elastoplastic and failure laws need to be homogenized over the RVEs depicted in Figure 4.12, so as to determine the elastoplastic behavior of a piece of cortical/tabecular bone illustrated in Figure 4.12(f). This is achieved in the framework of continuum micromechanics [308] by means of stress and strain averaging rules [115, 123] and concentration-influence relations [182]; applied to each of the RVEs depicted in Figure 4.12. As regards the extrafibrillar RVE, homogeneous strains $\mathbf{E}_{ef}$ are prescribed in terms of displacements

$$\boldsymbol{\xi}(\mathbf{x}) = \mathbf{E}_{ef} \cdot \mathbf{x} \qquad (4.34)$$

at the boundary of the RVE - $\mathbf{x}$ is the "microscopic" location vector with a resolution much smaller than the RVE. This boundary condition implies that kinematically compatible microstrains $\boldsymbol{\varepsilon}(\mathbf{x})$

$$\boldsymbol{\varepsilon}(\mathbf{x}) = \nabla^s \boldsymbol{\xi}(\mathbf{x}) \qquad (4.35)$$

fulfill the following strain average rule [91, 308]

$$\mathbf{E}_{ef} = f_{HA}^{ef} \int_{\phi=0}^{2\pi} \int_{\theta=0}^{\pi} \boldsymbol{\varepsilon}_{HA,\phi\theta} \frac{\sin\theta}{4\pi} d\phi d\theta + (1 - f_{HA}^{ef}) \boldsymbol{\varepsilon}_{ic} \qquad (4.36)$$

with f_{HA}^{ef} as the volume fraction of hydroxyapatite within the extrafibrillar RVE, and ε_{ic} as the (average) strains in the inter crystalline space. Moreover, when applying the principle of virtual powers to this RVE, resulting in the so-called Hill's lemma [308], one arrives at an additional stress average rule for macroscopic stresses acting on the extrafibrillar RVE,

$$\boldsymbol{\Sigma}_{ef} = f_{HA}^{ef} \int_{\phi} \int_{\theta} \sigma_{HA,\phi\theta} \frac{\sin\theta}{4\pi} d\phi d\theta + (1 - f_{HA}^{ef})\sigma_{ic} \qquad (4.37)$$

with the microstresses $\sigma(\mathbf{x})$ fulfilling the equilibrium condition

$$\text{div } \sigma(\mathbf{x}) = 0 \qquad (4.38)$$

Linearity of Eqn. (4.38), (4.35),(4.34), and (4.29) implies the strains in the ($\phi\theta$)-oriented mineral phase to depend multi-linearly on the homogeneous strains $\mathbf{E}_{ef}$ and on the plastic (micro-)strains $\varepsilon_{HA,\phi\theta}^{p}$ found in all other mineral phases,

$$\varepsilon_{HA,\phi\theta} = \mathbb{A}_{HA,\phi\theta} : \varepsilon_{ef} + \int_{\Phi} \int_{\Theta} \mathbb{D}_{\phi\theta\Phi\Theta} : \varepsilon_{HA,\Phi\Theta}^{p} \frac{\sin\Theta}{4\pi} d\Phi d\Theta \qquad (4.39)$$

similarly, the total microstrains ε_{ic} found in in the intercrystalline pores read as

$$\varepsilon_{ic} = \mathbb{A}_{ic} : \varepsilon_{ef} + \int_{\Phi} \int_{\Theta} \mathbb{D}_{ic,\Phi\Theta} : \varepsilon_{HA,\Phi\Theta}^{p} \frac{\sin\Theta}{4\pi} d\Phi d\Theta \qquad (4.40)$$

with $\mathbb{A}_{HA,\phi\theta}$ as the concentration tensor of the hydroxyapatite phase oriented in direction ($\phi\theta$), and $\mathbb{D}_{\phi\theta\Phi\Theta}$ accounting for the influence of plastic strains occurring in the ($\Phi\Theta$)-oriented phase, on the total strains occurring in the mineral phase oriented in ($\phi\theta$)-direction. These concentration and influence tensors are derived from extended "eigenstressed" Eshelby problems [83, 308]; as given in more detail in [94,226]. Finally, repeated use of Hill's lemma yields the upscaled "macroscopic" elastoplastic constitutive equation as

$$\boldsymbol{\Sigma}_{ef} = \mathbb{C}_{ef} : (\mathbf{E}_{ef} - \mathbf{E}_{ef}^{p}) \qquad (4.41)$$

where $\mathbb{C}_{ef}$ is the homogenized stiffness tensor of the extrafibrillar space, reading as

$$\mathbb{C}_{ef} = f_{HA}^{ef} \mathbb{C}_{HA} : \int_{\theta} \int_{\phi} \mathbb{A}_{HA,\phi\theta} \frac{\sin\theta}{4\pi} d\phi d\theta + (1 - f_{HA}^{ef})\mathbb{C}_{H_2O} : \mathbb{A}_{ic} \qquad (4.42)$$

and the extrafibrillar plastic strains $\mathbf{E}_{ef}^{p}$ fulfill

$$\mathbf{E}_{ef}^{p} = \mathbb{C}_{ef}^{-1} : f_{HA}^{ef} \int_{\phi} \int_{\theta} {}^{t}\mathbb{A}_{HA,\phi\theta} : \mathbb{C}_{HA} : \varepsilon_{HA,\phi\theta}^{p} \frac{\sin\theta}{4\pi} d\phi d\theta \qquad (4.43)$$

whereby the superscript t denotes the transpose of the concentration tensor ($^t\mathbb{A}_{ijkl} = \mathbb{A}_{klij}$). Equations (4.29–4.43) allow one to determine the plastic events in the hydrated crystal phases caused by extrafibrillar loading - once Eqn. (4.36, 4.37, 4.39, 4.42, 4.43) are discretized in space, here by means of the numerical scheme proposed in [13], and Eqn. (4.31) and (4.32) are discretized in (chronological) time, here by means of the return mapping algorithm [264, 265]. In particular, the multisurface plasticity concept is realized for Mohr-Coulomb plasticity [47]. This is done for all RVEs depicted in Figure 4.12, so as to relate macroscopic loading at the level of cortical/trabecular bone, to plastic strains in the crystalline, extrafibrillar, extracellular, and extravascular phases in Figure 4.12, until the molecular collagen stresses fulfill failure criterion (4.33).

Within this theoretical framework, two types of "safety factors", "loading degrees", or "distances to failure" are determined:

- The macroscopic, trabecular bone-related stresses $\boldsymbol{\Sigma}_{macro}$ determined in each finite element are first multiplied with a factor χ_y related to just reaching the yield limit defined by equality in Eqn. (4.30);

$$\boldsymbol{\Sigma}_{macro,y} = \chi_y \boldsymbol{\Sigma}_{macro} \tag{4.44}$$

This factor is called the yield safety factor; it is larger than one for elastic deformation states, and reduces to one once yielding starts. Its inverse is the "yield loading degree" or "distance to yielding", being smaller than one for elastic deformation states, and increasing towards one when approaching yielding states.

- Secondly, the aforementioned element-specific macroscopic stresses are multiplied with a factor χ_{ult} related reaching the ultimate load defined by equality in Eqn. (4.33);

$$\boldsymbol{\Sigma}_{macro,ult} = \chi_{ult} \boldsymbol{\Sigma}_{macro} \tag{4.45}$$

This factor is called the (local, material-based) ultimate safety factor; it is larger than one for deformation states the macroscopic bone material can still withstand, and reduces to one once the material fails (through collagen tearing). Its inverse is the "ultimate loading degree" or "distance to failure", being smaller than one for bearable deformation states, and increasing towards one when approaching material failure.

4.2.3 *Results*

The micromechanics-based porosity-stiffness relations based on the hierarchical representation depicted in Figure 4.12, see also Eq. (4.23) and (4.24), in combi-

nation with the X-ray physics-based grey value-to-porosity conversion scheme described in companion paper Part I [21], yields organ-specific grey value-to-stiffness relations as depicted in Figure 4.14.

Combination of the latter with the porosity maps illustrated in Figure 4.9 of the companion paper Part I [21], allows for assembly of mechanical property maps as depicted in Figure 4.16. The latter evidences the very inhomogeneous nature of the organ: The left side of the vertebra organ is less porous, and hence, denser and stiffer than its right-hand side. Feeding these properties into the differently fine Finite Element models described in Section 4.2.2.2 and Figure 4.13, yields very similar results in terms of the strain energy density (see Figure 4.17), which underlines the sufficient accuracy of the employed Finite Element meshes. However, there are truly significant differences between the homogeneous and heterogeneous simulations. Given the employed traction boundary conditions, this indicates that the homogeneous simulations by far overestimate the stiffness of the investigated organ. Stress levels obtained, under axial "dead load", in both homogeneous and heterogeneous simulations reach the level of material yielding (see Figure 4.18), more pronouncedly so in the heterogeneous simulations [compare Figure 4.18(a-c) to Figure 4.18(d-e)]; while this load level is characterized by a "safety factor" of about 10 (for homogeneous simulations) and 5 (for heterogeneous simulations) from material failure [compare Figure 4.19(a-c) to 4.19(a-d)]. Corresponding element-wise increase of the linear elastically determined stress tensors up to the level of material failure is evoking remarkably non-linear strain evolutions, as is seen in Figure 4.15.

4.2.4 *Discussion*

To the best knowledge of the authors, we here provided the first calibration-free, X-ray physics- and multiscale mechanics-based fracture risk analysis tool applied to human vertebrae. The results obtained for a human lumbar vertebra aged 15 years indicate plastic deformations to even occur under normal physiological loading, while the safety factor against ultimate fracture is around five. The corresponding ultimate load amounts to 4614 N, which lies well within the broad range of values determined experimentally on different human vertebrae [42, 62, 198, 225]. Our ultimate load particularly well agrees with the values of ultimate load measured on vertebrae of similar mean BMD [42, 62, 77], and for a bone of similar mean porosity [138, 225]. It is very interesting that our failure also agrees very well with those determined for femurs, both experimentally [258] and by means of FE strength computations [85]. This indicates larger domains of the skeleton to be designed for bearing the same level of loading. Thereby, the critical load may well be attained in extreme sport activities, as compressive forces of 8676 N in the
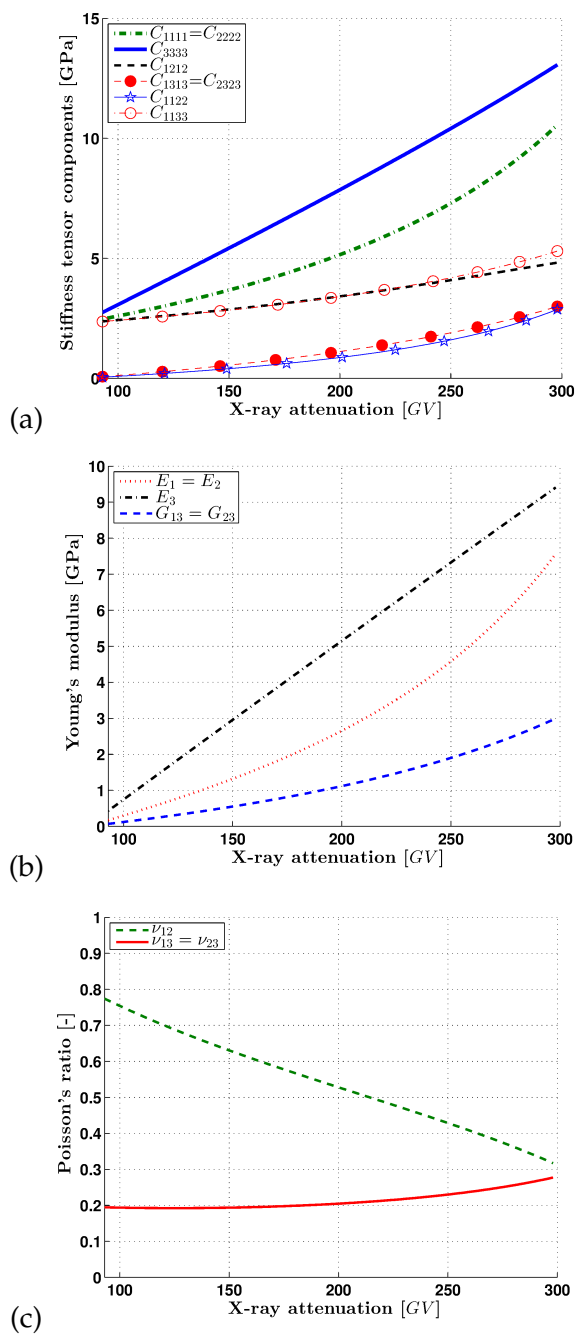
Figure 4.14.: Translation of X-ray attenuation information into tissue elasticity: (a) stiffness tensor components, (b) Young's and shear moduli, and (c) Poisson's ratios; 1,2 ... transverse direction, 3 ... axial direction

106
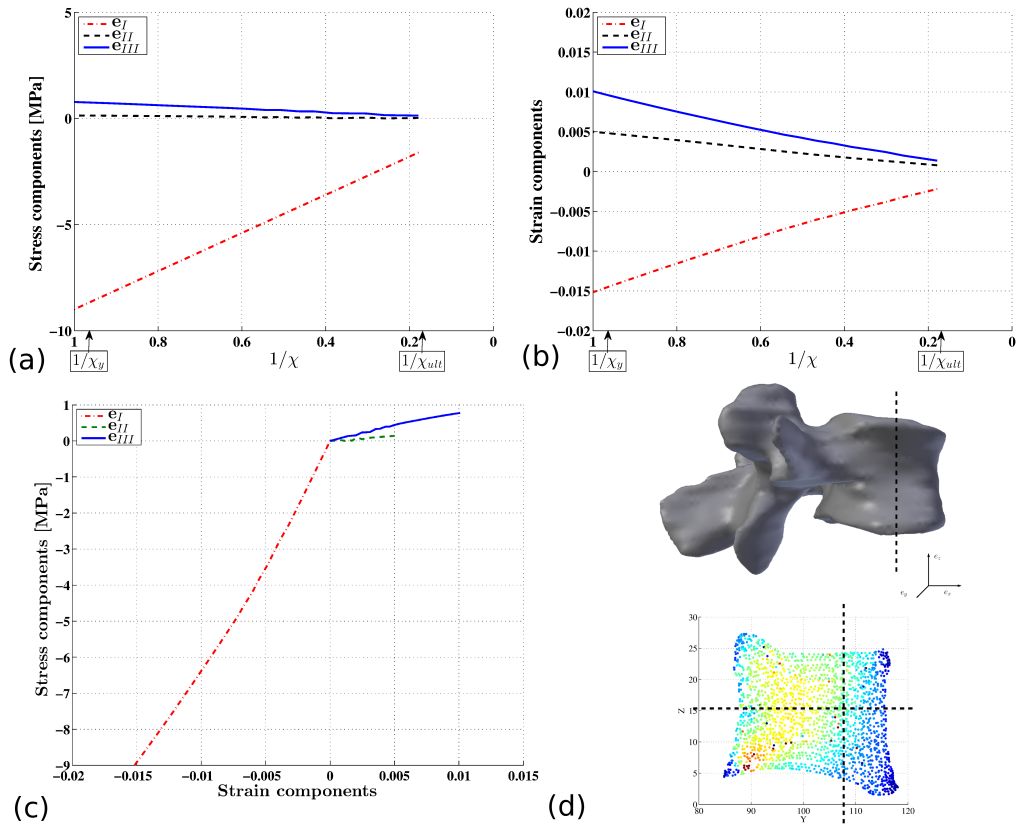
Figure 4.15.: (a) Evolution of the principal stresses along the loading degree; (b) Evolution of the principal strains along the loading degree; (c) Stress-strain curve; (d) Location of the chosen element on a cross section of the vertebral body

block action of an american football player, 7500 N during a golf swing, or 7756 N during torso weight lifting [100].

A particular feature of our new method is the consistent consideration of heterogeneous elasticity and strength properties throughout the organ - importance of heterogeneity for fracture loads has been repeatedly stated [31]. In our case, the heterogeneity results from the bone remodeling induced by the natural asymetry of the human body, with the right part of the middle section of the vertebra being less porous, and therefore stiffer than the left-hand part, see Figure 4.16(a). Resulting stress concentrations govern the organ's compliance and safety margin against fracture: stiffness and strength properties based on an averaged homogeneous vascular porosity would overestimate the strain energy density by a factor of 5, and the safety factor by a factor of 2.
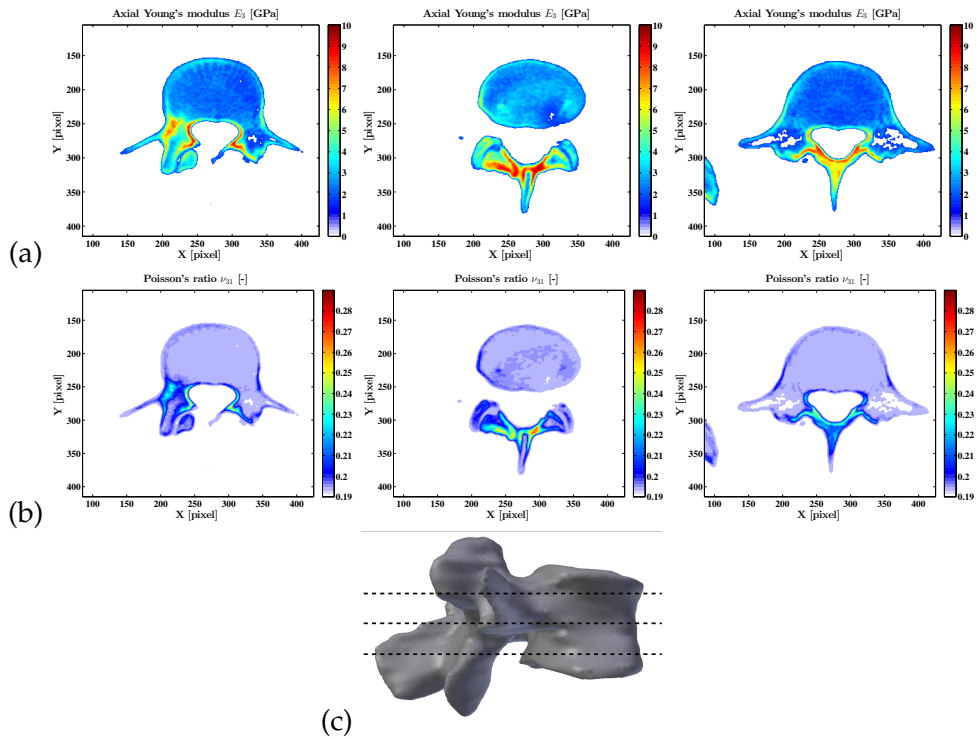
Figure 4.16.: Property maps in CT slice orthogonal to e_z:(a) axial Young's modulus, and (b) axial Poisson's ratio; (c) locations of the mapped cross sections
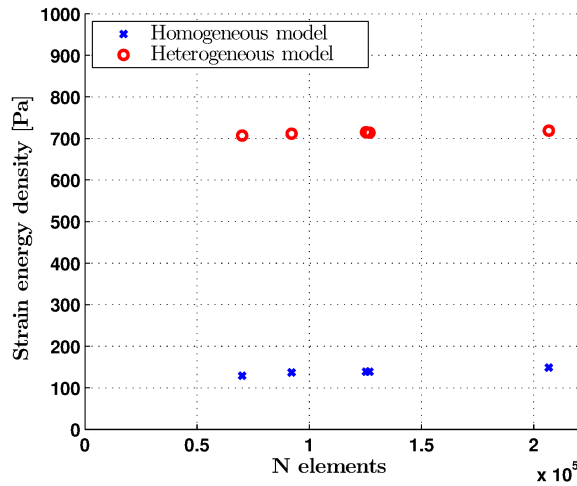
Figure 4.17.: Convergence study: strain energy density averaged over all finite elements of the investigated FE mesh.

4.2.5 *Acknowledgments*

108
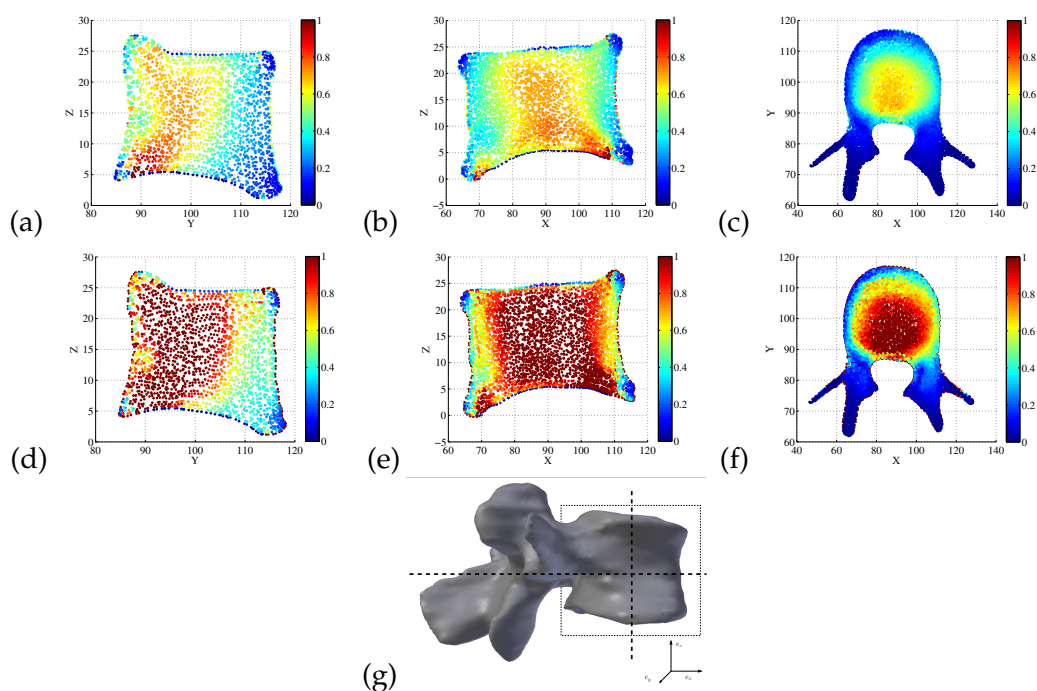
Figure 4.18.: Maps of the "yield loading degree" [MPa^{-1}]: across the sagittal plane through the vertebral body, for (a) homogeneous, and (d) heterogeneous Finite Element model, across the coronal plane, for (b) homogeneous, and (e) heterogeneous FEM; across the transverse plane, for (c) homogeneous, and (f) heterogeneous FEM. (g) 3D representation of the organ and position of the slices. Cross-sectional dimensions are in millimeters

109

Figure 4.19.: Maps of the "ultimate loading degree" $[\text{MPa}^{-1}]$: across the sagittal plane through the vertebral body, for (a) homogeneous, and (d) heterogeneous Finite Element model, across the coronal plane, for (b) homogeneous, and (e) heterogeneous FEM; across the transverse plane, for (c) homogeneous, and (f) heterogeneous FEM. (g) 3D representation of the organ and position of the slices. Cross-sectional dimensions are in millimeters

NOMENCLATURE

Variables

A area

$\mathbb{A}$ strain concentration tensor

$\mathbb{C}$ stiffness tensor

C_{ijkl} stiffness tensor component

$\mathbb{D}_{ic,\Phi\Theta}$ influence tensor accounting for the influence of plastic strains in the Phi Theta-oriented hydrated mineral phase on the total strains in the inter-crystalline pores

$\mathbb{D}_{\phi\theta\Phi\Theta}$ influence tensor accounting for the influence of plastic strains in the (Φ, Θ)-oriented hydrated mineral phase on the total strains in the (ϕ, θ)-oriented phase

C_{ijkl}^{-1} compliance tensor component

$\mathbf{E}$ macroscopic strain

E Young's modulus

f_i^j volume fraction of phase i (if specified, in the RVE j; otherwise, in the macro-scopic RVE)

$\mathcal{F}$ yield function

$\mathcal{G}$ flow potential

$\mathbb{I}$ fourth-order identity tensor

k_i bulk modulus of constituent i

l characteristic length

$\mathbb{P}$ Hill tensor or morphological tensor

V_n volume of the n-th finite element

$\mathbf{x}$ (microscopic) position vector inside the RVE

β proportionality constant

δ_{ij} Kronecker delta

ε microscopic strain tensor

$\dot{\lambda}$ plastic multiplier

μ_i shear modulus of constituent i

ν Poisson's ratio

$\boldsymbol{\xi}$ displacement

σ microscopic stress

$\boldsymbol{\Sigma}$ macroscopic stress

ϕ_i^j porosity of space i (if specified, in the RVE j; otherwise, in the macroscopic RVE)

χ risk factor

ψ macroscopic strain energy density

$\overline{\psi}$ strain energy density averaged over organ

Subscripts
1   ... in radial direction
2   ... in circumferential direction
3   ... in axial direction
col   ... of collagen
cort   ... of cortical bone
cyl   ... of cylindrical inclusions
dev   ... deviatoric part
end   ... of the bony endplate
ef   ... of the extrafibrillar space
exvas   ... at extravascular scale
HA ... of hydroxyapatite
H_2O ... of water
hom   ... homogenized
ic   ... of the inter crystalline space
lac   ... of lacunae
macro   ... at macroscopic scale
org   ... of organic matter
organ   ... of the full organ
sph   ... of spherical inclusions
vas   ... of vascular porosity
vol   ... volumetric part
ult   ... ultimate
y ... at start of yield
$\phi, \theta, \Phi, \Theta$ ... Euler angles defining the orientation of the crystal needles

Superscripts
I,II,III   ... eigenvalues
ef   ... in the extrafibrillar space
iso   ... in an isotropic phase
p ... plastic
trab   ... of trabecular bone
ult   ... ultimate
y ... at start of yield
∞ ... at infinite boundary of auxiliary matrix in Eshelby's inclusion problem

5

A MULTISCALE ANALYTICAL APPROACH FOR BONE REMODELING SIMULATIONS: LINKING SCALES FROM COLLAGEN TO TRABECULAE (COLLOCA ET AL., 2014)

AUTHORED BY M. COLLOCA, R. BLANCHARD, C. HELLMICH, B. VAN RIETBERGEN, AND K. ITO
PUBLISHED IN *BONE*, VOLUME 64, PAGES 303–313

TYPE OF COLLABORATION

This paper results from a collaboration between the Institute for Mechanics of Materials and Structures of TU Wien and the TU Eindhoven. Keito Ito and Bert van Rietbergen set up the research strategy, in particular the development of an analytical bone remodeling scheme realized by Michele Colloca, and also took the lead in research and result presentation. Michele Colloca also performed all the Finite Element analyses and their comparisons to the analytical scheme. The latter is essentially informed through a bone micromechanics model developed at TU Wien, and adapted and re-programmed by the thesis author for the coupling with the remodeling algorithms developed at TU Eindhoven,- she also provided support in research documentation. Christian Hellmich supported the conceptual design and the documentation of the aforementioned coupling strategy.

5.1 INTRODUCTION

Bone is a dynamic porous material which is continuously resorbed and subsequently formed built and rebuilt in a process called bone remodeling influenced by both mechanical and biological factors [60,98,180,228,256]. Moreover, it is a hierarchical material whose architecture differs at each level of hierarchy and whose mechanical properties can vary considerably, even on the same specimen, due to bone heterogeneity [71,117,240]. The density of bone is modulated by two groups of cells: the osteoclasts which resorb bone and osteoblasts which deposit new bone [222]. The actions of these actor cells are thought to be mediated by osteocytes which are the most numerous cells in bone. It has been hypothesized that the

osteocytes can sense the local mechanical stimulus, in turn controlling the activity of osteoblasts and osteoclasts within a basic multicellular unit (BMU) [8, 82, 146]. Several mathematical models have been proposed in an attempt to elucidate the features of bone adaptation at the different scales, though at the organ, tissue and cell level, these models merely exist in isolation [292]. By integrating numerical equations into finite element models, it was shown that the load-driven bone remodeling algorithm based on mechanosensory theory can explain many features of bone adaptation at the tissue- and cell-level [132, 249], e.g. the formation of load-adapted microstructures, as well as the loss of bone mass and microstructural integrity after disuse or increased osteoclast activity (associated with decreased estrogen levels). However, using such analyses for patient-specific predictions of bone remodeling is difficult because of the limited resolution of in-vivo imaging techniques and the huge computational cost involved for such detailed bone remodeling analyses. A method to reduce the computational time in the above mentioned analyses and to deal with the fact that at most sites (e.g. hip and spine) no patient bone microarchitecture can be measured would be to implement the bone remodeling theory in a multi-scale framework that can translate structural changes at the cell-level to changes in bone density at the organ level. By using an analytical formulation of the bone remodeling equation integrated with multiscale micromechanical models, that use generalized structural models at each level of organization [95], such multi-step homogenization schemes can provide a very flexible framework to derive mechanical properties at any level. By integrating such models with bone remodeling equations, it will be possible to predict bone remodeling at these different levels in a very efficient manner. The concept of integrating multi-scale modeling and bone remodeling has been introduced in earlier studies. Coelho et al. [50] presented a multiscale model for bone tissue adaptation that considered two levels, whole bone and trabecular architecture. The bone density distribution predictions were evaluated at the macroscale level, taking into account mechanical properties as well as surface density and permeability of the trabecular structure at the microscale level. Hambli et al. [110] developed a multiscale approach for bone remodeling simulation integrating finite element models at the macro level and 3D neural network computation techniques at the mesolevel. The authors did not, however, include in their bone remodeling formulation cellular activities and biological factors that affect bone apposition and resorption. In their investigation, Podshivalov et al. [230] presented a new 3D multiscale FE method based on domain-based multiresolution hierarchical geometric modeling and multiscale material properties of trabecular bone. The goal was to design a computational tool as infrastructure for computerized systems aiming at interactively analyzing bone structures. None of these models can explicitly account at the nanolevel for collagen and hydroxyapatite contributions on stiffness and volume fraction of the bone tissue at higher levels. Also, most of these studies

rely on computational tools to solve equations at each included level, whereas a true multiscale approach would benefit from an analytical description that spans multiple levels. Going in the direction to integrate bone structural information at different scales and the remodeling process, in recent works [53, 54] we proposed an analytical model in which the bone remodeling process was studied on the basis of two connected scales, tissue and cell levels respectively, with the dependency on osteoblast and osteoclast activities in terms of bone apposition and resorption rates and on the estimation of strain energy density (SED), as mechanical stimulus. In that work, we were able to show that organ-level bone remodeling models that represented the bone microstructure by a simplified regular structure could predict bone density changes in good agreement with micro-structural models that represented the actual micro-architecture. However, the results were limited to two levels only and the remodeling signal was based on the average tissue-level SED, whereas for the bone remodeling more accurate SED values at the bone matrix surfaces are necessary. In the present study we therefore extendt this work by combining the earlier developed remodeling theory with a multi-scale framework that can account for (changes in) bone mechanical properties at all levels of bone structural organization (Fig. 5.1). Using this model it is possible to get more accurate estimates of the stresses that the osteocytes sense by using more elaborate models of the bone microstructure and bone tissue composition. In particular, specific goals of this study are: 1) to derive, as mechanical stimulus sensed by the osteocytes, the micromechanics-derived SED based on an Eshelby matrix-inclusion problem in order to accurately and efficiently predict the stress distributions in a representative volume element of trabecular bone; 2) to test the accuracy of the multiscale analytical model by comparing the bone volume fraction predictions to those obtained from the earlier computational models that represent the full bone microstructure; 3) to demonstrate its multiscale capabilities by investigating in children bones the effects of age-dependent changes in collagen and hydroxyapatite content that are defined at the nanometer scale on the bone volume fraction at the millimeter scale.

5.2 METHODS

5.2.1 *Analytical approach for bone remodeling simulations*

In the bone remodeling theory adopted for this study, it is assumed that the osteocytes inside the bone tissue sense mechanical loading and transmit a signal to the osteoblasts on the bone matrix surface to form bone properly. while the osteoclasts are assumed to be attracted by effects of local micro-damage [86].The formulation of this theory as implemented in a validated analytical model [53] is expressed

in terms of net linear rate $dl_{BM}(x,t)/dt$ of bone apposition or resorption of bone matrix at a particular trabecular surface location x at time t determined by

$$\frac{dl_{BM}}{dt} = \frac{dl_{OBL}(x,t)}{dt} - \frac{dl_{OCL}(x,t)}{dt} \tag{5.1}$$

where $dl_{OBL}(x,t)/dt$ and $dl_{OCL}(x,t)/dt$ are the linear bone formation rate (μm/day) and linear bone resorption rate (μm/day), respectively. Bone remodeling is assumed to occur on the internal surfaces of the bone matrix or on the walls of the voids and the rate of change of bone volume fraction is influenced by the amount of internal surface available for cellular activity as experimentally evidenced [82, 222]. In the proposed multiscale analytical framework proposed in this study, remodeling equations at the tissue level, that can account for bone tissue properties as determined by lower levels (cell and collagen levels) and that can represent the bone density evolution at higher levels (e.g. organ level), are developed (Fig. 5.1). As a starting point, we consider the analytical expression of the rate of change of bone volume fraction in the RVE of trabecular bone at the tissue level, when modulated by mechano-biological and geometric feedback as given in [52], can be expressed by:

$$\frac{d(BV/TV)}{dt} = \frac{dl_{OBL}(x,t)}{dt} - \frac{dl_{OCL}(x,t)}{dt} \cdot \alpha \cdot BS/TV \tag{5.2}$$

with α as a fraction of the bone specific surface BS/TV [μm^2/μm^3] that is available for the cellular activities and expressed as a function of the bone volume fraction (BV/TV) by adopting the relationship of Martin [192]

$$\begin{aligned}
\frac{BS}{TV} &= 0.0323(1 - \frac{BS}{TV}) - 0.0939(1 - \frac{BS}{TV})^2 + 0.134(1 - \frac{BS}{TV})^3 - \\
&\quad -0.101(1 - \frac{BS}{TV})^4 + 0.0288(1 - \frac{BS}{TV})^5
\end{aligned} \tag{5.3}$$

For the bone apposition activity through osteoblasts dl_{OBL}/dt, we adopt the following expression

$$\frac{dl_{OBL}}{dt} = \tau \cdot \mu \cdot \psi_{BM} \tag{5.4}$$

where τ is the bone formation time constant [μm^3/(nmol·day], μ the osteocyte mechanosensitivity [nmol/(MPa·μm^2)] and ψ_{BM} [MPa] is the "microscopic" strain energy density as "felt" by the osteocytes being uniformly dispersed into the bone matrix. It is derived from a continuum micromechanics model based on Eshelby's matrix-inclusion problem, as described in the following section in more detail. For

the bone resorption activity through osteoclasts, we adopt the following relationship

$$\frac{dl_{OCL}(x,t)}{dt} = A_{ocl} \qquad (5.5)$$

with a constant resorption rate A_{ocl} [μm/day]. Eq. (5.2) represents a non linear differential equation of the first order that, in addition to the initial condition $BV/TV(t=0)$, forms an initial value problem to be solved numerically.
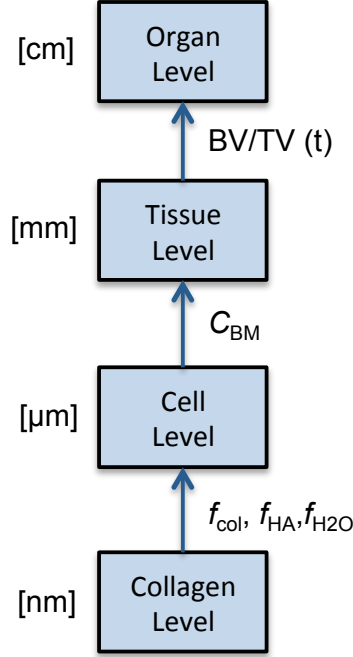
Figure 5.1.: Block-diagram of the proposed multiscale analytical model. Volume fraction of hydroxyapatite (f_{HA}), collagen (f_{col}) and water (f_{H_2O}) at the nano scale affect the stiffness of the bone matrix ($\mathbb{C}_{BM}$) at the micro scale which in turn affect the strain energy density and bone volume fraction change over time (t) at the millimeter scale.

5.2.2 *Micromechanics-derived strain energy density as mechanobiological stimulus*

The microscopic strain energy density in the trabecular bone RVE (Fig. 5.2) is assumed as the mechanical stimulus sensed by the osteocytes regulating the bone remodeling process. It is defined by means of an Eshelby-problem micromechanics model [308], similar to that undergoing extensive experimental validation in Ref. [117] and to that used for micromechanics-supported finite element models

of human mandibles to simulate the effects of atrophy on the bone density distribution [120].
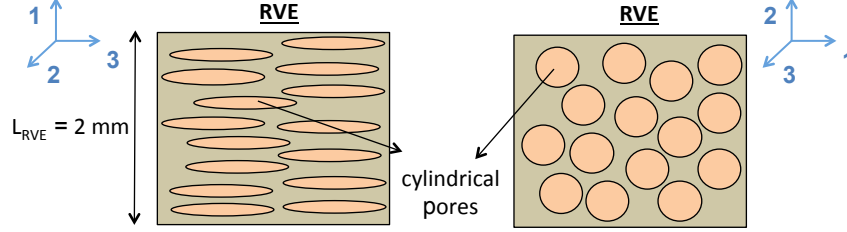
Figure 5.2.: Trabecular bone RVE modeled as a two-phase material: bone matrix and cylindrical inclusions. In the base frame 1 is the radial direction, 2 the circumferential direction and 3 the axial direction.

Moreover, it is assumed that the macroscopic stress states act on the boundary of a trabecular bone RVE with their magnitudes equivalent to the maximum strain energy density rate [249], and the directions of principal stresses e_I, e_{II}, e_{III} (with stress tensors $\Sigma = \Sigma_{11}e_I \otimes e_I + \Sigma_{22}e_{II} \otimes e_{II} + \Sigma_{33}e_{III} \otimes e_{III}$) coincide with the material directions of the transversely isotropic material. For this specific case, the "microscopic" strain energy density at the level of the solid bone matrix reads as

$$\psi_{BM} = \frac{1}{2}\varepsilon_{BM} : \mathbb{C}_{BM} : \varepsilon_{BM} \tag{5.6}$$

where ε_{BM} is the average (microscopic) strain tensor in the solid bone matrix, which is related to the macroscopic strain tensor E through the fourth-order concentration tensors $\mathbb{A}_{BM}$

$$\varepsilon_{BM} = \mathbb{A}_{BM} : E \tag{5.7}$$

where

$$\mathbb{A}_{BM} = \left[\phi[\mathbb{I} + \mathbb{P}^{BM}_{cyl} : (\mathbb{C}_P - \mathbb{C}_{BM})]^{-1} + (1 - \phi)\mathbb{I}\right]^{-1} \tag{5.8}$$

and it is function of the volume fraction of the porosity ϕ, the stiffness tensor of the bone matrix $\mathbb{C}_{BM}$, the stiffness tensor of the porosity $\mathbb{C}_P$ and of Hill's morphology tensor expressed by

$$\mathbb{P}^{BM}_{cyl} = \begin{pmatrix} P^{BM}_{1111} = P^{BM}_{2222} & P^{BM}_{1122} & P^{BM}_{1133} = 0 \\ P^{BM}_{2211} = P^{BM}_{1122} & P^{BM}_{2222} = P^{BM}_{1111} & P^{BM}_{2233} = 0 \\ 0 & 0 & 0 \end{pmatrix}_{e_I, e_{II}, e_{III}} \tag{5.9}$$

with the components of P^{BM}_{ijkl} according to Eq.(76) to (81) of Ref. [117]

$$P^{BM}_{1111} = P^{BM}_{2222} = \frac{1}{8}\frac{5C_{1111} - 3C_{1122}}{(C_{1111} - C_{1122}) \cdot C_{1111}} \tag{5.10}$$

$$P_{1122}^{BM} = \frac{-1}{8} \frac{C_{1111} + C_{1122}}{(C_{1111} - C_{1122})C_{1111}} \tag{5.11}$$

$$P_{2323}^{BM} = P_{1313}^{BM} = \frac{1}{8} C_{2323} \tag{5.12}$$

$$P_{1212}^{BM} = \frac{1}{8} \frac{3C_{1111} - C_{1122}}{(C_{1111} - C_{1122})C_{1111}} \tag{5.13}$$

Choosing the base frame to coincide with the aforementioned material directions, the stiffness of the bone matrix reads as

$$\mathbb{C}_{BM} = \begin{pmatrix} C_{1111} & C_{1122} & C_{1133} \\ C_{1122} & C_{1111} & C_{1133} \\ C_{1133} & C_{1133} & C_{3333} \end{pmatrix}_{\mathbf{e}_I, \mathbf{e}_{II}, \mathbf{e}_{III}} \tag{5.14}$$

In fact, the bone matrix is characterized by a transversely isotropic elasticity tensor and modeled as mineral foam of hydroxyapatite which is "reinforced" predominantly in the longitudinal direction by collagen fibrils, while the transverse stiffness is mainly governed by the mineral concentration. Relevant values for this tensor will be introduced in Section 5.3.3. The stiffness tensor of the porosity $\mathbb{C}_P$ was chosen as that of fat $\mathbb{C}_{fat}$ and expressed in function only of the bulk modulus k_{fat} by using the corresponding elastic constants given in [185]

$$\mathbb{c}_{Fat} = 3k_{Fat}\mathbb{J} \tag{5.15}$$

with $\mathbb{J}$ the volumetric part of fourth-order identity tensor $\mathbb{I}$ where

$$J_{ijkl} = \frac{1}{3}\delta_{ij}\delta_{kl} \quad \text{with} \begin{cases} \delta_{ij} = 1 & \text{if } i = j \\ \delta_{ij} = 0 & \text{otherwise} \end{cases} \tag{5.16}$$

Hence

$$\mathbb{C}_{Fat} = 3k_{Fat}\mathbb{J} = 3k_{Fat} \begin{pmatrix} 1/3 & 1/3 & 1/3 \\ 1/3 & 1/3 & 1/3 \\ 1/3 & 1/3 & 1/3 \end{pmatrix} = \begin{pmatrix} k_{Fat} & k_{Fat} & k_{Fat} \\ k_{Fat} & k_{Fat} & k_{Fat} \\ k_{Fat} & k_{Fat} & k_{Fat} \end{pmatrix} \tag{5.17}$$

Collecting all the terms entering Eq. (5.6), a closed-form expression for the microscopic strain energy density can be found:

$$
\begin{aligned}
\psi_{BM} =& \frac{1}{2}[(A_{1111}^2 + A_{1122}^2)(2C_{1122}^{BM}E_{11}E_{22} + C_{1111}^{BM}(E_{11}^2 + E_{22}^2)) + \\
& + 2A_{1122}A_{1133}(C_{1111}^{BM} + C_{1122}^{BM}) + C_{1133}^{BM})(E_{11} + E_{22})E_{33} + \\
& + (2A_{1133}^2(C_{1111}^{BM} + C_{1122}^{BM}) + 4A_{1133}C_{1133}^{BM} + C_{3333}^{BM})E_{33}^2 + 2A_{1111}] \\
& (A_{1122}(2C_{1111}^{BM}E_{11}E_{22} + C_{1122}^{BM}(E_{11}^2 + E_{22}^2)) + A_{1133}(C_{1111}^{BM} + C_{1122}^{BM})C_{1133}^{BM}) \\
& (E_{11} + E_{22})E_{33}]
\end{aligned}
\tag{5.18}
$$

and it is a function of ϕ, C_{1111}, C_{1122}, C_{1133}, C_{3333} and k_{Fat}. The components of the concentration tensor $\mathbb{A}_{BM}$ can be found in the Appendix.

5.2.3 *Micromechanics-derived bone matrix stiffness in adults and children*

The stiffness of the bone matrix is time- and space-invariant in adult healthy tissue [87, 120, 126] and depends on its composition, i.e. on the volume fractions of its principal constituents, namely hydroxyapatite (HA), collagen (col), and water (H_2O). In [190], the average tissue elasticity properties were successfully identified through a coupled approach comprising 10 MHz pulse transmission ultrasound with universal rules governing the composition and the hierarchical mechanical functioning of mineralized tissues, resulting in the following stiffness tensor of extracellular bone tissue:

$$
\mathbb{C}_{BM}^{adult} = \begin{pmatrix}
C_{1111} & C_{1122} & C_{1133} & 0 & 0 & 0 \\
C_{1122} & C_{1111} & C_{1133} & 0 & 0 & 0 \\
C_{1133} & C_{1133} & C_{3333} & 0 & 0 & 0 \\
0 & 0 & 0 & 2C_{2323} & 0 & 0 \\
0 & 0 & 0 & 0 & 2C_{2323} & 0 \\
0 & 0 & 0 & 0 & 0 & 2C_{1212}
\end{pmatrix} =
$$

$$
= \begin{pmatrix}
12.7 & 6.2 & 6.4 & 0 & 0 & 0 \\
6.2 & 12.7 & 6.4 & 0 & 0 & 0 \\
6.4 & 6.4 & 20.2 & 0 & 0 & 0 \\
0 & 0 & 0 & 7.9 & 0 & 0 \\
0 & 0 & 0 & 0 & 7.9 & 0 \\
0 & 0 & 0 & 0 & 0 & 6.5
\end{pmatrix} \quad \text{in GPa}
\tag{5.19}
$$

Although this composition is rather constant in healthy adults, it is known to vary during development and with diseases, e.g. osteogenesis imperfecta. This variation stems from a variation in the bone tissue composition, i.e. from its min-

eral, collagen, and water contents. The latter were derived from age-dependent weight fractions of ash per mass of dry bone WF_{ash}^{dry}, as provided by Currey [65], through the following steps: First, the ash fraction was converted into a mineral fraction [285],

$$WF_{HA}^{dry} = WF_{ash}^{dry} 1.066 \qquad (5.20)$$

considering 6.6% of the bone mineral burning at ashing temperatures well beyond 600 centigrades [105], as encountered with a Bunsen burner as used by Currey [65]. This quantity is related to the apparent mineral mass density ρ_{HA}^* in physiological tissue, being proportional to the mineral concentration, through

$$\rho_{HA}^* = WF_{HA}^{dry}(\rho^{BM} - \rho_{H_2O}^*) \qquad (5.21)$$

where ρ^{BM} is the mass density of the extracellular bone matrix, and $\rho_{H_2O}^*$ is the apparent mass density of water, i.e. the mass of water per volume of extracellular bone tissue. The extracellular mass density and the apparent mass densities of mineral ρ_{HA}^*, of water $\rho_{H_2O}^*$, and of organics $\rho_{org}^* = \rho^{BM} - \rho_{HA}^* - \rho_{H_2O}^*$, are all related by bilinear functions, see Fig. 5.3(a), so that Eq. (5.21) allows for assigning to each of Currey's experimental value for WF_{HA}^{dry}, values for ρ^{BM}, ρ_{HA}^*, $\rho_{H_2O}^*$, and ρ_{org}^*, see Table 5.1. We observe that the tissue mass densities nicely approach the "adult" value of $\rho^{BM} = 1.90$ g/cm^3 identified in [190]. The aforementioned apparent mass density values give access to the volume fractions of hydroxyapatite, of collagen, and of water, via: with $\rho_{H_2O}^*$ the apparent mass density of water and considering the relationship $\rho_{org}^* = \rho^{BM} - \rho_{H_2O}^* - \rho_{HA}^*$. The bone matrix mass density and the apparent mass densities of mineral, water and organics are related by bilinear relationships explicited by [285], see Fig. 5.3(a) and Table 5.1. The aforementioned apparent mass density values give access to the volume fractions of hydroxyapatite, collagen and water via:

$$f_{HA} = \frac{\rho_{HA}^*}{\rho_{HA}}, \ f_{col} = 0.9 \times \frac{\rho_{org}^*}{\rho_{org}}, f_{H_2O} = \frac{\rho_{H_2O}^*}{\rho_{H_2O}} \qquad (5.22)$$

with the real mass densities of water, organics and hydroxyapatite amounting to ρ_{H_2O}=1 g/cm^3, $\rho_{org} = 1.41$ g/cm^3 [170], and $\rho_{HA} = 3$ g/cm^3 [105,118,170]. From the volume fractions of (5.22), we retrieve the age-dependent tissue mass density ρ^{BM} according to $\rho^{BM} = f_{HA}\rho_{HA} + f_{org}\rho_{org} + f_{H_2O}\rho_{H_2O}$, which we approximate by means of a linear fit between age and mass density ρ^{BM} (coefficient of determination $R^2 = 0.72$). Then, the general compositional rules given in [285] give access to tissue mineral and collagen content at any age, see Table 5.2 for chosen ages between 6 and 13 years. Based on this linear relation occurring during growth, we here investigated the effects of such compositional changes on the bone volume fraction for children of ages between 6 and 13 years, see Table 5.2.

Table 5.1.: Constituent volume fractions in juvenile femoral bone tissue tested by Currey [65] (HA= Hydroxyapatite, col=collagen, H_2O=water)

Age (year) [65]	WF_{ash}^{dry} given [65]	WF_{HA}^{dry} Eq. (5.20)	$\rho^B M$ Eq. (5.21)	ρ_{col}^* Fig. 5.3	ρ_{HA}^* Fig. 5.3	$\rho_{(H_2O)}^*$ Fig. 5.3
4.1	0.605	0.645	1.541	0.359	0.652	0.531
5.9	0.617	0.658	1.606	0.384	0.738	0.484
9.7	0.640	0.682	1.773	0.447	0.960	0.366
11.8	0.632	0.674	1.705	0.421	0.870	0.414
14	0.619	0.659	1.613	0.386	0.748	0.479
14.8	0.649	0.692	1.865	0.482	1.083	0.300
16.8	0.648	0.691	1.854	0.478	1.068	0.308
26.5	0.664	0.708	1.947	0.496 71.201	0.251	

Table 5.2.: Constituent volume fractions of bone tissues of children (HA= Hydroxyapatite, col=collagen, H_2O=water)

Age (year)	ρ^{BM}	f_{HA} [-]	f_{col} [-]	f_{H_2O} [-]
6	1.6	0.244	0.241	0.515
8	1.65	0.266	0.253	0.481
10	1.69	0.284	0.263	0.454
12	1.73	0.302	0.272	0.426
13	1.75	0.310	0.277	0.413

The corresponding age-dependent volume fractions of mineral, water, and collagen components served as inputs for the 4-step micromechanical homogenization scheme developed in [285], from which the stiffness tensors for the extracellular bone matrix were obtained, see Fig. 5.3(b) and Table 5.3.

The stiffness increase with age as predicted in Table 5.3 agrees well with that observed in *in-vivo* ultrasound experiments on the os calcis bones of children aged 6 through 13 years [137].

5.2.4 *Three-dimensional micro-FE and analytical test models for bone modeling and remodeling simulations*

The test model represented a 2×2×2 mm bone cubic region consisting of 226981 cubic voxels. Each voxel was considered as a hexahedral element containing eight integration points. An element-by-element FE solver was used to calculate the strain energy density in each cubic voxel by which the domain of interest was discretized [280]. The bone sample was loaded by tensile loading distributions in the orthogonal x, y and z directions, as displayed in Fig. 5.4. The applied loading
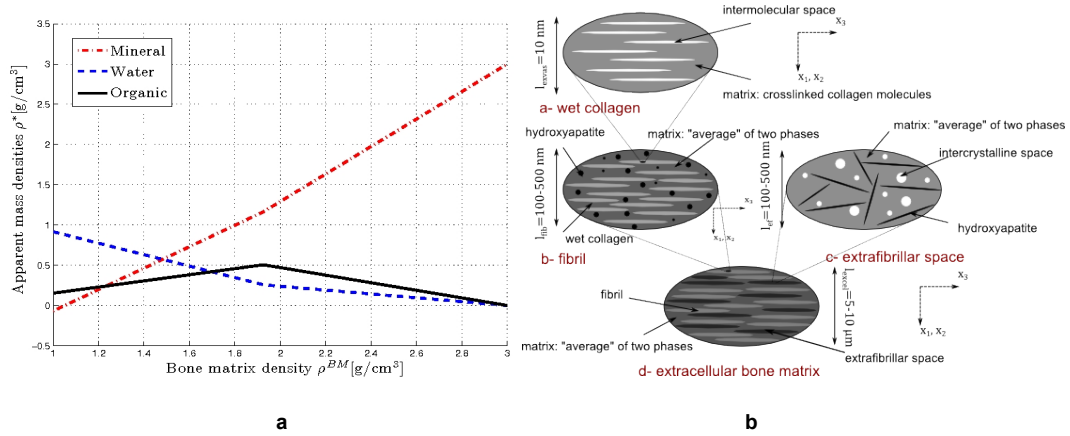
Figure 5.3.: a) Apparent mass densities of water, hydroxyapatite, and organic matter, as functions of the overall mass density of extracellular bone matrix, according to [285]; b) four-step homogenization scheme after [285].

Table 5.3.: Model-predicted stiffness tensor components of young healthy bone tissues

Age [year]	C_{1111} [GPa]	C_{3333} [GPa]	C_{1122} [GPa]	C_{1133} [GPa]	C_{2323} [GPa]	C_{1212} [GPa]
6	10.514	13.390	4.855	5.402	2.946	2.826
8	11.708	14.811	5.142	5.754	3.415	3.283
10	12.779	16.098	5.401	6.065	3.837	3.690
12	13.696	17.548	5.692	6.407	4.307	4.138
13	14.613	18.343	5.853	6.592	4.562	4.380

magnitudes were chosen by means of a numerical model developed to estimate in vivo bone loading based on bone morphology [45]. In the analytical model the same stresses were assumed to work on the sides of the RVE, and the corresponding (micro-)stresses and (micro-)strains at the bone tissue level were determined to obtain the tissue level SED. Using the earlier developed computational bone remodeling simulation model that implements the micro-FE model, the development and adaptation of bone micro-architecture were simulated and, at each time point, the volume fraction was calculated and compared to the volume fraction predicted by the analytical model. In particular, in order to study the evolution of bone volume fraction by solving both the analytical and micro-FE initial value problems with their own initial conditions, two simulation series were performed. In the first one, the bone modeling simulation was obtained by starting from a regular grid (Fig. 5.4) as initial configuration. In the second one, starting with

Table 5.4.: Parameter values used in the proposed multiscale analytical model. (a) [185], (b) [190]

Parameter	Symbol	Value	Unit
Bone formation time constant	τ	18	$\mu\text{m}^3/(\text{nmol}\cdot\text{day})$
Osteocyte mechanosensitivity	μ	1.0	$\text{nmol}/(\text{MPa}\cdot\mu\text{m}^2)$
Bone resorption rate	A_{ocl}	0.17	$\mu\text{m/day}$
	σ_x	1.1	
Applied stresses	σ_y	0.7	MPa
	σ_z	1.5	
Bone specific surface fraction	α	0.8	-
Bulk modulus	k_{Fat}	$1.33^{(a)}$	MPa
	C_{1111}	$7 \cdot 10^{3(b)}$	
Bone matrix elastic constants	C_{1122}	$6.2 \cdot 10^{3(b)}$	MPa
	C_{1133}	$6.4 \cdot 10^{3(b)}$	
	C_{3333}	$20.2 \cdot 10^{3(b)}$	
Radial and circumferential Young's moduli	$E_1^*=E_2^*$	$9 \cdot 10^{3(b)}$	MPa
Axial Young's modulus	E_3^*	$15.8 \cdot 10^{3(b)}$	MPa

the equilibrium condition reached in the first simulation series, changes in bone cellular activity, mechanotransduction and loading parameters were set to study their effects on the remodeling system response.
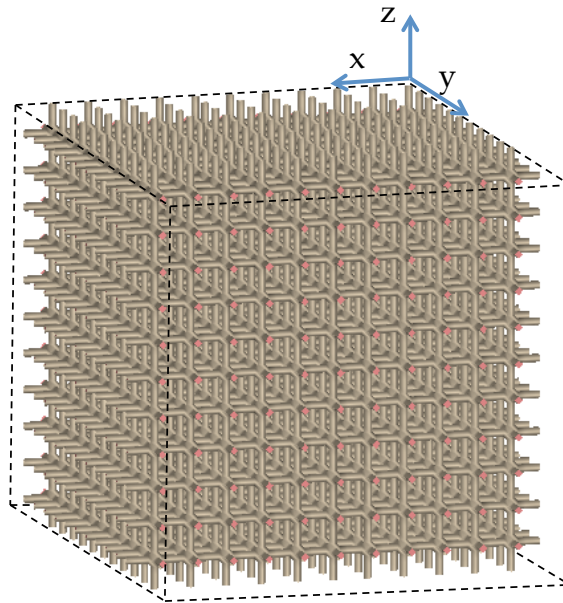
Figure 5.4.: Three-dimensional initial bone microstructure as a regular grid.

In the following, we will use the term "analytical solution" when referring to the analytical model [Eq.(5.2)] and to the "numerical solution", which is taken as the reference, when referring to the bone remodeling algorithm that implements the micro-FE model, see Sect 5.3.4. In all cases, the % difference relative to the numerical predictions of bone volume fraction evolution was evaluated at equilibrium.
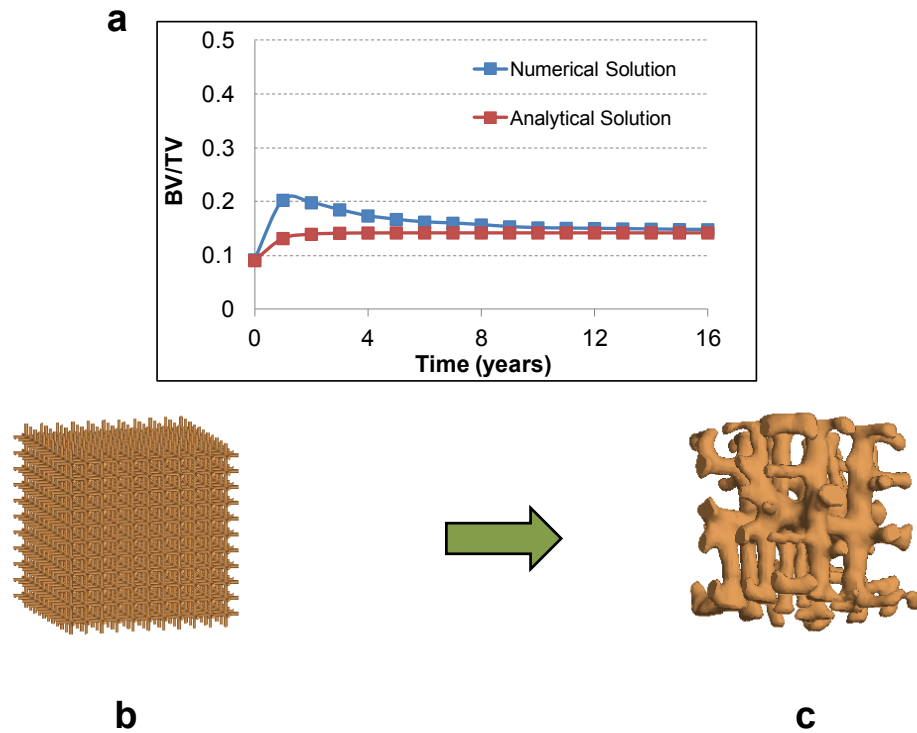
Figure 5.5.: Evolution of bone volume fraction (a) starting from a bone regular grid (b) and final adapted bone microstructure (c) during bone modeling.

5.3.1 *Bone modeling*

The evolution of the RVE bone volume fraction is displayed in Fig. 5.5a where the numerical and analytical solutions are compared. Model parameters adopted in this simulation were defined according to bone physiological values as listed in Table 5.4. A regular grid (Fig. 5.5b) represented the initial configuration. After a transient period, the system reached an equilibrium condition in which the amount of bone formation was balanced by the amount of bone resorption; hence the bone volume fraction became constant. Initially BV/TV increased quickly

as an effect of high mechanical signals, while resorption of poorly loaded tissue lagged behind as in [249]. Good agreement between analytical and numerical curves was found, with a difference less than 4% at the equilibrium, even though the transient behavior was different. In Fig. 5.5c, the final developed and adapted bone microstructure at equilibrium is shown.
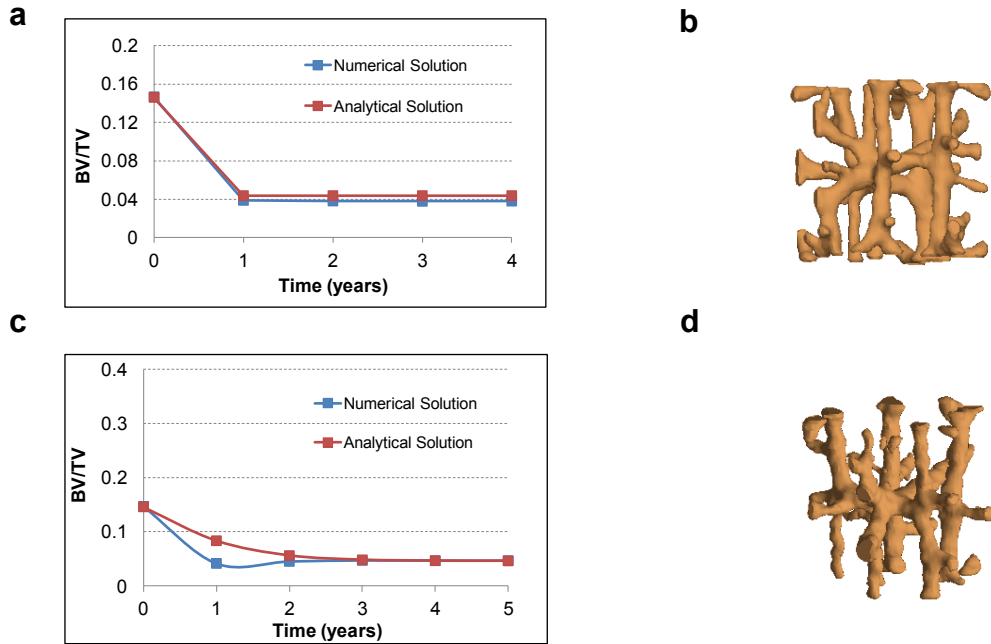
Figure 5.6.: Evolution of the bone volume fraction (a,c) and adaptation of the bone microstructure (b,d) when the initial osteoclast activity (A_{ocl}) is increased (a,b) and the initial osteoblast activity (τ) is decreased (c,d) by a factor of 10.

5.3.2 *Bone remodeling*

Starting from the homeostatic bone microstructure of Fig. 5.5c, a second simulation was performed in which the osteoclast activity A_{ocl} was increased and the osteoblast activity τ was decreased by a factor of 10 with respect to the initial value. Such changes could, e.g. represent the effect of estrogen deficiency as in post-menopausal osteoporosis [80] in the first case, and the result of bone degenerative diseases [282] in the second one. In Fig. 5.6 the analytical and numerical outcomes with their corresponding adapted microstructures are compared, showing the expected bone loss in case of increased osteoclast activity (Fig. 5.6a-b) with a difference of 14.4% between predictions of the analytical and numerical model, and in case of decreased osteoblast activity (Fig. 5.6c-d) with a difference 1%. Dur-

ing the transient phase, the analytical solution somewhat underestimated the bone density in case of τ decreasing. A new simulation series was designed to predict changes in bone volume fraction after increasing the loading magnitude and the osteocyte mechanosensitivity μ to 200%, or decreasing them to 50% of the original value, respectively (Figs. 5.7-5.8). The numerical model showed the expected increase in bone mass with increased mechanosensitivity and loading magnitude, and the decrease after the reduction of the same parameters. The analytical models predicted these changes quantified in 13.3% difference for the increased loading case (Fig. 5.7a-b) and in 0.6% for the decreased loading case (Fig. 5.7c-d). As far as the osteocyte mechanosensitivity is concerned, by comparing the two models the calculated difference were 11.7% (Fig.5.8 a-b) when was increased and 10.1% (Fig. 5.8c-d) when it was decreased.
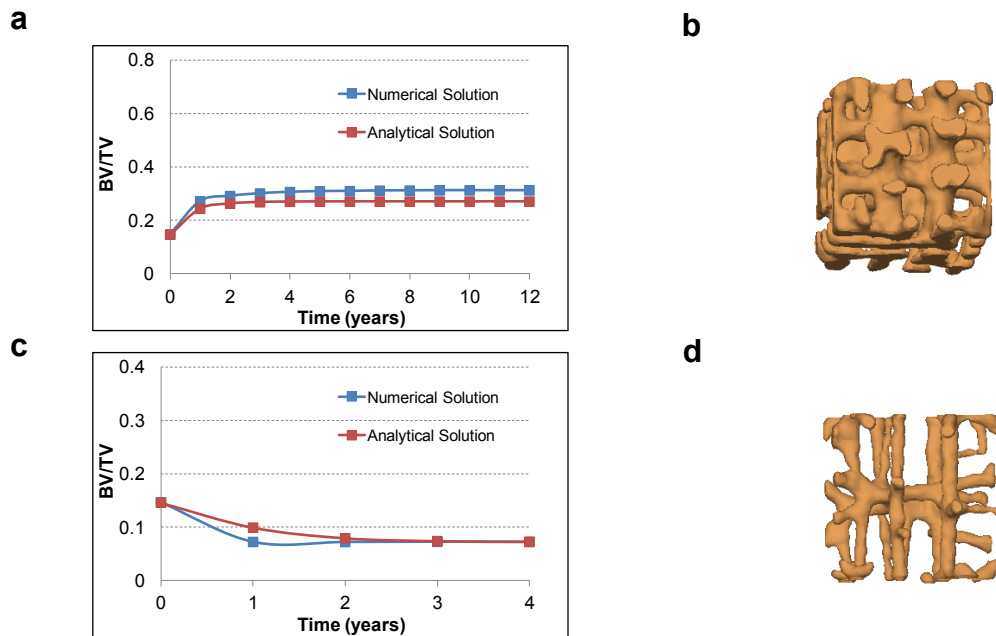
Figure 5.7.: Evolution of the bone volume fraction (a,c) and adaptation of the bone microstructure (b,d) when the loading magnitude ($\sigma_x, \sigma_y, \sigma_z$) is increased by 200% (a,b) and decreased by 50% (c,d).

5.3.3 *Effect of changes in bone tissue level composition on bone volume fraction*

For the bone matrix stiffness tensors given in Table 5.3, the bone volume fraction evolution in a mm-sized trabecular bone sample was predicted and plotted in Fig. 5.9a by adopting the multiscale analytical model presented in Sect. 5.3.1 and the loading conditions and mechano-transduction parameters listed in Table
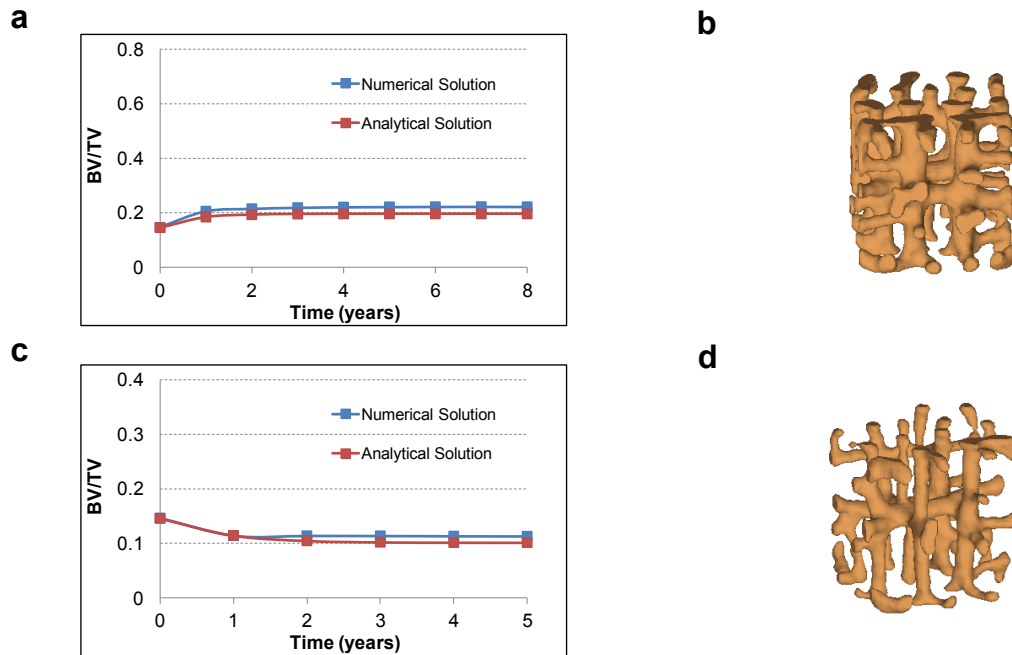
Figure 5.8.: Evolution of the bone volume fraction (a,c) and adaptation of the bone microstructure (b,d) when the the osteocyte mechanosensitivity (μ) is increased by 200% (a,b) and decreased by 50% (c,d).

5.4. Each bone volume fraction evolution curve in Fig. 5.9a is characterized by a different volume fraction of collagen (nanometer scale) in the range of 0.243-0.277 and different volume fractions of water and hydroxyapatite see Table 5.2. Due to these differences in composition, a different elasticity tensor of the bone matrix (micrometer scale) results, and after remodeling, differences in bone volume fraction (millimeter scale) are found, ranging from 0.155-0.130 in the equilibrium state (Fig. 5.9b).

5.4 DISCUSSION

In this study, a multiscale analytical model is proposed to simulate the bone adaptation at the tissue level while accounting for cell activity and material composition parameters at lower levels. The implementation of the multi-scale framework enabled us to describe the bone composition as a two-phase material at different levels. At the tissue level, it was modeled as a bone matrix with cylindrical voids. This assumption allowed for finding a closed-form solution for the mechanical stimulus sensed by the osteocytes. Such a mechanical stimulus was represented by a micromechanics-derived strain energy density based on an Eshelby matrix-
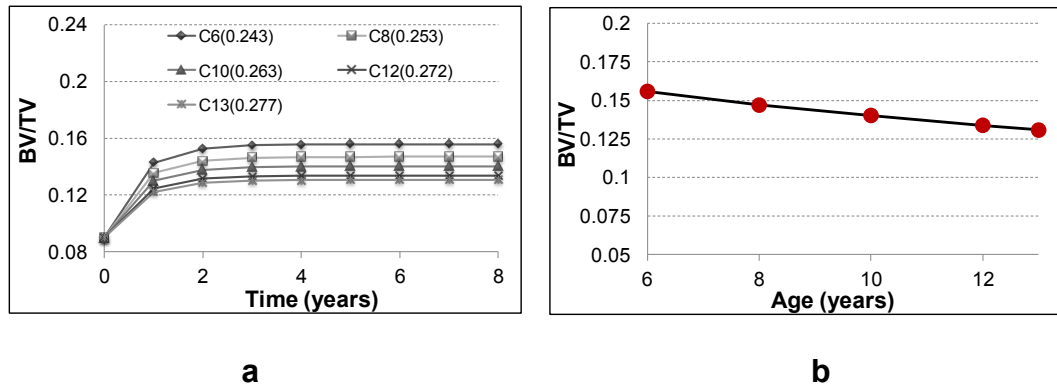
Figure 5.9.: (a) Evolution of the BV/TV at the millimeter scale as function of the volume fraction of collagen (f_{col}) at the nanometer scale during bone remodeling; (b) Predictions of bone volume fraction equilibrium values as function of the age of healthy children. In the plot legend, the nomenclature of each investigated case begins with the letter "C" (child), followed by the age of the child in year and the corresponding volume fraction of the collagen in brackets.

inclusion problem that linked two different scales, typical RVE (mm) and pore (μm) scales, respectively, and accurately predicted the stress/strain states on the trabecular surface where it is hypothesized the bone remodeling is taking place. At the bone matrix level, the material was considered as a mineral foam of hydroxyapatite which is "reinforced" predominantly in the longitudinal direction by collagen fibrils as shown in [90, 117]. This enabled us to describe the anisotropic elastic properties at higher levels as a function of this basic composition. Hence, the first goal of this study was accomplished even though the closed-form solution for the strain energy density was only possible when the inclusions dispersed in the matrix are assumed to have spherical or cylindrical geometry. The analytical results in terms of bone volume fraction evolution were compared to the corresponding numerical ones coming from a previously validated micro-FE-based bone remodeling algorithm [52, 53]. In the investigated cases (see Figs. 5.5-5.8), the percentage difference between the results of the micro-FE model and the present multi-scale model at equilibrium was between 0.6 and 14.4%. Such agreement indicates that the micromechanics-derived strain energy density based on an Eshelby matrix-inclusion problem well represented the energy calculated in the micro-FE numerical while reducing the computational time by a factor of almost one million. The best agreement between analytical and numerical results is found with 0.6% difference at the equilibrium for the bone remodeling simulation (see Fig. 5.7) and 1% difference at the equilibrium when the bone formation time constant initial value is decreased by a factor of 10 (see Fig. 5.6). How-

ever, it should be noted that in the micro-FE model of bone remodeling trabecular bone material properties were assumed to be isotropic whereas in the multi-scale model they were anisotropic, with a higher stiffness in the trabecular longitudinal direction in which the collagen is oriented. The fact that good agreement in results was obtained is likely because the mechanical behavior at the bone tissue level is dominated by the modulus in the trabecular longitudinal direction: for the most common loading modes (compression, tension and bending), only the modulus in the longitudinal direction plays a role [183]. Hence, by specifying an isotropic modulus in the micro-FE models equal to the longitudinal modulus in the anisotropic multi-scale model, good agreement in mechanical behavior is expected. As a consequence, based on these observations it is further possible to implement easily the analytical model for whole bones applications (e.g. radius, femurs and vertebras) in which micro or continuum FE analysis and corresponding meshes under isotropic material assumption are exploited for the calculation of the micromechanics-based strain energy density. Looking at the dynamic response of the analytical bone remodeling system, the model is found temporally stable and consistent with experimental observations of bone density changes during disuse and aging [43, 99]. However, in the analytical simulations of Fig. 5.6c-d and Fig. 5.7c-d the BV/TV was not in agreement with the numerical results during the transient phase. This might relate to difference in the available free surface for both cell types between the analytical and numerical model. The response of the bone system in transient behavior can be further improved by changing parameters related to this free surface or by choosing optimal values for the time constant. The third goal of this paper was to investigate the effects of collagen and hydroxyapatite changes at the nanometer scale on the bone volume fraction at the millimeter scale. Since the bone matrix of adult healthy tissue exhibits a stiffness which is time- and space-invariant when averaged over a millimeter-sized domain [87, 120, 126], and hence $\mathbb{C}_{BM}$ in Eq. (5.6) is constant for adult healthy tissue, it is interesting to also investigate diseased, medicated, or juvenile tissue, where this constancy is not observed. Since the elasticity of bone tissue in children changes with respect to age, the stiffness-dependent micro-mechanical signal sensed by the osteocytes is age-dependent as well, so that even age-independent osteocyte behavior cannot impede bone volume fractions from depending on age during development. This goal was accomplished as demonstrated by the outcome of the micromechanical model and the multistep homogenization scheme adopted in this study which allowed to take into account the volume fraction of the elementary components (hydroxyapatite, collagen and water) of healthy children and to derive from this composition the elastic constants of the bone matrix. In turn, the elasticity tensors of the bone matrix determined different and associate strain energy density levels stored in the trabecular bone sample (millimeter level) and hence different predictions for the evolution of the bone volume fraction at

the equilibrium state in the range of 0.13-0.15 (Fig. 5.9). These results suggest that the age-dependent nano-level properties in the bone matrix composition affect the cellular activities independently from the pre-existing architecture. The evolution of the bone volume fraction over the time is different in the range of age 6-13 years because of the increase in bone tissue mineralization during growth. The increased mineralization leads to an increase in bone tissue stiffness and thus lower strains in the bone tissue. As a consequence, the mechanical signal sensed by the osteocytes is reduced, which, in turn, affects the osteoblast activity. These results also suggest that younger healthy children have denser bones (i.e. lower vascular porosity) with respect to older healthy children. A reduction of bone density (i.e. an increase of vascular porosity) with age is also shown in [269] where the authors determined microstructural and strength variables of the distal radius of healthy girls by high-resolution peripheral computerized tomography and micro-finite element analysis and quantified low trabecular vBMD and thickness in the distal radius associated with reduced bone strength and increased fracture risk during growth. The aforementioned increase of vascular porosity is also consistent with the decrease of bone formation with increased age between 3 and 18 months, as evidenced by de Pollak et al. [72] in terms of histomorphometric indices. A few limitations of the present study should be mentioned as well. First, at the tissue level the bone was modeled as a closed structure build of bone matrix with cylindrical voids whereas in reality it is an open structure and the voids shape is more complex. The reason for this simplification is that it enables finding analytical solutions. It would be possible to include more realistic microstructural models for the bone at this level. However, such models would require numerical approaches for the calculation of the SED and thus will require more CPU time. Since the solutions of the numerical and analytical model based on the cylindrical voids model are very close, this model seems adequate. Second, in our study only the activity of the osteoblast cells was mechano-regulated, while the osteoclast activity was assumed to be not dependent on the mechanical stimulus. However, in the literature it is suggested that the osteocytes control both the osteoblast and osteoclast activities [164, 277]. This choice was made to stay in agreement with the remodeling theory used in earlier numerical studies [132]. It should be noted, however, that it would be straightforward to also make osteoclast activity dependent on the mechanical signal, but in earlier studies this did not lead to large differences in the result [30]. Third, as in these earlier studies, we used strain energy density as the mechanical stimulus, whereas others have proposed other stimuli such as fluid flow and microdamage [11, 51]. However, it was shown earlier that the results of the bone remodeling simulations are not very sensitive to the actual signal chosen [249]. Also, it should be mentioned that the framework developed here would enable analyses of fluid flow as well as microdamage, which take place at much lower levels than that of the bone structure. Fourth, we did not explicitly model

the actual biochemical messenger pathways. Accounting for this in more detail as proposed by others [228, 256] may further improve the simulations. Here also, we would like to emphasize that the framework developed in this investigation would enable accounting for such biochemical interactions. Still, we expect the main results of our study remain unaltered by introduction of the aforementioned further details. Fifth, the osteocyte lacunae microporosity was not included in the present formulation since it is assumed that the mechanical stimulus sensed by the osteocytes is the strain energy density in the extracellular matrix. The multi-step homogenization scheme based on micromechanics and adopted in this study, however, enables the inclusion of as many phases as required and could also represent the porosity of the lacunar-canalicular network. For example, lacunar porosity was considered in multiscale models for bone strength [92] as well as for fast and slow wave propagation and attenuation through the hierarchical lacunar-vascular pore system in bone [210]. Our present choice to take, as mechanical stimulus, the strain energy density in the extravascular bone matrix, is consistent with our approach to let the cells always deposit bone matrix of the same quality, i.e. with a constant osteocyte density (or lacunar porosity) per volume element of extravascular bone matrix. Interestingly, such a constant lacunar porosity across bone matrices of different ages or species actually suggests itself when one compares scanning electron micrographs from different anatomical sites [28, 270]. Accordingly, when keeping the aforementioned idea of a constant "working mode" of the osteoblastic cells, then the additional explicit introduction of the lacunar-canalicular network would not alter any of our results. This is why we did not implement them for the scope and the contents of the present study. Coincidently, this choice has been also made in a recent multiscale systems biology-micromechanics approach [256]. However, extension of the model to the lacunar-canalicular network along the micromechanical lines sketched further above does make a lot of sense if one also wishes to test the effect of using alternative hypotheses for load adaptive bone remodeling at lower scales, e.g. fluid-flow and microdamage, on the density distribution at the organ level. Finally, although our discussion was mainly focusing on trabecular bone, the analytical approach can be straightforwardly applied to cortical bone. Actually, the micromechanical representation depicted in Fig. 5.2 also holds for the latter, as was evidenced by various studies reporting satisfactory agreement between respective model predictions and corresponding experimental results [108, 111, 117].

5.5 CONCLUSIONS

The multiscale analytical model developed in this study for the simulation of bone remodeling relates the effects of structural changes at the nanometer level to changes in bone density at higher levels. Such an analytical formulation includes

the feedback from the osteoclast/osteoblast activity and includes influences from mechanical stimuli and surface area available for remodeling. Furthermore, the multiscale analytical model allows for 1) coupling dynamic loading variables at the time scale of seconds to the adaptive processes at the scale of year; 2) for simultaneously exploring the effects of mechanobiological and geometric stimuli relating local loading conditions in the bone matrix to bone cells involved in bone remodeling; 3) for taking into account of variations of collagen volume fraction that affects the stiffness of bone matrix linking the above mentioned scales (tissue and cell levels) to the third mineralized collagen level (100-50 nm). To the knowledge of the authors, it is the first time that in the literature such a novelty is found. The proposed model provides new insights on how mechanical properties and structures of bone at the organ level are affected by the mechanical properties and hierarchical structural levels at lower scales in both healthy and pathological conditions. Moreover, since our model's CPU demands are also dramatically, i.e. by the factor of one million, decreased as compared to conventional approaches in the field, it also holds the promise to provide an accurate and efficient tool for large scale simulating patient-specific bone remodeling simulations in a clinical everyday setting, in particular for organs such as the hip or spine, where an accurate assessment of bone micro-architecture is not possible. In such analyses, the effect of macroscopic load transfer mechanisms, such as reduced trabecular load level due to the existence of thickening cortical shells, could be studied as well, in addition to the microscopic load transfer mechanism focused on this paper.

5.6 APPENDIX

A_{BM} - Strain concentration tensor

$$A_{1111}^{BM} = \frac{C_{1122}(C_{1122} - 2k_{Fat})(\phi - 1) + C_{1111}^2(1 + 2\phi) + C_{1111}(2k_{Fat}(1 + \phi) - C_{1122}\phi)}{(C_{1111} + C_{1122} + 3C_{1111}\phi - C_{1122}\phi)(C_{1122} - 2k_{Fat})(\phi - 1) + C_{1111}(1 + \phi)}$$
(5.23)

$$A_{1122}^{BM} = \frac{C_{1111}(C_{1111} - 3C_{1122} + 4k_{Fat})\phi}{(C_{1111} + C_{1122} + 3C_{1111}\phi - C_{1122}\phi)(C_{1122} - 2k_{Fat})(\phi - 1) + C_{1111}(1 + \phi)}$$
(5.24)

$$A_{1133}^{BM} = \frac{k_{Fat} - C_{1133})\phi}{(C_{1122} - 2k_{Fat})(\phi - 1) + C_{1111}(1 + \phi)}$$
(5.25)

$$A_{2211}^{BM} = A_{1122}^{BM}$$
(5.26)

$$A_{2222}^{BM} = A_{1111}^{BM} \tag{5.27}$$

$$A_{2233}^{BM} = A_{1133}^{BM} \tag{5.28}$$

$$A_{3311}^{BM} = A_{3322}^{BM} = 0 \tag{5.29}$$

$$A_{3333}^{BM} = 1 \tag{5.30}$$

ACKNOWLEDGMENTS

NOMENCLATURE

Variables
$\mathbb{A}$ fourth order concentration tensor
A_{ijkl} concentration tensor component
BS bone surface
BV bone volume
$\mathbb{C}$ stiffness tensor
C_{ijkl} stiffness tensor component
e_I, e_{II}, e_{III} principal direction
E macroscopic strain
E_i Young's modulus in direction i
f volume fraction
$\mathbb{I}$ fourth order identity tensor
$\mathbb{J}$ volumetric part of the identity tensor
J_{ijkl} component of the volumetric part of the identity tensor
k bulk modulus
l experimentally measured length
L geometric length
$\mathbb{P}$ fourth order Hill tensor
P_{ijkl} hill tensor component
t time
TV total volume
WF weight fraction

x bone surface location
α fraction of the bone specific surface available for the cellular activities
δ_{ij} Kronecker delta
ε microscopic strain
μ osteocyte mechanosensitivity
ρ mass density
σ microscopic stress tensor
Σ macroscopic stress tensor
Σ_{ii} macroscopic stress tensor component in principal direction i
τ bone formation time constant
ϕ porosity
ψ microscopic strain energy density

Subscripts
ash ... in ashed bone
BM ... of bone matrix
col ... of collagen
cyl ... accounting for cylindrical inclusions
Fat ... of fat
HA ... of hydroxyapatite
H_2O ... of water
OBL ... of osteoblasts
OCL ... of osteoclasts
org ... of organic matter
P ... of pores

Superscripts
$adult$ ... for an adult patient
BM ... in the bone matrix
dry ... dried
$*$ ... apparent

6

CONCLUSION AND OUTLOOK

The clinical need for information and prediction in order to adopt "softer" methods for the patients, drives the field of biomechanics to better understand, by means of non-invasive techniques -such as Computed Tomography-, the biochemical composition and the microstructure of bone.

The use of imaging techniques having different resolutions allows one to look into different aspects of the bone material. The use of microCT *ex vivo* yields the direct assessment of the bone matrix composition, and makes possible to measure mineralization grade or collagen content, and opens up the investigation of diseases affecting the bone matrix.

The development of the clinical applications on the other side, although presenting lower resolution images, is interesting so as to assess of the patient-specificity of the measurement. This is of particular importance to understand the mechanical changes endured by the skeleton. As outlined by the results of Chapter 4, the heterogeneity in bone density resulting from the natural bone remodeling process, here in the spine of a young patient, is a very important aspect to consider. The combination of the research work presented in Chapter 5, with the results of the patient-specific composition maps of Chapter 4 could, in the future, open new areas of research, particularly in the validation of bone remodeling algorithms. The clinical problems which could take profit of this research are as broad as low pack pain, induced by the deformation of the bones and further of the intervertebral discs, as well as diseases consisting in the disturbance of the bone remodeling, such as osteoporosis.

Furthermore, the novel combination of microstructural analysis and mechanical properties applied to a ceramic biomaterial is in line with the extensive research done on biocompatible materials, aiming to appropriately replace bone or induce regeneration of bone.

BIBLIOGRAPHY

[1] http://www.nist.gov/pml/data/xraycoef/index.cfm/.

[2] Chapter 2 gross and elemental content of reference man. Annals of the ICRP/ICRP Publication, 23(0):273–334, 1975. Report of the Task Group on Reference Man.

[3] Dassault Systèmes ABAQUS, Inc. Analysis User's Manual version 6.10. 2010.

[4] J.C. Adams. The Fortran 2003 handbook: The complete syntax, features and procedures. 2009.

[5] M. Akao, H. Aoki, and K. Kato. Mechanical properties of sintered hydroxyapatite for prosthetic applications. Journal of Materials Science, 16:809 – 812, 1981.

[6] O. Akkus, A. Polyakova-Akkus, F. Adar, and M.B. Schaffler. Aging of microstructural compartments in human compact bone. Journal of Bone and Mineral Research, 18(6):1012 – 1019, 2003.

[7] M. A. Ali and B. Singh. The effect of porosity on the properties of glass fibre-reinforced gypsum plaster. Journal of Materials Science, 10(11):1920–1928, 1975.

[8] U. Andreaus, M. Colloca, and D. Iacoviello. An optimal control procedure for bone adaptation under mechanical stimulus. Control Engineering Practice, 20(6):575–583, 2012.

[9] I.H. Arita, D.S. Wilkinson, M.A. Mondragón, and V.M. Castaño. Chemistry and sintering behaviour of thin hydroxyapatite ceramics with controlled porosity. Biomaterials, 16:403–408, 1995.

[10] K. Arvidson, B.M. Abdallah, L. Applegate, N. Baldini, E. Cenni, E. Gomez-Barrena, D. Granchi, M. Kassem, Y.T. Konttinen, K. Mustafa, D.P. Pioletti, T. Sillat, and A. Finne-Wistrand. Bone regeneration and stem cells. Journal of Cellular and Molecular Medicine, 15(4):718–46, 2011.

[11] M. Azami, A. Samadikuchaksaraei, and S.A. Poursamar. Synthesis and characterization of a laminated hydroxyapatite/gelatin nanocomposite scaffold

with controlled pore structure for bone tissue engineering. International Journal of Artificial Organs, 33(2):86–95, 2010.

[12] V. Baca, Z. Horak, P. Mikulenka, and V. Dzupa. Comparison of an inhomogeneous orthotropic and isotropic material models used for FE analyses. Medical Engineering & Physics, 30:924–930, 2008.

[13] P.B. Badel and J.B. Leblond. A note on integration schemes for the microplane model of the mechanical behaviour of concrete. Communications in Numerical Methods in Engineering, 20(1):75–81, 2004.

[14] Y. Benveniste. A new approach to the application of Mori-Tanaka's theory in composite materials. Mechanics of Material, 6(2):147–157, 1987.

[15] I. Bergman and R. Loxley. Two Improved and Simplified Methods for the Spectrophotometric Determination of Hydroxyproline. Analytical Chemistry, 35(12):1961–1965, 1963.

[16] R. Bhowmik, K. Katti, and D.R. Katti. Mechanics of molecular collagen is influenced by hydroxyapatite in natirual bone. Journal of Materials Science, 42:8824 – 8837, 2007.

[17] R. Bhowmik, K.S. Katti, and D.R. Katti. Mechanisms of load-deformation behavior of molecular collagen in hydroxyapatite-tropocollagen molecular system: steered molecular dynamics study. Journal of Engineering Mechanics, 135(5):413–421, 2009.

[18] R.M. Biltz and E.D. Pellegrino. The chemical anatomy of bone. Journal of Bone and Joint Surgery, 51-A(3):456 – 466, 1969.

[19] D.M. Black, M. Steinbuch, L. Palermo, P. Dargent-Molina, R. Lindsay, M.S. Hoseyni, and O. Johnell. An assessment tool for predicting fracture risk in postmenopausal women. Osteoporosis International, 12(7):519–528, 2001.

[20] R. Blanchard, A. Dejaco, E. Bongaers, and C. Hellmich. Intravoxel bone micromechanics for microct-based finite element simulations. Journal of Biomechanics, 46(15):2710–2721, 2013.

[21] R. Blanchard, A. Malandrino, Z. Sant, and C. Hellmich. Patient-specific fracture risk assessment of vertebrae. part I: Hierarchical intravoxel X-ray physics for CT grey value to bone composition conversion. Journal of Biomechanical Engineering, 2014. submitted.

[22] N. Bohr. I. On the constitution of atoms and molecules. Philosophical Magazine Series 6, 26(151):1–25, 1913.

[23] G. Boivin and P.J. Meunier. The degree of mineralization of bone tissue measured by computerized quantitative contact microradiography. Calcified Tissue International, 70:503 – 511, 2002.

[24] L. Bonar, S. Lees, and H. Mook. Neutron diffraction studies of collagen in fully mineralized bone. Journal of Molecular Biology, 181:265–270, 1985.

[25] J.M. Boone. Handbook of Medical Imaging, volume 3, chapter X-ray production, interaction, and detection in diagnostic imaging.

[26] E. Bossy, M. Talmant, F. Peyrin, L. Akrout, P. Cloetens, and P. Laugier. In in vitro study of the ultrasonic axial transmission technique at the radius: 1 MHz velocity measurements are sensitive to both mineralization and introcortical porosity. Journal of Bone and Mineral Research, 19(9):1548 – 1556, 2004.

[27] R.A. Brooks and G. Di Chiro. Beam hardening in X-ray reconstructive tomography. Physics in Medicine and Biology, 21(3):390–398, 1976.

[28] J.A. Buckwalter, M.J. Glimcher, R.R. Cooper, and R. Recker. Bone biology, Part I: Structure, blood supply, cells, matrix, and mineralization. The Journal of Bone and Joint Surgery, 77-A(8):1256 – 1275, 1995.

[29] P.R. Buenzli, P. Pivonka, B.S. Gardiner, and D.W. Smith. Modelling the anabolic response of bone using a cell population model. Journal of Theoretical Biology, 307:42 – 52, 2012.

[30] E.H. Burger and J. Klein-Nulend. Mechanotransduction in bone-role of the lacuno-canalicular network. FASEB Journal, 13:101–112, 1999.

[31] D. Bürklein, E. Lochmüller, V. Kuhn, J. Grimm, R. Barkmann, R. Müller, and F. Eckstein. Correlation of thoracic and lumbar vertebral failure loads with in situ vs. ex situ dual energy X-ray absorptiometry. Journal of Biomechanics, 34(5):579–87, 2001.

[32] C. M. Burns. XCIV. The effect of the continued ingestion of mineral acid on growth of body and bone and on the composition of bone and of the soft tissues. Biochemical Journal, 23(5):860 – 867, 1929.

[33] A.H. Burstein, J.D. Currey, V.H. Frankel, and D.T. Reilly. The ultimate properties of bone tissue: the effects of yielding. Journal of Biomechanics, 5:35–44, 1972.

[34] A.H. Burstein, D.T. Reilly, and M. Martens. Aging of bone tissue: mechanical properties. The Journal of Bone and Joint Surgery. American volume, 58:82–86, 1976.

[35] A.H. Burstein, J.M. Zika, K.G. Heiple, and L. Klein. Contribution of collagen and mineral to the elastic-plastic properties of bone. The Journal of Bone and Joint Surgery. American volume, 57:956–961, 1975.

[36] R. Cancedda, A. Cedola, A. Giuliani, V. Komlev, S. Lagomarsino, M. Mastro-giacomo, F. Peyrin, and F Rustichelli. Bulk and interface investigations of scaffolds and tissue-engineered bones by X-ray microtomography and X-ray microdiffraction. Biomaterials, 28:2505 – 2524, 2007.

[37] J. Catanese, E.P. Iverson, R.K. Ng, and T.M. Keaveny. Heterogeneity of the mechanical properties of demineralized bone. Journal of Biomechanics, 32:1365 – 1369, 1999.

[38] A. Cedola, M. Mastrogiacomo, S. Lagomarsino, R. Cancedda, C. Giannini, A. Guagliardi, M. Ladisa, M. Burghammer, F. Rustichelli, and V. Komlev. Orientation of mineral crystals by collagen fibres during in vivo bone en-gineering: an X-ray diffraction imaging study. Spectrochimica Acta Part B, 62:642 – 647, 2007.

[39] H. Cezayirlioglu, E. Bahniuk, D.T. Davy, and K.G. Heiple. Anisotropic yield behavior of bone under combined axial force and tension. Journal of Biomechanics, 18(1):61 – 69, 1985.

[40] E. Charrière, S. Terrazzoni, C. Pittet, Ph Mordasini, M. Dutoit, J. Lemaître, and Ph Zysset. Mechanical characterization of brushite and hydroxyapatite cements. Biomaterials, 22:2937–2945, 2001.

[41] Q. Chen, F. Baino, S. Spriano, N.M. Pugno, and C. Vitale-Brovarone. Mod-elling of the strength-porosity relationship in glass-ceramic foam scaffolds for bone repair. Journal of the European Ceramic Society, 2014. Article in Press.

[42] X. Cheng, P. Nicholson, S. Boonen, G. Lowet, P. Brys, J. Aerssens, G. van der Perre, and J. Dequeker. Prediction of vertebral strength in vitro by spinal bone densitometry and calcaneal ultrasound. Journal of Bone and Mineral Research, 12(10):1721–1728, 1997.

[43] T. Chevalley, J. Bonjour, B. van Rietbergen, R. Rizzoli, and S. Ferrari. Frac-tures in healthy females followed from childhood to early adulthood are as-sociated with later menarcheal age and with impaired bone microstructure at peak bone mass. Journal of Clininical Endocrinology and Metabolism, 97:4174–4181, 2012.

[44] H. Chick, V. Korenchevsky, and M. Roscoe. LXXXIII. The difference in chem-ical composition of the skeletons of young rats fed (1) on diets deprived of

fat-soluble vitamins and (2) on a low phosphorus rachitic diet, compared with those of normally nourished animals of same age. Biochemical Journal, 20(3):621–631, 1926.

[45] P. Christen, K. Ito, R. Mueller, M.R. Rubin, D.W. Dempster, J.P. Bilezikian, and B. van Rietbergen. Patient-specific bone modelling and remodelling simulation of hypoparathyroidism based on human iliac crest biopsies. Journal of Biomechanics, 45:2411–2416, 2012.

[46] D.L. Christiansen, E.K. Huang, and F.H. Silver. Assembly of type I collagen: fusion of fibril subunits and the influence of fibril diameter on mechanical properties. Matrix Biology, 19:409–420, 2000.

[47] J. Clausen, L. Damkilde, and L. Andersen. Efficient return algorithms for associated plasticity with multiple yield planes. International Journal for Numerical Methods in Engineering, 66(6):1036–1059, 2006.

[48] R.L. Coble and W.D. Kingery. Effect of porosity on physical properties of sintered alumina. Journal of the American Ceramic Society, 39(11):377–385, 1956.

[49] D.D. Cody, G.J. Gorss, F.J. Hou, H.J. Spencer, S.A. Goldstein, and D.P. Fyhrie. Femoral strength is better predicted by finite element models than QCT and DXA. Journal of Biomechanics, 32:1013 – 1020, 1999.

[50] P.G. Coelho, P. Rui Fernandes, and H. Carrio Rodrigues. Multiscale modeling of bone tissue with surface and permeability control. Journal of Biomechanics, 44(2):321–329, 2011.

[51] A. Çolak. Physical and mechanical properties of polymer-plaster composites. Materials Letters, 60(16):1977–1982, 2006.

[52] M. Colloca, R. Blanchard, C. Hellmich, K. Ito, and B. van Rietbergen. Evolution of bone volume fraction in bone remodeling: a multiscale analytical investigation. In Proceedings of the 11th International Symposium on Computer Methods in Biomechanics and Biomedical Engineering. Taylor & Francis Group, 2013.

[53] M. Colloca, K. Ito, and B. van Rietbergen. An analytical approach to investigate the evolution of bone volume fraction in bone remodeling simulation at the tissue and cell level. Journal of Biomechanical Engineering, 136(3):, 2014.

[54] M. Colloca, B. van Rietbergen, R. Blanchard, C. Hellmich, and K. Ito. From cell level to organ level: a multiscale approach for bone remodeling simulation. Journal of Biomechanics, 45:470, 2012.

[55] A. Compton. The scattering of X-rays. Journal of the Franklin Institute, 198(1):57 – 72, 1924.

[56] A. Cong, J.O. Den Buijs, and D. Dragomir-Daescu. In situ parameter identification of optimal density–elastic modulus relationships in subject-specific finite element models of the proximal femur. Medical Engineering & Physics, 33(2):164 – 173, 2011.

[57] B. Couteau, M.-C. Hobatho, R. Darmana, J.-C. Brignola, and J.-Y. Arlaud. Finite element modeling of the vibrational behavior of the human femur using CT-based individualized geometrical and material properties. Journal of Biomechanics, 31:383 – 386, 1998.

[58] S.C. Cowin. Remarks on the paper entitled 'Fabric and elastic principal directions of cancellous bone are closely related'. Journal of Biomechanics, 30(11/12):1191–1192, 1997.

[59] S.C. Cowin. Remarks on the paper entitled 'fabric and elastic principal directions of cancellous bone are closely related'. Journal of Biomechanics, 30(11/12):1191–1192, 1997.

[60] S.C. Cowin, L. Moss-Salentijn, and Moss M.L. Candidates for the mechanosensory system in bone. Journal of Biomechanical Engineering, 113:191–197, 1991.

[61] F. Craciun, C. Galassi, E. Roncari, A. Filippi, and G. Guidarelli. Electroelastic properties of porous piezoelectric ceramics obtained by tape casting. Ferroelectrics, 205(1):49–67, 1998.

[62] R. P. Crawford, C. E. Cann, and T. M. Keaveny. Finite element models predict in vitro vertebral body compressive strength better than quantitative computed tomography. Bone, 33(4):744–750, 2003.

[63] E.O. Crawley, W.D. Evans, and G. M. Owen. A theoretical analysis of the accuracy of single-energy CT bone measurements. Physics in Medicine and Biology, 33(10):1113–1127, 1988.

[64] L. Cristofolini, M. Juszczyk, S. Martelli, F. Taddei, and M. Viceconti. In vitro replication of spontaneous fractures of the proximal human femur. Journal of Biomechanics, 12, 2007.

[65] J. Currey. Changes in the impact energy absorption of bone with age. Journal of Biomechanics, 12:459–469, 1979.

[66] J. Currey. What determines the bending strength of compact bone? Journal of Experimental Biology, 202(18):2495–2503, 1999.

[67] J. D. Currey. Physical characteristics affecting the tensile failure properties of compact bone. Journal of Biomechanics, 23:837–844, 1990.

[68] J.D Currey. Differences in the tensile strength of bone of different histological types. Journal of Anatomy, 93, 1959.

[69] J.D. Currey. The effects of strain rate, reconstruction and mineral content on some mechanical properties of bovine bone. Journal of Biomechanics, 8:81–86, 1975.

[70] J.D Currey. Tensile yield in compact bone is determined by strain, post-yield behaviour by mineral content. Journal of Biomechanics, 37(4):549–56, 2004.

[71] J.D. Currey. The structure and mechanics of bone. Journal of Materials Science, 47:41–54, 2012.

[72] C. De Pollak, E. Arnaud, D. Renier, and P.J. Marie. Age related changes in bone formation, osteoblastic cell proliferation, and differentiation during postnatal osteogenesis in human calvaria. Journal of Cellular Biochemistry, 64(1):128–139, 1997.

[73] G. De With, H. van Dijk, N. Hattu, and K. Prijs. Preparation, microstructure and mechanical properties of dense polycrystalline hydroxyapatite. Journal of Materials Science, 1981.

[74] A. Dejaco, V.S. Komlev, J.Jaroszewicz, W. Swieszkowski, and Ch. Hellmich. Micro CT-based multiscale elasticity of double-porous (pre-cracked) hydroxyapatite granules for regenerative medicine. Journal of Biomechanics, 45(6):1068 – 1075, 2012.

[75] A. Diaz. Characterisation of porous silicon nitride materials produced with starch. Journal of the European Ceramic Society, 24(2):413 – 419, 2004. 8th International Conference on Ceramic Processing.

[76] R.P. Dickenson, W.C. Hutton, and J.R. Stott. The mechanical properties of bone in osteoporosis. The Journal of Bone and Joint Surgery. British volume, 63-B:233–238, 1981.

[77] E. N. Ebbesen, J. S. Thomsen, H. Beck-Nielsen, H. J. Nepper-Rasmussen, and Li Mosekilde. Lumbar vertebral body compressive strength evaluated by dual-energy X-ray absorptiometry, quantitative computed tomography, and ashing. Bone, 25:713–724, 1999.

[78] E.N. Ebbesen, J.S. Thomsen, H. Beck-Nielsen, H.J. Nepper-Rasmussen, and L. Mosekilde. Vertebral bone density evaluated by dual-energy X-ray absorptiometry and quantitative computed tomography in vitro. Bone, 23(3):283–90, 1998.

[79] L. Eberhardsteiner, C. Hellmich, and S. Scheiner. Layered water in crystal interfaces as source for bone viscoelasticity: Arguments from a multiscale approach. Computer Methods in Biomechanics and Biomedical Engineering, 17(1):48–63, 2014.

[80] F. Eckstein, D. Burstein, and T.M. Link. Quantitative MRI of cartilage and bone: degenerative changes in osteoarthritis. NMR in Biomedicine, 19:822–854, 2006.

[81] A. Einstein. Über einen die Erzeugung und Verwandlung des Lichtes betreffenden heuristischen Gesichtspunkt. Annalen der Physik, 322(6):132–148, 1905.

[82] E.F. Eriksen and M. Kassem. The cellular basis of bone remodeling. Triangle, 31:45–57, 1992.

[83] J. Eshelby. The determination of the elastic field of an ellipsoidal inclusion, and related problems. Proceedings of the Royal Society of London. Serie A, Mathematical and Physical Sciences, 241(1226):376–396, 1957.

[84] F.G. Evans and M. Lebow. The strength of human compact bone as revealed by engineering technics. American Journal of Surgery, 83(3):326–31, 1952.

[85] C. Falcinelli, E. Schileo, L. Balistreri, F. Baruffaldi, B. Bordini, M. Viceconti, U. Albisinni, F. Ceccarelli, L. Milandri, A. Toni, and F. Taddei. Multiple loading conditions analysis can improve the association between finite element bone strength estimates and proximal femur fractures: A preliminary study in elderly women. Bone, 67:71–80, 2014.

[86] N.L. Fazzalari, J.S. Kuliwaba, and M.R. Forwood. Cancellous bone microdamage in the proximal femur: influence of age and osteoarthritis on damage morphology and regional distribution. Bone, 31(6):697–702, 2002.

[87] L. Feng and I. Jasiuk. Multi-scale characterization of swine femoral cortical bone. Journal of Biomechanics, 44:313 – 320, 2011.

[88] J. W. Fenner, B. Brook, G. Clapworthy, P. V. Coveney, V. Feipel, H. Gregersen, D. R. Hose, P. Kohl, P. Lawford, K. M. McCormack, D. Pinney, S. R. Thomas, S. Van Sint Jan, S. Waters, and M. Viceconti. The EuroPhysiome, STEP and a roadmap for the virtual physiological human. Philosophical Transactions of the Royal Society A-Mathematical Physical and Engineering Sciences, 366(1878):2979–2999, 2008.

[89] A. Fritsch, L. Dormieux, and Ch. Hellmich. Porous polycrystals built up by uniformly and axisymmetrically oriented needles: Homogenization of elastic properties. Comptes Rendus Mécanique, 334:151 – 157, 2006.

[90] A. Fritsch, L. Dormieux, Ch. Hellmich, and J. Sanahuja. Micromechanics of crystal interfaces in polycrystalline solid phases of porous media: fundamentals and application to strength of hydroxayapatite biomaterials. Journal of Materials Science, 42:8824 – 8837, 2007.

[91] A. Fritsch, L. Dormieux, Ch. Hellmich, and J. Sanahuja. Experimentally validated micromechanical model for elasticity and strength of hydroxyapatite biomaterials, page 17. Technische Universität Wien, 2008.

[92] A. Fritsch, L. Dormieux, Ch. Hellmich, and J. Sanahuja. Mechanical behaviour of hydroxyapatite biomaterials: An experimentally validated micromechanical model for elasticity and strength. Journal of Biomedical Materials Research, 88A:149 – 161, 2009.

[93] A. Fritsch, C. Hellmich, and L. Dormieux. The role of disc-type crystal shape for micromechanical predictions of elasticity and strength of hydroxyapatite biomaterials. Philosophical Transactions of the Royal Society A: Mathematical, Physical and Engineering Sciences, 368(1917):1913–1935, 2010.

[94] A. Fritsch, C. Hellmich, and P. Young. Micromechanics-derived scaling relations for poroelasticity and strength of brittle porous polycrystals. Journal of Applied Mechanics, 80(2), 2013.

[95] A. Fritsch and Ch. Hellmich. 'Universal' microstructural patterns in cortical and trabecular, extracellular and extravacular bone materials: Micromechanics-based prediction of anisotropic elasticity. Journal of Theoretical Biology, 244:597 – 620, 2007.

[96] A. Fritsch, Ch. Hellmich, and L. Dormieux. Ductile sliding between mineral crystals followed by rupture of collagen crosslinks: experimentally supported micromechanical explanation of bone strength. Journal of Theoretical Biology, 260:230 – 252, 2009.

[97] H.M. Frost. The laws of bone structure. Thomas, Springfield, Illinois, USA, 1964.

[98] H.M Frost. Bone "mass" and the "mechanostat": A proposal. The Anatomical Record, 219(1):1–9, 1987.

[99] D.P. Fyhrie and M.B. Schaffler. The adaptation of bone apparent density to applied bone. Journal of Biomechanics, 28(2):135 – 146, 1995.

Bibliography

[100] C.J. Gatt, T.M. Hosea, R.C. Palumbo, and J.P. Zawadsky. Impact loading of the lumbar spine during football blocking. American Journal of Sports Medicine, 25(3):317–321, 1997.

[101] O. Gauthier, R. M'uller, D. Von Stechow, B. Lamy, P. Weiss, J. . Bouler, E. Aguado, and G. Daculsi. In vivo bone regeneration with injectable calcium phosphate biomaterial: A three-dimensional micro-computed tomographic, biomechanical and SEM study. Biomaterials, 26(27):5444–5453, 2005.

[102] A. Gautieri, M.J. Buehler, and A. Redaelli. Deformation rate controls elasticity and unfolding pathways of single tropocollagen molecules. Journal of the Mechanical Behavior of Biomedical Materials, 2:130–137, 2009.

[103] E. Gentleman, A.N. Lay, D.A. Dickerson, E.A. Neuman, G.A. Livesay, and K.C. Dee. Mechanical characterization of collagen fibers and scaffolds for tissue engineering. Biomaterials, 24:3805–3813, 2003.

[104] A. Giuliani, A. Manescu, M. Langer, F. Rustichelli, V. Desiderio, F. Paino, A. De Rosa, L. Laino, R. D'Aquino, and V. Tirino. Three years after transplants in human mandibles, histological and in-line holotomography revealed that stem cells regenerated a compact rather than a spongy bone: Biological and clinical implications. Stem Cells Translational Medicine, 2(4):316–324, 2013.

[105] J.K. Gong, J.S. Arnold, and H. Cohn, S. The density of organic and volatile and non-volatile inorganic components of the bone. The Anatomical Record, 149:319 – 324, 1964.

[106] J.K. Gong, J.S. Arnold, and S.H. Cohn. Composition of trabecular and cortical bone. The Anatomical Record, 149(3):325–332, 1964.

[107] R.W. Goulet, S.A. Goldstein, M.J. Ciarelli, J.L. Kuhn, M.B. Brown, and L.A. Feldkamp. The relationship between the structural and orthogonal compressive properties of trabecular bone. Journal of Biomechanics, 27(4):375 – 389, 1994.

[108] M. Granke, Q. Grimal, A. Saied, P. Nauleau, F. Peyrin, and P. Laugier. Change in porosity is the major determinant of the variation of cortical bone elasticity at the millimeter scale in aged women. Bone, 49:1020–1026, 2011.

[109] V. A. D. Grosso and C. W. Mader. Speed of sound in pure water. Journal of the Acoustical Society of America, 52(5B):14421446, 1972.

[110] R. Hambli, H. Katerchi, and C.L. Benhamou. Multiscale methodology for bone remodelling simulation using coupled finite element and neural network computation. Biomechanics and Modeling in Mechanobiology, 10(1):133–145, 2011.

[111] E. Hamed, Y. Lee, and I. Jasiuk. Multiscale modeling of elastic properties of cortical bone. Acta Mechanica, 213:131–154, 2010.

[112] F. S. Hammett. A biochemical study of bone growth. I. Changes in the ash, organic matter and water during growth (mus norvegicus albinus). The Journal of Biological Chemistry, 64:409 – 428, 1925.

[113] F.S. Hammett. Studies of the thyroid apparatus: XIV. The growth of the humerus and femur of male and female albino rats thyro-parathyroidectomized and parathyroidectomized when 100 days of age. The Journal of Experimental Zoology, 39(3):465–504, 1924.

[114] K. Hasegawa, Y. Hasegawa, and A. Nagano. Estimation of bone mineral density and architectural parameters of the distal radius in hemodialysis patients using peripheral quantitative computed tomography. Journal of Biomechanics, 37(5):751–756, 2004.

[115] Z. Hashin. Analysis of composite materials – a survey. Journal of Applied Mechanics (ASME), 50(3):481–503, 1983.

[116] W. Heitler. The Quantum Theory of Radiation, chapter Radiation process in first approximation, page 242. third edition edition, 1984.

[117] C. Hellmich, F. . Ulm, and L. Dormieux. Can the diverse elastic properties of trabecular and cortical bone be attributed to only a few tissue-independent phase properties and their interactions? arguments from a multiscale approach. Biomechanics and Modeling in Mechanobiology, 2(4):219–238, 2004.

[118] Ch. Hellmich. Microelasticity of bone. 480:289 – 332, 2005.

[119] Ch. Hellmich, J.-F. Barthélémy, and L. Dormieux. Mineral-collagen interactions in elasticity of bone ultrastructure – a continuum micromechanics approach. European Journal of Mechanics A-Solids, 23:783 – 810, 2004.

[120] Ch. Hellmich, C. Kober, and B. Erdmann. Micromechanics-based conversion of CT data into anisotropic elasticity tensors, applied to FE simulations of a mandible. Annals of Biomedical Engineering, 36(1):108 – 122, 2008.

[121] Ch. Hellmich, H.W. Müllner, and Ch. Kohlhauser. Mechanical (triaxial) tests on biological materials and biomaterials. Technical Report DNRT3-1.2-3, Network of excellence 'Knowledge-based Multicomponent Materials

for Durable and Safe Performance –KMM-NoE', sponsored by the European Commission, October 2006.

[122] A. Hershey. The elasticity of an isotropic aggregate of anisotropic cubic crystals. Journal of Applied Mechanics (ASME), 21:236 – 240, 1954.

[123] R. Hill. Elastic properties of reinfored solids: some theoretical principles. Journal of the Mechanics and Physics of Solids, 11:357 – 362, 1963.

[124] S.T. Ho and D.W. Hutmacher. A comparison of micro CT with other techniques used in the characterization of scaffolds. Biomaterials, 27(8).

[125] A.J. Hodge and J.A. Petruska. Recent studies with the electron microscope on ordered aggregates of the tropocollagen molecule. Academic Press, London and New York, 1963.

[126] C. E. Hoffler, K. E. Moore, K. Kozloff, P. K. Zysset, and S. A. Goldstein. Age, gender, and bone lamellae elastic moduli. Journal of Orthopaedic Research, 18:432–437, 2000.

[127] J. Hsieh. Computed Tomography: principles, design, artifacts, and recent advances. second edition edition, 2009.

[128] S. Huang, Z. Li, Z. Chen, Q. Chen, and N. Pugno. Study on the elastic-plastic behavior of a porous hierarchical bioscaffold used for bone regeneration. Materials Letters, 112:43–46, 2013.

[129] J.H. Hubbel. Photon mass attenuation and energy-absorption coefficients. The International Journal of Applied Radiation and Isotopes, 33(11):1269 – 1290, 1982.

[130] J.H. Hubbel and S.M. Seltzer. Tables of X-ray mass attenuation coefficients and mass energy-absorption coefficients from 1 keV to 20 MeV for elements Z=1 to 92 and 48 additional substances of dosimetric interest. National Institute of Standards and Technologies, 2011.

[131] T.B. Huff and J.-X. Cheng. In vivo coherent anti-Stokes Raman scattering imaging of sciatic nerve tissue. Journal of Microscopy, 225:175–182, 2007.

[132] R. Huiskes, R. Ruimerman, G.H.v. Lenthe, and J.D. Janssen. Effects of mechanical forces on maintenance and adaptation of form in trabecular bone. Nature, 405:704 – 706, 2000.

[133] P.A. Hulme, S.K. Boyd, and S.J. Ferguson. Regional variation in vertebral bone morphology and its contribution to vertebral fracture strength. Bone, 41:946–957, 2007.

[134] W.C. Hutton, B.M. Cyron, and J.R. Stott. The compressive strength of lumbar vertebrae. Journal of Anatomy, 129(Pt 4):753–8, 1979.

[135] D. F. Jackson and D. J. Hawkes. X-ray attenuation coefficients of elements and mixtures. Physics Reports, 70(3):169–233, 1981.

[136] S. V. N. Jaecques, H. Van Oosterwyck, L. Muraru, T. Van Cleynenbreugel, E. De Smet, M. Wevers, I. Naert, and J. Vander Sloten. Individualised, micro CT-based finite element modelling as a tool for biomechanical analysis related to tissue engineering of bone. Biomaterials, 25(9):1683–1696, 2004.

[137] M. Jaworski, M. Lebiedowski, R.S. Lorenc, and J. Trempe. Ultrasound bone measurement in pediatric subjects. Calcified Tissue International, 56(5):368–371, 1995.

[138] G Jiang, J Luo, P Pollintine, P Dolan, M a Adams, and R Eastell. Vertebral fractures in the elderly may not always be "osteoporotic". Bone, 47(1):111–6, 2010.

[139] Y. Jiang, J. Zhao, E.-Y. Liao, R.-C. Dai, X.-P. Wu, and H.K. Genant. Application of micro-CT assessment of 3-D bone microstructure in preclinical and clinical studies. Journal of Bone and Mineral Metabolism, 23(1):122–131, 2005.

[140] A. Seibert J.M. Boone. An accurate method for computer-generating tungsten anode X-ray spectra from 30 to 140 kV. Medical Physics, 24(11):1661–1670, 1997.

[141] A. C. Jones, C. H. Arns, A. P. Sheppard, D. W. Hutmacher, B. K. Milthorpe, and M. A. Knackstedt. Assessment of bone ingrowth into porous biomaterials using MICRO-CT. Biomaterials, 28(15):2491–2504, 2007.

[142] D.B. Jones, H. Nolte, J-G. Scholbbers, E. Turner, and D. Veltel. Biochemical signal transduction of mechanical strain in osteoblast-like cells. Biomaterials, 12(2):101 – 110, 1991.

[143] J. Jowsey. Studies of haversian systems in man and some animals. Journal of Anatomy, 100(4):857–864, 1966.

[144] A.C. Kak and M. Slaney. Principles of Computerized Tomographic Imaging. 1988.

[145] W. A. Kalender. Computed tomography; fundamentals, system technology, image quality, applications. Publicis-MCD-Verl., Mnchen, 2000.

[146] Y. Kameo, T. Adachi, and M. Hojo. Effects of loading frequency on the functional adaptation of trabeculae predicted by bone remodeling simulation. J Mech Behav Biomed Mater, 4(6):900–908, 2011.

[147] D. Kaspar, W. Seidl, C. Neidlinger-Wilke, A. Beck, L. Claes, and A. Ignatius. Proliferation of human-derived osteoblast-like cells depends on the cycle number and frequency of uniaxial strain. Journal of Biomechanics, 35(7):873 – 880, 2002.

[148] E.P. Katz and S.-T. Li. Structure and function of bone collagen fibrils. Journal of Molecular Biology, 80:1 – 15, 1973.

[149] J.L. Katz and K. Ukraincik. On the anisotropic elastic properties of hydroxyapatite. Journal of Biomechanics, 4:221 – 227, 1971.

[150] M. Kaye and R. P. Kusy. Genetic lineage, bone mass, and physical activity in mice. Bone, 17(2):131–135, 1995.

[151] Brian W. Kernighan and Dennis M. Ritchie. The C Programming Language. Prentice-Hall, 1988.

[152] J.H. Keyak and Y. Falkinstein. Comparison of in situ and in vitro CT scan-based finite element model predictions of proximal femoral fracture load. Medical Engineering and Physics, 25(9):781–787, 2003.

[153] J.H. Keyak, I.Y. Lee, and H.B. Skinner. Correlations between orthogonal mechanical properties and density of trabecular bone: Use of different densitometric measures. Journal of Biomedical Materials Research, 28(11):1329–1336, 1994.

[154] J.H. Keyak, S.A. Rossi, K.A. Jones, and H.B. Skinner. Prediction of femoral fracture load using automated finite element modeling. Journal of Biomechanics, 31(2):125 – 133, 1998.

[155] R. Khanna, D.R. Katti, and K.S. Katti. AFM and nanoindentation studies of bone nodules on chitosan- polygalacturonic acid-hydroxyapatite nanocomposites. CMES - Computer Modeling in Engineering and Sciences, 87(6):530–555, 2012.

[156] R. Khanna, K.S. Katti, and D.R. Katti. Nanomechanics of surface modified nanohydroxyapatite particulates used in biomaterials. Journal of Engineering Mechanics, 135(5):468–478, 2009.

[157] A. Koivukangas, J. Tuukkanen, P. Lehenkari, R. Peura, R. Hannuniemi, K. Kippo, T. Jämsä, and P. Jalovaara. Microstructural properties of bone

in rat vertebra after long-term clodronate treatment. Journal of Bone and Mineral Metabolism, 20:223–227, 2002.

[158] V. Komlev, F. Peyrin, M. Mastrogiacomo, M. Hausard, A. Cedola, F. Rustichelli, A. Papadimitropoulos, and R. Cancedda. Kinetics of *in vivo* bone deposition by bone marrow stromal cells into porous calcium phosphate scaffolds: an X-ray computed microtomography study. Tissue Engineering, 12(12):3449 – 3458, 2006.

[159] V.S. Komlev, M. Mastrogiacomo, R.C. Pereira, F. Peyrin, F. Rustichelli, and R. Cancedda. Biodegradation of porous calcium phosphate scaffolds in an ectopic bone formation model studied by X-ray computed microtomography. European Cells and Materials, 19:136 – 146, 2010.

[160] S.P. Kotha and N. Guzeslu. Modeling the tensile mechanical behavior of bone along the longitudinal direction. Journal of Theoretical Biology, 219:269–279, 2002.

[161] K. Kumar Phani. Young's modulus-porosity relation in gypsum systems. American Ceramic Society Bulletin, 65(12):1584–1586, 1986.

[162] D. Lacroix, A. Chateau, M-P. Ginebra, and J. A. Planell. Micro-finite element models of bone tissue-engineering scaffolds. Biomaterials, 27(30):5326 – 5334, 2006.

[163] T.F Lang, G Guglielmi, C van Kuijk, A De Serio, M Cammisa, and H.K Genant. Measurement of bone mineral density at the spine and proximal femur by volumetric quantitative computed tomography and dual-energy X-ray absorptiometry in elderly women with and without vertebral fractures. Bone, 30(1):247–250, 2002.

[164] E. Lau, S. Al-Dujaili, A. Guenther, D. Liu, L. Wang, and L. You. Effect of low-magnitude, high-frequency vibration on osteocytes in the regulation of osteoclasts. Bone, 46(6):1508–1515, 2010.

[165] N. Laws. The determination of stress and strain concentrations at an ellipsoidal inclusion in an anisotropic material. Journal of Elasticity, 7:91–97, 1977.

[166] S. C. Lee, B. S. Coan, and Mary L. Bouxsein. Tibial ultrasound velocity measured in situ predicts the material properties of tibial cortical bone. Bone, 21:119–125, 1997.

[167] S. Lees. A model for bone hardness. Journal of Biomechanics, 14(8):561 – 567, 1981.

[168] S. Lees. Ultrasonic measurements of deer antler, bovine tibia and tympanic bulla. Journal of Biomechanics, 15(11):867 – 874, 1982.

[169] S. Lees. Water content in type I collagen tissues calculated from the generalized packing model. International Journal of Biological Macromolecules, 8:66 – 72, 1986.

[170] S. Lees. Considerations regarding the structure of the mammalian mineralized osteoid from viewpoint of the generalized packing model. Connective Tissue Research, 16:281 – 303, 1987.

[171] S. Lees. Mineralization of type I collagen. Biophysical Journal, 85:204 – 207, 2003.

[172] S. Lees, J.M. Ahern, and M. Leonard. Parameters influencing the sonic velocity in compact calcified tissues of various species. Journal of the Acoustical Society of America, 74(1):28–33, 1983.

[173] S. Lees, P. Cleary, J.D. Heeley, and E.L. Gariepy. Distribution of sonic plesio-velocity in a compact bone sample. Journal of Acoustic Society of America, 66(3):641– 646, 1979.

[174] S. Lees, P.F. Cleary, J.D. Heeley, and E.L. Gariepy. Distribution of sonic plesio-velocity in a compact bone sample. Journal of the Acoustical Society of America, 66(3):641–646, 1979.

[175] S. Lees and C.L. Davidson. A theory relating sonic velocity to mineral content in bone, pages 179 – 187. 1979.

[176] S. Lees, D. Hanson, and E.A. Page. Some acoustical properties of the otic bones of a fin whale. Journal of the Acoustical Society of America, 99(4):2421 – 2427, 1995.

[177] S. Lees, D. Hanson, E.A. Page, and H.A. Mook. Comparison of dosage-dependent effects of beta-aminopropionitrile, sodium fluoride, and hydro-cortisone on selected physical properties of cortical bone. Journal of Bone and Mineral Research, 9(9):1377 – 1389, 1994.

[178] S. Lees and E.A. Page. A study of some properties of mineralized turkey leg tendon. Connective Tissue Research, 28:263 – 287, 1992.

[179] S. Lees, M. Pineri, and M. Escoubes. A generalized packing model for type I collagen. International Journal of Biological Macromolecules, 6, 1984.

[180] V. Lemaire, F.L. Tobin, L.D. Greller, C.R. Cho, and Suva L.J. Modeling the interactions between osteoblast and osteoclast activities in bone remodeling. Journal of Theoretical Biology, 229(3):293–309, 2004.

[181] S.K.L. Levengood, S.J. Polak, M.J. Poellmann, D.J. Hoelzle, A.J. Maki, S.G. Clark, M.B. Wheeler, and A.J.W. Johnson. The effect of BMP-2 on micro- and macroscale osteointegration of biphasic calcium phosphate scaffolds with multiscale porosity. Acta Biomaterialia, 6(8):3283–3291, 2010.

[182] V.M. Levin. Thermal expansion coefficient of heterogeneous materials. Inzh. Zh. Mekh. Tverd. Tela, 2(1):83–94, 1967.

[183] X.J. Li, W.S.S. Jee, S.Y. Chow, and D.M. Woodbury. Adaptation of cancellous bone to aging and immobilization in the rat: A single photon absorptiometry and histomorphometry study. The Anatomical Record, 227(1):12–24, 1990.

[184] L. Liang, P. Rulis, and W.Y. Ching. Mechanical properties, electronic structure and bonding of α-and β-tricalcium phosphates with surface characterization. Acta Biomaterialia, 6(9):3763–3771, 2010.

[185] E. Linder-Ganz and G. Amit. Mechanical compression-induced pressure sores in rat hindlimb: muscle stiffness, histology, and computational models. Journal of Applied Physiology, 96(6):2034–2049, 2004.

[186] D.-M. Liu. Preparation and characterisation of porous hydroxyapatite bioceramic via a slip-casting route, volume 24, pages 441–446. 1998.

[187] Q. Lv, M. Deng, B.D. Ulery, L.S. Nair, and C.T. Laurencin. Nano-ceramic composite scaffolds for bioreactor-based bone engineering basic research. Clinical Orthopaedics and Related Research, 471(8):2422–2433, 2013.

[188] Q. Lv, L. Nair, and C.T. Laurencin. Fabrication, characterization, and in vitro evaluation of poly(lactic acid glycolic acid)/nano-hydroxyapatite composite microsphere-based scaffolds for bone tissue engineering in rotating bioreactors. Journal of Biomedical Materials Research - Part A, 91(3):679–691, 2009.

[189] J. A. MacNeil and S. K. Boyd. Bone strength at the distal radius can be estimated from high-resolution peripheral quantitative computed tomography and the finite element method. Bone, 42(6):1203–1213, 2008.

[190] A. Malandrino, A. Fritsch, O. Lahayne, K. Kropik, H. Redl, J. Noailly, D. Lacroix, and Ch. Hellmich. Anisotropic tissue elasticity in human lumbar vertebra, by means of a coupled ultrasound-micromechanics approach. Materials Letters, 78:154–158, 2012.

[191] R. I. Martin and P. W. Brown. Mechanical properties of hydroxyapatite formed at physiological temperature. Journal of Materials Science: Materials in Medicine, 6:138–143, 1995.

[192] R.B. Martin. Porosity and specific surface of bone. CRC Critical Reviews in Biomedical Engineering, 10(3):179, 1984.

[193] R.B. Martin and D.B. Burr. Structure, Function, and Adaptation of Compact Bone. Raven Press, New York, NY, USA, 1989.

[194] T. D. Mast. Empirical relationships between acoustic parameters in human soft tissues. Acoustics Research Letters Online, 1(2):37–42, 2000.

[195] M. Mastrogiacomo, V. Komlev, M. Hausard, F. Peyrin, F. Turquier, S. Casari, A. Cedola, F. Rustichelli, and R. Cancedda. Synchroton radiation micro-tomography of bone engineered from bone marrow stromal cells. Tissue Engineering, 10(11/12):1767 – 1774, 2004.

[196] M. Mastrogiacomo, A. Papadimitropoulos, A. Cedola, F. Peyrin, P. Giannoni, S.G. Pearce, M. Alini, C. Giannini, A. Guagliardi, and R. Cancedda. Engineering of bone using bone marrow stromal cells and a silicon-stabilized tricalcium phosphate bioceramic: Evidence for a coupling between bone formation and scaffold resorption. Biomaterials, 28(7):1376–1384, 2007.

[197] MATLAB. version 7.10.0 (R2010a). The MathWorks Inc., Natick, Massachusetts, 2010.

[198] R.J. McBroom, W.C. Hayes, W.T. Edwards, R.P. Goldberg, and A.A. White. Prediction of vertebral body compressive fracture using quantitative computed tomography. The Journal of Bone and Joint Surgery. American volume, 67:1206–1214, 1985.

[199] R.N. McCarthy, L.B. Jeffcott, and R.N. McCartney. Ultrasound speed in equine cortical bone: effects of orientation, density, porosity and temperature. Journal of Biomechanics, 23(11):1139 – 1143, 1990.

[200] K.M. Meek, N.J. Fullwood, P.H. Cooke, G.F. Elliott, D.M. Maurice, A.J. Quantock, R.S. Wall, and C.R. Worthington. Synchrotron X-ray diffraction studies of the cornea, with implications for stromal hydration. Biophysical Journal, 60(2):467–74, 1991.

[201] S. Meille. Étude du comportement mécanique du plâtre pris en relation avec sa microstructure [Study of the mechanical behaviour of gypsum with regards to its microstructure]. PhD thesis, INSA, Lyon, France, 2001.

[202] E. Melan. Zur Plastizität des räumlichen Kontinuums. Ingenieur-Archiv, 9(2):116–126, 1938.

[203] L.J. Melton III, E.J. Atkinson, W.M. O'Fallon, H.W. Wahner, and B.L. Riggs. Long-term fracture prediction by bone mineral assessed at different skeletal sites. Journal of Bone and Mineral Research, 8(10):1227–1233, 1993.

[204] L.J. Melton III, B.L. Riggs, G.H. van Lenthe, S.J. Achenbach, R. Müller, M.L. Bouxsein, S. Amin, E.J. Atkinson, and S. Khosla. Contribution of in vivo structural measurements and load/strength ratios to the determination of forearm fracture risk in postmenopausal women. Journal of Bone and Mineral Research, 22(9):1442–1448, 2007.

[205] C. L. Morgan and M. D. Miller. Basic principles of computed tomography. Baltimore, Md. : University Park Press, 1983.

[206] E.F. Morgan, H.H. Bayraktar, and T.M. Keaveny. Trabecular bone modulus-density relationships depend on anatomic site. Journal of Biomechanics, 36(7):897–904, 2003.

[207] T. Mori and K. Tanaka. Average stress in matrix and average elastic energy of materials with misfitting inclusions. Acta Metallurgica, 21(5):571 − 574, 1973.

[208] C. Morin and C. Hellmich. Mineralization-driven bone tissue evolution follows from fluid-to-solid phase transformations in closed thermodynamic systems. Journal of Theoretical Biology, 335:185–197, 2013.

[209] C. Morin, C. Hellmich, and P. Henits. Fibrillar structure and elasticity of hydrating collagen: A quantitative multiscale approach. Journal of Theoretical Biology, 317:384–393, 2013.

[210] C. Morin and Ch. Hellmich. A multiscale poromicromechanical approach to wave propagation and attenuation in bone. Ultrasonics, 54(5):1251–1269, 2014.

[211] L. Mulder, J.H. Koolstra, J.MJ. den Toonder, and T. MGJ van Eijden. Relationship between tissue stiffness and degree of mineralization of developing trabecular bone. Journal of Biomedical Materials Research, 84A:508–515, 2008.

[212] o. Nalcioglu and R.Y. Lou. Post-reconstruction method for beam hardening in computerised tomography. Physics in Medicine and Biology, 24(2):330–340, 1979.

[213] A.N. Natali, E.L. Carniel, and P.G. Pavan. Investigation of bone inelastic response in interaction phenomena with dental implants. Dental Materials, 24(4):561–569, 2008.

[214] C.M Neu, F Manz, F Rauch, a Merkel, and E Schoenau. Bone densities and bone size at the distal radius in healthy children and adolescents: a study using peripheral quantitative computed tomography. Bone, 28(2):227–232, 2001.

[215] Q. Ni and D. P. Nicolella. The characterization of human cortical bone microdamage by nuclear magnetic resonance. Measurement Science and Technology, 16:659–668, 2005.

[216] K.K. Nishiyama, H.M. Macdonald, S. Moore, T. Fung, S.K. Boyd, and H. McKay. Cortical porosity is higher in boys compared with girls at the distal radius and distal tibia during pubertal growth: an HR-pQCT study. Journal of Bone and Mineral Research, 27(2):273–82, 2012.

[217] S. Nuzzo, M.H. Lafage-Proust, E. Martin-Badosa, G. Boivin, T. Thomas, C. Alexandre, and F. Peyrin. Synchrotron radiation microtomography allows the analysis of three-dimensional microarchitecture and degree of mineralization of human iliac crest biopsy specimens: Effects of etidronate treatment. Journal of Bone and Mineral Research, 17(8):1372–1382, 2002.

[218] W. Pabst, E. Gregorov, and G. Tich. Elasticity of porous ceramicsa critical study of modulusporosity relations. Journal of the European Ceramic Society, 26(7):1085 – 1097, 2006.

[219] W. Pabst, E. Gregorov, G. Tich, and E. Tnov. Effective elastic properties of alumina-zirconia composite ceramics part 4. Tensile modulus of porous alumina and zirconia. Ceramics - Silikaty, 48(4):165–174, 2004.

[220] F. Padilla, F. Peyrin, and P. Laugier. Prediction of backscatter coefficient in trabecular bones using a numerical model of three-dimentional microstructure. Journal of the Acoustical Society of America, 113(2):1122–1129, 2003.

[221] H. Pan, J. Tao, and R. Tang. Molecular simulation of water behaviors on crystal faces of hydroxyapatite. Frontiers of Chemistry in China, 2(2):156 – 163, 2007.

[222] A.M. Parfitt. Osteonal and hemi-osteonal remodeling: The spatial and temporal framework for signal traffic in adult human bone. Journal of Cell Biochemistry, 55(3):273–286, 1994.

[223] J.G.J. Peelen, B.V. Rejda, and K. de Groot. Preparation and properties of sintered hydroxylapatite. Ceramurgia International, 4:71–74, 1978.

[224] L. Peng, J. Bai, X. Zeng, and Y. Zhou. Comparison of isotropic and orthotropic material property assignments on femoral finite element models under two loading conditions. Medical Engineering & Physics, 28:227–233, 2006.

[225] E. Perilli, A.M. Briggs, S. Kantor, J. Codrington, J.D. Wark, I.H. Parkinson, and N.L. Fazzalari. Failure strength of human vertebrae: Prediction using

bone mineral density measured by dxa and bone volume by micro-CT. Bone, 50(6):1416–1425, 2012.

[226] B. Pichler and Ch. Hellmich. Estimation of influence tensors for eigenstresses multiphase elastic media with nonaligned inclusion phases of arbitrary ellipsoidal shape. Journal of engineering mechanics, 136(8):1043–1053, 2010.

[227] P. Pivonka and S.V. Kamarova. Mathematical modeling in bone biology: From intracellular signaling to tissue mechanics. Bone, 47(2):181 – 189, 2010.

[228] P. Pivonka, J. Zimak, D.W. Smith, B.S. Gardiner, C.R. Dunstan, N.A. Sims, T.J. Martin, and G.R. Mundy. Model structure and control of bone remodeling: a theoretical study. Bone, 43(2):249–263, 2008.

[229] M. Planck. über das gesetz der energieverteilung im normalspektrum. Annalen der Physik, 4:553.

[230] L. Podshivalov, A. Fischer, and P.Z. Bar-Yoseph. 3D hierarchical geometric modeling and multiscale FE analysis as a base for individualized medical diagnosis of bone structure. Bone, 48(4):693–703, 2011.

[231] K.S. Prostak and S. Lees. Visualization of crystal-matrix structure. In situ demineralization of mineralized turkey leg tendon and bone. Calcified Tissue International, 59:474 – 479, 1996.

[232] J. Radon. über die Bestimmung von Funktionen durch ihre Integralwere längs gewisser Mannigfaltigkeiten. [on the determination of functions from their integrals along certain manifolds]. SB Leipzig, 29(69), 1917.

[233] D.T. Reilly and A.H. Burstein. The elastic and ultimate properties of compact bone tissue. Journal of Biomechanics, 8:393 – 405, 1975.

[234] D.T. Reilly, A.H. Burstein, and V.H. Frankel. The elastic modulus for bone. Journal of Biomechanics, 7:271–275, 1974.

[235] G.A.P. Renders, L. Mulder, G.E.J. Langenbach, L. J. Ruijven, and T. M.G.J. van Eijden. Biomechanical effect of mineral heterogeneity in trabecular bone. Journal of Biomechanics, 41(13):2793–2798, 2008.

[236] G.A.P. Renders, L. Mulder, L.J. van Ruijven, G.E.J. Langenbach, and T.M.G.J. van Eijden. Mineral heterogeneity affects predictions of intratrabecular stress and strain. Journal of Biomechanics, 44(3):402 – 407, 2011.

[237] C. Renghini, V. Komlev, F. Fiori, E. Verné, F. Baino, and C. Vitale-Brovarone. Micro-CT studies on 3-D bioactive glass-ceramic scaffolds for bone regeneration. Acta Biomaterialia, 5:1328–1337, 2009.

[238] C. Reynaud. Mechanical properties and mechanical behaviour of SiC dense-porous laminates. Journal of the European Ceramic Society, 25(5):589 – 597, 2005.

[239] J.Y. Rho, M.C. Hobatho, and R.B. Ashman. Relations of mechanical properties to density and CT numbers in human bone. Medical Engineering & Physics, 17(5):347 – 355, 1995.

[240] J.Y. Rho, L. Kuhn-Spearing, and P. Zioupos. Mechanical properties and the hierarchical structure of bone. Medical Engineering & Physics, 20(2):92–102, 1998.

[241] J.Y. Rho, P. Zioupos, J.D. Currey, and G.M. Pharr. Microstructural elasticity and regional heterogeneity in human femoral bone of various ages examined by nano-indentation. Journal of Biomechanics, 35:189 – 198, 2002.

[242] B. van Rietbergen, H. Weinans, R. Huiskes, and A. Odgaard. A new method to determine trabecular bone elastic properties and loading using micromechanical finite-element models. Journal of Biomechanics, 28:69 – 81, 1995.

[243] B.L. Riggs and A.M. Parfitt. Drugs used to treat osteoporosis: The critical need for a uniform nomenclature based on their action on bone remodeling. Journal of Bone and Mineral Research, 20(2):177–184, 2005.

[244] C.M. Riggs, L.C. Vaughan, G.P. Evans, L.E. Lanyon, and A. Boyde. Mechanical implications of collagen fibre orientation in cortical bone of equine radius. Anatomy and Embryology, 187:239 – 248, 1993.

[245] H. Ritzel, M. Amling, M. Pösl, M. Hahn, and G. Delling. The thickness of human vertebral cortical bone and its changes in aging and osteoporosis: a histomorphic analysis of the complete spinal column from thirty-seven autopsy specimen. Journal of Bone and Mineral Research, 12(1):89–95, 1997.

[246] S.D. Rockhoff, E. Sweet, and J. Bleustein. The relative contribution of trabecular and cortical bone to the strength of human lumbar vertebrae. Calcified Tissue Research, 3:163–175, 1969.

[247] G. Rossum. Python reference manual. Technical report, Amsterdam, The Netherlands, The Netherlands, 1995.

[248] M. Rougvie and R. Bear. An X-ray diffraction investigation of swelling by collagen. Journal of the American Leather Chemists Association, 48(12):735–751, 1953.

[249] R. Ruimerman, P. Hilbers, B. van Rietbergen, and Huiskes R. A theoretical framework for strain-related trabecular bone maintenance and adaptation. Journal of Biomechanics, 38(4):931–941, 2005.

[250] H.-S. Ryu, H.-J. Youn, K.S. Hong, B.-S. Chang, C.-K. Lee, and S.-S. Chung. An improvement in sintering property of -tricalcium phosphate by addition of calcium pyrophosphate. Biomaterials, 23(3):909 – 914, 2002.

[251] J. Sanahuja, L. Dormieux, S. Meille, C. Hellmich, and A. Fritsch. Micromechanical explanation of elasticity and strength of gypsum: From elongated anisotropic crystals to isotropic porous polycrystals. Journal of Engineering Mechanics, 136(2):239–253, 2010.

[252] C. Sandino, S. Checa, P. J. Prendergast, and D. Lacroix. Simulation of angiogenesis and cell differentiation in a CaP scaffold subjected to compressive strains using a lattice modeling approach. Biomaterials, 31(8):2446–2452, 2010.

[253] C. Sandino and D. Lacroix. A dynamical study of the mechanical stimuli and tissue differentiation within a CaP scaffold based on micro-CT finite element models. Biomechanics and Modeling in Mechanobiology, 10(4):565–576, 2011.

[254] C. Sandino, J.A. Planell, and D. Lacroix. A finite element study of mechanical stimuli in scaffolds for bone tissue engineering. Journal of Biomechanics, 41(5):1005 – 1014, 2008.

[255] Z. Sant, M. Cauchi, and M. Spiteri. Analysis of stress-strain distribution within a spinal segment. Journal of Mechanics of Materials and Structures, 7(3):255–263, 2012.

[256] S. Scheiner, P. Pivonka, and C. Hellmich. Coupling systems biology with multiscale mechanics, for computer simulations of bone remodeling. Computer Methods in Applied Mechanics and Engineering, 254:181–196, 2013.

[257] S. Scheiner, R. Sinibaldi, B. Pichler, V. Komlev, C. Renghini, C. Vitale-Brovarone, F. Rustichelli, and Ch. Hellmich. Micromechanics of bone tissue-engineering scaffolds, based on resolution error-cleared computer tomography. Biomaterials, 30:2411–2419, 2009.

[258] E. Schileo, F. Taddei, L. Cristofolini, and M. Viceconti. Subject-specific finite element models implementing a maximum principal strain criterion are able to estimate failure risk and fracture location on human femurs tested *in vitro*. Journal of Biomechanics, 41:356–367, 2008.

[259] R. Schneider, G. Faust, U. Hindenlang, and P. Helwig. Inhomogeneous, orthotropic material model for the cortical structure of long bones modelled on the basis of clinical CT or density data. Computer Methods in Applied Mechanics and Engineering, 198(27-29):2167–217, 2009.

[260] N. P. Schumann, F. H.W. Biedermann, D.Arnold, H. A. Jinnah, R. Grassme, M. S. Fischer, and H. C. Scholle. Treadmill locomotion in normal mice - step related multi-channel EMG profiles of thigh muscles. Pathophysiology, 13:245–255, 2006.

[261] S.M. Seltzer. Calculation of photon mass energy-transfer and mass energy absorption coefficients. Radiation Research, 136(2):147–170, 1993.

[262] M.Y. Shareef, P.F. Messer, and R.v. Noort. Fabrication, characterization and fracture study of a machinable hydroxyapatite ceramic. Biomaterials, 14(1):69 – 75, 1993.

[263] M.J. Silva, C. Wang, T.M. Keaveny, and W.C. Hayes. Direct and computed tomography thickness measurements of the human, lumbar vertebral shell and endplate. Bone, 15(4):409–414, 1994.

[264] J. C. Simo and T. J. R. Hughes. Computational Inelasticity, volume 7. 1998. Interdisciplinary Applied Mathematics.

[265] J.C. Simo and R.L. Taylor. Consistent tangent operators for rate-independent elastoplasticity. Computer Methods in Applied Mechanics and Engineering, 48(1):101 – 118, 1985.

[266] K Singer, S Edmondston, R Day, P Breidahl, and R Price. Prediction of thoracic and lumbar vertebral body compressive strength: correlations with bone mineral density and vertebral region. Bone, 17(2):167–74, 1995.

[267] J. G. Skedros, S. C. Su, and R. D. Bloebaum. Biomechanical implications of mineral content and microstructural variations in cortical bone of horse, elk, and sheep calcanei. The Anatomical Record, 249:297–316, 1997.

[268] Belgium Skyscan NV, Kontich. Skyscan Nrecon user guide, 2010.

[269] D. Sommerfeldt and C. Rubin. Biology of bone and how it orchestrates the form and function of the skeleton. Eur Spine J, 10(2):86–95, 2001.

[270] K. Tai, G. Pelled, D. Sheyn, A. Bershteyn, L. Han, I. Kallai, Y. Zilberman, C. Ortiz, and D. Gazit. Nanobiomechanics of repair bone regenerated by genetically modified mesenchymal stem cells. Tissue Engineering: Part A, 14(10):1709–1720, 2008.

[271] S. Tavella, A. Ruggiu, A. Giuliani, F. Brun, B. Canciani, A. Manescu, K. Marozzi, M. Cilli, D. Costa, Y. Liu, F. Piccardi, R. Tasso, G. Tromba, F. Rustichelli, and R. Cancedda. Bone turnover in wild type and pleiotrophin-transgenic mice housed for three months in the international space station (ISS). PLoS ONE, 7(3):e33179, 2012.

[272] E.-I. Tazawa. Effect of self stress on flexural strength of gypsum-polymer composites. Advanced Cement Based Materials, 7(1):1–7, 1998.

[273] N. Trabelsi, C. Milgrom, and Z. Yosibash. Patient-specific FE analyses of metatarsal bones with inhomogeneous isotropic material properties. Journal of the Mechanical Behavior of Biomedical Materials, 29:177–189, 2014.

[274] N. Trabelsi and Z. Yosibash. Patient-specific finite-element analyses of the proximal femur with orthotropic material properties validated by experiments. Journal of Biomechanical Engineering, 133(6), 2011.

[275] C.H. Turner, S.C. Cowin, J.Y. Rho, R.B. Ashman, and J.C. Rice. The fabric dependence of the orthotropic elastic constants of cancellous bone. Journal of Biomechanics, 23(6):549 – 561, 1990.

[276] M.R. Urist, R.J. DeLange, and G.A.M. Finerman. Bone cell differentiation and growth factors. Science, 220:680 – 686, 1983.

[277] R.F. van Oers, R. Ruimerman, E. Tanck, P.A. Hilbers, and R. Huiskes. A unified theory for osteonal and hemi-osteonal remodeling. Bone, 42(2):250–259, 2008.

[278] B. van Rietbergen, R. Huiskes, F. Eckstein, and P. Rüegsegger. Trabecular bone tissue strains in the healthy and osteoporotic human femur. Journal of Bone and Mineral Research, 18(10):1781 – 1788, 2003.

[279] B. van Rietbergen, R. Müller, D. Ulrich, P. Rüegsegger, and R. Huiskes. Tissue stresses and strain in trabeculae of a canine proximal femur can be quantified from computer reconstructions. Journal of Biomechanics, 32:165–173, 1999.

[280] B. van Rietbergen, H.H. Weinans, R. Huiskes, and B.J.W. Polman. Computational strategies for iterative solutions of large FEM applications employing voxel data. International Journal for Numerical Methods in Engineering, pages 2743–2767, 1996.

[281] L.J. van Ruijven, L. Mulder, and T.M.G.J. van Eijden. Variations in mineralization affect the stress and strain distributions in cortical and trabecular bone. Journal of Biomechanics, 40:1211–1218, 2007.

[282] E. Verhulp, B. van Rietbergen, and R. Huiskes. Comparison of micro-level and continuum-level voxel models of the proximal femur. Journal of Biomechanics, 39(16):2951–2957, 2006.

[283] C. Verna, B. Melsen, and F. Melsen. Differences in static cortical bone remodeling parameters in human mandible and iliac crest. Bone, 25(5):577 – 583, 1999.

[284] M.-C. von Doernberg, B. von Rechenberg, M. Bohner, S. Grnenfelder, G.H. van Lenthe, R. Mller, B. Gasser, R. Mathys, G. Baroud, and J. Auer. In vivo behavior of calcium phosphate scaffolds with four different pore sizes. Biomaterials, 27(30):5186–5198, 2006.

[285] J. Vuong and Ch. Hellmich. Bone fibrillogenesis and mineralization: Quantitative analysis and implications for tissue elasticity. Journal of Theoretical Biology, 287:115–130, 2011.

[286] N.J. Wachter, P. Augat, M. Mentzel, M.R. Sarkar, G.D. Krischak, L. Kinzl, and L.E. Claes. Predictive value of bone mineral density and morphology determined by peripheral quantitative computed tomography for cancellous bone strength of the proximal femur. Bone, 28(1):133–9, 2001.

[287] D.W. Wagner, D.P. Lindsey, and G.S. Beaupre. Deriving tissue density and elastic modulus from microCT bone scans. Bone, 49(5):931–938, 2011.

[288] K. Wakashima and H. Tsukamoto. Mean-field micromechanics model and its application to the analysis of thermomechanical behaviour of composite materials. Materials Science and Engineering: A, 146(1-2):291 – 316, 1991.

[289] W.R. Walsh. Ion concentration effects on bone streaming potentials and zeta potentials. Biomaterials, 14(5):331 – 336, 1993.

[290] G. Wang, S. Zhao, H. Yu, C.A. Miller, P.J. Abbas, B.J. Gantz, S.W. Lee, and J.T. Rubinstein. Design, analysis and simulation for development of the first clinical micro-CT scanner. Academic Radiology, 12(4):511–525, 2005.

[291] Y. Wang, M.C. Battié, S.K. Boyd, and T. Videman. The osseous endplates in lumbar vertebrae: thickness, bone mineral density and their associations with age and disk degeneration. Bone, 48(4):804–809, 2011.

[292] D. Webster and R. Mller. In silico models of bone remodeling from macro to nanofrom organ to cell. Wiley Interdisciplinary Reviews: Systems Biology and Medicine, 3(2):241–251, 2011.

[293] T. Wehner, U. Wolfram, T. Henzler, F. Niemeyer, L. Claes, and U. Simon. Internal forces and moments in the femur on the rat during gait. Journal of Biomechanics, 43:2473–2479, 2010.

[294] S. Weiner and H.D. Wagner. The material bone: structure - mechanical function relations. Annual Review of Materials Science, 28:271 – 298, 1998.

[295] W.J. Whitehouse, E.D. Dyson, and C.K. Jackson. The scanning electron microscope in studies of trabecular bone from a human vertebral body. Journal of Anatomy, 108(Pt 3):481–96, April 1971.

[296] E.E. Wilson, A. Awonusi, M.D. Kohn, M.M.J. Tecklenburg, and L.W. Beck. Three structural roles for water in bone observed by solid-state NMR. Biophysical Journal, 90:3722–3731, 2006.

[297] D.C. Wirtz, N. Schiffers, T. Pandorf, K. Radermacher, D. Weichert, and R. Forst. Critical evaluation of known bone material properties to realize anisotropic FE-simulation of the proximal femur. Journal of Biomechanics, 33:1325–1330, 2000.

[298] J. Wolff. Das Gesetz der Transformation der Knochen,.

[299] U. Wolfram, H.-J. Wilke, and P.K. Zysset. Rehydration of vertebral trabecular bone: Influences on its anisotropy, its stiffness and the indentation work with a view to age, gender and vertebral level. Bone, 46:348 – 354, 2010.

[300] S. Wroe, K. Moreno, P. Clausen, C. McHenry, and D. Curnoe. High-resolution three- dimensional computer simulation of homonid cranial mechanics. The Anatomical Record, 290:1248–1255, 2007.

[301] C.H. Yan, R.T. Whalen, G.S. Beaupre, S.Y. Yen, and S. Napel. Reconstruction algorithm for polychromatic ct imaging: application to beam hardening correction. Medical Imaging, IEEE Transactions on, 19(1):1–11, Jan 2000.

[302] N. Yoganandan, J. B. Myklebust, J. F. Cusick, A. Sances, and C. R. Wilson. Functional biomechanics of the thoracolumbar vertebral cortex. Clinical Biomechanics, 3:11–18, 1988.

[303] Z. Yosibash, R. Padan, L. Joskowicz, and C. Milgrom. A CT-based high-order Finite Element analysis of the human proximal femur compared to in-vitro experiments. Journal of Biomechanical Engineering, 129(3):297–309, 2007.

[304] Z. Yosibash, N. Trabelsi, and C. Hellmich. Subject-specific p-FE analysis of the proximal femur utilizing micromechanics-based material properties. International Journal for Multiscale Computational Engineering, 6(5):483–498, 2008.

[305] W.S. Yu, K.Y. Chan, F.W.P. Yu, B.K.W. Ng, K.M. Lee, L. Qin, T.P. Lam, and J.C.Y. Cheng. Bone structural and mechanical indices in Adolescent Idiopathic Scoliosis evaluated by high-reolution peripheal quantitative computed tomography (HR-pQCT). Bone, 61:109–115, 2014.

[306] D. Zaffe. Some considerations on biomaterials and bone. Micron, 36:583 – 592, 2005.

[307] D. Zahn and O. Hochrein. Computational study of interfaces between hydroxyapatite and water. Physical Chemistry Chemical Physics, 5:4004–4007, 2003.

[308] A. Zaoui. Continuum micromechanics: survey. Journal of Engineering Mechanics (ASCE), 128(8):808–816, 2002.

[309] O.C. Zienkiewicz and R.L. Taylor. The Finite Element method, page 313. McGraw-Hill, London, UK, 1994.

[310] L. Zylberberg, W. Traub, V. de Buffrenil, F. Allizard, T. Arad, and S. Weiner. Rostrum of a toothed whale: Ultrastructural study of a very dense bone. Bone, 23:241 – 247, 1998.

APPENDIX

A

SOFTWARE CODES FOR INTRAVOXEL BONE MICROMECHANICS

This chapter gives a selection of computer codes written in Matlab programming language [197], which are related to the developments described in Chapter 2, published in (Blanchard et al, 2013).

```matlab
%%%%%%%%%%%%%%%%%%%%%%%%%%%%%%%%%%%%%%%%%%%%%%%%%%%%%%%%%%%%%%%%%%%
%                                                               %
% mainScript.m: main script to extract voxel-specific material  %
%               properties from the CT images                   %
% written by:   Romane Blanchard from previous code of A. Fritsch and  %
%               A. Dejaco                                        %
% dependencies: findpeaks.m, dispHisto.m, fun_NIST.m, relation_mu_GV.m,%
%               Ctensor.m, figures.m                            %
% IMWS--TU WIEN                                                  %
%                                                               %
%%%%%%%%%%%%%%%%%%%%%%%%%%%%%%%%%%%%%%%%%%%%%%%%%%%%%%%%%%%%%%%%%%

close all; clear all; clc;
disp(['starts analysis of the CT images'])

%% Initialization
images_count=536;
pixels_count = 720; % it's a square!
photon_energy=10;  %keV
rho_org = 1.41;  % g/cm3
rho_HA = 3;  % g/cm3
rho_w  = 1;  % g/cm3
rho_ec_rat=2;   %g/cm3

%% Finds X_air and X_solid_peak
disp(['run findpeaks.m...'])
[X_peak, X_air,X_threshold, n_all, voxels, X_solid] =...
   findpeaks(images_count, pixels_count);
disp('done')
```

```matlab
%% Displays the histogram
disp(['*'])
disp(['histogram'])
dispHisto(n_all, images_count, voxels);
disp(['...done'])

%% Calculates the X-ray attenuation coefficient
disp(['*'])
disp(['calculation of the X-ray attenuation coefficients'])
[mu_HA, mu_col,mu_w]=fun_NIST(photon_energy);
disp(['calculation...done'])


%% Volume fractions
disp(['*******************************'])
disp(['calculation of a, b and attenuation coefficients mu_ec and mu_air'])

[exfHA, exforg, exfw, exmu_ec, a, b]=relation_mu_GV(rho_ec_rat, rho_HA,...
    rho_w, rho_org, mu_HA, mu_col, mu_w, X_air, X_solid)

disp(['volume fractions'])
[fHA, forg, fw, rho_T, barfHA, barforg, barfw, muT_threshold, rangemuT]=...
    volume_fractions(rho_w, rho_org, rho_HA, mu_HA, mu_w, mu_col, a, b)

disp(['*'])
disp(['Calculates the stiffness tensor components...'])

[C1111, C3333, C1122, C1133, C2323, rC1111, rC3333, rC1122, rC1133,...
    rC2323, rangex]=Ctensor(rho_T, rho_HA);

disp(['calculation...done'])

disp(['*'])
disp(['Calculates the engineering values...'])
for i=1:256
    C=[rC1111(i), rC1122(i), rC1133(i), 0, 0, 0;...
                rC1122(i), rC1111(i), rC1133(i), 0, 0, 0;...
                rC1133(i), rC1133(i), rC3333(i), 0, 0, 0;...
                0, 0, 0, rC2323(i), 0, 0;...
                0, 0, 0, 0, rC2323(i), 0;...
                0, 0, 0, 0, 0, (rC1111(i)-rC1122(i))/2];

        D=inv(C);

        E1(i)=1/D(1,1);
        E3(i)=1/D(3,3);
        nu12(i)=-D(1,2)*E1(i);
        nu13(i)=-D(1,3)*E3(i);
        G12(i)=E1(i)/(2*(1+nu12(i)));
```

167

```matlab
end

%% Writes data tables

datatable2=[rangex' rangemuT' rC1111' rC1122', rC1133', rC3333', rC2323'];
fid2=fopen(['Stiffness tensor components'],'w');
fprintf(fid2, 'GS    muec  C1111 C1122 C1133 C3333 C2323\r\n');
fprintf(fid2,'%3.0f  %5.2f %8.4f %8.4f %8.4f %8.4f  %8.4f\r\n',datatable2');
fclose(fid2);

datatable=[rangex' rangemuT' barfHA' barforg' barfw' E1' E3' nu12' nu13' G12'];
fid=fopen(['engineering_table.txt'],'w');
fprintf(fid,' GS    muec    fHA    fcol      fHA        E1        E3      nu12...
         nu13      G12\r\n');
fprintf(fid, '%3.0f  %5.2f  %5.4f  %5.4f  %8.4f  %8.4f  %8.4f  %8.4f  %8.4f...
    %8.4f\r\n',datatable');
fclose(fid);


figures(E1, E3, G12, rangex, nu12, nu13, rC1111, rC1122, rC1133, rC3333,...
    rC2323, barfHA, barforg, barfw);


disp(['calculation...done'])
save(['workspace.mat'])


%%%%%%%%%%%%%%%%%%%%%%%%%%%%%%%%%%%%%%%%%%%%%%%%%%%%%%%%%%%%%%%%%%%%%%%%%%%
%                                                                       %
% Function findpeaks.m                                                   %
%                                                                       %
%%%%%%%%%%%%%%%%%%%%%%%%%%%%%%%%%%%%%%%%%%%%%%%%%%%%%%%%%%%%%%%%%%%%%%%%%%%


function [X_peak, X_air,X_threshold, n_all,voxels, X_solid] =...
   findpeaks(images_count, pixels_count)


% initial values
n_all = 0;
voxels = 0;

% frequency count vector for all images (for histogram)
n_all = zeros(1,256);
% bins for histogram
bins = 0:255;

pixels_count=720;
images_count=536;
voxels=pixels_count*pixels_count;
```

```matlab
tic

% loop over all CT images
for i=1:images_count

    % read image
    slice = imread(['./originalImages/','harry_mpfemur__rec',num2str(i),...
    '.bmp']);

    % ————————————————————————————————————————————————————————————
    % collect info for histogram

    slice2 = double(slice); % convert to double
    slice_vec = reshape(slice2,voxels,1);  % make vector
    [n, xout] = hist(slice_vec, bins);  % n...frequency count
    n_all = n_all + n;

    % ————————————————————————————————————————————————————————————

    % standard grey values X of pores and solid
    array_X_air(i) = double(min(min(slice)));
    array_X_solid(i) = double(max(max(slice)));
end % next CT image (ii)

    % X_air = most frequent GS
    [xx,indx_air] = max(n_all);
    X_air = bins(indx_air);

    % X_peak = local max.
    [xx,indx_solid] = max(n_all(75:255));
    X_peak = bins(indx_solid+74);

    % X_threshold = local min.
    [xx,indx] = min(n_all(indx_air+1:indx_solid));
    X_threshold = indx_solid; %bins(indx+indx_air+1—1);

X_solid=136;      %mean(el_grey(:,2));


%%%%%%%%%%%%%%%%%%%%%%%%%%%%%%%%%%%%%%%%%%%%%%%%%%%%%%%%%%%%%%%%%%%%%%%%
%                                                                    %
% Function dispHisto.m                                               %
%                                                                    %
%%%%%%%%%%%%%%%%%%%%%%%%%%%%%%%%%%%%%%%%%%%%%%%%%%%%%%%%%%%%%%%%%%%%%%%%

function []=dispHisto(n_all, images_count, voxels)
bins=0:255;
figure1=figure
axes1 = axes('Parent',figure1,'FontWeight','bold','FontSize',14);
bar(bins, n_all/(images_count*voxels),'k');
```

```matlab
box(axes1,'on');
grid(axes1,'on');
hold(axes1,'all');
axis([0 255 0 0.05]);
xlabel('X—ray attenuation (Grey value — GV)','FontSize', 16, 'FontName',...
        'Times','FontWeight', 'bold');
ylabel('Probability density','FontSize', 16, 'FontName', 'Times',...
        'FontWeight', 'bold');
% Create arrow
annotation(figure1,'arrow',[0.229183841714757 0.229183841714757],...
    [0.280155015197568 0.145896656534954]);

% Create textbox
annotation(figure1,'textbox',...
    [0.205212604015331 0.279525165737261 0.0475706310861756 0.0395136778115502],...
    'String',{'GV_{thr}=75'},...
    'FitBoxToText','on','FontSize', 16, 'FontName', 'Times');

figure2=figure
axes2 = axes('Parent',figure2,'FontWeight','bold','FontSize',14);
bar(bins,n_all/(images_count*voxels),'k');
box(axes2,'on');
grid(axes2,'on');
hold(axes2,'all');
axis([75 255 0 0.0015]);
xlabel('X—ray attenuation (Grey value — GV)','FontSize', 16, 'FontName',...
        'Times','FontWeight', 'bold');
ylabel('Probability density','FontSize', 16, 'FontName', 'Times',...
        'FontWeight', 'bold');

cumFreq=0;

figure4 = figure('XVisual',...
    '0x29 (TrueColor, depth 24, RGB mask 0xff0000 0xff00 0x00ff)');
% cumFreq(1)=n_all(1);
for i=2:length(n_all)
cumFreq(i)=n_all(i)+cumFreq(i—1);
end
plot(bins, cumFreq/(images_count*voxels—n_all(1)),'k', 'Linewidth',3);
grid on
xlabel('X—ray attenuation (Grey scale —GS)','Fontsize', 14');
ylabel('Cumulative frequency','Fontsize', 14);
% axis([0 2000 0 1]);
```

```matlab
%%%%%%%%%%%%%%%%%%%%%%%%%%%%%%%%%%%%%%%%%%%%%%%%%%%%%%%%%%%%%%%%%%%%%%%%%%%
%                                                                       %
% Function fun_NIST.m                                                   %
%                                                                       %
%%%%%%%%%%%%%%%%%%%%%%%%%%%%%%%%%%%%%%%%%%%%%%%%%%%%%%%%%%%%%%%%%%%%%%%%%%%

function [mu_HA,mu_col,mu_w] = fun_NIST(photon_energy)
% photon energy in keV

% from NIST database
% column 1 = photon energy [MeV]
% column 2 = mass attenuation coefficient (without coherent scattering)
%   [cm2/g]

 %photon_energy=10;
% HA
NIST_HA = ...
   [0.0050   313.0000
    0.0060   192.0000
    0.0080    87.9000
    0.0100    47.2000
    0.0150    14.9000
    0.0200     6.5600
    0.0300     2.1000
    0.0400     0.9880
    0.0500     0.5870
    0.0600     0.4070
    0.0800     0.2590 ];

% figure
% plot(NIST_HA(:,1), NIST_HA(:,2),NIST_col(:,1), NIST_col(:,2) )

% collagen
NIST_col = ...
   [5.000E-03 3.24E+01
    6.000E-03 1.87E+01
    8.000E-03 7.86E+00
    1.000E-02 4.05E+00
    1.500E-02 1.30E+00
    2.000E-02 6.50E-01
    3.000E-02 3.24E-01
    4.000E-02 2.43E-01
    5.000E-02 2.10E-01
    6.000E-02 1.93E-01
    8.000E-02 1.74E-01];


% water
NIST_w = ...
   [5.000E-03 4.26E+01
    6.000E-03 2.46E+01
```

```
    8.000E—03 1.04E+01
    1.000E—02 5.33E+00
    1.500E—02 1.67E+00
    2.000E—02 8.10E—01
    3.000E—02 3.76E—01
    4.000E—02 2.68E—01
    5.000E—02 2.27E—01
    6.000E—02 2.06E—01
    8.000E—02 1.84E—01 ];



% mineral
rho_HA = 3.0; % [g/cm^3]

% collagen
rho_col = 1.41; % [g/cm^3]

% water
rho_w = 1.0;          % [g/cm^3]

% spline interpolation HA
energy = NIST_HA(:,1)*1000;
mu_sur_rho_HA = NIST_HA(:,2);
cfun = fit(energy,mu_sur_rho_HA, 'cubicspline');
% figure
% plot(cfun)
mu_sur_rho_HA = feval(cfun,photon_energy);

% spline interpolation collagen
energy = NIST_col(:,1)*1000;
mu_sur_rho_col = NIST_col(:,2);
cfun = fit(energy,mu_sur_rho_col, 'cubicspline');
mu_sur_rho_col = feval(cfun,photon_energy);

% spline interpolation water
energy = NIST_w(:,1)*1000;
mu_sur_rho_w = NIST_w(:,2);
cfun = fit(energy,mu_sur_rho_w, 'cubicspline');
mu_sur_rho_w = feval(cfun,photon_energy);

% X—ray attenuation coefficients [cm^(—1)]
mu_w   = mu_sur_rho_w*rho_w;
mu_col = mu_sur_rho_col*rho_col;
mu_HA  = mu_sur_rho_HA*rho_HA;

%% plot of the NIST curves
figure1 = figure('XVisual',...
    '0x29 (TrueColor, depth 24, RGB mask 0xff0000 0xff00 0x00ff)');

axes1 = axes('YScale','log','YGrid','on','XGrid','on','FontWeight',...
```

```matlab
        'bold','FontSize',14);
xlim(axes1,[5 25]);
ylim(axes1,[0.1 1000]);
box(axes1,'on');
hold(axes1,'all');

% Create multiple lines plot
plot1=plot(energy, NIST_HA(:,2),energy,NIST_col(:,2),energy, NIST_w(:,2),...
    'MarkerFaceColor','auto','LineWidth',3,...
    'Parent',axes1);
set(plot1(1),'Marker','>','LineStyle','-.','Color', [0 0.498039215803146 0]);
set(plot1(2),'Marker','square','LineStyle','--', 'Color', 'r');
set(plot1(3),'Marker','o', 'Color', 'b');

xlabel('Photon energy [keV]','FontWeight','bold','FontSize',14);
ylabel('$\mu_i$/$\rho_i$ $\mathbf{[cm^2/g]}$','Interpreter','latex',...
    'FontWeight','bold',...
    'FontSize',16);
legend('hydroxyapatite','collagen','water');

%%plot of the NIST curves
figure2 = figure('XVisual',...
    '0x29 (TrueColor, depth 24, RGB mask 0xff0000 0xff00 0x00ff)');
axes1 = axes('YScale','log','YGrid','on','XGrid','on','FontWeight',...
     'bold','FontSize',14);
xlim(axes1,[5 25]);
ylim(axes1,[0.1 1000]);
box(axes1,'on');
hold(axes1,'all');

% Create multiple lines plot
plot1=plot(energy, NIST_HA(:,2)*rho_HA,energy,NIST_col(:,2)*rho_col,energy,...
NIST_w(:,2)*rho_w,'MarkerFaceColor','auto','LineWidth',3, 'Parent',axes1);
set(plot1(1),'Marker','>','LineStyle','-.','Color', [0 0.498039215803146 0]);
set(plot1(2),'Marker','square','LineStyle','--', 'Color', 'r');
set(plot1(3),'Marker','o', 'Color', 'b');
xlabel('Photon energy [keV]','FontWeight','bold','FontSize',14);
ylabel('$\mu_i$ $\mathbf{[cm^{1}]}$','Interpreter','latex',...
    'FontWeight','bold',...
    'FontSize',16);
legend('hydroxyapatite','collagen','water');


%%%%%%%%%%%%%%%%%%%%%%%%%%%%%%%%%%%%%%%%%%%%%%%%%%%%%%%%%%%%%%%%%%%%%%%%%%%%
%                                                                        %
% Function relation_mu_GV.m                                              %
%                                                                        %
%%%%%%%%%%%%%%%%%%%%%%%%%%%%%%%%%%%%%%%%%%%%%%%%%%%%%%%%%%%%%%%%%%%%%%%%%%%%

function[exfHA, exforg, exfw, exmu_ec, a, b]=relation_mu_GV(rho_ec_rat,...
    rho_HA, rho_w, rho_org, mu_HA, mu_col, mu_w, X_air, X_solid)
```

```matlab
rhoHAcrit=1.18;   %g/cm3

rhoHAapp=1.7042*rho_ec_rat-2.1125;

A=0.29; B=0.17;   %g/cm3
Atilde=((A*rhoHAcrit+B)*rho_HA)/(rho_org*(rho_HA-rhoHAcrit));

if rhoHAapp<=rhoHAcrit
    exfHA=(rho_ec_rat-B*(1-(rho_w-rho_org))-rho_w)/(rho_HA(1+A-(A*rho_w/...
    rho_org))-rho_w);
    exforg=(A*rho_HA*exfHA+B)/rho_org;
    exfw=1-exfHA-exforg;

    exmu_ec=exfHA*mu_HA+mu_w*exfw+mu_col*exforg;
    mu_air=0;
    a=(exmu_ec-mu_air)/(X_solid-X_air);
    b=(X_solid*mu_air-X_air*exmu_ec)/(X_solid-X_air);
else
    exfHA=1+(rho_ec_rat-rho_HA)/(rho_HA+rho_w*(Atilde-1)-rho_org*Atilde);
    exforg=Atilde*(1-exfHA);
    exfw=1-exfHA-exforg;

    exmu_ec=exfHA*mu_HA+mu_w*exfw+mu_col*exforg;
    mu_air=0;
    a=(exmu_ec-mu_air)/(X_solid-X_air);
    b=(X_solid*mu_air-X_air*exmu_ec)/(X_solid-X_air);

end


%%%%%%%%%%%%%%%%%%%%%%%%%%%%%%%%%%%%%%%%%%%%%%%%%%%%%%%%%%%%%%%%%%%%%%%%%%%%
%                                                                        %
% Function volume_fractions.m                                            %
%                                                                        %
%%%%%%%%%%%%%%%%%%%%%%%%%%%%%%%%%%%%%%%%%%%%%%%%%%%%%%%%%%%%%%%%%%%%%%%%%%%%

function[fHA, forg, fw, rho_T, barfHA, barforg, barfw, muT_threshold, rangemuT]...
=volume_fractions(rho_w, rho_org, rho_HA, mu_HA, mu_w, mu_col,a,b)

X_threshold=75;
rangeGS=0:255;
rangemuT=rangeGS*a+b;
muT_threshold=X_threshold*a+b;
mu_org=mu_col;


for i=1:length(rangemuT)
    muT=rangemuT(i)

    A=0.29; B=0.17; rhoHAcrit=1.18;
```

174

```matlab
%volume fraction of hydroxyapatite

fHA=((mu_org − mu_w)*rho_HA*(B + A*rhoHAcrit) + (−muT + mu_w)*(rho_HA −...
    rhoHAcrit)*rho_org)/(((mu_org − mu_w)*rho_HA*(B +A*rhoHAcrit) +...
    −mu_HA+ mu_w)*(rho_HA−rhoHAcrit)*rho_org);

%volume fraction of water
fw=((muT − mu_HA)*(B*rho_HA + A *rho_HA* rhoHAcrit + (−rho_HA + rhoHAcrit)...
    *rho_org))/(−(mu_org −mu_w) *rho_HA *(B + A *rhoHAcrit) +...
    (mu_HA − mu_w) *(rho_HA −rhoHAcrit) *rho_org);

%volume fraction of organic matter
forg=−(((muT − mu_HA)* rho_HA *(B +A *rhoHAcrit))/(−(mu_org − mu_w)*...
    rho_HA* (B + A *rhoHAcrit) + (mu_HA −mu_w)* (rho_HA − rhoHAcrit)...
    *rho_org));


barfHA(i)=fHA;
barforg(i)=forg;
barfw(i)=fw;

rho_T(i)=fHA*rho_HA+forg*rho_org+fw*rho_w;
end



%%%%%%%%%%%%%%%%%%%%%%%%%%%%%%%%%%%%%%%%%%%%%%%%%%%%%%%%%%%%%%%%%%%%%%%%%
%                                                                     %
% Function Ctensor.m                                                  %
%                                                                     %
%%%%%%%%%%%%%%%%%%%%%%%%%%%%%%%%%%%%%%%%%%%%%%%%%%%%%%%%%%%%%%%%%%%%%%%%%

function[C1111, C3333, C1122, C1133, C2323, rC1111, rC3333, rC1122,...
    rC1133, rC2323, rangex]=Ctensor(rho_T, rho_HA, X_threshold)
rangex=linspace(0,255,256)

%Initialization
rC1111=0; rC3333=0; rC1122=0;rC1133=0; rC2323=0;
X_threshold=100;

for i=1:256

x=rho_T(i)/rho_HA;
C1111_HA=137;     %GPa

C1111=(4.6826*x^3−6.0171*x^2+2.8081*x−0.447)*C1111_HA;

C3333=(−6.8447*x^4+17.63*x^3−13.5048*x^2+4.2118*x−0.4573)*C1111_HA;

C1122=(−11.0152*x^5+29.7474*x^4−28.7144*x^3+12.587*x^2−2.3375*x+0.1188)...
    *C1111_HA;
```

```matlab
C1133=(-5.0088*x^4+13.7237*x^3-12.4876*x^2+4.8307*x-0.6745)*C1111_HA;

C2323=(4.1245*x^5-14.9352*x^4+21.9578*x^3-15.1486*x^2+4.9459*x-0.6169)...
    *C1111_HA;

rC1111(i)=C1111;
rC3333(i)=C3333;
rC1122(i)=C1122;
rC1133(i)=C1133;
rC2323(i)=C2323;

end


figure
hold on
plot(rho_T, rC1111, rho_T, rC3333, rho_T, rC1122, rho_T, rC1133, rho_T, rC2323)
legend('C_{1111}','C_{3333}','C_{1122}','C_{1133}','C_{2323}')
xlabel('\rho_T')
ylabel('Stiffness')
grid on


%%%%%%%%%%%%%%%%%%%%%%%%%%%%%%%%%%%%%%%%%%%%%%%%%%%%%%%%%%%%%%%%%%%%%%%%%%
%                                                                      %
% Function figures.m                                                   %
%                                                                      %
%%%%%%%%%%%%%%%%%%%%%%%%%%%%%%%%%%%%%%%%%%%%%%%%%%%%%%%%%%%%%%%%%%%%%%%%%%

function[]=figures(E1, E3, G12, rangex, nu12, nu13, rC1111, rC1122, rC1133,...
 rC3333,rC2323, barfHA, barforg, barfw);

rangeGS=rangex;
close all;


figure0 = figure('XVisual',...
    '0x29 (TrueColor, depth 24, RGB mask 0xff0000 0xff00 0x00ff)');
axes0 = axes('Parent',figure0,'FontWeight','bold','FontSize',14);
hold on; grid on;
plot0=plot(rangeGS, barfHA, rangeGS, barforg, rangeGS, barfw);
set(plot0(1), 'Linewidth', 2, 'DisplayName', 'f_{HA}','LineStyle',...
    '-.','Color', [0 0.498039215803146 0]);
set(plot0(2),'LineStyle','--','Linewidth', 2,...
    'DisplayName', 'f_{org}', 'Color', 'r');
set(plot0(3), 'Linewidth', 2, 'DisplayName', 'f_{water}',...
    'Color', 'b');
xlabel('X-ray attenuation (grey values GV)', 'FontSize', 16, 'FontName', 'Times');
ylabel('Volume fractions [-]', 'FontSize', 16, 'FontName', 'Times' );
legend0=legend('$f_{HA}$', '$f_{org}$', '$f_{water}$');
```

```matlab
set(legend0,'FontSize', 16,'Interpreter','latex');
axis([75 255 0 1])


figure1 = figure('XVisual',...
    '0x29 (TrueColor, depth 24, RGB mask 0xff0000 0xff00 0x00ff)');
axes1 = axes('Parent',figure1,'FontWeight','bold','FontSize',14);
hold on;grid on
plot1=plot(rangex,E1, rangex, E3, rangex,G12);
set(plot1(1), 'Linewidth', 2, 'LineStyle', '——', 'DisplayName', 'E_{1}');
set(plot1(2), 'Linewidth', 2, 'DisplayName', 'E_{3}');
set(plot1(3), 'Linewidth', 2, 'LineStyle', '—.', 'DisplayName', 'G_{12}');
legend1=legend('$E_{1}$','$E_{3}$','$G_{12}$');
set(legend1,'FontSize', 16,'FontWeight','bold',...
    'Interpreter','latex');
xlabel('X—ray attenuation (grey values GV)', 'FontSize', 16, 'FontName',...
    'Times','FontWeight', 'bold');
ylabel('Young''s and shear moduli [GPa]', 'FontSize', 16,...
    'FontName','Times','FontWeight', 'bold');
axis([75 255 0 100]);


figure2 = figure('XVisual',...
    '0x29 (TrueColor, depth 24, RGB mask 0xff0000 0xff00 0x00ff)');
axes2 = axes('Parent',figure2,'FontWeight','bold','FontSize',14);
hold on; grid on;
plot2=plot(rangex, nu12, rangex, nu13);
set(plot2(1), 'Linewidth', 2, 'LineStyle', '——', 'DisplayName', 'nu_{12}');
set(plot2(2), 'Linewidth', 2, 'DisplayName', 'nu_{13}');
legend2=legend('$\nu_{12}$','$\nu_{13}$')
set(legend2,'FontSize', 16,'Fontweight',...
    'bold','Interpreter','latex');
xlabel('X—ray attenuation (grey values GV)', 'FontSize', 16, 'FontName',...
'Times', 'FontWeight', 'bold');
ylabel('Poisson''s ratios [—]', 'FontSize', 16, 'FontName', 'Times',...
    'Fontweight','bold');
axis([75 255 0 0.8])


figure3 = figure('XVisual',...
    '0x29 (TrueColor, depth 24, RGB mask 0xff0000 0xff00 0x00ff)');
axes3 = axes('Parent',figure3,'FontWeight','bold','FontSize',14);
hold on; grid on;
plot3=plot(rangex, rC1111, rangex, rC3333, rangex, rC1122, rangex, rC1133,...
    rangex, rC2323);
set(plot3(1), 'Linewidth', 2, 'DisplayName', 'C_{1111}');
set(plot3(2), 'Linewidth', 2, 'LineStyle', '——', 'DisplayName', 'C_{3333}');
set(plot3(3), 'Linewidth', 2, 'LineStyle', '—.', 'DisplayName', 'C_{1122}');
set(plot3(4), 'Linewidth', 2, 'LineStyle', ':', 'DisplayName', 'C_{1133}');
set(plot3(5), 'Linewidth', 2,'MarkerSize',6,'Marker','.', 'LineStyle',...
    'none', 'DisplayName', 'C_{2323}');
```

```matlab
legend3=legend('$C_{1111}$','$C_{3333}$','$C_{1122}$','$C_{1133}$','$C_{2323}$')
set(legend3,'FontSize', 16,'Interpreter','latex');
xlabel('X-ray attenuation (grey values GV)', 'FontSize', 16, 'FontName', 'Times')
ylabel('Stiffness tensor components [GPa]', 'FontSize', 16, 'FontName', 'Times')
axis([75 255 0 100])

end
```

SOFTWARE CODES FOR INTRAVOXEL ANALYSIS OF CERAMIC BIOMATERIALS

This chapter gives a selection of computer codes written in Matlab programming language [197], which are related to the developments described in Chapter 3, to be published in (Czenek et al, 2014).

```matlab
%%%%%%%%%%%%%%%%%%%%%%%%%%%%%%%%%%%%%%%%%%%%%%%%%%%%%%%%%%%%%%%%%%%%%%%%%%%
%                                                                       %
% mainScript_Efunction.m: main script to backcompute the photon energy  %
%                        from histogram landmarks                       %
%                                                                       %
% dependencies:fun_NIST_A, import_images                                %
% last update: June 2014                                                %
% IMWS——TU WIEN                                                         %
%                                                                       %
%%%%%%%%%%%%%%%%%%%%%%%%%%%%%%%%%%%%%%%%%%%%%%%%%%%%%%%%%%%%%%%%%%%%%%%%%%%

close all; clear all; clc;
disp(['starts script'])

% Loop over the scaffolds:
% (to study only one scaffold, erase/comment "for scaffold_iteration=1:12"
% and assign scaffold_iteration=number of the scaffold (from 1 to 12))
for scaffold_iteration=1:12
    switch scaffold_iteration
        % cases 1—6: empty
        case 1 %I
            folder='empty_8bit'
            scaffold_number=1 %used for calculation a and b; 1—20
            scaffold='scaffold1'
            images_count=1170
        case 2 %II
            folder='empty_8bit'
            scaffold_number=2 %used for calculation a and b; 1—20
            scaffold='scaffold2'
            images_count=994
```

```matlab
case 3 %III
    folder='empty_8bit'
    scaffold_number=4 %used for calculation a and b; 1—20
    scaffold='scaffold4'
    images_count=854
case 4 %IV
    folder='empty_8bit'
    scaffold_number=5 %used for calculation a and b; 1—20
    scaffold='scaffold5'
    images_count=804
case 5 %V
    folder='empty_8bit'
    scaffold_number=7 %used for calculation a and b; 1—20
    scaffold='scaffold7'
    images_count=880
case 6 %VI
    folder='empty_8bit'
    scaffold_number=8 %used for calculation a and b; 1—20
    scaffold='scaffold8'
    images_count=802

    % cases 7 and 8: 3 weeks
case 7 %I
    folder='3weeks_8bit'
    scaffold_number=11 %used for calculation a and b; 1—20
    scaffold='scaffold1_3w'
    images_count=770
case 8 %II
    folder='3weeks_8bit'
    scaffold_number=12 %used for calculation a and b; 1—20
    scaffold='scaffold2_3w'
    images_count=1000
    % cases 9 and 10: 6 weeks
case 9 %II
    folder='6weeks_8bit'
    scaffold_number=14 %used for calculation a and b; 1—20
    scaffold='scaffold4_6w'
    images_count=906
case 10 %IV
    folder='6weeks_8bit'
    scaffold_number=15 %used for calculation a and b; 1—20
    scaffold='scaffold5_6w'
    images_count=918

    % cases 11 and 12: 8 weeks
case 11 %V
    folder='8weeks_8bit'
    scaffold_number=17 %used for calculation a and b; 1—20
    scaffold='scaffold7_8w'
    images_count=1015
case 12 %VI
```

```matlab
        folder='8weeks_8bit'
        scaffold_number=18 %used for calculation a and b; 1—20
        scaffold='scaffold8_8w'
        images_count=826
end


% Directory name to read the images —— Agnes
dir=['/ct_images/',folder,'/',scaffold];
% Directory name —— Romane
%dir=['~/Documents/Agnes/BACKUP/ct_images/',folder,'/',scaffold];


% If the .mat file exists, loads the file, else run the script
% import_images to save the .mat_file
if exist(['raw_volume/',folder,'_',scaffold,'_','raw_volume.mat'])==0;
    import_images;
else
    load(['raw_volume/',folder,'_',scaffold,'_','raw_volume.mat']);
end

% Table 1
GV_AIR = [77; 55; 70; 44; 42; 59; 64; 65; 39; 36; 37; 57; 80; 56; 71; 44;...
71; 39; 55; 62; 82];
GV_AL =  [165;157;159;168;165;167;163;144;180;184;184;133;185;155;171;179;...
177;122;169; 105; 130];
GV_max = [245;240;0;239;246;  0; 240;235; 0;   0;240; 167;   0;  198;212;...
0; 227;157;0;0];
GV_SC_vec =[204;193;188;190;203;195;196;191;185;189;194;138; 194; 163; ...
178; 188; 191;128;180; 198]; %peak of GV


% Mass densities
rho_bTCP = 3.07;    % g/cm3 mass density of CaP scaffold
rho_ETH = 0.789;    % g/cm3 mass density of ethanol

% Loop over the energies [kev]
disp(['loop over energy...']);

for ii=1:100
    photon_energy=ii;

    % Computes the X—ray attenuation coefficient depending on energies (Fig. 3)
    fun_NIST_A;

    % Saves the attenuation coefficients as vectors
    mu_bTCP_vec(ii)=mu_bTCP_theoretical; mu_ETH_vec(ii)=mu_ETH_theoretical;
    mu_AL_vec(ii)=mu_AL_theoretical; mu_AIR_vec(ii)=mu_AIR_theoretical;
end
disp(['done']);
```

```matlab
%% Assignements
% Peaks from histogram, to be modified
GV_left=GV_AIR(scaffold_number); % left peak (air)
GV_phantom= GV_AL(scaffold_number); % GV of the phantom that you recorded
                % after cropping
GV_right= GV_SC_vec(scaffold_number); % maximum grey value of the histogram


% assigns attenuation coefficients
mu_left_vec=mu_AIR_vec;
mu_phantom_vec=mu_AL_vec;
mu_right_vec=mu_bTCP_vec;

% Computes coefficients a and b, still depending on the energy [Eq.(2)]
b_vec= (mu_left_vec*GV_phantom-mu_phantom_vec*GV_left)./(GV_phantom-GV_left)
a_vec=(mu_left_vec-mu_phantom_vec)./(GV_left-GV_phantom)

% Computes the attenuation coefficient at the top of the scaffold peak
mu_peak_vec=a_vec*GV_right+b_vec;

% ratio to find energy as minimum of the curve Eq.(7)
ratio=mu_peak_vec./mu_bTCP_vec;
ratio4plot(scaffold_iteration,:)=ratio;

% nanoporosity at the peak of scaffold Eq.(4) and (5)
if scaffold_number<=10
    phi_peak_vec=(mu_peak_vec-mu_bTCP_vec)./(mu_AIR_vec-mu_bTCP_vec);
else
    phi_peak_vec=(mu_peak_vec-mu_bTCP_vec)./(mu_ETH_vec-mu_bTCP_vec);
end
% saves the nanoporosity for each scaffold in an vector
phi4plot(scaffold_iteration, :)=phi_peak_vec;

% Finds the maximum of the curve, or unique value
[maxR, maxIndex]=max(phi_peak_vec(5:100));
% Saves in a vector the scaffold number (1 to 12), the value at the
% maximum of the curve and the index of the maximum
uniquePoint(scaffold_iteration,:)=[scaffold_iteration, maxR, maxIndex];


end

disp(['Plotting...']);
%% Plots
% energy values
xaxis=1:100;
% time (in weeks)
xaxis2=[0 0 0 0 0 0 3 3 6 6 8 8];

% Nanoporosity as function of the energy for all 12 scaffolds
```

```matlab
figure0=figure;
axes0 = axes('Parent',figure0,'FontWeight','bold','FontSize',14);
hold(axes0,'all');
grid (axes0,'on');
plot(xaxis, phi4plot(1,:),'LineWidth',3,'Color',[0 0 0]);
plot(xaxis, phi4plot(2,:),'LineWidth',2,'LineStyle','——','Color',[0 0 0]);
plot(xaxis, phi4plot(3,:), 'Marker','o','LineWidth',1,'LineStyle','none',...
'Color',[0 0 0]);
plot(xaxis, phi4plot(4,:),'LineWidth',3,'LineStyle',':','Color',[0 0 0]);
plot(xaxis, phi4plot(5,:),'LineWidth',2,'LineStyle','—.','Color',[0 0 0]);
plot(xaxis, phi4plot(6,:), 'LineWidth',1,...
    'Color',[0.0392156876623631 0.141176477074623 0.415686279535294]);
plot(xaxis, phi4plot(7,:),'LineWidth',3,'Color',...
[1 0.694117665290833 0.39215686917305]);
plot(xaxis, phi4plot(8,:), 'LineWidth',2,'LineStyle','——',...
    'Color',[1 0.694117665290833 0.39215686917305]);
plot(xaxis, phi4plot(9,:),'Marker','o','LineWidth',1,'LineStyle','none',...
'Color',[0 0 1]);
plot(xaxis, phi4plot(10,:),'LineWidth',3,'LineStyle',':','Color',[0 0 1]);
plot(xaxis, phi4plot(11,:), 'LineWidth',2,'LineStyle','—.',...
    'Color',[0.847058832645416 0.160784319043159 0]);
plot(xaxis, phi4plot(12,:), 'Color',[0.847058832645416 0.160784319043159 0]);
xlim([5 50]);
ylim([0 0.6]);
% Create xlabel
xlabel({'Energy [keV]'},'FontWeight','bold','FontSize',16,...
    'FontName','Times');
% Create ylabel
ylabel({'Nanoporosity [cm^{−1}]'},'FontWeight','bold','FontSize',16,...
    'FontName','Times');
% Create legend
legend0 = legend({'scaffold I', 'scaffold II', 'scaffold III', 'scaffold IV',...
    'scaffold V', 'scaffold VI', 'scaffold I, 3 weeks after culture',...
    'scaffold II, 3 weeks after culture', 'scaffold III, 6 weeks after culture',...
    'scaffold IV, 6 weeks after culture', 'scaffold V, 8 weeks after culture', ...
    'scaffold VI, 8 weeks after culture'}, 'Fontname', 'Times',...
    'Location','EastOutside', 'Fontsize', 14);
hold off;
```

```matlab
%%%%%%%%%%%%%%%%%%%%%%%%%%%%%%%%%%%%%%%%%%%%%%%%%%%%%%%%%%%%%%%%%%%%
% main.m  : main script for determination of the linear relation    %
%           between grey values and attenuation coefficients,       %
%           convertion the voxel-specific grey values to            %
%           voxel-specific attenuation coefficients, voxel-specific  %
%           nanoporosities and elastic properties                   %
%                                                                   %
% Written by:  Romane Blanchard, Agnes Czenek, and Alexander Dejaco %
% Dependencies: import_images.m, fun_NIST_A.m, images_cleaning.m,    %
%       hom_func.m, generate_grey_el.m, generate_color_rhoec.m      %
% IMWS-TU WIEN                                                      %
%%%%%%%%%%%%%%%%%%%%%%%%%%%%%%%%%%%%%%%%%%%%%%%%%%%%%%%%%%%%%%%%%%%%


clear all
close all
clc

% PARAMETERS

folder='8weeks_8bit'
scaffold_number=17 %used for calculation a and b; 1-20
scaffold='scaffold7_8w'
images_count=1015
dir=['/ct_images/',folder,'/',scaffold];

rho_bTCP = 3.07;    % g/cm3 mass density of CaP scaffold
rho_ETH = 0.789;    % g/cm3 mass density of ethanol


% List of grey value landmarks for all stacks of images
% GV = [1.e;2e;3e;  4e; 5e; 6e; 7e; 8e; 9e; 10e;1.3w;2.3w;3.3w;4.6w;5.6w;6.6w;
%   7.8w;8.8w;9.8w;   10.8w]
%     1   2   3   4   5   6   7   8   9   10  11   12   13   14   15   16
% [0:255] !!
GV_AIR_vec = [77; 55; 70; 44; 42; 59; 64; 65; 39; 36; 37;  57;  80;  56;
71;...
  44; 71; 39; 55; 62];
GV_ETH_vec = [77; 55; 70; 65; 60; 59; 76; 65; 62; 62; 58;  68;  95;  70;
85;...
  63; 84; 50; 68; 62];
GV_AL_vec =  [165;157;159;168;165;167;163;144;180;184;184;133; 185; 155; 171;...
 179; 177;122;169; 105];
GV_SC_vec =  [204;193;188;190;203;195;196;191;185;189;194;138; 194; 163; 178;...
 188; 191;128;180; 198];

%Maximum value of GV for Gaussian distrib.
%   GV = [1.e;2e;3e;  4e; 5e; 6e; 7e; 8e; 9e; 10e;1.3w;2.3w;3.3w;4.6w;5.6w;
%   6.6w;7.8w;8.8w;9.8w;   10.8w]
%       1   2   3   4   5   6   7   8   9   10  11   12   13   14   15 16
GV_E21 = [266;274;0;310;306;  0; 276;234; 0;   0;352; 220;   0;  268;286;...
   0; 298;217;0;0]
```

```matlab
GV_max = [245;240;0;239;246;  0; 240;235; 0;   0;240; 167;   0;  198;212;...
    0; 227;157;0;0]

% Single grey values of the selected scaffold
GV_AIR= GV_AIR_vec(scaffold_number);
GV_ETH= GV_ETH_vec(scaffold_number);
GV_AL= GV_AL_vec(scaffold_number);
GV_SC= GV_SC_vec(scaffold_number);

% Photon energy determined in mainScript_Efunction
photon_energy=21;

% Imports 8—bit CT images
import_images
%save(['raw_volume/',folder,'_',scaffold,'_','raw_volume.mat'])

%load(['raw_volume/',folder,'_',scaffold,'_','raw_volume.mat'])

% Gets attenuatuion coeffcients for the computed photon energy
fun_NIST_A

% Computatuion of the linearity constants
b=(mu_AIR_theoretical*GV_AL—mu_AL_theoretical*GV_AIR)/(GV_AL—GV_AIR)
a=(mu_AIR_theoretical—mu_AL_theoretical)/(GV_AIR—GV_AL)

% Computation of the nanoporosity
[nanop,threshold]=nanopores(a, b, GV_ETH, GV_AL, GV_E21, GV_max, hist_all,...
 mu_ETH_theoretical, mu_AIR_theoretical, mu_bTCP_theoretical,folder,scaffold,...
 scaffold_number);

% Application of the threshold onto the images
image_cleaning

% grey value vector of bone material
GV_vector=(threshold:GV_max(scaffold_number));
% nanoporosity of the bone
nanop_clean=nanop(GV_vector);


%% Homogenization step for discs of hydroxyapatite in air
hom_func


%% Write data tables
datatable=[GV_vector' nanop_clean' E_hom' nu_hom'];
fid=fopen(['engineering_table_',folder,scaffold,'.txt'],'w');
%fprintf(fid,' GV    porosity    Ehom    nuhom  \r\n');
fprintf(fid, '%3.0f  %2.4f  %3.4f  %3.4f  \r\n',datatable');
fclose(fid);

%% Reduction of image size by grouping of voxels + Generation of txt files
```

```matlab
% with element number and porosity/Young's modulus/Poisson's ratio
 generate_grey_el

%% Generation of color maps
 generate_color_rhoec


%%%%%%%%%%%%%%%%%%%%%%%%%%%%%%%%%%%%%%%%%%%%%%%%%%%%%%%%%%%%%%%%%%%%%%%%%
%                                                                     %
% Subscript import_images.m                                           %
%                                                                     %
%%%%%%%%%%%%%%%%%%%%%%%%%%%%%%%%%%%%%%%%%%%%%%%%%%%%%%%%%%%%%%%%%%%%%%%%%

slice=imread([dir,'/raw/',scaffold,'_0000.tif']);
%slice=imread([dir,'/raw/',scaffold,'_0000.tif']);

build_dimx=size(slice,1);
build_dimy=size(slice,2);
build_dimz=images_count;
voxels=build_dimx*build_dimy;

volumes=zeros(build_dimx,build_dimy,images_count,'uint8');
hist_all=zeros(1,256); %empty variable for matlab to be quicker


for i=1:images_count
    if i<11
        slice = imread([dir,'/raw/',scaffold,'_000',num2str(i-1),'.tif']);
    elseif i>10 && i<101
        slice = imread([dir,'/raw/',scaffold,'_00',num2str(i-1),'.tif']);
    elseif i>100 && i<1001
        slice = imread([dir,'/raw/',scaffold,'_0',num2str(i-1),'.tif']);
    else
        slice = imread([dir,'/raw/',scaffold,'_',num2str(i-1),'.tif']);
    end
    volumes(:,:,i)=uint8(slice);
    disp(['imported ',num2str(i),'/',num2str(images_count)]);

    slice2 = double(slice); % convert to double
    slice_vec = reshape(slice2,voxels,1);  % make vector
    n = hist(slice_vec, 0:255);  % n...frequency count
    hist_all = hist_all + n;
end


%%%%%%%%%%%%%%%%%%%%%%%%%%%%%%%%%%%%%%%%%%%%%%%%%%%%%%%%%%%%%%%%%%%%%%%%%
%                                                                     %
% Subscript image_cleaning.m                                          %
%                                                                     %
%%%%%%%%%%%%%%%%%%%%%%%%%%%%%%%%%%%%%%%%%%%%%%%%%%%%%%%%%%%%%%%%%%%%%%%%%
```

186

```matlab
% Loop over the three dimentions of the space through the CT images
for z=1:(build_dimz)
    for y=1:build_dimy
        for x=1:build_dimx

            if (volumes(x,y,z) < threshold)
                volumes(x,y,z) = 0; % Below threshold is put to zero
            else
                if (volumes(x,y,z) > GV_max(scaffold_number));
            % above GV_max is put to equal to GV_max to get [0:255]
                    volumes(x,y,z) = GV_max(scaffold_number);

                end
            end

        end
    end
    disp(['running ',num2str(z),'/',num2str(build_dimz)])
end

save(['cleaned_volume/',folder,'_',scaffold,'_','cleaned_volume.mat'])

% Writes "clean" images
for z=1:build_dimz
    disp(['running ',num2str(z),'/',num2str(build_dimz)])
    imwrite(volumes(:,:,z),[dir,'/cleaned/',scaffold,'_',num2str(z),'.tif']);
end


%%%%%%%%%%%%%%%%%%%%%%%%%%%%%%%%%%%%%%%%%%%%%%%%%%%%%%%%%%%%%%%%%%%%%%%%%%
%                                                                      %
% Function nanopores.m                                                 %
%                                                                      %
%%%%%%%%%%%%%%%%%%%%%%%%%%%%%%%%%%%%%%%%%%%%%%%%%%%%%%%%%%%%%%%%%%%%%%%%%%

function [nanop,threshold]=nanopores(a, b, GV_ETH, GV_AL, GV_E21, GV_max,...
    hist_all, mu_ETH_theoretical, mu_AIR_theoretical, mu_bTCP_theoretical,...
    folder,scaffold,scaffold_number)

% Array [0 GVmax]
bins=0:GV_max(scaffold_number);

% Translation from GV to attenuation coefficients using a and b
mu = bins*a+b

% Condition if the scaffolds were scanned in air or ethanol
if scaffold_number <= 10 %scaffolds before cell culture (scaffolds used are: 1,2,4,5,7, an
    nanop = (mu-mu_bTCP_theoretical)/(mu_AIR_theoretical-mu_bTCP_theoretical);
else
    nanop = (mu-mu_bTCP_theoretical)/(mu_ETH_theoretical-mu_bTCP_theoretical); % scaffolds
```

187

```matlab
end

% min value should always be between GV_ethanol and GV_aluminium !?
indx_lower=GV_ETH; % ethanol
indx_higher=GV_AL; % aluminium

% Computes the minimum between the peak of ethanol and the peak of
% bone=threshold
[xx,indx]=min(hist_all(indx_lower:indx_higher));
threshold=(indx_lower+indx)-1


%%%%%%%%%%%%%%%%%%%%%%%%%%%%%%%%%%%%%%%%%%%%%%%%%%%%%%%%%%%%%%%%%%%%%%%
%                                                                   %
% Function hom_func.m                                               %
% Power functions from Fritsch et al., ASME 2013 to compute         %
% homogenized Young's modulus and Poisson's ratio                   %
%                                                                   %
%%%%%%%%%%%%%%%%%%%%%%%%%%%%%%%%%%%%%%%%%%%%%%%%%%%%%%%%%%%%%%%%%%%%%%%

% Values from Liang et al., Acta Biomaterialia 6 (2010)
E_s= 110.3; %[GPa]
nu_s= 0.276;

%% Data from Fritsch et al., ASME 2013 (Tables 3 and 5) for disks
% coefficients for Young's modulus
Be=0.9867; Ce=2.053;

% coefficients for Poisson's ratio
Av=-1.0521*nu_s+0.2197;
Bv=2.2684*nu_s-0.4645;
Cv=-0.8121*nu_s+0.1662;
Dv=0.3602*nu_s-0.0718;
Ev=0.2394*nu_s+0.1496;

%% Loop over the nanoporosities between threshold and maximum GV
for i=1:length(nanop_clean)
    phi=nanop_clean(i); % phi is the porosity

    %Displays advancement
    if mod(i, 50)==0
        disp([num2str(i),'/', num2str(length(nanop_clean))]);
    end

    % Homogenized Young's modulus [Eq.(37), Fritsch et al.]
    E_hom(i)=E_s*Be*(1-phi)^Ce;

    % Homogenized Poisson's ratio [Eq.(50), Fritsch et al.]
    nu_hom(i)=Av*(1-phi)^4+Bv*(1-phi)^3+Cv*(1-phi)^2+Dv*(1-phi)+Ev;
```

```
end
```

SOFTWARE CODES FOR FRACTURE RISK ASSESSMENT OF VERTEBRAE

This chapter gives a selection of computer codes written in Matlab [197], Python [247] and Fortran [4] programming languages, which are related to the developments described in Chapter 4, to be published in (Blanchard et al, 2014).

```matlab
%%%%%%%%%%%%%%%%%%%%%%%%%%%%%%%%%%%%%%%%%%%%%%%%%%%%%%%%%%%%%%%%%%
%                                                              %
% energy_cort.m: script to find the peak of energy and         %
% the mass density of extracellular bone material              %
% dependencies: — fun_NIST.m                                   %
%               — relation_mu_GV.m                             %
% IMWS——TU WIEN                                                %
%                                                              %
%%%%%%%%%%%%%%%%%%%%%%%%%%%%%%%%%%%%%%%%%%%%%%%%%%%%%%%%%%%%%%%%%

close all; clear all; clc;
disp(['starts script'])

%% Initialization
% from Malandrino et al., 2011
rho_HA=3;           % g/cm3
rho_org=1.42;       % g/cm3 from Morin et al., 2013
rho_w=1;            % g/cm3
rho_soft=1.04;      % g/cm3 mean mass density of the tissues surrounding
                    % the spine: muscle, blood, kidney, Liver, spleen
                    % and spinal cord from Mast, 2000
rho_fat=0.95;       % g/cm3 from Mast, 2000

% Porosities
phi_lac=0.1;        % lacunar porosity
phi_vas_cort=0;   % macroscopic cortical porosity

% Characteristic lengths
l_cort=0.26;         %mm
l_pixel=0.324;       %mm
```

```matlab
% Peaks from histogram
GV_fat=72;
GV_soft=84;
GV_max=164;
GV_ante_max=156;
GV_air=0;




% System of equations [Eq. (1)]
% syms l1 l2 GVev lpixel GVsoft lcort GVmax GVmax_1
% S=solve((l1/lpixel)*GVev+(1-l1/lpixel)*GVsoft==GVmax,...
%          (l2/lpixel)*GVev+(1-l2/lpixel)*GVsoft==GV_ante_max,...
%           l1+l2==lcort, l1, l2, GVev);

% Theoretical GV_BM considering the size of the cortical shell and the
% pixel size [Eq. (2)]
GV_ev=(l_pixel/l_cort)*(GV_max+GV_ante_max-2*GV_soft)+GV_soft;
l1=(l_cort*(GV_max - GV_soft))/(GV_max + GV_ante_max - 2*GV_soft);
l2=(l_cort*(GV_ante_max - GV_soft))/(GV_max + GV_ante_max - 2*GV_soft);

% volume fraction of water in the middle peak (soft tissues) as composite
%of water and collagen [Eq. (6)]
phi_w_soft=(rho_soft-rho_org)/(rho_w-rho_org);


%% Loop over the energies
disp(['loop over energy...']);
for ii=1:100
    close all
    photon_energy=ii;

    % Computes the X-ray attenuation coefficient depending on energies
    fun_NIST;

    % computes the attenuation coefficient of the soft material from average
    % laws for attenuation coefficients and mass densities (Eq. (4))
    mu_soft=mu_w*phi_w_soft+mu_col*(1-phi_w_soft);


    % Computes coefficients a and b with values assigned to left and right
    % peaks (consequence of Eq. (2a)-(2b))
    a= (mu_fat-mu_soft)/(GV_fat-GV_soft);
    b= (mu_fat*GV_soft-mu_soft*GV_fat)/(GV_soft-GV_fat);

    % arrays of a and b for all energies for plotting
    a_vec(ii)=a; b_vec(ii)=b;

    % Computes the attenuation coefficient of the max GV (Eq. (2c))
    mu_BM=a*GV_ev+b;
```

```matlab
% Computation of volume fractions fHA, forg, fH2O
% critical apparent mass density of HA (see Vuong & Hellmich between Eq. 24
% and 25).
rhoHAcrit=1.18;  %g/cm3

% variation of extracellular mass density between 1,5 and 2 in 100
% steps
rho_ec_vec=linspace(1.5,2,100);

% Loop over the mass density of extracellular bone matrix
for jj=1:length(rho_ec_vec)
    curr_rho_ec=rho_ec_vec(jj);

    % slope of Jenny's curve computed by Claire
    rhoHAapp=1.7042*curr_rho_ec—2.1125;

    % constants of the first branch of the bilinear relation between rho^*_org
    % and rho_HA^*
    A=0.29; B=0.17;  %g/cm3

    % volume fractions from Vuong and Hellmich
    if rhoHAapp<=rhoHAcrit
        % expression of forg=(A*rhoHA*fHA+B)/rhoorg and fw=1—fHA—forg
        % in fHA*rhoHA=rhoec—forg*rhoorg—fw*rhow
        exfHA=(curr_rho_ec—B*(1—(rho_w/rho_org))—rho_w)/(rho_HA*(1+A—(A*rho_w/...
            rho_org))—rho_w);
        %Eq. 22 Vuong and Hellmich
        exforg=(A*rho_HA*exfHA+B)/rho_org;
        exfw=1—exfHA—exforg;

        %expression from Eq. 23 of Vuong and Hellmich without apparent
    %mass densities
        Atilde=((A*rhoHAcrit+B)*rho_HA)/(rho_org*(rho_HA—rhoHAcrit));

    else
        % simplification of fHA from forg=Atilde*(1—exfHA) and fw=1—fHA—forg
        % in fHA*rhoHA=rhoec—forg*rhoorg—fw*rhow
        exfHA=1+(curr_rho_ec—rho_HA)/(rho_HA+rho_w*(Atilde—1)—rho_org*Atilde);
        % from Eq. 23 of Vuong and Hellmich
        exforg=Atilde*(1—exfHA);
        exfw=1—exfHA—exforg;

    end

    % attenuation coefficient of extracellular bone matrix [Eq.(7)]
    mu_ec_vec(jj)=exfHA*mu_HA+exforg*mu_col+exfw*mu_w;

end

% attenuation of extravascular bone matrix when zero vascular porosity
mu_exvas_comp=mu_BM;
```

```matlab
    % attenuation of extravascular bone matrix [Eq. (8)]
    mu_ev_vec=phi_lac*mu_w+ (1-phi_lac)*mu_ec_vec;


    % Ratio R [Eq. (9)]; on lines: evolution by increasing mass density,
    %on columns: evolution by increasing energy
    ratio_mu(ii,:)=mu_exvas_comp./mu_ev_vec;


    % Saves the attenuation coefficients as vectors for all energies
    mu_HA_vec(ii)=mu_HA;
    mu_col_vec(ii)=mu_col;
    mu_w_vec(ii)=mu_w;
    mu_fat_vec(ii)=mu_fat;

end

% Computation of points for Fig. 6(b)
%Selects ratio_mu very close to 1 for each combination of mass density and
%energy
n=1;
for kk=1:100
    for ll=1:length(rho_ec_vec)
        if ratio_mu(kk,ll)<1.005 && ratio_mu(kk,ll)>0.995
            %[energy, rho_ec, R]
            curve_rho_ec(n,:)=[kk rho_ec_vec(ll) ratio_mu(kk,ll)]
            n=n+1;
        end

    end
end

%Finds minimum of points close to 1 for each energy step and assign one
%point per energy step
n=1
for ll=2:length(curve_rho_ec)
    curr_e=curve_rho_ec(ll,1);
    if curr_e==curve_rho_ec(ll-1,1);
        continue
    else
    [idx]=find(curve_rho_ec(:,1)==curr_e);
    [minval, minidx]=min(curve_rho_ec(idx,2));
    curve_rho_ec_final(n,:)=[curr_e, minval];
    n=n+1
    end
end

disp(['Plotting...']);

%% Plots
```

```matlab
xaxis=1:100;

%Plots Fig. 6(b)
figure1=figure
axes1 = axes('Parent',figure1,'FontWeight','bold','FontSize',16,...
 'XMinorTick','on');
grid(axes1,'on');
hold(axes1,'all');
plot1=plot(curve_rho_ec_final(:,1), curve_rho_ec_final(:,2),'k', 'Linewidth',...
 3, 'Markersize',5);
set(plot1(1), 'MarkerFaceColor',[0 0 0],'MarkerEdgeColor',[0 0 0]);
xlabel('\textbf{Energy [keV]}','FontSize',18, 'interpreter', 'latex');
ylabel({'\textbf{Extracellular Mass density $\rho_{ec}$ [g/cm$^{3}$]}'},...
'FontSize',16, 'interpreter', 'latex');
axis([1 50 1.5 2])
%Create arrow
annotation(figure1,'arrow',[0.593181385421325 0.593181385421325],...
    [0.426070592139572 0.116209168918599]);
%Create arrow
annotation(figure1,'arrow',[0.594016109962227 0.319699499165275],...
    [0.425307305741241 0.425316455696203]);
hold off

% Plots Fig. 3
figure2=figure
axes21 = axes('Parent',figure2,'FontWeight','bold','FontSize',16);
grid(axes21,'on');
hold(axes21,'all');
plot21=plot(xaxis, a_vec, xaxis, b_vec);
set(plot21(1), 'Color', 'k' , 'Linewidth', 2);
set(plot21(2), 'Color', 'k' , 'Linewidth', 2, 'LineStyle','——');
xlabel({'\textbf{Energy [keV]}'},'FontName','Times','FontSize',16,...
 'interpreter', 'latex');
ylabel({'\textbf{Proportionality constants [cm$^{-1}$]}'},'FontName',...
'times','FontSize',16, 'interpreter', 'latex');
legend2 = legend({'$a(\mathcal{E})$', '$b(\mathcal{E})$'}, 'Fontname', ...
'times', 'interpreter', 'latex');
axis([1 100 -50 20])
hold off

% Plots Fig. 6(a)
figure3=figure
axes1 = axes('Parent',figure3,...
    'FontWeight','bold',...
    'FontSize',16, 'XTick',[0 10 20 30 40 50 60 70 80 90 100]);
grid(axes1,'on');
hold(axes1,'all');
for kk=1:length(rho_ec_vec)
    plot1(kk)=plot(xaxis, ratio_mu(:,kk));
end
set(plot1(1), 'Color', 'k' , 'Linewidth', 2);
```

```matlab
set(plot1(2),'LineStyle',':', 'Color', 'k' , 'Linewidth', 2 );
set(plot1(3),'LineStyle','—', 'Color', 'k' , 'Linewidth', 2);
set(plot1(4),'Marker','.','LineWidth',0.5, 'Color', 'k');
set(plot1(5),'Marker','>','LineWidth',0.5, 'Color', 'k' );
set(plot1(6),'LineStyle','—.', 'Color', 'k' , 'Linewidth', 2);
xlabel('\textbf{Energy [keV]}','FontSize',18, 'interpreter', 'latex');
ylabel('\textbf{Ratio R [−]}','FontSize',18, 'interpreter', 'latex');
legend1 = legend({'$\rho_{ec}$=1.5 g/cm$^3$', '$\rho_{ec}$=1.6 g/cm$^3$',...
    '$\rho_{ec}$=1.7 g/cm$^3$','$\rho_{ec}$=1.8 g/cm$^3$',...
'$\rho_{ec}$=1.9 g/cm$^3$','$\rho_{ec}$=2 g/cm$^3$'} , 'interpreter', 'latex');
axis([0 100 0.5 2])
hold off;
% save('fig_energy_104.fig','figure3')


%plot of the NIST curves
figure4 = figure('XVisual',...
    '0x29 (TrueColor, depth 24, RGB mask 0xff0000 0xff00 0x00ff)');
axes4 = axes('YScale','log','YGrid','on','XGrid','on','FontWeight',...
    'bold','FontSize',14);
xlim(axes4,[5 80]);
ylim(axes4,[0.1 10000]);
box(axes4,'on');
hold(axes4,'all');
% Create multiple lines using matrix input to semilogy
plot4=semilogy(xaxis, mu_HA_vec ,xaxis, mu_col_vec ,xaxis, mu_w_vec,...
    xaxis, mu_fat_vec ,'MarkerFaceColor','auto','LineWidth',3,'Parent',axes4);
% semilogy1 = semilogy(energy,NIST_col(:,2),NIST_HA(:,2),NIST_w(:,2),...
%     'MarkerFaceColor','auto','LineWidth',3,...
%     'Parent',axes1);
set(plot4(1),'LineStyle','—.','Color', [0 0.498039215803146 0]);
set(plot4(2),'LineStyle','—','LineStyle','—', 'Color', 'r');
set(plot4(3),'Marker','o', 'Color', 'b');
set(plot4(4), 'Color', 'k');
xlabel({'\textbf{Photon energy [keV]}'},'FontSize',16, 'fontname', 'times',...
    'interpreter', 'latex');
ylabel({'\textbf{$\mu_i$ [cm$^{−1}$]}'},...
    'FontSize',16, 'fontname', 'times', 'interpreter', 'latex');
legend({'hydroxyapatite','collagen','water', 'adipose tissue'},'FontSize',...
16, 'fontname',...
    'times', 'interpreter', 'latex');
```

```matlab
%%%%%%%%%%%%%%%%%%%%%%%%%%%%%%%%%%%%%%%%%%%%%%%%%%%%%%%%%%%%%%%%%%%%%%
%                                                                  %
% mainScript.m: main script to extract voxel-specific material     %
%               properties from the CT images                      %
% written by:   Romane Blanchard from previous codes of A. Fritsch and %
%               A. Dejaco                                          %
% dependencies: - fun_NIST.m                                       %
%               - relation_mu_GV.m                                 %
%               - hom_micro_elas.m                                 %
%               - plots.m                                          %
% IMWS--TU WIEN                                                    %
%                                                                  %
%%%%%%%%%%%%%%%%%%%%%%%%%%%%%%%%%%%%%%%%%%%%%%%%%%%%%%%%%%%%%%%%%%%%%%

close all; clear all; clc;
disp(['starts script'])

micromecha_path=addpath('~/Documents/TU/micromechanics/');
%% Initialization

% CT parameters
photon_energy=24;%keV back-computed
GV_cort=298;
GV_fat=72;
threshold=93;
% Bone
rho_ec=1.67;          % mass density of extracellular bone
                      %        in g/cm3 from Malandrino, 2011
rho_HA=3;             % g/cm3
rho_org=1.42;         % g/cm3
rho_w=1;              % g/cm3
rho_fat=0.95;         % g/cm3 from Mast, 2000
rho_soft=1.052;       % g/cm3 from Mast, 2000

phi_lac=0.1;          % lacunar porosity
phi_vas_cort=0;       % macroscopic cortical porosity

% Stiffness tensors

% Stiffness derived by Claire from the back-computed density
c1111=10.343; c2222=10.343; c3333=12.804;
c1122=4.757; c1133=5.239; c2233=5.239;
c2323=5.817/2; c1313=5.817/2; c1212=5.586/2;

cExvas=[c1111    c1122    c1133    0       0       0;
        c1122    c2222    c2233    0       0       0;
        c1133    c2233    c3333    0       0       0;
        0        0        0       2*c2323  0       0;
        0        0        0        0      2*c1313  0;
        0        0        0        0       0      2*c1212];
```

```matlab
% Pores

I=[1     0    0    0    0    0;
   0     1    0    0    0    0;
   0     0    1    0    0    0;
   0     0    0    1    0    0;
   0     0    0    0    1    0;
   0     0    0    0    0    1];

Ivol=[1/3   1/3 1/3 0    0    0;
   1/3   1/3 1/3 0    0    0;
   1/3   1/3 1/3 0    0    0;
   0     0   0   0    0    0;
   0     0   0   0    0    0;
   0     0   0   0    0    0];
Idev=I—Ivol;
kPores=2.3;
muPores=1E—05;
cPores=2*muPores*Idev+3*kPores*Ivol;



%% Calculates the X—ray attenuation coefficient
disp(['*'])
disp(['calculation of the X—ray attenuation coefficients'])
fun_NIST;

disp(['calculation...done'])

disp(['*****************************'])
disp(['calculation of a, b and attenuation coefficients mu_ec and mu_air'])

relation_mu_GV;

mu_cort=mu_w*phi_vas_cort+mu_ev*(1—phi_vas_cort);

%coefficients a and b with soft
a= (mu_fat—mu_cort)/(GV_fat—GV_cort);
b= mu_cort— (mu_fat—mu_cort)/(GV_fat—GV_cort)*GV_cort;


%% Elastic properties

GV_range=threshold:GV_cort;
mu_range=a*GV_range+b;

fPoresRange=(mu_range—mu_ev)/(mu_w—mu_ev);

hom_micro_elas;

%% Plot
plots;
```

```matlab
fileResults=fopen('elasticityValues.txt','w');
%fprintf(fileResults,'GV Porosity  E1  E2  E3  nu12 nu31 nu23 G12 G13 G23\r\n');
for ll=1:length(GV_range)
fprintf(fileResults, '%d %d %d %d %d %d %d %d %d %d %d\r\n', GV_range(ll),...
    fPoresRange(ll),E1_range(ll), E2_range(ll), E3_range(ll),...
    nu12_range(ll), nu13_range(ll), nu23_range(ll), G12_range(ll),...
    G13_range(ll), G23_range(ll));
end
fclose(fileResults);

save('engineeringvalues.mat')


%%%%%%%%%%%%%%%%%%%%%%%%%%%%%%%%%%%%%%%%%%%%%%%%%%%%%%%%%%%%%%%%%%%%%%%
%                                                                   %
% Base script for generation of input files                         %
% written by:   Romane Blanchard                                    %
%                                                                   %
% dependencies: centroids.m, interp.m, barycentricCoordinates.m,    %
%         generation_elementSet.m                                   %
% IMWS——TU WIEN                                                     %
%                                                                   %
%%%%%%%%%%%%%%%%%%%%%%%%%%%%%%%%%%%%%%%%%%%%%%%%%%%%%%%%%%%%%%%%%%%%%%%


close all; clear all; clc

%% Vertebral body L3
% Finite Element model
el_size=0; % 3 25 2 15 or 0
Path=['./Model_es',num2str(el_size),'/'];
analysis_type='ho'; % ho or he

% Nodes coordinates
N=importdata([Path,'L3—nodes.txt']);

% Element list
L3=importdata([Path,'clean_solid_es',num2str(el_size),'.txt']);
L3_cort_shell=importdata([Path,'clean_cortical_es',num2str(el_size),'.txt']);
L3_superend=importdata([Path,'clean_superEP_es',num2str(el_size),'.txt']);
L3_inferend=importdata([Path,'clean_inferEP_es',num2str(el_size),'.txt']);

% Images
dimx=512;
dimy=512;
dimz=34;
pixel_length=0.3242;

% grey value—specific material properties
el_val=load('elasticityValues.txt');
```

```matlab
% computes centroids of elements
centroids

disp(['centroids done']);

switch analysis_type
    case 'he'

        % Assign grouping factor depending on the ratio of the average FE element
        % length over the pixel size
        grouping_factor=floor(FE_element_size/pixel_length);

        % Loads information from images
        load(['./JPGfiles/clean_mf1','.mat']);

        % Generates point cloud from images
        interp

        % Interpolation between point cloud and FE mesh
        listcentroidsL3=load([Path, 'listcentroidsL3_es',num2str(el_size),...
            '.txt']) ;
        pointcloud=load([Path, 'pointcloud_es',num2str(el_size),'.txt']);

        barycentricCoordinates


    case 'ho'

end

% Imports list of centroids with their corresponding GV
elGV=importdata([Path, 'elementCentroidGV_es', num2str(el_size),'.txt']);
% Finds mean GV value in the model and gets the corresponding Young's
% modulus and Poisson's ratio
[lineGVmean, colGVmean]=find(el_val(:,1)==floor(mean(elGV(:,2))));


%% generation of abaqus input file

inputfile=fopen([Path, 'L3', analysis_type, '_es', num2str(el_size),...
    '.inp'],'w');

% Title
fprintf(inputfile, '**********************************************\r\n');
fprintf(inputfile, '** Script for model of a vertebral body L3\r\n');
fprintf(inputfile, '** from Dr. Z. Sant, University of Malta\r\n');
fprintf(inputfile, '** written by R. Blanchard, TU WIEN/ IMWS\r\n');
fprintf(inputfile, '**********************************************\r\n');

%Heading
fprintf(inputfile,'*Heading\r\n');
```

```matlab
fprintf(inputfile, '** Job name: L3_es%i\r\n', el_size);
fprintf(inputfile,'*Preprint,echo=NO,model=NO,history=NO,contact=NO\r\n');

% Parts
fprintf(inputfile,'**PARTS\r\n');
fprintf(inputfile,'*Part, name=L3BODY\r\n');
fprintf(inputfile, '*Node\r\n');

% prints nodes with coordinates

fprintf(inputfile,' %6.0f, %4.8f, %4.8f, %4.8f\r\n', N(:, 1:4)');
fprintf(inputfile, '**\r\n');
%prints solid elements with nodes
fprintf(inputfile, '*Element, type=C3D4, elset=SOLIDVERTEBRA\r\n');
fprintf(inputfile,'%7.0f, %7.0f, %7.0f, %7.0f, %7.0f\r\n', L3(:, 1:5)');
fprintf(inputfile, '**\r\n');
%prints cortical shell elements with nodes
fprintf(inputfile, '*Element, type=S3, elset=CORTICALSHELL\r\n');
fprintf(inputfile,'%7.0f, %7.0f, %7.0f, %7.0f\r\n',L3_cort_shell(:, 1:4)');
fprintf(inputfile, '**\r\n');
%prints endplates shell elements with nodes
fprintf(inputfile, '*Element, type=S3, elset=LOWERENDPLATE\r\n');
fprintf(inputfile,' %7.0f, %7.0f, %7.0f, %7.0f\r\n', L3_inferend(:, 1:4)');
fprintf(inputfile, '**\r\n');
fprintf(inputfile, '*Element, type=S3, elset=UPPERENDPLATE\r\n');
fprintf(inputfile,' %7.0f, %7.0f, %7.0f, %7.0f\r\n', L3_superend(:, 1:4)');
fprintf(inputfile, '**\r\n');

% Solid sections
fprintf(inputfile, '**************************** SOLID SECTIONS *******');
fprintf(inputfile, '************************\r\n');

switch analysis_type
    case 'ho'
        fprintf(inputfile, '** Section: Section-3-SOLIDVERTEBRA\r\n');
        fprintf(inputfile, '*Solid Section, elset=SOLIDVERTEBRA,');
        fprintf(inputfile, 'material=TRABECULARBONE\r\n');
        fprintf(inputfile, ',\r\n');
    case 'he'
end
fprintf(inputfile,'** Section: Section-3-ENDPLATES\r\n');
fprintf(inputfile,'*Shell Section, elset=UPPERENDPLATE, material=ENDPLATEBONE\r\n');
fprintf(inputfile,'1.,5\r\n');
fprintf(inputfile,'*Shell Section, elset=LOWERENDPLATE, material=ENDPLATEBONE\r\n');
fprintf(inputfile,'1.,5\r\n');
fprintf(inputfile,'*Shell Section, elset=CORTICALSHELL, material=CORTICALBONE\r\n');
fprintf(inputfile,'0.23,5\r\n');

switch analysis_type
    case 'ho'
    case 'he'
```

```matlab
        tot_count=0;
        counter=0;
        E3=el_val(:,5);
        nu13=el_val(:,7);

        for i=1:length(E3)
            n=i+99;
            curr_indexes=find(elGV(:,2)==n);
            curr_elSet=elGV(curr_indexes,1);
            counter=counter+length(curr_indexes);

            if isempty(curr_elSet)==0
                fprintf(file,'*Elset, elset=_Gray');
                fprintf(file,'%d',n);
                fprintf(file,', internal\n');
                a=0;
                for j=1:length(curr_elSet)
                    a=a+1;

                    fprintf(file,'%7.0f', curr_elSet(j));
                    if j<length(curr_elSet)
                        fprintf(file,',');
                    end

                    if a==16
                        fprintf(file,'\n');
                        a=0;
                    end

                end
                fprintf(file,'\n');
                fprintf(file,'*Solid Section, elset=_Gray');
                fprintf(file,'%3.0f',n);
                fprintf(file,', material=Gray');
                fprintf(file,'%3.0f',n);
                fprintf(file,'\n');
                fprintf(file,'1.,\n');
            end
        end
end
fprintf(inputfile, '*End Part\r\n');
fprintf(inputfile, '**\r\n');
fprintf(inputfile, '**\r\n');

% Assembly
fprintf(inputfile, '********************************** ASSEMBLY *******');
fprintf(inputfile, '***************************\r\n');
fprintf(inputfile, '*Assembly, name=Assembly\r\n');
fprintf(inputfile, '*Instance, name=L3BODY, part=L3BODY\r\n');
fprintf(inputfile, '*End Instance\r\n');
fprintf(inputfile, '*Nset, nset=PINNEDSURF, elset=L3BODY.LOWERENDPLATE\r\n');
```

```matlab
fprintf(inputfile, '*Surface, type=ELEMENT, name=LOADSURF\r\n');
fprintf(inputfile, 'L3BODY.UPPERENDPLATE, SPOS\r\n');
fprintf(inputfile, '*End Assembly\r\n');


% Materials
fprintf(inputfile, '********************************** MATERIAL *******');
fprintf(inputfile, '*************************\r\n');


fprintf(inputfile, '*Material, name=CORTICALBONE\r\n');
fprintf(inputfile, '*Elastic\r\n');
% Assigns last value of the GV/elastic properties look—up table, porosity=0
fprintf(inputfile, '%d, %d \r\n', el_val(length(el_val), 5)*1e3,...
    el_val(length(el_val), 7));
switch analysis_type
    case 'ho'
        fprintf(inputfile, '*User Output Variables\r\n');
        fprintf(inputfile, '1,\r\n');
        fprintf(inputfile, '*Material, name=ENDPLATEBONE\r\n');
    case 'he'
        fprintf(inputfile, '*Material, name=ENDPLATEBONE\r\n');
        fprintf(inputfile, '*User Output Variables\r\n');
        fprintf(inputfile, ' 1,\r\n');
end


fprintf(inputfile, '*Elastic\r\n');
% Assigns last value of the GV/elastic properties look—up table, porosity=0
fprintf(inputfile, '%d, %d \r\n', el_val(length(el_val), 5)*1e3,...
    el_val(length(el_val), 7));


switch analysis_type
    case 'ho'
        fprintf(inputfile, '*Material, name=TRABECULARBONE\r\n');
        fprintf(inputfile, '*Elastic\r\n');
        % Assigns the elastic properties of the mean GV of the model
        fprintf(inputfile, '%d, %d \r\n', el_val(lineGVmean,5)*1e3,...
            el_val(lineGVmean,7));
    case 'he'
        tot_count=0;
        counter=0;
        E3=el_val(:,5);
        nu13=el_val(:,7);
        % Loop over all grey values
        for i=1:length(E3)
            n=i+99;
            curr_indexes=find(elGV(:,2)==n);
            curr_elSet=elGV(curr_indexes,1);
            counter=counter+length(curr_indexes);
            fprintf(inputfile,'*Material, name=Gray');
            fprintf(inputfile,'%3.0f',n);
            fprintf(inputfile,'\n');
            fprintf(inputfile,'*Elastic,TYPE=ISOTROPIC\n');
```

```matlab
            fprintf(inputfile,'%10.3f',E3(i)*1e3);
            % Ehome * e9 => [Pa] [N/m^2]
            fprintf(inputfile,',');
            fprintf(inputfile,'%10.3f',nu13(i));
            fprintf(inputfile,'\n');
        end
end

% Step definition
fprintf(inputfile, '****************************** STEP DEFINITION ***');
fprintf(inputfile, '**************************\r\n');
fprintf(inputfile, '** STEP: Step—1\r\n');
fprintf(inputfile, '*Step, name=Step—1\r\n');
fprintf(inputfile, '*Static\r\n');
fprintf(inputfile, '1., 1., 1e—05, 1.\r\n');

% Boundary conditions definition
fprintf(inputfile, '*********************************BOUNDARY CONDITIONS');
fprintf(inputfile, '*************************\r\n');
fprintf(inputfile, '** BOUNDARY CONDITIONS\r\n');
fprintf(inputfile, '** Name: Disp—BC—1 Type: Symmetry/Antisymmetry/Encastre\r\n');
fprintf(inputfile, '*Boundary\r\n');
fprintf(inputfile, 'PINNEDSURF, PINNED\r\n');
fprintf(inputfile, '** LOADS\r\n');
fprintf(inputfile, '** Name: SURFFORCE—1   Type: Pressure Unit pressure:1 MPa\r\n');
fprintf(inputfile, '*Dsload\r\n');
fprintf(inputfile, 'LOADSURF, P, 1\r\n');

% Controls
fprintf(inputfile, '** CONTROLS\r\n');
fprintf(inputfile, '*Controls, reset\r\n');
fprintf(inputfile, '*Controls, analysis=discontinuous\r\n');

% Outputs
fprintf(inputfile, '********************************** OUTPUTS *******');
fprintf(inputfile, '*************************\r\n');
fprintf(inputfile, '** OUTPUT REQUESTS\r\n');
fprintf(inputfile, '*Restart, write, frequency=1\r\n');
fprintf(inputfile, '** FIELD OUTPUT: F—Output—1\r\n');
fprintf(inputfile, '*Output, field, variable=ALL\r\n');
fprintf(inputfile, '*Element Output, directions=YES\r\n');
fprintf(inputfile, 'UVARM\r\n');
fprintf(inputfile, '** HISTORY OUTPUT: H—Output—1\r\n');
fprintf(inputfile, '*Output, history, variable=ALL\r\n');
fprintf(inputfile, '*End Step\r\n');

% End Input file

disp(['input file generated!'])
```

```
%%%%%%%%%%%%%%%%%%%%%%%%%%%%%%%%%%%%%%%%%%%%%%%%%%%%%%%%%%%%%%%%%%%%
%                                                                %
% User subroutine to print the orientation of the elements building   %
% up the cortical shell                                          %
% written by: Romane Blanchard, with the support of Markus Lukacevic   %
% IMWS, TUWIEN                                                   %
%                                                                %
%%%%%%%%%%%%%%%%%%%%%%%%%%%%%%%%%%%%%%%%%%%%%%%%%%%%%%%%%%%%%%%%%%%%


      SUBROUTINE UVARM(UVAR,DIRECT,T,TIME,DTIME,CMNAME,ORNAME,
     1 NUVARM,NOEL,NPT,LAYER,KSPT,KSTEP,KINC,NDI,NSHR,COORD,
     2 JMAC,JMATYP,MATLAYO,LACCFLA)
      INCLUDE 'ABA_PARAM.INC'
C
      CHARACTER*80 CMNAME,ORNAME
      CHARACTER*3 FLGRAY(15)
      DIMENSION UVAR(NUVARM),DIRECT(3,3),T(3,3),TIME(2)
      DIMENSION ARRAY(15),JARRAY(15),JMAC(*),JMATYP(*),COORD(*)

C     The dimensions of the variables FLGRAY, ARRAY and JARRAY
C     must be set equal to or greater than 15.

      open (unit = 10, file = '~/Documents/VertebraProject/usefulThings/
      orient0c.txt', status='unknown', position='append')
      write(10, "(2I8, 9F16.8)" ) NOEL, NPT, DIRECT(1:3,1), DIRECT(1:3,2),
      DIRECT(1:3,3)
C     print *,'NOEL, NPT', NOEL, NPT, T(1:3,1)
      close (unit = 10)

      RETURN
      END



%%%%%%%%%%%%%%%%%%%%%%%%%%%%%%%%%%%%%%%%%%%%%%%%%%%%%%%%%%%%%%%%%%%%
%                                                                %
% User subroutine to print the orientation of the elements building   %
% up the endplates                                               %
% written by: Romane Blanchard, with the support of Markus Lukacevic   %
% IMWS, TUWIEN                                                   %
%                                                                %
%%%%%%%%%%%%%%%%%%%%%%%%%%%%%%%%%%%%%%%%%%%%%%%%%%%%%%%%%%%%%%%%%%%%


      SUBROUTINE UVARM(UVAR,DIRECT,T,TIME,DTIME,CMNAME,ORNAME,
     1 NUVARM,NOEL,NPT,LAYER,KSPT,KSTEP,KINC,NDI,NSHR,COORD,
     2 JMAC,JMATYP,MATLAYO,LACCFLA)
      INCLUDE 'ABA_PARAM.INC'
C
      CHARACTER*80 CMNAME,ORNAME
      CHARACTER*3 FLGRAY(15)
```

```fortran
      DIMENSION UVAR(NUVARM),DIRECT(3,3),T(3,3),TIME(2)
      DIMENSION ARRAY(15),JARRAY(15),JMAC(*),JMATYP(*),COORD(*)

C     The dimensions of the variables FLGRAY, ARRAY and JARRAY
C      must be set equal to or greater than 15.

      open (unit = 10, file = '~/Documents/VertebraProject/usefulThings/...
      orient0e.txt', status='unknown', position='append')
      write(10, "(2I8, 9F16.8)" ) NOEL, NPT, DIRECT(1:3,1),...
      DIRECT(1:3,2), DIRECT(1:3,3)
C     print *,'NOEL, NPT', NOEL, NPT, T(1:3,1)
      close (unit = 10)

      RETURN
      END
```

```python
%%%%%%%%%%%%%%%%%%%%%%%%%%%%%%%%%%%%%%%%%%%%%%%%%%%%%%%%%%%%%%%%%%%%%%%%
%                                                                    %
% Python script to import the results from abaqus in one command     %
% written by:   Romane Blanchard IMWS-TUWIEN                         %
%                                                                    %
%%%%%%%%%%%%%%%%%%%%%%%%%%%%%%%%%%%%%%%%%%%%%%%%%%%%%%%%%%%%%%%%%%%%%%%%

#import abaqus functions
#from abaqus import *
from odbAccess import *
from abaqusConstants import *
from odbMaterial import *
from odbSection import *

#import python functions
#from tabular import tabular

el_size=raw_input('el_size?')
analysis=raw_input('analysis type?')

#set the path
odbPath='./Model_es{0}/L3{1}_es{2}.odb'.format(el_size, analysis, el_size)

#open odb file
odb=openOdb(path=odbPath)

#create variable for the first step
lastFrame=odb.steps['Step-1'].frames[1]

#variable which refers to displacement U, stress S, and strain E
displacement=lastFrame.fieldOutputs['U']
stress=lastFrame.fieldOutputs['S']
strain=lastFrame.fieldOutputs['E']
#variable which refers to volume of elements
```

```python
volumes=lastFrame.fieldOutputs['EVOL']

#variables which refers to element sets
cortical=odb.rootAssembly.instances['L3BODY'].elementSets['CORTICALSHELL']
trabecular=odb.rootAssembly.instances['L3BODY'].elementSets['SOLIDVERTEBRA']
upperendplate=odb.rootAssembly.instances['L3BODY'].elementSets['UPPERENDPLATE']
lowerendplate=odb.rootAssembly.instances['L3BODY'].elementSets['LOWERENDPLATE']

#variable that refers to the stress tensor of the element set in the last frame
# of the first set
field_U_trab=displacement.getSubset(region=trabecular, position=NODAL)
fieldValues_U_trab=field_U_trab.values

f_trab=open('./Model_es{0}/U{1}_trab_es{2}.txt'.format(el_size, analysis,
 el_size), 'w')
#print field output for trabecular core
for v in fieldValues_U_trab:
    f_trab.write(str(v.elementLabel)+' '),
    for component in v.data:
        f_trab.write(str(component)+' '),
    f_trab.write('\r\n')
#close the txt files
f_trab.close()

#variable that refers to the stress tensor of the element set in the last
#frame of the first set
field_V_trab=volumes.getSubset(region=trabecular, position=WHOLE_ELEMENT)
fieldValues_V_trab=field_V_trab.values

#variable that refers to the stress tensor of the element set in the last
# frame of the first set
field_V_cort=volumes.getSubset(region=cortical, position=WHOLE_ELEMENT)
fieldValues_V_cort=field_V_cort.values

#variable that refers to the stress tensor of the element set in the last frame
# of the first set
field_V_upperend=volumes.getSubset(region=upperendplate, position=WHOLE_ELEMENT)
fieldValues_V_upperend=field_V_upperend.values

#variable that refers to the stress tensor of the element set in the last frame
# of the first set
field_V_lowerend=volumes.getSubset(region=lowerendplate, position=WHOLE_ELEMENT)
fieldValues_V_lowerend=field_V_lowerend.values

#opens the txt files with the results
f_trab=open('./Model_es{0}/V{1}_trab_es{2}.txt'.format(el_size, analysis,
 el_size), 'w')
f_cort=open('./Model_es{0}/V{1}_cort_es{2}.txt'.format(el_size, analysis,
 el_size), 'w')
f_upperend=open('./Model_es{0}/V{1}_superend_es{2}.txt'.format(el_size,
 analysis, el_size), 'w')
```

```python
f_lowerend=open('./Model_es{0}/V{1}_inferend_es{2}.txt'.format(el_size,
 analysis, el_size), 'w')


#print field output for trabecular core
for v in fieldValues_V_trab:
    f_trab.write(str(v.elementLabel)+' '),
    f_trab.write(str(v.data)+' '),
    f_trab.write('\r\n')
#close the txt files
f_trab.close()

#print field output for cortical shell
for v in fieldValues_V_cort:
    f_cort.write(str(v.elementLabel)+' '),
    f_cort.write(str(v.data)+' '),
    f_cort.write('\r\n')
#close the txt files
f_cort.close()

#print field output for upper endplate
for v in fieldValues_V_upperend:
    f_upperend.write(str(v.elementLabel)+' '),
    f_upperend.write(str(v.data)+' '),
    f_upperend.write('\r\n')
#close the txt files
f_upperend.close()

#print field output for upper endplate
for v in fieldValues_V_lowerend:
    f_lowerend.write(str(v.elementLabel)+' '),
    f_lowerend.write(str(v.data)+' '),
    f_lowerend.write('\r\n')
#close the txt files
f_lowerend.close()

#variable that refers to the stress tensor of the element set in the last
# frame of the first set
field_S_cort=stress.getSubset(region=cortical, position=INTEGRATION_POINT)
field_S_trab=stress.getSubset(region=trabecular, position=INTEGRATION_POINT)
field_S_upperend=stress.getSubset(region=upperendplate,
 position=INTEGRATION_POINT)
field_S_lowerend=stress.getSubset(region=lowerendplate,
 position=INTEGRATION_POINT)

fieldValues_S_cort=field_S_cort.values
fieldValues_S_trab=field_S_trab.values
fieldValues_S_upperend=field_S_upperend.values
fieldValues_S_lowerend=field_S_lowerend.values

#opens the txt files with the results
```

```python
f_trab=open('./Model_es{0}/S{1}_trab_es{2}.txt'.format(el_size, analysis,
 el_size), 'w')
f_cort=open('./Model_es{0}/S{1}_cort_es{2}.txt'.format(el_size, analysis,
 el_size), 'w')
f_upperend=open('./Model_es{0}/S{1}_superend_es{2}.txt'.format(el_size,
 analysis, el_size), 'w')
f_lowerend=open('./Model_es{0}/S{1}_inferend_es{2}.txt'.format(el_size,
 analysis, el_size), 'w')

#print field output for trabecular core
for v in fieldValues_S_trab:
    f_trab.write(str(v.elementLabel)+' '),
    for component in v.data:
        f_trab.write(str(component)+' '),
    f_trab.write('\r\n')

#print field output for cortical shell
for v in fieldValues_S_cort:
    f_cort.write(str(v.elementLabel)+' '),
    for component in v.data:
        f_cort.write(str(component)+' '),
    f_cort.write('\r\n')

#print field output for upper endplate
for v in fieldValues_S_upperend:
    f_upperend.write(str(v.elementLabel)+' '),
    for component in v.data:
        f_upperend.write(str(component)+' '),
    f_upperend.write('\r\n')

#print field output for lower endplate
for v in fieldValues_S_lowerend:
    f_lowerend.write(str(v.elementLabel)+' '),
    for component in v.data:
        f_lowerend.write(str(component)+' '),
    f_lowerend.write('\r\n')

#close the txt files
f_trab.close()
f_cort.close()
f_upperend.close()
f_lowerend.close()

#variable that refers to the strain tensor of the element set in the last
# frame of the first set
field_E_cort=strain.getSubset(region=cortical, position=INTEGRATION_POINT)
field_E_trab=strain.getSubset(region=trabecular, position=INTEGRATION_POINT)
field_E_upperend=strain.getSubset(region=upperendplate,
 position=INTEGRATION_POINT)
field_E_lowerend=strain.getSubset(region=lowerendplate,
 position=INTEGRATION_POINT)
```

```python
fieldValues_E_cort=field_E_cort.values
fieldValues_E_trab=field_E_trab.values
fieldValues_E_upperend=field_E_upperend.values
fieldValues_E_lowerend=field_E_lowerend.values

#opens the txt files with the results
f_trab=open('./Model_es{0}/E{1}_trab_es{2}.txt'.format(el_size, analysis,
 el_size), 'w')
f_cort=open('./Model_es{0}/E{1}_cort_es{2}.txt'.format(el_size, analysis,
 el_size), 'w')
f_upperend=open('./Model_es{0}/E{1}_superend_es{2}.txt'.format(el_size,
 analysis, el_size), 'w')
f_lowerend=open('./Model_es{0}/E{1}_inferend_es{2}.txt'.format(el_size,
 analysis, el_size), 'w')

#print field output for trabecular core
for v in fieldValues_E_trab:
    f_trab.write(str(v.elementLabel)+' '),
    for component in v.data:
        f_trab.write(str(component)+' '),
    f_trab.write('\r\n')

#print field output for cortical shell
for v in fieldValues_E_cort:
    f_cort.write(str(v.elementLabel)+' '),
    for component in v.data:
        f_cort.write(str(component)+' '),
    f_cort.write('\r\n')

#print field output for upper endplate
for v in fieldValues_E_upperend:
    f_upperend.write(str(v.elementLabel)+' '),
    for component in v.data:
        f_upperend.write(str(component)+' '),
    f_upperend.write('\r\n')

#print field output for lower endplate
for v in fieldValues_E_lowerend:
    f_lowerend.write(str(v.elementLabel)+' '),
    for component in v.data:
        f_lowerend.write(str(component)+' '),
    f_lowerend.write('\r\n')

#close the txt files
f_trab.close()
f_cort.close()
f_upperend.close()
f_lowerend.close()
```

```matlab
%%%%%%%%%%%%%%%%%%%%%%%%%%%%%%%%%%%%%%%%%%%%%%%%%%%%%%%%%%%%%%%%%%%%%%%%%%
%                                                                      %
% Subscript centroids.m                                                %
% Computes centroids of elements                                       %
% dependencies: clean_solid_esX.txt and L3—nodes.txt                   %
% written by: Romane Blanchard, IMWS, TUWIEN                           %
%                                                                      %
%%%%%%%%%%%%%%%%%%%%%%%%%%%%%%%%%%%%%%%%%%%%%%%%%%%%%%%%%%%%%%%%%%%%%%%%%%


% Initialization
el_size_counter=0;
% opens txt file
file_centroids=fopen([Path, 'listcentroidsL3_es', num2str(el_size),...
 '.txt'],'w');

% Node numbers
N1_L3=L3(:,2); N2_L3=L3(:,3); N3_L3=L3(:,4); N4_L3=L3(:,5);
% Element number
elnum_L3=L3(:,1);
% Node number
Nnumber=N(:,1);

tic;
% Loop over the elements
for i=1:length(L3)

    if (mod(i,1000)==0)
        clc
        disp([(num2str((i*100)/length(L3))),'%'])
        toc
    end

    % Reallocation to current node and element number
    curr_el=elnum_L3(i);
    curr_node1=N1_L3(i);
    curr_node2=N2_L3(i);
    curr_node3=N3_L3(i);
    curr_node4=N4_L3(i);

    % finds the node coordinates of the 4 nodes of the current element
    [idx1, val]=find(N(:,1)==curr_node1);
    x1=N(idx1,2); y1=N(idx1,3); z1=N(idx1,4);
    [idx2, val]=find(N(:,1)==curr_node2);
    x2=N(idx2,2); y2=N(idx2,3); z2=N(idx2,4);
    [idx3, val]=find(N(:,1)==curr_node3);
    x3=N(idx3,2); y3=N(idx3,3); z3=N(idx3,4);
    [idx4, val]=find(N(:,1)==curr_node4);
    x4=N(idx4,2); y4=N(idx4,3); z4=N(idx4,4);

    % computes coordinates of the center of the element
```

```matlab
    xg=(x1+x2+x3+x4)/4;
    yg=(y1+y2+y3+y4)/4;
    zg=(z1+z2+z3+z4)/4;

    % computes length of the element edges
    l1=norm([x2—x1, y2—y1, z2—z1]);
    l2=norm([x3—x2, y3—y2, z3—z2]);
    l3=norm([x1—x3, y1—y3, z1—z3]);
    l4=norm([x4—x1, y4—y1, z4—z1]);
    l5=norm([x4—x2, y4—y2, z4—z2]);
    l6=norm([x4—x3, y4—y3, z4—z3]);

    % sum of the sizes for averaging
    el_size_counter=el_size_counter+(l1+l2+l3+l4+l4+l6)/6;

    % prints the coordinates in the txt file
    fprintf(file_centroids, '%7.0f  %7.6f  %7.6f  %7.6f\r\n',...
    curr_el, xg, yg, zg);

end

% closes txt file
fclose(file_centroids);

% averages the edge length
FE_element_size=el_size_counter/length(L3);
% display mean edge length in the command window
disp(['mean element edge length: ', num2str(FE_element_size), ' mm.']);


%%%%%%%%%%%%%%%%%%%%%%%%%%%%%%%%%%%%%%%%%%%%%%%%%%%%%%%%%%%%%%%%%%%%%%%%%
%                                                                     %
% Subscript interp.m                                                  %
% Generation of the point cloud for the interpolation                %
% dependencies: clean34.mat and listcentroidsL3_esX.txt              %
% written by: Romane Blanchard, IMWS, TUWIEN                          %
%                                                                     %
%%%%%%%%%%%%%%%%%%%%%%%%%%%%%%%%%%%%%%%%%%%%%%%%%%%%%%%%%%%%%%%%%%%%%%%%%


% all the measures are in millimeters

% Creation of the pointcloud for the vertebra
dX=pixel_length*grouping_factor; % X indent
offsetZ=—10; % offset
dZ=1.25; % Z indent
curr_xp=dX; % current point

% opens the text file
filePC=fopen([Path, 'pointcloud_es',num2str(el_size),'.txt'],'w');
tic;
```

```matlab
% loop over the x axis
for x=floor(dimx/grouping_factor):-1:1

    if (mod(x,10)==0)
        clc
        disp([(num2str((x*100)/(dimx/grouping_factor))),'%'])
        toc
    end

    curr_yp=dX;
    curr_xp=curr_xp+dX;

    % loop over y axis
    for y=1:floor(dimy/grouping_factor)
        curr_zp=offsetZ;
        curr_yp=curr_yp+dX;

        %loop over z axis
        for z=dimz:-1:1
            curr_zp=curr_zp+dZ;
            % if the value of the pixel is over the threshold,
            % prints point cloud
            if reduced_voxels(x,y,z)>100
                fprintf(filePC, '%6.8f  %6.8f  %6.8f  %6.8f\r\n', curr_xp,...
                    curr_yp, curr_zp, reduced_voxels(x,y,z));
            else
                continue
            end

        end
    end
end

%close txt file
fclose(filePC);

%% Plots the point cloud and the mesh in 3D for visual check
pointcloud=load([Path, 'pointcloud_es',num2str(el_size),'.txt']);
listcentroidsL3=load([Path, 'listcentroidsL3_es', num2str(el_size), '.txt']);
figure
hold on
plot3(listcentroidsL3(:,2), listcentroidsL3(:,3),listcentroidsL3(:,4),'rx');
plot3(pointcloud(:,2), pointcloud(:,1), pointcloud(:,3),'x');
legend('Finite elements centroids', 'Point cloud')
xlabel('coord x'); ylabel('coord y'); zlabel('coord z');
```

```matlab
%%%%%%%%%%%%%%%%%%%%%%%%%%%%%%%%%%%%%%%%%%%%%%%%%%%%%%%%%%%%%%%%%%%%%%%%
%                                                                    %
% Subscript barycentricCoordinates.m                                 %
% Research of the barycentric coordinates in 3D space                %
% — interpolation mesh/pointcloud                                    %
% written by: Claire Morin and Romane Blanchard —— IMWS              %
%                                                                    %
%%%%%%%%%%%%%%%%%%%%%%%%%%%%%%%%%%%%%%%%%%%%%%%%%%%%%%%%%%%%%%%%%%%%%%%%

%% Initialization

dz=1.25;
dx=pixel_length*grouping_factor; dy=dx;
zVector=-10:1.25:42.5;

%% Loads data needed for the computation
% list of element with centroids
mesh=listcentroidsL3(:,2:4); %p
% point cloud generated in interp.m
pc = [pointcloud(:,2), pointcloud(:,1), pointcloud(:,3), pointcloud(:,4)];

% opens the text file
file=fopen([Path, 'elementCentroidGV_es', num2str(el_size), '.txt'],'w');

%% Loop over the centroid of the elements
for i=1:length(mesh)


    if (mod(i,50)==0)
        clc
        disp([num2str(i),'/',num2str(length(mesh))]);
    end

    %finds the closest plane
    curr_z= mesh(i,3);
    [dist,idx]=sort(abs(curr_z-zVector(:)));
    z_plane=zVector(idx(1));

    % selects the points located on the current plane
    pointsOnPlane=pc(find(pc(:,3)==z_plane),:);

    %if it doesn't find points...
    while isempty(pointsOnPlane)==1
        %...looks at the next plane
        z_plane=z_plane+dz*sign(curr_z-zVector(idx(1)));
        %and fix the points above and below the 1st and last planes
        if z_plane>32.5
            z_plane=32.5;
        elseif z_plane<-8.75
            z_plane=-8.75;
        end
```

```matlab
    pointsOnPlane=pc(find(pc(:,3)==z_plane),:);

end


%finds the 3 closest neighbors on the current plane
[neighborIds neighborDistances] = kNearestNeighbors(pointsOnPlane(:,1:3),...
    mesh(i,:), 3);

% declares the 3 neighboring points
p1 = pointsOnPlane(neighborIds(1),1:3);
p2 = pointsOnPlane(neighborIds(2),1:3);
p3 = pointsOnPlane(neighborIds(3),1:3);

%if the points are colinear, point 3 is moved out to form a triangle
if p1(1)==p2(1)
    p3(1)=p1(1)+dx*sign(mesh(i,1)-p1(1));
    p3(2)=p1(2);
elseif p1(2)==p2(2)
    p3(2)=p1(2)+dx*sign(mesh(i,2)-p1(2));
    p3(1)=p1(1);
end

% calculates the normal to the triangle
n=cross((p2-p1),(p3-p1));

% the triangle is divided in 3 triangles Ta,Tb,Tc
% calculates the normal na, nb, nc to the triangles Ta,Tb,Tc
na=cross((p3-p2),(mesh(i,:)-p2));
nb=cross((p1-p3),(mesh(i,:)-p3));
nc=cross((p2-p1),(mesh(i,:)-p1));

% calculates the barycentric coordinates
lambda(i,1)=sum(n.*na)/sum(n.*n);
lambda(i,2)=sum(n.*nb)/sum(n.*n);
lambda(i,3)=sum(n.*nc)/sum(n.*n);
if norm(n)<1e-5
    lambda(i,1)=1;
    lambda(i,2)=0;
    lambda(i,3)=0;
end

% calculates the coordinates of the barycentric centers
lambdaCoord=lambda;
checkLambda(i,:)=[lambdaCoord(i,1),lambdaCoord(i,1),lambdaCoord(i,1)]...
    .*p1+[lambdaCoord(i,2),lambdaCoord(i,2),...
    lambdaCoord(i,2)].*p2+[lambdaCoord(i,3),...
    lambdaCoord(i,3),lambdaCoord(i,3)].*p3;

% recalculation of the barycentric coordinates if the point is outside the
% triangle (lambda<0)
```

```matlab
    if lambda(i,1)<0
        sum1=lambda(i,2)+lambda(i,3);
        lambda(i,2)=lambda(i,2)/sum1;
        lambda(i,3)=lambda(i,3)/sum1;
        lambda(i,1)=0;
    end
    if lambda(i,2)<0
        sum1=lambda(i,1)+lambda(i,3);
        lambda(i,1)=lambda(i,1)/sum1;
        lambda(i,3)=lambda(i,3)/sum1;
        lambda(i,2)=0;
    end

    if lambda(i,3)<0
        sum1=lambda(i,2)+lambda(i,1);
        lambda(i,2)=lambda(i,2)/sum1;
        lambda(i,1)=lambda(i,1)/sum1;
        lambda(i,3)=0;
    end

    % calculates the grey value at each element centroid
    GVc(i)= floor(lambda(i,1)*pointsOnPlane(neighborIds(1),4)+...
        lambda(i,2)*pointsOnPlane(neighborIds(2),4)+...
        lambda(i,3)*pointsOnPlane(neighborIds(3),4));

    %prints it to the file elementCentroidGV.txt
    fprintf(file,'%7.0f %4.0f \r\n', listcentroidsL3(i,1), GVc(i));

    matrixByPlane(i,:)=[mesh(i,1) mesh(i,2) z_plane GVc(i)];
end

% close txt file
fclose(file);
% compares the barycentric centers with the actual mesh
diff=checkLambda-mesh;

%% Figure
save('workspace.mat');

% plots the distance between the mesh and the barycenter
figure
hold on
plot1=plot(diff(:,1), 'b');
plot2=plot(diff(:,2), 'r');
plot3=plot(diff(:,3),'g');
xlabel('Element centroids');
ylabel('Mesh-barycenter difference');
title('Distance between the mesh and the barycentric centers');
legend('\lambda_x', '\lambda_y', '\lambda_z');
```

```matlab
%%%%%%%%%%%%%%%%%%%%%%%%%%%%%%%%%%%%%%%%%%%%%%%%%%%%%%%%%%%%%%%%%%%%
%                                                                %
% Base script for post-processing of FE analyses, for computation of   %
%   strain energy density, yielding surfaces and strength        %
% written by:   Romane Blanchard (the strength model written by  %
% Claire Morin)                                                  %
%                                                                %
% dependencies: python_script_output2.py, clean_orient.m,        %
% shellBaseTransformation.m, SEDcomparison.m                     %
% IMWS--TU WIEN                                                  %
%                                                                %
%%%%%%%%%%%%%%%%%%%%%%%%%%%%%%%%%%%%%%%%%%%%%%%%%%%%%%%%%%%%%%%%%%%%


close all; clear all; clc;

method_flag=3; %0 for basic result processing,
%1 for SED,
%2 for yielding surfaces,
%3 for strength

% L3 body, variables to be modified
el_size=0; % 3, 25, 2, 15, 0
Path=['./Model_es', num2str(el_size), '/'];
analysis_type='he'; % he or ho
part='trab'; %lowerend, upperend, cort, trab
part2='trab'; % inferend, superend, cort, trab

% density ultrastructure
rhoult =  1.67;
%number of points where the strength is computed
res_number_4strength=2;
startpoint=1;
% element vs grey values list
el_grey=importdata([Path, 'elementCentroidGV_es',num2str(el_size),'.txt']);


switch method_flag
    case 0

        % Exporting of results from odb database
        if exist([Path,'E',analysis_type, '_', part, '_es', el_size, '.txt'],...
                'file')==0;
            status=system('abq6121 python python_script_output2.py')
        end

        % Loading of results
        % Young's modulus and Poisson's ratio in function of GV
        load(['engineeringvalues.mat'])

        % strains from abaqus
```

```matlab
    strains=load([Path,'E',analysis_type,'_', part2,'_es',...
        num2str(el_size),'.txt']);

    % Stress components in local base
    stressComponents=importdata([Path, 'S',analysis_type,'_', part2,...
        '_es', num2str(el_size), '.txt']);

    % In case of shell elements, abaqus exports 2x the elements,
    % we keep only the first half of the file
    switch part2
        case 'cort'
            strains(length(strains)/2+1:length(strains),:)=[];
            stressComponents(length(stressComponents)/2+1:...
                length(stressComponents),:)=[];
        case 'inferend'
            strains(length(strains)/2+1:length(strains),:)=[];
            stressComponents(length(stressComponents)/2+1:...
                length(stressComponents),:)=[];
        case 'superend'
            strains(length(strains)/2+1:length(strains),:)=[];
            stressComponents(length(stressComponents)/2+1:...
                length(stressComponents),:)=[];
        case 'trab'
    end

    % element volumes
    el_vol=importdata([Path, 'V',analysis_type,'_',part2,'_es',...
        num2str(el_size),'.txt']);

    %% Checks if the array lengths are coherent
    if length(stressComponents)~=length(strains) || ...
            length(stressComponents)~=length(el_vol)
        disp([ 'Warning, different length of arrays '])
        break
    end

    %% Cleans the orientation files, the user subroutine is exporting
%the orientations for the cortical shell (c) when the homogeneous model
% is running, and the endplates shell elements (e) when the
%heterogeneous model is running
    switch analysis_type
        case 'ho'
            stack='c';
        case 'he'
            stack='e';
    end
    localBaseFrames=importdata ([Path, 'orient', num2str(el_size),...
        stack, '.txt']);
    clean_orient

    %%
```

```matlab
        % Orientation of local base frames
        switch part2
            case 'cort'
                localBases=importdata([Path,'localBaseFrames_es',...
                    num2str(el_size), 'c.txt']);
                % Transformation of stresses in the global base frame
                X=stressComponents; value='S';
                shellBaseTransformation
                clear X; clear value;

                % Transformation of strain in global base frame
                X=strains; value='E';
                shellBaseTransformation
                clear X; clear value;

            case 'inferend'
                localBases=importdata([Path,'localBaseFrames_es',...
                    num2str(el_size), 'e.txt']);
                % Transformation of stresses in the global base frame
                X=stressComponents; value='S';
                shellBaseTransformation
                clear X; clear value;

                % Transformation of strain in global base frame
                X=strains; value='E';
                shellBaseTransformation
                clear X; clear value;

            case 'superend'
                localBases=importdata([Path,'localBaseFrames_es',...
                    num2str(el_size), 'e.txt']);
                % Transformation of stresses in the global base frame
                X=stressComponents; value='S';
                shellBaseTransformation
                clear X; clear value;

                % Transformation of strain in global base frame
                X=strains; value='E';
                shellBaseTransformation
                clear X; clear value;
            case 'trab'
        end

    case 1
        % element volumes
        el_vol=importdata([Path, 'V',analysis_type,'_',part2,'_es',...
            num2str(el_size),'.txt']);

        % Imports strains in global corrdinate system
        switch part2
            case 'cort'
```

```matlab
                strains=importdata([Path, 'E_InGlobalCoordinates_es',...
                    num2str(el_size), '_', part, '.txt']);
            case 'inferend'
                strains=importdata([Path, 'E_InGlobalCoordinates_es',...
                    num2str(el_size), '_', part, '.txt']);
            case 'superend'
                strains=importdata([Path, 'E_InGlobalCoordinates_es',...
                    num2str(el_size), '_', part, '.txt']);
            case 'trab'
                % strains from abaqus
                strains=load([Path,'E',analysis_type,'_', part2,'_es',...
                    num2str(el_size),'.txt']);
        end


        % elastic properties
        load('engineeringvalues.mat');
        % Computation of the strain energy density
        disp([analysis_type,num2str(el_size),part]);
        SEDcomparison


    case 2 % computation of the yielding surfaces

        addpath('~/Documents/micromechanics/strength/')


        % Pressure applied on the model [in MPa]
        appliedpressure = 1;
        % import of data from Abaqus [in MPa]
        % Imports strains in global corrdinate system

        switch part2
            case {'cort', 'inferend','superend'}
                fvas=0;

                % imports the file for the corresponding part
                switch part2
                    case 'cort'
                        Sinput=importdata([Path, 'S_InGlobalCoordinates_es',...
                            num2str(el_size), '_', part, '.txt']);
                    case 'inferend'
                        Sinput=importdata([Path, 'S_InGlobalCoordinates_es',...
                            num2str(el_size), '_', part, '.txt']);
                    case 'superend'
                        Sinput=importdata([Path, 'S_InGlobalCoordinates_es',...
                            num2str(el_size), '_', part, '.txt']);
                end

                %Stresses in MPa to GPa
                Sinput=[Sinput(:,1), Sinput(:,2:7)/1000];
```

```matlab
            % strength model for homogeneous properties
            main_yielding_surface;

        case 'trab'
            Sinput=importdata([Path, 'S', analysis_type, '_', part,...
                '_es', num2str(el_size), '.txt']);
            %Stresses in MPa to GPa
            Sinput=[Sinput(:,1), Sinput(:,2:7)/1000];
            switch analysis_type
                case 'ho'
                    % porosity of the homogeneous model
                    fvas =  0.86;
                    main_yielding_surface

                case 'he'
                    GVinput=importdata([Path,'elementCentroidGV_es',...
                        num2str(el_size), '.txt']);
                    poroInput=importdata('elasticityValues.txt');

                    % strength model for heterogeneous properties
                    main_yielding_surface_heterogeneous
            end

            mean(Soutput(:,2))
            min(Soutput(:,2))
            max(Soutput(:,2))

    end


case 3  % computation of the strength for a selection of points

    micromecapath=addpath('~/Documents/micromechanics/strength/');

    switch part2
        case {'cort', 'inferend','superend'}
            fvas=0;

            % imports the file for the corresponding part
            switch part2
                case 'cort'
                    Sinput=importdata([Path, 'S_InGlobalCoordinates_es',...
                        num2str(el_size), '_', part, '.txt']);
                case 'inferend'
                    Sinput=importdata([Path, 'S_InGlobalCoordinates_es',...
                        num2str(el_size), '_', part, '.txt']);
                case 'superend'
                    Sinput=importdata([Path, 'S_InGlobalCoordinates_es',...
                        num2str(el_size), '_', part, '.txt']);
            end
```

```matlab
                  %Stresses in MPa to GPa
                  Sinput=[Sinput(:,1), Sinput(:,2:7)/1000];
                  main_strength

            case 'trab'
                  Sinput=importdata([Path, 'S', analysis_type, '_', part,...
                      '_es', num2str(el_size), '.txt']);
                  %Stresses in MPa to GPa
                  Sinput=[Sinput(:,1), Sinput(:,2:7)/1000];
                  end

            switch analysis_type
                case 'ho'
                      %porosity of the homogeneous model
                      fvas =  0.86;
                    main_strength

                case 'he'
                    GVinput=importdata([Path,'elementCentroidGV_es',...
                        num2str(el_size), '.txt']);
                    poroInput=importdata('elasticityValues.txt');
                    main_strength
            end
        end

end


%%%%%%%%%%%%%%%%%%%%%%%%%%%%%%%%%%%%%%%%%%%%%%%%%%%%%%%%%%%%%%%%%%%%%%%%%%
%                                                                      %
% Subscript shellBaseTransformation.m                                  %
% Change of base for stress or strain components from the local base   %
% defined for each and every shell elements to the global base defined %
% for the solid elements                                               %
% written by: Romane Blanchard, IMWS, TUWIEN                           %
%                                                                      %
%%%%%%%%%%%%%%%%%%%%%%%%%%%%%%%%%%%%%%%%%%%%%%%%%%%%%%%%%%%%%%%%%%%%%%%%%


% global coordinate systems
vglobal1=[1;0;0];
vglobal2=[0;1;0];
vglobal3=[0;0;1];

% %% Example for first element
% % vectors generated by abaqus, local coordinate system
% vabaq1=[-0.42790074; 0.88853981; 0.16552331];
% vabaq2=[0.36077480 ; 0.00000000; 0.93265296];
% vabaq3=[0.83145263 ; 0.47154805;-0.28865453];

% Definition of the transformation matrix from Festigkeitlehre Skriptum p6
```

221

```matlab
% dot(vglobal1, vabaq1)=cos(e1', e1), etc
% Q=[dot(vglobal1, vabaq1), dot(vglobal1, vabaq2), dot(vglobal1, vabaq3);...
%    dot(vglobal2, vabaq1), dot(vglobal2, vabaq2), dot(vglobal2, vabaq3);...
%    dot(vglobal3, vabaq1), dot(vglobal3, vabaq2), dot(vglobal3, vabaq3)];

% In general case:
% Q= | e1,x   e2,x   e3,x |
%    | e1,y   e2,y   e3,y |
%    | e1,z   e2,z   e3,z |

% Stress matrix:
% sigma=| S11   S12   S13 |
%       | S12   S22   S23 |
%       | S13   S23   S33 |

% opens text file
file=fopen([Path,value,'_InGlobalCoordinates_es',num2str(el_size),'_', part,...
 '.txt'], 'w');

% Initialization of variables
counter=0;
counter_error=0;

%% Loop over the shell elements
for i=1:length(X)

    % Current element from file containing the stress components
    curr_el=X(i,1) - (X(1,1)-localBases(1,1));
    counter=counter+1;

    % Construction of the stress matrix in local base
    curr_X_mat=[X(i,2), X(i,5), 0;...
                X(i,5), X(i,3), 0;...
                0     , 0     , X(i,4)];

    % Coordinates of the element-specific local base in the global base
    [idx,val]=find(localBases(:,1)==curr_el);
    curr_local_coord1=localBases(idx(1), 3:5);
    curr_local_coord2=localBases(idx(1), 6:8);
    curr_local_coord3=localBases(idx(1), 9:11);

    % Transformation matrix
    curr_Q=[curr_local_coord1', curr_local_coord2', curr_local_coord3'];

    % Computation of the stress components in the global base
    curr_X_global=curr_Q*curr_X_mat*curr_Q';

    % Results table
    X_global_array(counter, 1:7)=[curr_el, curr_X_global(1,1),...
    curr_X_global(2,2), curr_X_global(3,3), curr_X_global(1,2),...
    curr_X_global(1,3), curr_X_global(2,3)];
```

```matlab
end

% Sorting of the result table with ascending element number
[val_sort, idx_sort]=sort(X_global_array(:,1), 'ascend');
X_global_sorted=X_global_array(idx_sort, :);

% prints the new stresses in the text file
fprintf(file, '%i  %i  %i  %i  %i  %i %i\r\n', X_global_sorted');
% close text file
fclose(file);

disp(['end']);



%%%%%%%%%%%%%%%%%%%%%%%%%%%%%%%%%%%%%%%%%%%%%%%%%%%%%%%%%%%%%%%%%%%%%
%                                                                 %
% Subscript SEDcomparison.m                                       %
% Strain energy density for homogeneous and heterogeneous         %
% computations                                                    %
% written by: Romane Blanchard, IMWS, TUWIEN                      %
%                                                                 %
%%%%%%%%%%%%%%%%%%%%%%%%%%%%%%%%%%%%%%%%%%%%%%%%%%%%%%%%%%%%%%%%%%%%%

% Initialization of variables
elnum=0;
GVnum=0;
counter1=0;counter2=0;counter3=0;

% opens text file
fp_strain_energy_density = fopen([Path,...
    'SED_',part2,'_', analysis_type,'_es',num2str(el_size),'.txt'],'w');


%% computation of the isotropic stiffness tensor
for i=1:length(E3_range)
    E=E3_range(i)*10^3; % MPa
    nu=nu13_range(i);
    stiff_tensor=(E/(1+nu))*[(1-nu)/(1-2*nu), nu/(1-2*nu),nu/(1-2*nu),0,0,0;...
        nu/(1-2*nu), (1-nu)/(1-2*nu),nu/(1-2*nu), 0,0,0;...
        nu/(1-2*nu),nu/(1-2*nu),(1-nu)/(1-2*nu),0,0,0;...
        0,0,0,1, 0, 0;...
        0,0,0,0,1,0;...
        0,0,0,0,0,1];
    GVnum=i+92;
    cell_stiff(i,:)={GVnum, stiff_tensor};

% computation of the transversally isotropic stiffness in GPa
stiff_tensor_trans=...
[C1111_range(i)  C1122_range(i)  C1133_range(i)    0        0        0;
 C1122_range(i)  C2222_range(i)   C1133_range(i)   0        0        0;
```

```matlab
 C1133_range(i)  C1133_range(i)   C3333_range(i)   0        0            0;
   0               0               0      2*C2323_range(i)  0           0;
   0               0               0               0   2*C1313_range(i) 0;
   0               0               0               0        0   2*C1212_range(i)];
cell_stiff_trans(i,:)={GVnum, stiff_tensor_trans*1000}; %saves in MPa
end


%% computation of the eigenstrains
tic
% Loop over the strain list (=number of elements)
for ii=1:length(strains)

     % display advancement of the computation
    if (mod(ii,1000)==0)
        toc
        clc
        disp([num2str(ii),'/', num2str(length(strains))]);
        tic
    end

    % strain matrix
    strain_tensor=[strains(ii,2), strains(ii,7), strains(ii,6);
                   strains(ii,7), strains(ii,3), strains(ii,5);
                   strains(ii,6), strains(ii,5), strains(ii,4)];
    % computation of eigenstrains
    eig_strain_tensor(ii,1:3)=eig(strain_tensor)'; %in MPa
end

%% ordering of the eigenstrains
    [M, idx]=max(eig_strain_tensor, [], 2);
    col1=find(idx==1);
    col2=find(idx==2);
    col3=find(idx==3);

    pstrain(col1,:)=[strains(col1,1), eig_strain_tensor(col1,1), ...
        eig_strain_tensor(col1,2),eig_strain_tensor(col1,3)];
    pstrain(col2,:)=[strains(col2,1), eig_strain_tensor(col2,2), ...
        eig_strain_tensor(col2,3),eig_strain_tensor(col2,1)];
    pstrain(col3,:)=[strains(col3,1), eig_strain_tensor(col3,3), ...
        eig_strain_tensor(col3,1),eig_strain_tensor(col3,2)];

    %% SED for different stacks and types of analysis
for kk=1:length(strains)

        if (mod(kk,1000)==0)
        toc
        clc
        disp([num2str(kk),'/', num2str(length(strains))]);
        tic
        end
```

```matlab
    % allocation to current element
    curr_element=strains(kk,1);
    % finds the grey value associated to the current element
    curr_grey_index=find(el_grey(:,1)==curr_element);
    % assigns grey value to current grey value
    curr_grey = el_grey(curr_grey_index,2);

    % allocates the current component of the stiffness tensor of the
    % current grey value to the current components
    % switches between different computations: homogeneous/heterogeneous
    % and cortical/trabecular
    switch analysis_type
        case 'ho'
            switch part
                case 'trab'
        curr_cell_stiff=cell_stiff_trans{17,2}(1:3, 1:3);
        curr_c3=curr_cell_stiff(3,3);
        curr_c1=curr_cell_stiff(1,1);
                case {'cort','lowerend','upperend'}
        curr_cell_stiff=cell_stiff_trans{206,2}(1:3, 1:3);
        curr_c3=curr_cell_stiff(3,3);
        curr_c1=curr_cell_stiff(1,1);
            end
        case 'he'
            switch part
                case 'trab'
        curr_cell_stiff=cell_stiff_trans{curr_grey-93+1,2}(1:3, 1:3);
        curr_c3=curr_cell_stiff(3,3);
        curr_c1=curr_cell_stiff(1,1);
                case {'cort','lowerend','upperend'}
        curr_cell_stiff=cell_stiff_trans{206,2}(1:3, 1:3);
        curr_c3=curr_cell_stiff(3,3);
        curr_c1=curr_cell_stiff(1,1);
            end
    end

    curr_e1=pstrain(kk,2);
    curr_e2=pstrain(kk,3);
    curr_e3=pstrain(kk,4);

    % computes the strain energy density
    psi_paper(kk)=(1/2)*pstrain(kk,2:4)*curr_cell_stiff*pstrain(kk,2:4)';
    fprintf(fp_strain_energy_density, '%i %i\n', curr_element, psi_paper(kk));
end
%%
vtot=sum(el_vol(:,2))
mean_psi_paper=(1/vtot)*sum(psi_paper.*el_vol(:,2)');
disp(['Mean SED [Pa]= ',num2str(mean_psi_paper*1e6)]);

fclose(fp_strain_energy_density);
```

Romane Blanchard

Curriculum Vitae

Education

February 2011–present	**PhD program**, *Institute for Mechanics of Materials and Structures*, Vienna University of Technology, Austria, Topic: Application of multiscale X-ray physics and engineering mechanics, to Computed Tomography-supported orthopaedics and bone remodeling.
September 2007– October 2010	**Ecole Nationale Supérieure d'Ingénieurs de Limoges- ENSIL, France**, *Master's degree in Material Sciences, Specialisation in Surface Treatments and Coatings*, Topic of the master thesis: Study of the Bauschinger Effect on pipeline applications.
September 2005–July 2007	**Preparation school for French Engineering School in Physics and Chemistry**, *Lycée Roosevelt, Reims, France*.
September 2002–June 2005	**Lycée Clémenceau, Reims, France**, *High school degree, specialization Physics and Chemistry, graduated with honours*.

Work experience

February 2011–present	**Project Assistant**, *Vienna University of Technology*, European project management, research work, dissemination: conference participation and redaction of publications, Member of the European project MySpine: patient-specific spinal treatment simulation.
April 2010– September 2010	**Intern**, *Voestalpine Grobblech GmbH, Technical University of Vienna*, Type of business: steel industry, research organisation. R&D, project management, planning of the experiments
May 2009 –July 2009	**Intern**, *Torino Polytechnic, Italy*, Research topic: Inclusion of carbon nanotubes in cement. Planning of experiments, research work
August 2008– September 2008	**Assistant in Laboratory in the Quality Service**, *Saica Emballages, Venizel, France*, Business type: paper industry. Taking of samples in industrial site, analyses following quality procedures

June 2008–July 2008	**CITRA, Centre d'Ingénierie en Traitements et Revêtements de surface Avancés, France**, *Type of business : technology transfer company in surface treatment technologies.* Implementation of the MSDS (Material Safety Data Sheets) database

Papers and Abstracts accepted for presentations in international conferences

July 1–4, 2012	**Intravoxel Micromechanics for Finite Element Simulation of a Mouse Femur**, R. Blanchard, A. Dejaco, E. Bongaers, and Ch. Hellmich, European Society of Biomechanics (ESB2012), Lisbon, Portugal.
September 10–14, 2012	**Multiscale Micromechanics-Based Elasticity From Micro-CT Scans of Mouse femur**, R. Blanchard, A. Dejaco, E. Bongaers, and Ch. Hellmich, 6th European Congress on Computational Methods in Applied Sciences and Engineering (ECCOMAS 2012), Vienna, Austria.
December 1–6, 2013	**Intravoxel bone micromechanics for microCT-based Finite Element simulations**, R. Blanchard, A. Dejaco, E. Bongaers, and Ch. Hellmich, Fall meeting of the Material Research society in Boston, MA, USA.
May 12–15, 2014	**Intra-voxel micro-elasto-plasticity for CT-based patient-specific fracture risk assessment of vertebrae**, R. Blanchard, C. Morin, A. Vella, Z. Sant, and Ch. Hellmich, Engineering Mechanics 2014, Svratka, Czech Republic.
July 20–25, 2014	**Intra-voxel micro-elasto-plasticity for CT-based patient-specific fracture risk assessment of vertebrae**, R. Blanchard, C. Morin, A. Vella, Z. Sant, and Ch. Hellmich, 11th world congress in computational mechanics, Barcelona, Spain.
August 5–8, 2014	**Intra-voxel micro-elasto-plasticity for CT-based patient-specific fracture risk assessment of vertebrae**, R. Blanchard, C. Morin, A. Vella, Z. Sant, and Ch. Hellmich, EMI 2014 Engineering Mechanics Institute Conference, McMaster university, Canada.

Publications in peer-referred journals

2013	**Intravoxel bone micromechanics for microCT-based finite element simulations**, R. Blanchard, A. Dejaco, E. Bongaers E., and Ch. Hellmich, Journal of Biomechanics 46(15), pp 2710-2721.
2014	**A multiscale approach for bone remodeling simulations: linking scales from collagen to trabeculae**, M. Colloca, R. Blanchard, Ch. Hellmich, K. Ito, and B. van Rietbergen, Bone, available online, http://dx.doi.org/10.1016/j.bone.2014.03.050.

Publications submitted or in preparation for peer-referred journals

submitted in May 2014	**Quantitative intravoxel analysis of microCT-scanned resorbing ceramic biomaterials**, A. Czenek, R. Blanchard, A. Dejaco, O. E. Sigurjónsson, G. Örlygsson, P. Gargiulio, and Ch. Hellmich, Journal of Material Research MRS.

submitted in August 2014	**Patient-specific fracture risk assessment of vertebrae. Part I: Hierarchical intravoxel X-ray physics for CT grey value to bone composition conversion**, R. Blanchard, A. Malandrino, Z. Sant, and Ch. Hellmich, Journal of Biomechanical Engineering ASME.
submitted in August 2014	**Patient-specific fracture risk assessment of vertebrae. Part II: Micro-elastoplasticity for composition to safety factor conversion**, R. Blanchard, C. Morin, A. Vella, Z. Sant, and Ch. Hellmich, Journal of Biomechanical Engineering ASME.
to be submitted in September	**How space flight laters mouse bone mechanics: combining X-ray physics, homogenization theory, and Finite element analyses**, K. Luczynski, R. Blanchard, A. Dejaco, A. Giuliani, R. Cancedda, and Ch. Hellmich.